BINDING SERVICES
Tel +44 (0)29 2087 4949
Fax +44 (0)29 20371921
e-mail bindery@cardiff.ac.uk

Gallium Nitride Processing for High Power Microwave Devices

Luke Farrant

ProQuest LLC
789 East Eisenhower Parkway
P.O. Box 1346
Ann Arbor, MI 48106-1346

Acknowledgements

I would like to thank everyone who helped me with any aspect of getting this PhD finished and submitted; I could not have done it without you. In particular I would like to mention Adrian Porch, Richard Perks, Chris Dunscombe, Dave Westwood, Gareth Edwards, Rolfe Jones, John Thompson, Karen Barnett, Angela Sobieserski, Tyrone Jones, Scott Lewis, Paul Tasker, Pete McGovern, Paul Senkans, Mark Dineen, Jeff Kettle and Hassan Hirshy. I would also like thank Cardiff University's School of Engineering and Oxford Instruments Plasma Technology for their funding of this PhD.

Abstract

This thesis contains literature reviews relating to inductively coupled plasmas and their use in etching gallium nitride with chlorine based plasmas. The properties of gallium nitride, how these properties make gallium nitride a suitable material for high power microwave transistors and how such transistors will help improve the systems in which they might be used are also reviewed. In this thesis, a novel, non-destructive method of measurement of the conductivity of a semiconductor through measurement of the increase in the bandwidth of the resonant peak of a microwave dielectric resonator when it is brought near a semiconductor wafer is presented. Using this method the conductivity of a thin gallium nitride film is obtained and found to be within the expected range; it was found to be very difficult to measure the conductivity of this gallium nitride wafer using a four-point probe, as the film was too thin. Also presented in this thesis are studies of the etch characteristics of gallium nitride and photoresist in mixed boron trichloride and chlorine plasmas generated in two Oxford Instruments inductively coupled plasma etchers (ICP 180 and 380). The ICP 380 was used to etch the mesa isolation of gallium nitride based heterojunction field effect transistors that were fabricated at Cardiff University. A method of making the angle of the mesa sidewall acute by melting of the photoresist is presented. An acute mesa-sidewall angle facilitated the easy traverse of the mesa edge by the gate metal. Characterisations of ohmic and Schottky contacts that were fabricated as part of the effort to produce a working gallium nitride based heterojunction field effect transistor are presented and reasons given for the failure of some of the ohmic contacts. The dc characteristics of the best transistor fabricated during the project are presented.

List of abbreviations

2-DEG	Two dimensional electron gas
CBM	Conduction band minimum
CH	Crystal-field split-off
dp	Decimal places
DR	Dielectric resonator
E_C	Energy of CBM
ECR	Electron cyclotron resonance
ECR-MBE	ECR assisted MBE
E_D	Donor energy
EDX	Energy dispersive x-ray
EIT	Extrapolated infrared transmission
EMF	Electromotive force
EXTR	Extrapolation of level-pressure graph
FEM	Finite element modelling
FET	Field effect transistor
FLAPW	Full-potential linearised augmented plane wave
FTIR	Fourier transform infrared spectroscopy
FWHM	Full width at half maximum
HCl	Hydrochloric acid
HCVD	Hydride chemical vapour deposition
HEMT	High electron mobility transistor
HF	High frequency
HF (acid)	Hydrofluoric acid
HFET	Heterojunction field effect transistor
HH	Heavy hole
HVPE	Hydride vapour phase epitaxy
ICP	Inductively coupled plasma
IL	Insertion Loss
IT	Infrared Transmission
LDA	Local density approximation
LEO	Lateral epitaxial overgrowth
LH	Light hole
LTP	Low temperature photoluminescence
MBE	Molecular beam epitaxy
MESFET	Metal semiconductor field effect transistor
MISHFET	Metal insulator HFET
MOCVD	Metal-organic chemical vapour deposition
MOS	Metal oxide semiconductor
MOSHFET	Metal oxide HFET
MQW	Multi quantum wells
N_I	Nitrogen interstitial

OES	Optical emission spectra
O_N	Oxygen in gallium site in GaN lattice
PA	Power amplifier
PR	Photoresist
QMS	Quadrapole mass spectrometry
RF	Radio frequency
RIE	Reactive ion etching or etcher
RTA	Rapid thermal annealer
SEM	Scanning electron microscope
Si_{Ga}	Silicon in gallium site in GaN lattice
SIMS	Secondary ion mass spectroscopy
TE	Transverse electric
TLM	Transfer length method
TM	Transverse magnetic
VBM	Valence band maximum
V_{Ga}	Gallium vacancy in GaN lattice
V_N	Nitrogen vacancy in GaN lattice
VTHEM	Variable temperature hall effect measurements
WZ	Wutzite
HTA1	HEMT test array 1

Table of Contents

1 Introduction

Since the discovery of the existence of electromagnetic radiation by James Clerk Maxwell and Heinrich Hertz in the late 19th Century mankind has engineered systems, more or less complex, to make use of the properties of these electromagnetic waves (principally their ability to travel long distances quickly without any intervening media and secondly their usefulness as a carrier of information once modulated). During the second world war, radar was a key innovation that lead to the defeat of the German *Luftwafer* and Allied air supremacy throughout the later stages of the war and could be said to be a key reason for their victory. Since then, new technologies have been invented (satellite navigation) or innovated (digital radio) that use RF radiation. These and older systems have constantly been improved i.e. made more efficient and smaller. An example of the now common use of radio frequency engineering is the now ubiquitous mobile phone and satellite television, the end products of multi-billion pound industries.

The emitters used in all forms of RF power applications require high power RF amplifiers emitting from tens to thousands of watts. Today's solid-state power amplifiers are made predominantly from silicon, though gallium arsenide (GaAs) and indium gallium phosphide (InGaP) are also used, depending on required specifications and purpose. With these materials there is a compromise between the higher powers available with Si based transistors and the high frequencies available with GaAs and InGaP. Si based transistors will handle tens to hundreds of watts but only at frequencies lower than 1GHz, GaAs based technologies generate less than ten watts of power but they will do so at tens of gigahertz. For high power RF technologies involving hundreds or thousands of watts power, vacuum tube technology needs to be used. A solid-state technology that could transmit hundreds or thousands of watts of RF power would be desirable for replacing large and expensive vacuum tube technologies such as those used in satellite communications and TV transmission. Such technology would also enable the improvement (miniturisation, increased efficiency and reduced costs) of systems that currently rely on silicon MOS power transistors.

Wide band gap semiconductors (silicon carbide (SiC); the III-nitrides gallium, aluminium and indium nitride (GaN, AlN and InN); and diamond) have for a long time been regarded as materials that could be engineered into high power transistors. SiC MESFETs are envisaged as replacements for Si MOS power switching transistors (although recently the use of the different poly-types of SiC to create a heterostructure means that SiC might find other applications in time). High mobility GaN and its heterostructured alloys with AlN and InN are expected to yield devices that will generate hundreds of watts across a broad range of RF frequencies. Such devices would enable a wide range of improvements in RF power amplifiers and the applications that utilise them.

Although SiC and the III-nitrides have been developed as power transistors for approximately similar amounts of time, the III-nitrides have seen the most rapid development. This is partly due to the greater funding allocated to research into the III-nitride device technology by the US military, partly due to the greater commercial interest in III-V microwave devices for wireless communications, but mainly due to the fact that III-nitride materials are used in the fabrication of light emitters which emit across the entire visible spectrum. At the time of writing, a state-of-the-art device developed by Toshiba Group had been reported that produced 174W at 6GHz.

Several problems are characteristic of engineering wide band gap semiconductors. Due to their strong bonds (the cause of their wide band gap and hence high power carrying ability) the materials are difficult to etch with wet chemical etching and hence any etching of these materials must be performed with dry or plasma etches which cause damage to the material. Similarly, because of the high bond strength (leading to dense/ hard/ un-reactive materials) good ohmic contacts are difficult to form in these materials. Finally, p-type doping of these semiconductors is also difficult hence making good bipolar devices extremely challenging if not impossible to produce.

Due to the challenges of fabricating bipolar devices, the research effort focussed on gallium nitride has focussed on unipolar devices. Heterojunction field effect transistors (HFETs) made with GaN and the alloy aluminium gallium nitride (AlGaN) are the most advanced device type at the time of writing. III-nitride HFETs are

typically made with the GaN forming the bulk of the material and possibly a cap layer, with the wider band gap AlGaN used to form the 2-DEG at the interface between the GaN and the AlGaN.

In order to make high power devices from this type of material several basic steps are necessary. A way is needed to isolate the source, drain and gate from each other so that current only flows between the source and drain in the region covered by the gate. Ohmic contacts with contact resistivities below $1x10^{-6}$ Ωcm^{-2} are required. A rectifying contact for source-drain current modulation is essential; for high frequency gallium nitride devices this implies a Schottky contact as the hole mobility in GaN is much lower than the electron mobility. Knowledge of the conductivity of the material allows the expected device performance to be calculated; hence, for all device work a method for verifying the conductivity of the wafers before any processing begins is indispensable. Other important aspects are the material quality and structure and device design.

Thesis outline

The second chapter of the thesis takes a more detailed look at gallium nitride based heterostructure field effect transistors (HFETs). What are the properties of this material that make devices fabricated from it so promising as high power radio frequency transistors? In this second chapter also, the effect of the characteristics of gallium nitride on the performance of the transistors produced from this material are also illuminated and the effect that these improved devices will have on the various systems incorporating them is discussed. Further on in this chapter, the formation mechanism of the two dimensional electron gases (2-DEGs) in AlGaN/GaN HFETs is discussed as it is notably different to the formation mechanism of the 2-DEGs in AlGaAs/GaAs devices. Finally, the various problems that are observed in AlGaN/GaN devices such as current slump, RF dispersion etc. are listed with a short discussion.

The third chapter of this thesis is an extensive, though not absolutely complete, literature review of the properties of gallium nitride. This third chapter is intended to

be a reference chapter to be used to find appropriate values for various properties of gallium nitride when the need arose; however, reading the chapter will give the reader a good foundation for work with the material. Many of the values quoted are based on very pure crystals of GaN, it is thought that this so-called bulk material gives a more accurate picture of the properties of gallium nitride than the flawed material grown epitaxially. In the future, with homoepitaxial growth as an option, epitaxial material with properties close to that of bulk material might be grown. The third chapter is split into sections in the following order: crystal properties, thermal properties, band-gap and related parameters, mechanical properties and electrical properties. In all these sections it is the most common form of gallium nitride that is dealt with, the form that crystallises in the wurtzite phase.

The fourth chapter deals with the problem of ensuring that a wafer once grown or bought is of a suitable conductivity for processing into devices. It is a great advantage in any such analytical procedure if the wafer being tested is left intact by the process of being tested, such as is the case with the four-point probe. Unfortunately, the four-point probe method only works if the sample being tested has a thick conductive region of several tens of microns, which was not the case for the samples being used in this work. Another commonly used method for evaluating the conductivity of a sample is the Van de Pauw Hall effect method; however, this method involves not only cleaving the wafer but also etching it and patterning it and then depositing patterned ohmic contacts; major steps for the inexperienced, all of which might affect the results, and this is before the actual test of the conductivity is even begun. Obviously a simple non-destructive method of measuring the conductivity of a wafer, like that of the four point probe, but applicable to wafers such as ours would have been an advantage in processing. Such a method, using the effect of microwave power dissipation by conduction in a wafer on the bandwidth of a microwave dielectric resonator's resonant peak was developed and used to characterise our wafers. In chapter four, the theory behind this method of measuring simply and non-destructively the conductivity of a semiconductor wafer is explained. The experimental method used to measure the conductivity of a wafer and the results that were gained testing the method on a GaN on sapphire wafer are presented. To the best of the author's knowledge, this method of measuring the conductivity of GaN wafers is novel and original work.

The first step in the fabrication of an orthodox field effect transistor is the device isolation. In this thesis, device isolation was performed by etching the HFET material. The machine used to do this etching was an Oxford Instruments ICP 380 and the etch chemistry used was BCl_3/Cl_2 i.e. chlorine based. In chapter five, a thorough literature review of the etching of gallium nitride in chlorine based plasmas is given. This review includes some basic theory about the parameters that control the etch rate of a material. Later on in the chapter, experimental work that was performed on an ICP 180 at the Oxford Instrument's site in Yatton is presented. This work was conducted in order to find an etch that was not only highly selective of gallium nitride over photoresist but that also had a reasonably high etch rate. Unfortunately neither a high selectivity nor a high etch rate were discovered in the course of the experiment and various mistakes led to a data quality that could have been much better. Important lessons were learnt from this experiment. Later results on the same machine showed that the Oxford Instruments machines are a lot different to those that commonly feature in the literature, since higher powers are required in order to get etch rates similar to those found in the literature. Also presented in this chapter are the results taken at Cardiff University using the ICP 380. These results include the variation of etch rate of GaN and the selectivity of GaN to photoresist as a function of five of the key plasma variables. These latter results were of a much better quality than those taken with the ICP 180. All these results are novel (no similar results taken with an Oxford Instruments machine have been published); however, gallium nitride has definitely been etched with BCl_3/Cl_2 plasmas before, though only one other study of the selectivity of GaN to photoresist in a BCl_3/Cl_2 plasma has been.

The sixth chapter presents the work carried out on the processes required for the fabrication of a gallium nitride based field effect transistor. These begin with a photoresist reflow method that was used to ensure that the sidewalls of the mesa isolation were of a sufficiently shallow angle so that the gate metal would experience no thinning on passing over the discontinuity at the mesa's edge. This problem of gate metal thinning had already been reported by a predecessor at Cardiff; however, this problem was not so pressing with the AlGaN/GaN material that was used here as only a very shallow etch was need to reach the 2-DEG and hence make sufficient isolation between devices. It has been noticed recently that the problem of RF dispersion has

been overcome in GaN based HFETs as is the case with GaAs based HFETs by making sure that the surface is far removed from the 2-DEG. If this becomes a standard method of preventing RF dispersion then photoresist reflow, coupled, with a mesa etch may prove useful. Other work presented in this chapter includes the work on the ohmic and Schottky contacts to this material and on the mesa etch. The etch depths were made as shallow as possible and, in the course of experiments, it was found that the shallowest mesa etch that could be processed with optical microscopes was about 50 nm. The ohmic contacts fabricated in this work were all of the form Ti/Al/spacer layer/Au with the spacer layer being either Ti, Ni or Ti/Pt. The thicknesses of the various metal layers were either taken directly from the literature or innovated from the literature values. Our results show, as has been remarked by papers in the literature, that just because a contact works with one material in one lab it is far from certain that it will work as well wherever it is applied. This means that for each material used, and for each lab that it is used in, experiments will have to be performed in order to ensure that a good contact is found. Of the contacts fabricated by the author, none showed the required low contact resistance. Possible reasons for this are given in the chapter. A workable Schottky contact is developed and analysed using IV characterisation.

Despite the fact that the sheet resistance of the material was higher than would have been ideally liked, and the fact that a good ohmic contact was never found, a batch of working FETs were fabricated and the dc transistor characteristic of the best of this set of devices is presented at the end of this chapter.

2 Gallium nitride based microwave devices

2.1 Why gallium nitride microwave devices?

Gallium nitride (GaN), aluminium nitride (AlN) and indium nitride (InN) and their alloys (AlGaN, InGaN) are classed jointly as the III-nitrides. Transistors fabricated from the III-nitrides have the potential to improve the performance of power amplifiers (PAs) beyond that which would be possible with conventional devices fabricated from the III-Vs or silicon. Some of the properties that make GaN especially suited for high frequency power amplification are:

1. A high bond strength: this is due to the more ionic nature of the III-nitride bonds compared to the predominantly covalent nature of Si and GaAs. The high atomic stability leads to a wide band gap: 3.43 – 3.44 eV at room temperature [1 & 2], a high breakdown voltage ~ 3MV/cm [3 & 4], and a hard, dense material resistant to radiation damage. The ionicity of the bonds increases for AlN, which has yet higher bond strength.

2. A relatively high thermal conductivity of 1.7 W/cm-K [5] (higher than that of Si), with lateral epitaxial overgrown (LEO) GaN measured to have a thermal conductivity greater than 2 W/cm-K [6].

3. High electron peak and saturation velocities over a wide range of temperatures. The simulated peak velocity varies from 3.3 x 10^7 cm/s at 77K to 2.1 x 10^7 cm/s at 1000K [7]; however the effect of interaction between hot electrons and hot phonons in real devices limits the saturated drift velocity to approximately 1x10^7 cm/s [8].

4. Ability to alloy with either AlN or InN, allowing heterostructure based devices to be fabricated.

A wide band gap means that there is a small intrinsic carrier density at a given temperature compared to silicon or gallium arsenide with their lower band gaps. Equation 2-1 gives the intrinsic carrier density in a semiconductor.

$$n_i = (N_c \cdot N_v)^{\frac{1}{2}} \exp\left(-\frac{E_g}{2k_B T}\right) \quad \text{Equation 2-1}$$

For GaN N_C and N_V are given by Equation 2-2 and Equation 2-3 respectively [9].

$$N_c \cong 4.3 \times 10^{14} \times T^{3/2} \ cm^{-3} \quad \text{Equation 2-2}$$

and

$$N_v \cong 8.9 \times 10^{15} \times T^{3/2} \ cm^{-3} \quad \text{Equation 2-3}$$

Combining Equation 2-1, Equation 2-2 and Equation 2-3 gives a room temperature intrinsic concentration for GaN of close to zero compared to ~ 1.5 x 10^{10} cm^{-3} for Si and 1.6 x 10^6 cm^{-3} for GaAs. From the above equations the intrinsic carrier density of GaN reaches ~ 5 x 10^6 cm^{-3} at T = 400°C. The wide band gap and high thermal conductivity means the ability to operate at high temperatures is only affected by the reduction in carrier velocity caused by increasing the channel temperature and the effect that this has on the output power (see Figure 2-1).

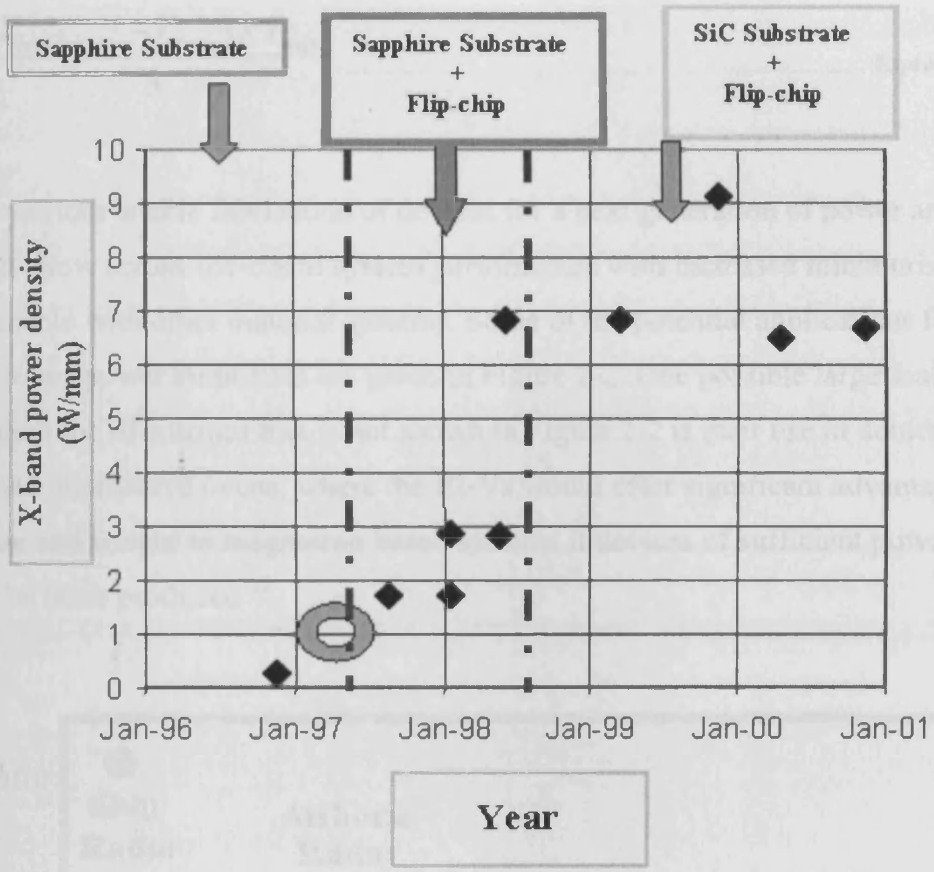

Figure 2-1 Showing the effect of improving thermal management on the X-band power density of power amplifiers using gallium nitride based transistors [10].

High electron velocities lead to the potential for high current densities. After [11] the saturated drain current of an HFET per unit gate width is given by

$$I_{dss} = qn_s v_s \quad \text{..... Equation 2-4}$$

where q is the electronic charge, n_s is the electron concentration in the two dimensional electron gas (2-DEG) and v_s is the saturation velocity. Inserting values of $n_s \geq 5 \times 10^{12}$ cm^{-2} and $v_s \geq 0.5 \times 10^7$ cm/s for a realistic HEMT gives a current density of ≥ 0.4 A/mm. High current densities coupled with high breakdown voltages (hundreds of volts with field-plate technology) mean high power devices. Equation 2-5 gives the approximate power performance to be expected from a device based on its dc IV characteristics.

$$P = \frac{(V_{breakdown} - V_{knee}) \times I_{max}}{8} \quad \text{Equation 2-5}$$

The III-nitrides enable fabrication of devices for a next generation of power amplifiers that will allow across-the-board system performance with increased miniaturisation, unobtainable with other material systems. Some of the potential applications for III-nitride based power amplifiers are given in Figure 2-2. One possible large scale application for III-nitrides that is not shown in Figure 2-2 is their use in domestic solid state microwave ovens, where the III-Vs would offer significant advantages in cost, size and weight to magnetron based systems if devices of sufficient power were ever to be mass produced [12].

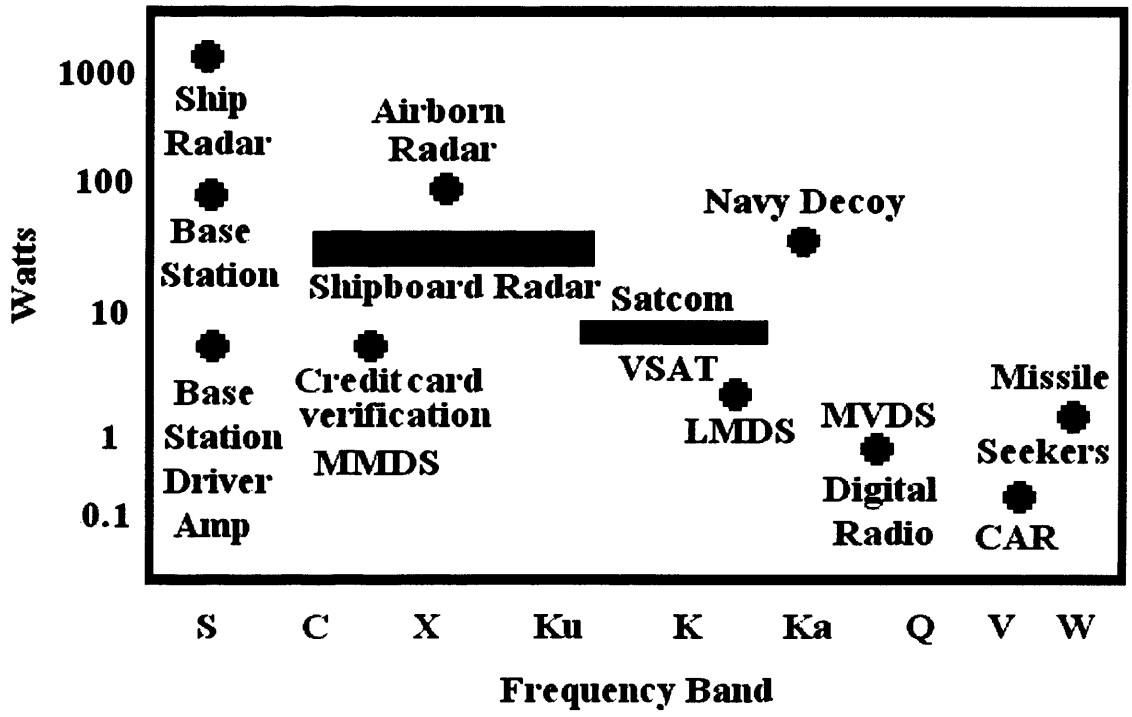

Figure 2-2 Some of the systems that the III-nitrides will enable or improve [13].

Table 2-1 shows the transistor characteristics that the III-nitride material system will improve and the effect that this improved device performance will have on system level performance. The III-nitrides are expected to offer an improved power per unit gate width compared to GaAs and Si based devices. Such an improvement means that fewer devices will be needed to reach the same output power. Using fewer devices

improves the efficiency of the amplifier and its reliability, whilst also increasing its input impedance. Increasing the impedance of the system makes matching to 50Ω easier, reducing system complexity and therefore both system size and cost.

Smaller devices also have intrinsically smaller capacitances, which facilitates the high frequency operation possible due to the high electron velocity of III-nitride HEMTs, thus setting the III-nitrides apart from SiC (Figure 2-3). A small capacitance also allows the device to be usefully matched to a 50Ω system over a wider bandwidth, or to the same bandwidth with less complex matching networks [14].

Need	Enabling feature	Performance advantage
High power / unit width	Wide band gap, high field	Compact, ease of matching
High voltage operation	High breakdown field	Eliminate / reduce step down
High linearity	HEMT topology	Optimum band allocation
High frequency	High electron velocity	Bandwidth, m-wave / mm-wave
High efficiency	High operating voltage	Power saving, reduced cooling
Low noise	High gain, high velocity	High dynamic range receivers
High temperature operation	Wide band gap	Rugged, reliable, reduced cooling
Thermal management	SiC substrates	High power devices with reduced cooling needs
Technology leverage	Direct band gap enabler for lighting	Driving force for low cost technology

Table 2-1 From left to right the first column gives the required transistor characteristic, the second column gives the material properties that enable the characteristic in the first column and the third column gives the system level advantage of the device characteristic (after [15]).

Operation over a wide spectrum opens up military applications such as electronic decoys (devices that admit large powers simultaneously over a wide range of frequencies in order to confuse missile tracking systems) and multiple-application single-antenna systems. Multiple-application single-antenna systems are, as the name suggests, where many applications such as communications, radar, jamming, weapon targeting and other electronic warfare procedures are all accomplished using the same hardware and a single antenna. Such systems would allow significant size, weight and cost reductions to both air and sea borne systems (which would no doubt eventually find use in the civilian marketplace) [13].

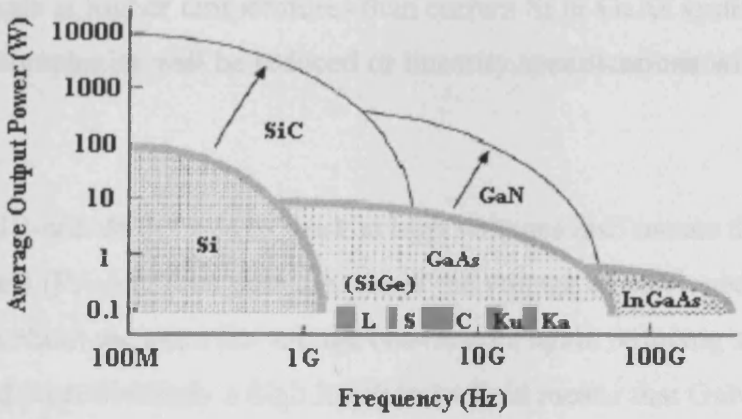

Figure 2-3 Average output power versus switching fequency for Si, GaAs and InGaAs devices with expected specification of SiC and GaN electronic devices [16]

One of the main factors that limits the size of a power amplifier today is the cooling fins and fans needed to keep it within the operational temperature range. Devices made from the III-nitrides, because of their wide-band gap, have a much lower intrinsic carrier concentration and hence will continue to operate at temperatures much higher than devices made from the III-Vs or from silicon. This, coupled with growth on SiC substrates (with a thermal conductivity of close to 4 W/cm-K), and the high efficiency that results in high voltage operation of a lesser number of devices, means that III-nitride device can be operated at higher temperatures, thus reducing the need for bulky cooling systems.

Third and fourth generation mobile telecommunications will require highly linear power amplification and it is expected that this power amplification will be produced

from base stations the size of a briefcase, able to be positioned at the top of lamp poles or church steeples. The next generation of mobile-phone base stations will require considerably less system complexity in order to be small enough. III-nitride devices have an intrinsically high linearity due to the high transconductance associated with heterostructure field effect transistors, which can be coupled with operation closer to A-class. The operation of A-class is intrinsically linear but also intrinsically inefficient. Operation in or near to A-class means decreased system complexity as the harmonic distortion from B-class operation no longer has to be compensated for. A greater inefficiency means a hotter device. There is thus a trade-off between linearity and efficiency and thus device temperature. GaN devices should be able to operate at higher temperatures than current Si or GaAs systems; hence either system complexity will be reduced or linearity specifications will be met,or both.

The ability of III-nitride devices to work at high voltages also means that III-nitride power amplifiers (PAs) will be able to work at the voltage of 28V used in commercial base stations without the need for voltage conversion, again reducing system complexity and cost. Similarly a high breakdown field means that GaN devices can be utilized in front end amplifiers without the need for diode protection and hence offer an improvement to GaAs power amplifiers [17].

For space applications it is advantageous if the amplifier is light-weight and reliable since it will cost less to put in orbit and less to maintain it there. Solid state amplifiers which are both light-weight and reliable would therefore be beneficial to satellite communications. Solid-state amplifiers, however, have never been able to produce sufficient power at the right frequencies, meaning that space applications still rely on the use of vacuum electronics. Vacuum electronics, although reliable and efficient, are also at the moment bulkier and more expensive to produce than solid state solutions (though currently work is being carried out to reduce the price of such units [18]). The III-nitrides have the potential to provide a high power, high frequency solid-state solution that is rugged and sufficiently radiation proof for space borne applications.

Apart from these intrinsic advantages, as pointed out in Table 2-1, the III-nitride material system also has the intrinsic advantage of having a direct band-gap, tuneable

over all of the visible spectrum into the UV. LEDs and lasers made from the III-nitrides enable a wide range of consumer applications such as full colour LED screens and blue laser optical disk readers, meaning that III-nitride technology (i.e. the technology associated with the growth and processing of the III-nitrides) has seen a much larger investment than would have been the case if the only applications of the materials were in the microwave part of the spectrum. This important difference between the III-nitrides and SiC has meant that III-nitrides have had a much quicker development time than SiC devices, which were initially thought to be competitive with the III-nitrides in the low GHz region but will now most likely see their use restricted to very high power, low frequency switching applications.

2.2 2-DEG formation in III-nitride HFETs

In Section 2.1 it was noted that GaN may be alloyed with AlN or InN; this has the effect of increasing or decreasing, respectively, the band gap of the alloy. The ability to engineer the band gap of the III-nitride material system means that heterostructure devices may be fabricated. The lack of a good p-type dopant for GaN has lead to concentration of research on unipolar devices (N.B. magnesium is the best known acceptor for GaN with an acceptor level approximately 250 meV above the valence band edge, leading to hole concentrations two orders of magnitude to low for practical devices to be easily fabricated). Heterostructure field effect transistors in particular have been focussed on due to their high mobility and high transconductance.

The formation mechanism of the 2-DEG in AlGaN/GaN base heterostructure devices is different to that of AlGaAs/GaAs devices. Due to the asymmetry of the wurtzite (WZ) GaN crystal in [0001] direction (Figure 2-4) (for an explanation of the notation used to describe wurtzite crystals see Appendix A), a spontaneous electrical polarisation (P_{SP}) occurs in the directions shown in Figure 2-5 (the direction of P_{SP} is dependent on the polarity of the crystal). As well as the spontaneous polarisation there is a strain-induced or piezoelectric polarisation P_{PE} caused by the lattice mismatch between the AlGaN and the GaN. The electric field caused by the spontaneous polarisation may be as large as 3MV/cm, with the piezoelectric polarisation having a magnitude of approximately 2MV/cm [19].

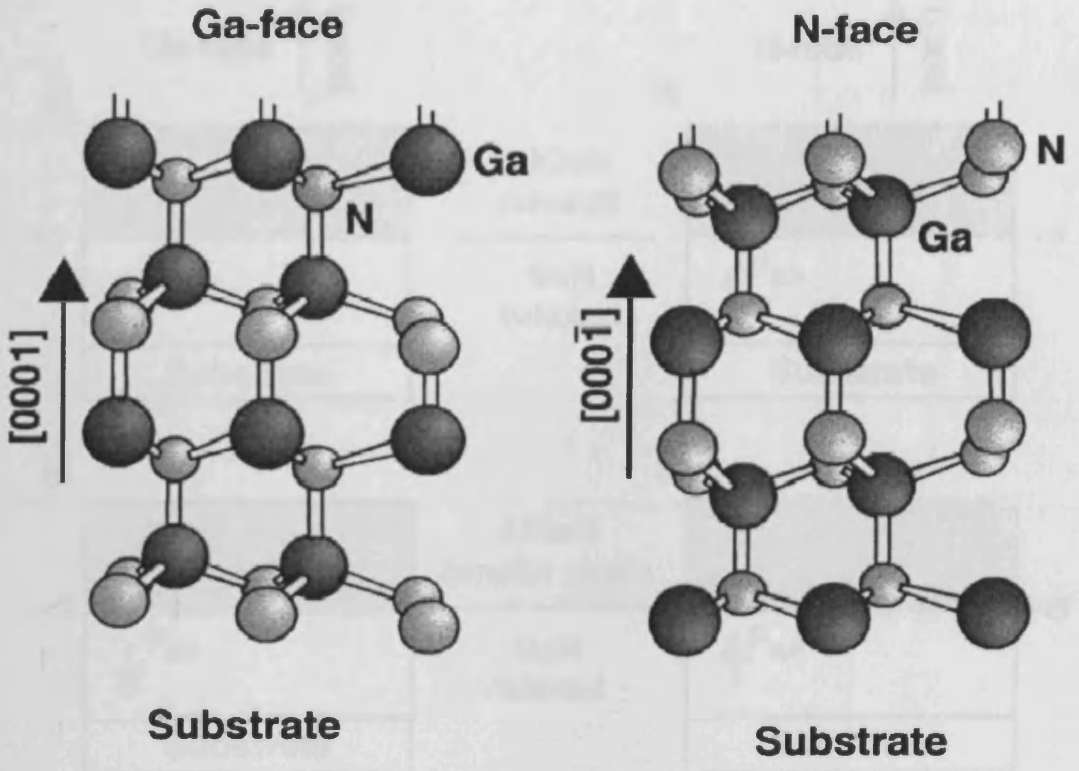

Figure 2-4. Stacking order of GaN showing lack of symmetry: Dark spheres Ga, Light spheres N. Also shown is the definition of the [0001] direction (from Ga to N) and (left) Ga-face and (right) N-face crystal polarity [19]

The total polarisation, P is given by the sum P_{SP} and P_{PE} and at a discontinuity in the polarisation such as that at a heterojunction there is an induced charge; hence at a heterojunction there will be a sheet charge density given by Equation 2-6 [19].

$$\sigma = P(top) - P(bottom)$$
$$\sigma = \left[P_{SP}(top) + P_{PE}(top)\right] - \left[P_{SP}(bottom) + P_{PE}(bottom)\right] \quad \text{..... Equation 2-6}$$

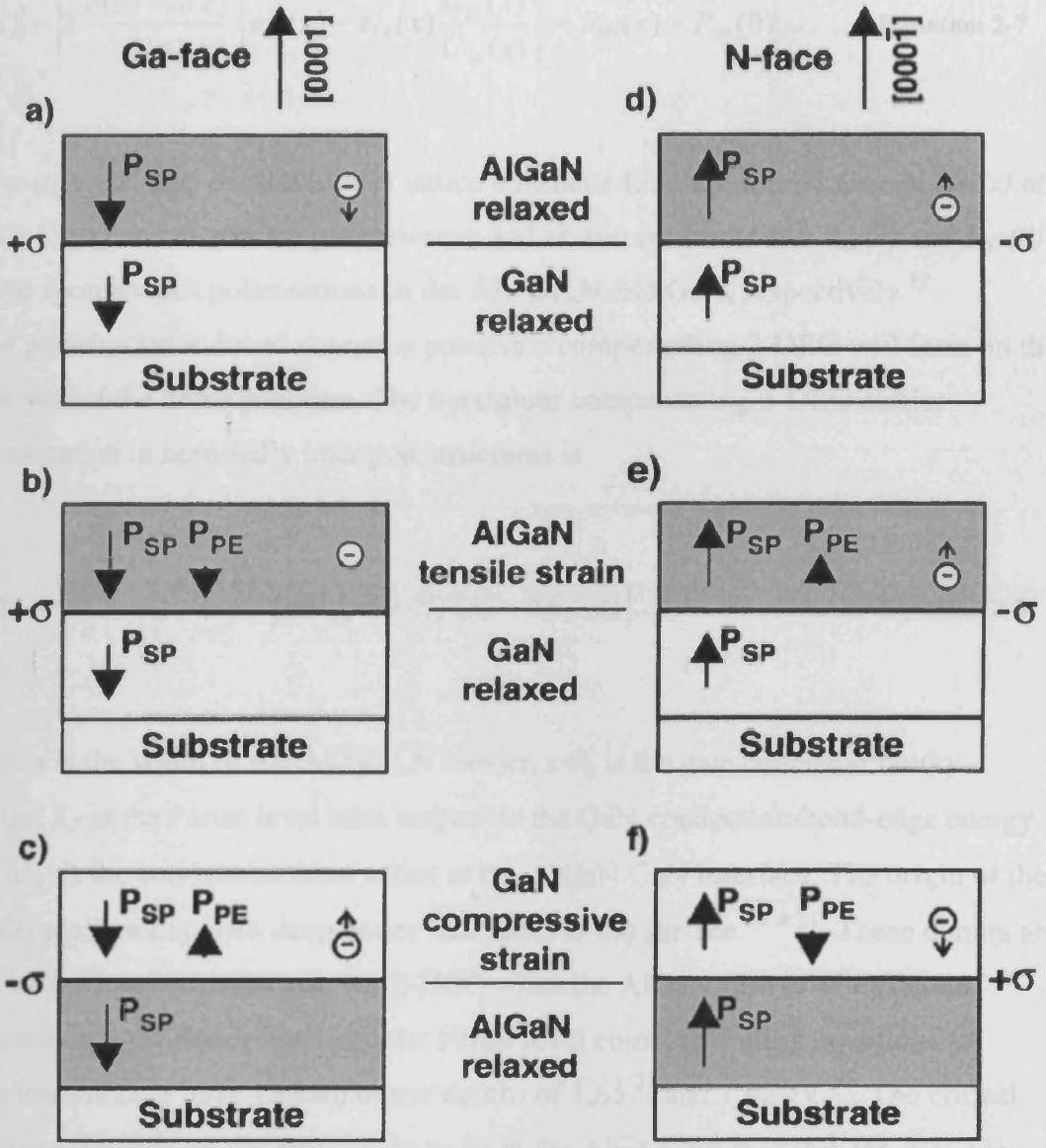

Figure 2-5 Schematic of heterostructures using AlGaN and GaN showing direction of spontaneous and piezoelectric polarisation vectors and sign of charge density induced at interfaces [19].

Depending on whether the film is anion or cation faced and depending on the strain in the component layers, the sum of the polarisations at the interface leads to either a positive or negative charge density at the heterojunction. Charge is also accumulated at the surface and at the substrate, as the polarisation charge densities are dipole like. For an N-face $GaN/Al_xGa_{1-x}N/GaN$ heterostructure the polarisation induced charge density is given by

$$|\sigma(x)| = \left| 2\frac{a(0)-a(x)}{a(x)}\left\{ e_{31}(x) - e_{33}(x)\frac{C_{13}(x)}{C_{33}(x)} \right\} + P_{SP}(x) - P_{SP}(0) \right| \quad \text{..... Equation 2-7}$$

where $a(0)$ and $a(x)$ are the (0001) lattice constants for GaN and $Al_xGa_{1-x}N$, $e_{31}(x)$ and $e_{33}(x)$, $C_{13}(x)$ and $C_{33}(x)$ are piezoelectric and elastic constants and $P_{SP}(x)$ and $P_{SP}(0)$ are the spontaneous polarisations in the $Al_xGa_{1-x}N$ and GaN, respectively [19].
If the polarisation induced charge is positive a compensating 2-DEG will form on the other side of the heterojunction. The maximum compensating 2-DEG carrier concentration in nominally undoped structures is

$$n_S(x) = \frac{\sigma(x)}{e} - \left(\frac{\varepsilon_0 \varepsilon(x)}{de^2} \right) \left[e\Phi_b(x) + E_F(x) - \Delta E_C(x) \right] \quad \text{..... Equation 2-8}$$

where d is the width of the $Al_xGa_{1-x}N$ barrier, $e\Phi_b$ is the gate contact Schottky–Barrier, E_F is the Fermi level with respect to the GaN conduction-band-edge energy, and ΔE_C is the conduction band offset at the AlGaN/GaN interface. The origin of the 2-DEG electrons is from deep donor like states at the surface [20 & 21]. These donors are only ionized and contribute to the 2-DEG when the AlGaN film is of sufficient thickness that the donor level and the Fermi level coincide. Fitting equations to experimental data have yielded donor depths of 1.65 [21] and 1.42 eV [20]. The critical thickness depends on the ratio of Ga to Al in the AlGaN but is ~ 35Å for $Al_{0.34}Ga_{0.64}N$ on GaN [21].

Figure 2-6 (a) shows the conduction band for a GaN/AlGaN/GaN heterostructure device and a AlGaN/GaN device. The two may be distinguished as the GaN/AlGaN/GaN device has a higher effective Schottky barrier due to the separation of the negative polarisation charge at the upper GaN/AlGaN interface and the positive charge at the metal/GaN interface. This effect is shown again in Figure 2-7 with the juxtaposed charges at the surface for AlGaN/GaN indicated.

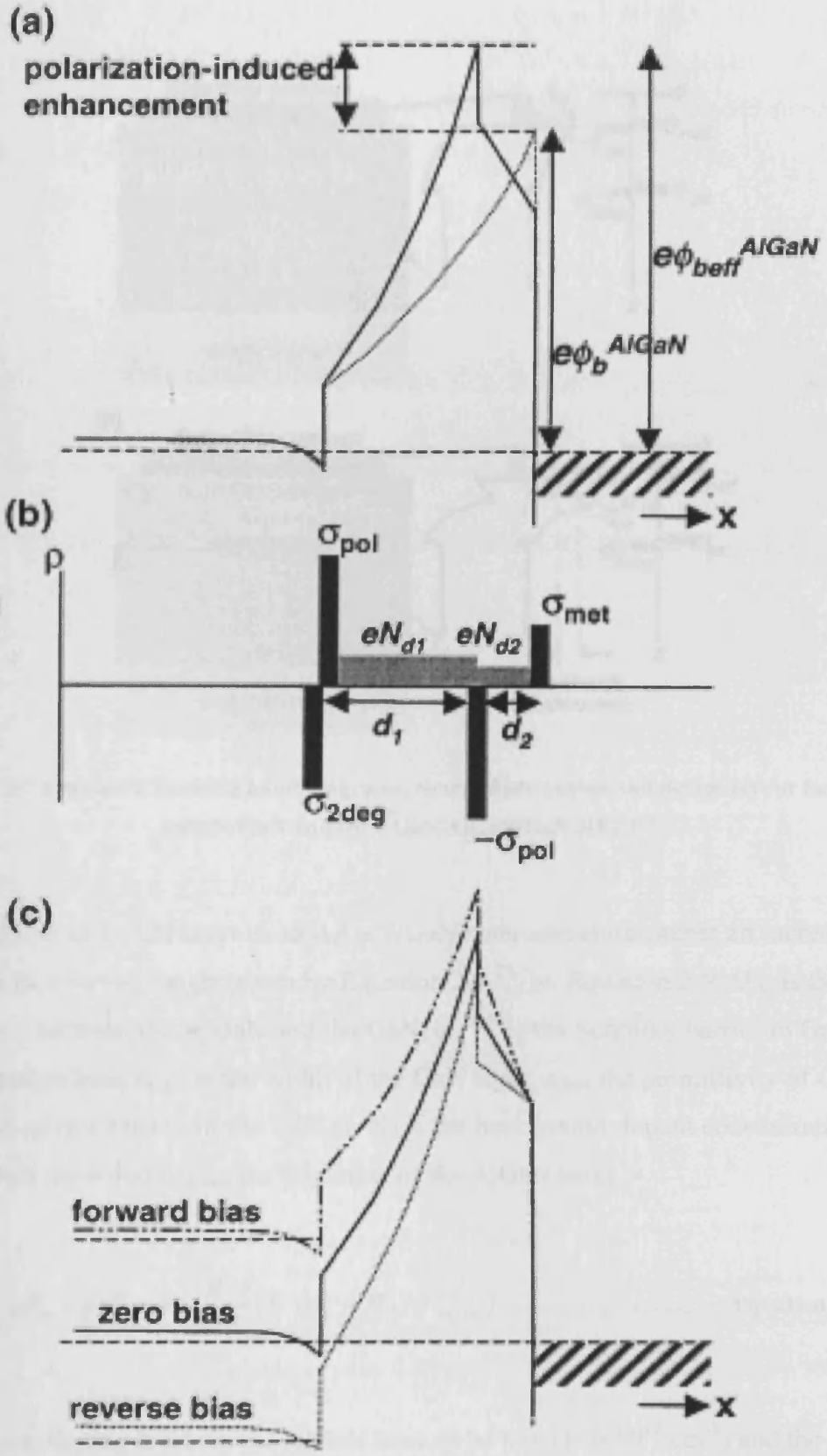

Figure 2-6 (a) Schematic diagrams of the conduction band in GaN/AlGaN/GaN and AlGaN/GaN heterostructure devices (b) the charge densities at equivalent points in (a) for GaN/AlGaN/GaN devices and (c) the band structure of a GaN/AlGaN/GaN heterostructure device under bias [22].

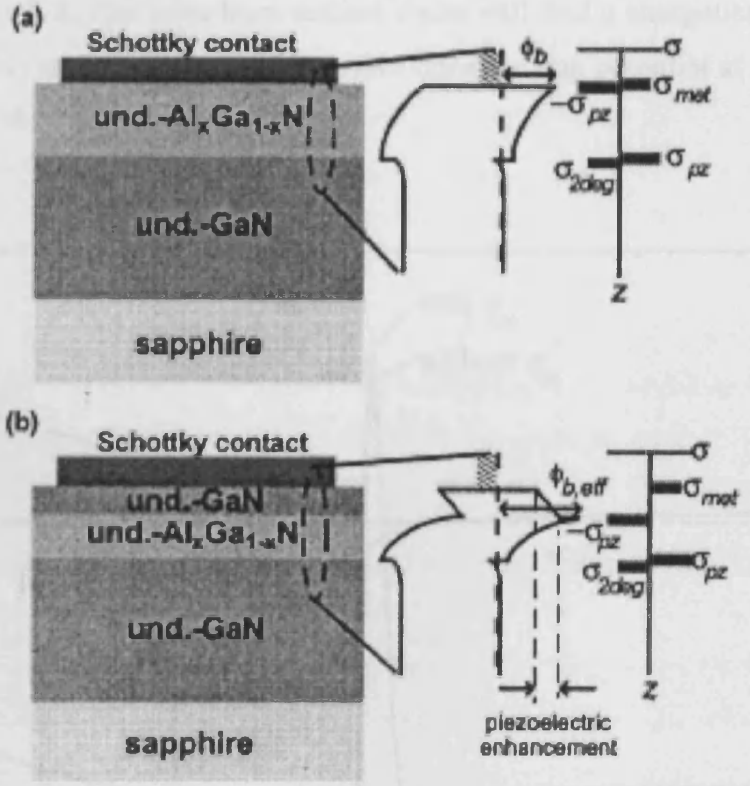

Figure 2-7 Schematic showing band diagrams, charge distribution and device layout for (a) an AlGaN/GaN and (b) a GaN/AlGaN/GaN HFET [23].

The addition of a GaN layer to an AlGaN/GaN heterostructure causes an increase in the Schottky barrier height given by Equation 2-9 [23]. In Equation 2-9 ΔE_C is the band gap offset between the AlGaN and the GaN, φ_B^{GaN} is the Schottky barrier to GaN, V is the applied bias, d_{GaN} is the width of the GaN layer, ε_{GaN} the permittivity of GaN, n_s the sheet carrier density in the 2-DEG, N_d is the background dopant concentration in the AlGaN layer and d_{AlGaN} the thickness of the AlGaN layer.

$$\phi_B^{eff} = \frac{1}{e}\Delta E_c + \phi_B^{GaN} - V + \frac{e \cdot d_{GaN}}{\varepsilon_{GaN}}(n_S - N_d \cdot d_{AlGaN}) \quad \text{..... Equation 2-9}$$

In practice, doping levels in the AlGaN have to be low (1-2x10^{17} cm^{-3}) and the GaN film >20Å before any great difference will be noticed [23].

A band diagram for a AlGaN/GaN heterostructure with no Schottky contact present is shown in Figure 2-8. Electrons from surface states will find it energetically favourable to form a 2-DEG at the AlGaN/GaN interface once the trap potential at the surface coincides with the Fermi level.

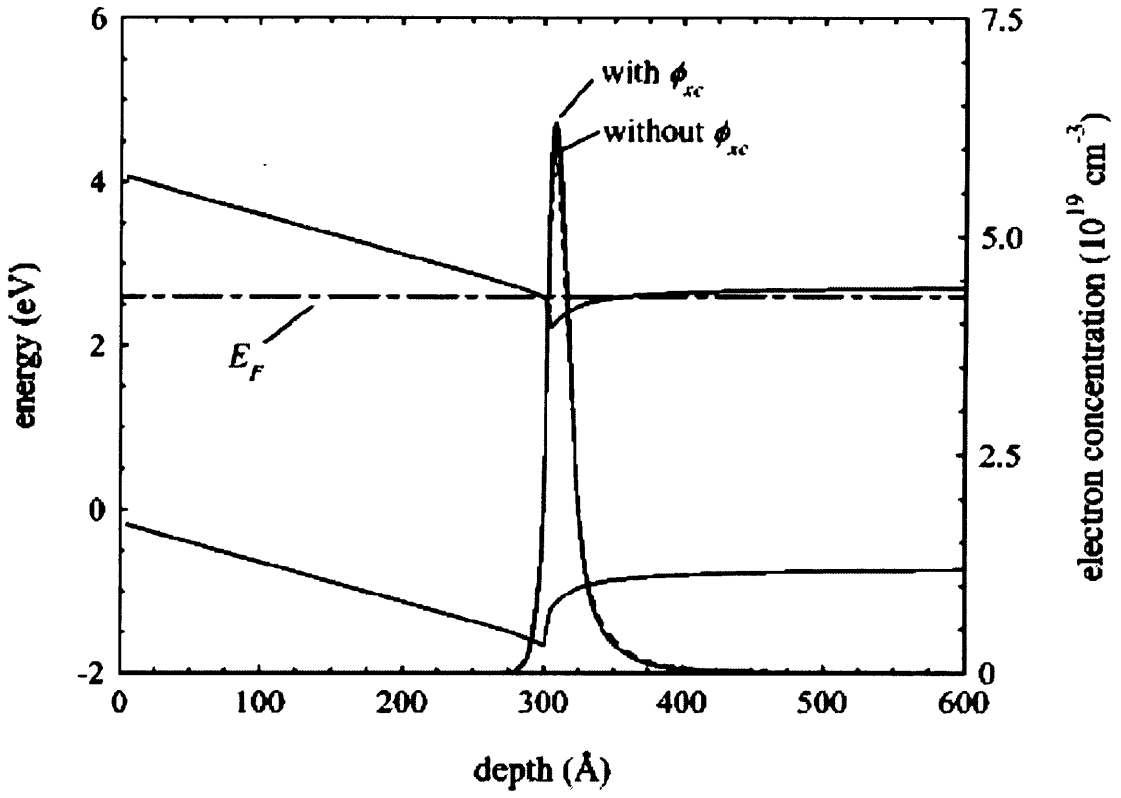

Figure 2-8 Band diagram for a $Al_{0.3}Ga_{0.7}N$/GaN heterostructure as calculated by Jogai [24], electron density as a function of depth from th surface is also shown.

2.3 Device problems

Several effects affect the performance of GaN field effect transistors. These problems are similar to those that affect GaAs based devices and include current collapse, RF current dispersion, RF dispersion, power drift and power slump [26]. Another problem is gate leakage.

2.3.1 Current collapse

Current collapse in GaAs was the label given to the persistent (yet recoverable) drop in drain current (I_d) achieved by heavily biasing the drain (Figure 2-9); however, with the III-nitrides it has been used to describe other effects as well [25]. It is thought that current collapse is caused by the injection of electrons from the conducting channel into traps in the buffer layer at high drain-source voltage (V_{ds}) [26]. The injection of electrons into traps depletes the conducting channel and hence reduces I_d. Evidence for the role of the buffer layer is that current collapse is observed only in devices grown on highly resistive buffer layers. In conducting buffers current collapse is not observed as the traps involved are already filled [26]. Evidence that traps are involved is the dependence of the collapse on the intensity and/or wavelength of light shone onto the device, and techniques using the wavelength dependence have been used to characterize the traps [26]. There is evidence to suggest that the traps causing current collapse are at least partly related to film dislocations [27]. Current collapse of this type has been observed in both MESFETs and HEMTs [28].

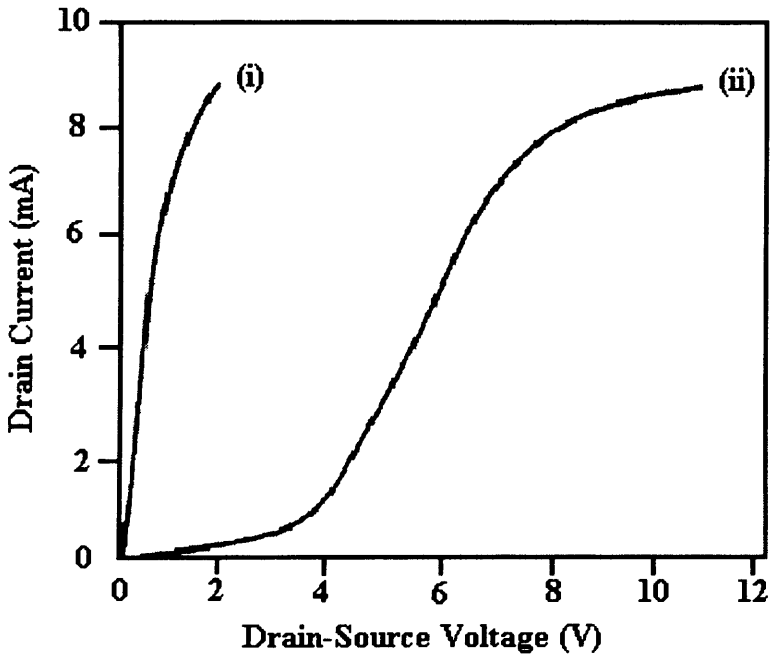

Figure 2-9 Drain current in a AlGaN/GaN HFET .i) before and ii) after the application of a 20V bias to the drain [29].

2.3.2 Gate leakage

Gate current reduces RF performance by drawing a current during the positive part of an RF cycle (reducing I_d and eventually leading to premature saturation (Figure 2-10)). In the negative part of a cycle, gate leakage allows a current to flow. Leaky gates increase the noise figure of the device and accelerate thermal stress degradation. Gate leakage current increases quickly with temperature, being approximately ten times greater at 300°C and one thousand times greater at 1000°C, thus leading to poor high temperature performance.

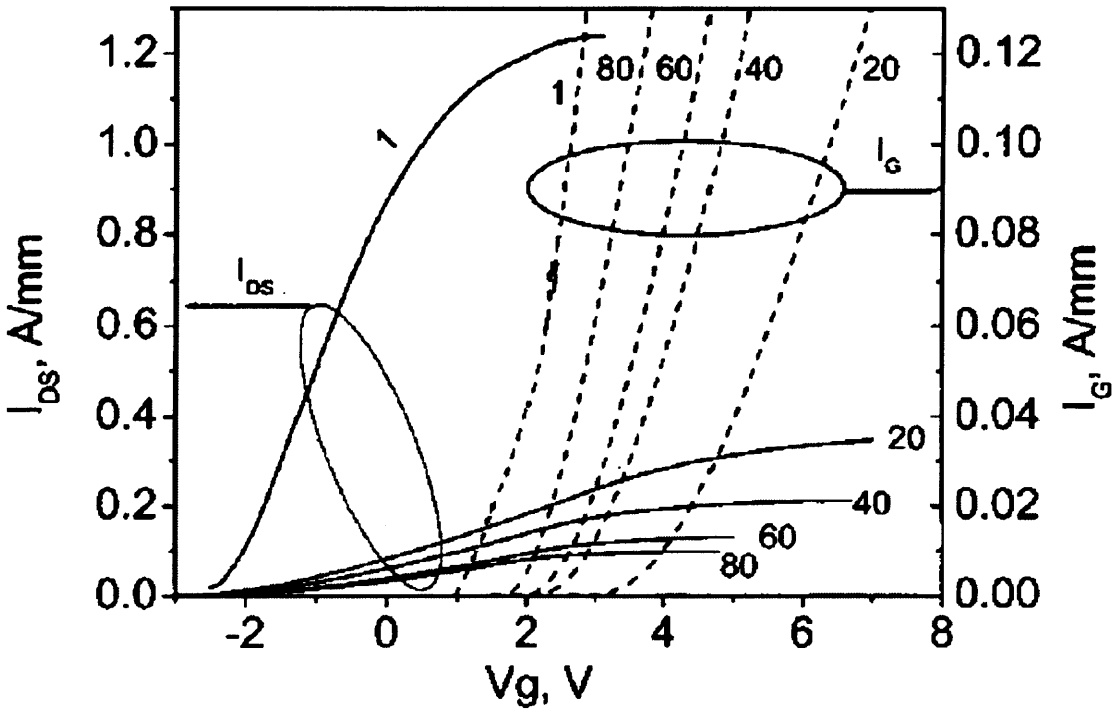

Figure 2-10 Drain current I_{DS} and gate current I_g as a function of gate voltage V_g. Note that the drain saturation current decreases for increasing gate length L_g from 1 to 80 μm. Also note that as I_{DS} saturates I_g increases dramatically, implicating gate leakage as the cause of saturation in these devices [30].

Ways of improving the gate leakage in a device include the inclusion of an insulating layer between the gate metal and the semiconductor, such as that found in MISHFETs [31] or MOSHFETs [32] or oxide/nitride/oxide MOS/MIS HFETS[33] (see Figure 2-11). Another way to reduce gate leakage in AlGaN/GaN HFETs or HEMTs is to increase the value of x in the $Al_xGa_{1-x}N$ barrier layer; this not only increases the Schottky

barrier height but also increases the band gap discontinuity between the AlGaN and GaN layers [34] (values and references to theory can be found in [35]).

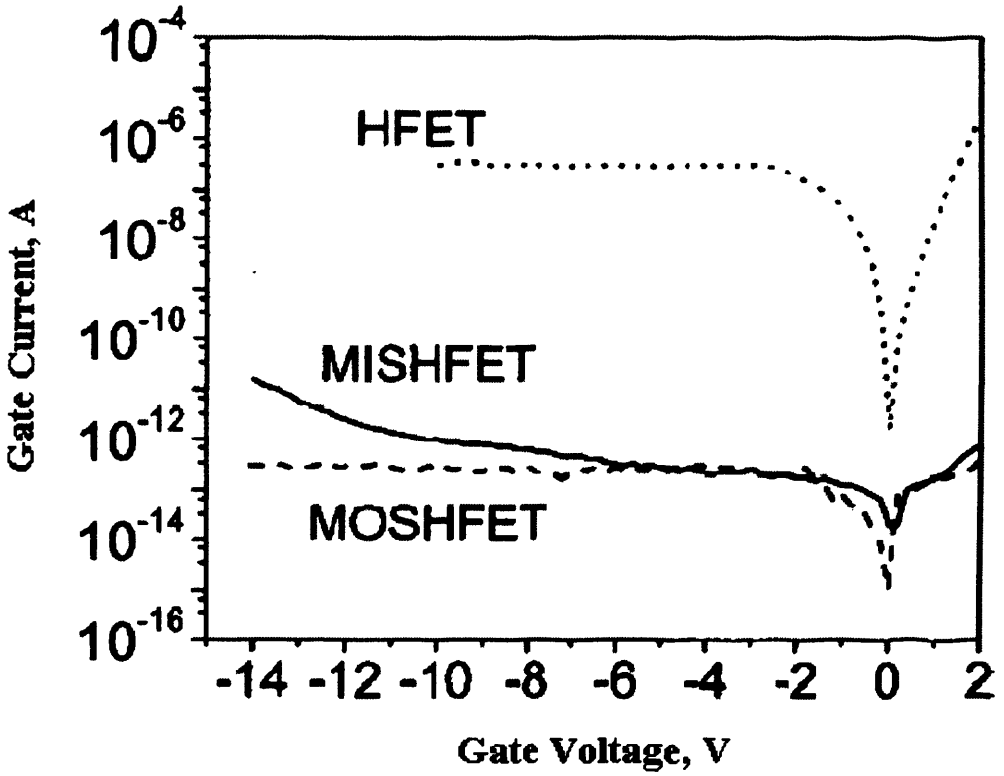

Figure 2-11 Gate current as a function of gate voltage for HFETs, MISHFETs utilizing a Si_3N_4 dielectric and MOSHFETs [36].

Increasing Al content increases the critical breakdown field in the AlGaN layer. Films with Al concentrations as high as 50% have been grown [34]; however, the superior properties gained by a high Al concentration comes at the price of reduced crystal quality and an increased number of traps, and a reduction in the strain in the AlGaN layer and thus a reduction in the 2-DEG concentration in this manner.

2.3.3 RF dispersion

It has been observed that when the drain and gate voltages of a device are pulsed rather than continuously biased there is a discrepancy between the dc and pulsed I-V characteristics known as dispersion (Figure 2-12). Furthermore, when the gate is pulsed from threshold to saturation there is a collapse in the I-V characteristics of the

device, whereas when the gate is pulsed from saturation to threshold no such collapse occurs (see Figure 2-13) [37]. Note that devices have been demonstrated where only the gate pulse, not the drain pulse, leads to current collapse [38]. This pulsed gate current collapse has been attributed as the cause of the discrepancy between the RF power expected from dc I-V curves and the RF power found in practice (Figure 2-14 [38]). There are two proposed mechanisms for the above effect; one is also linked to the observed reduction in current as the frequency of the gate signal is increased Figure 2-15.

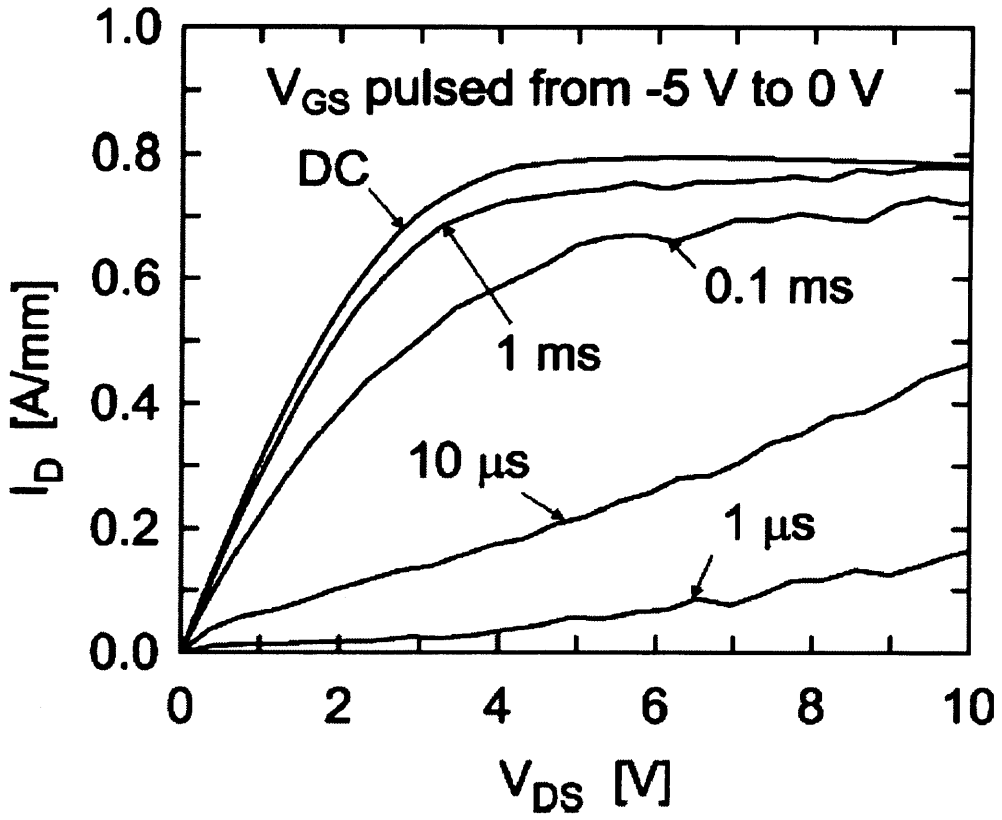

Figure 2-12 Dispersion between pulsed and dc HEMT characteristics stimulated by varying duration gate pulses [39].

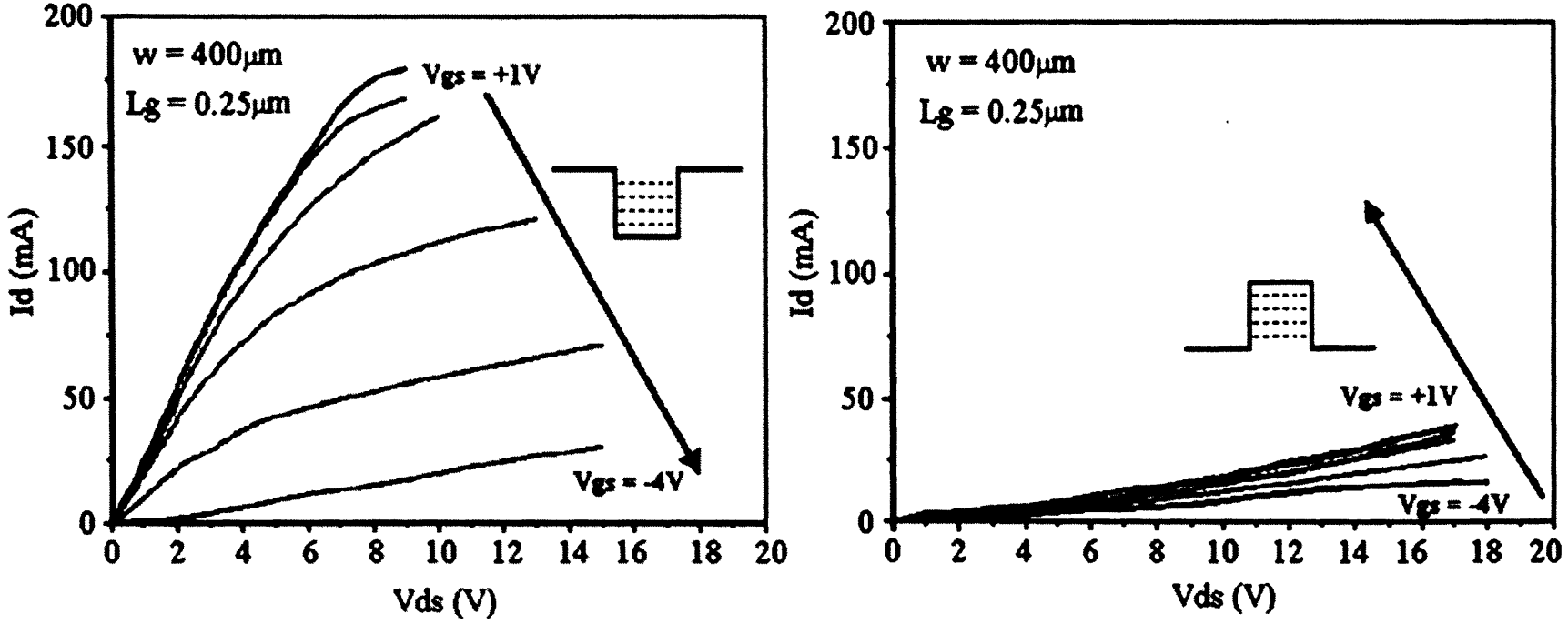

Figure 2-13 Pulsed I-V characteristics for (left) gate pulsed from open channel (1 V) to pinchoff (-4 V) and (right) gate pulsed from pinch off to open channel. The gate and drain pulses had a duration of 300ns and a frequency of 100kHz the quiescent bias points were; drain-source voltage 16V and gate-source voltage 1V [37]

The first of the two proposed mechanisms is that electrons from the gate are injected into states near or at the surface where they are trapped and cause a reduction in the 2-DEG density and hence current collapse [40]. The dependence of current collapse on gate voltage swing (Figure 2-13) suggests near surface traps. Near surface traps are also suggested by the dependence of the current collapse on temperature and light [41]. Ionised donor states are thought to exist at the surface, and it is electrons from this source that are thought to compose the majority of the carriers within the 2-DEG. Similar surface state traps affect GaAs devices [42]. Explanation is still required for the current collapse behaviour in MOSHFETs and MISHFETs see (Figure 2-16 [36]).

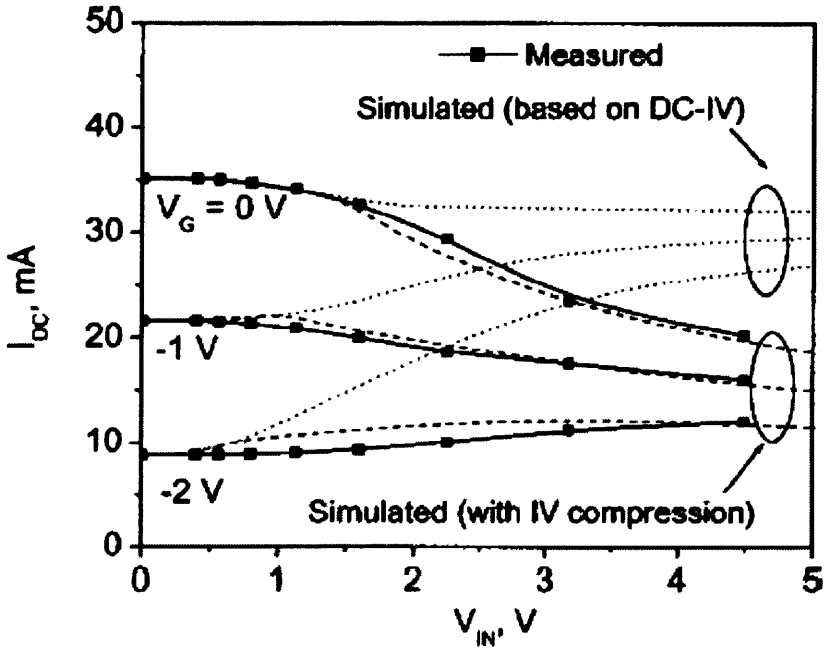

Figure 2-14 Measured (solid lines) and simulated (dotted and dash-dotted) output dc current dependence on input RF amplitude at 15V drain bias and different gate voltages for an AlGaN/GaN HFET. This shows the discrepancy between expected and measured output powers and how accounting for the effect of gate pulse current collapse gives an accurate prediction of the measured output [38].

Near surface states can also explain the observed collapse in drain current as the frequency of the gate voltage signal is increased (Figure 2-15). As the frequency of the gate signal is increased electrons that have been injected into trap states can no longer follow the signal and a stationary charge is formed at the surface. This surface charge acts as a virtual gate, depleting the active region [43, 40 & 37]. The virtual gate can

be modeled as a gate attached to the real gate through a lossy dielectric [43]. The large variation in the frequency at which the reduced current is observed is thought to be due to a large variation in the quality/conductivity of the device surfaces [37].

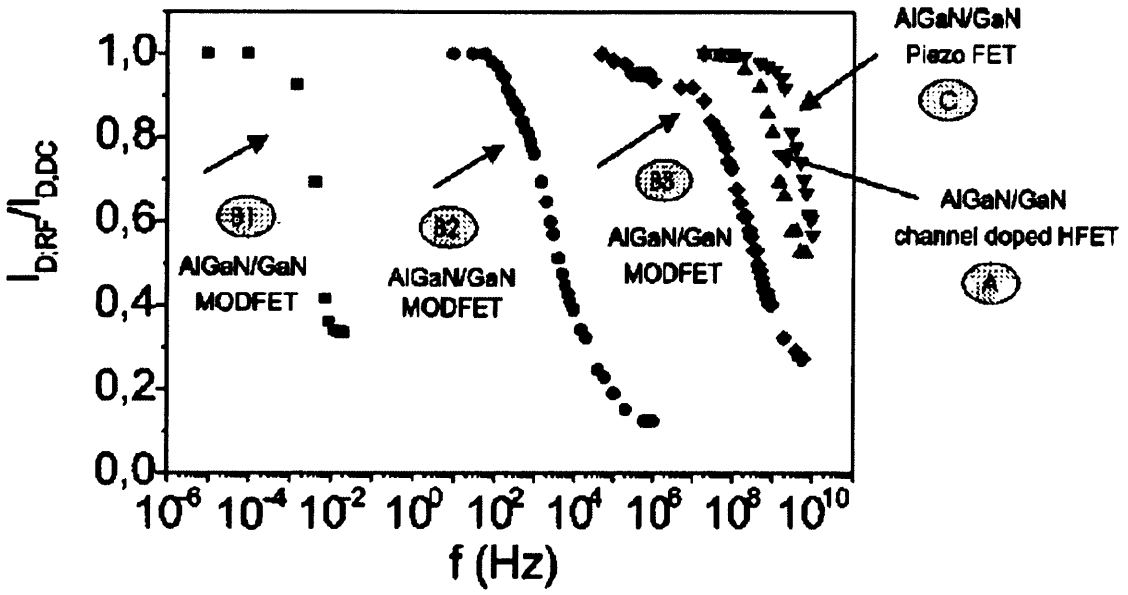

Figure 2-15 RF drain current normalised to dc drain current as a function of frequency for various AlGaN/GaN devices [37].

The second mechanism for dispersion is suggested over the course of several papers' [36, 38 & 44] and is that the gate voltage increases the tensile strain in the crystal directly beneath the gate. Because of this the gate-drain and gate-source regions are compressed and the 2-DEG electron density reduced. This theory is supported by evidence that the increase in resistance due to gate voltage pulses is found in both the gate-drain and gate-source regions [44]. It is also supported by the fact that passivation with Si_3N_4 (a hard substance that would presumably restrict the compression of the AlGaN) reduces the RF-current collapse, but that passivation with SiO_2 (a soft substance) does not. They also give evidence that suggests that surface states do not contribute to the collapse [38]. Recently; however, a p-type layer has been used as a type of passivation for an AlGaN/GaN HEMT [45]. The p-type layer, while not affecting the mechanical properties of the films, should isolate the surface from the rest of the device. This device also showed a reduced RF-current collapse. Other recent evidence is that Sc_2O_3 and MgO passivating films had a similar and slightly better effect on

RF-current collapse than that of SiN_x passivation [46]. Also suggestive of surface states is the pulsed gate current collapse observed in MESFETs [41].

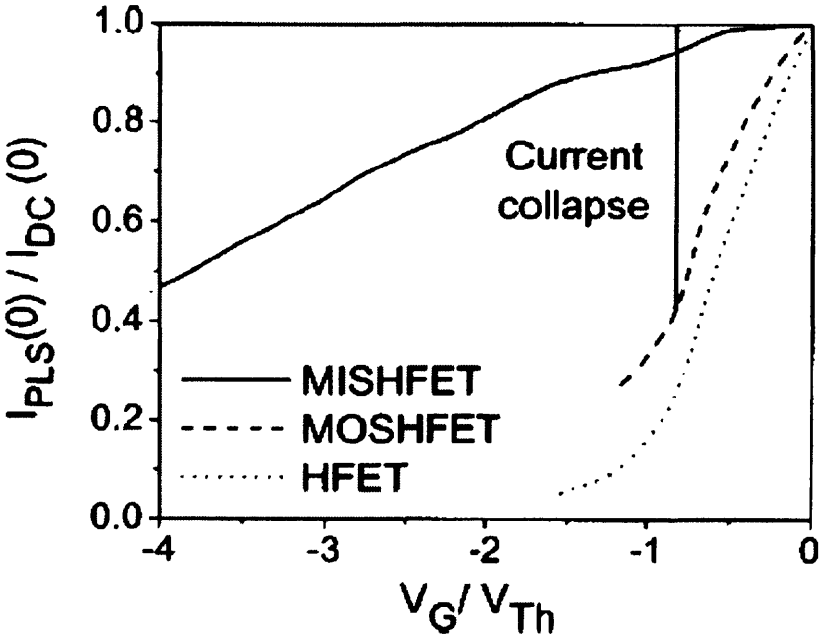

Figure 2-16 Graph showing pulsed drain return current as a function of gate voltage pulse amplitude. The gate voltage is normalised to the threshold voltage and the drain current is normalised to the dc current. The return current is the pulsed current when the gate voltage returns to zero. A large current collapse is observed in MISFETs only when the gate volatage is several times greater than the threshold voltage [36].

Passivation with silicon nitride has been shown to effectively mitigate dispersion [40 & 47] though nominally the same passivating layer on different devices will give different pulsed I-V characteristics, as shown in Figure 2-17. Another method that has successfully been used to reduce dispersion is the introduction of a doped layer between the heterojunction and the surface [48].

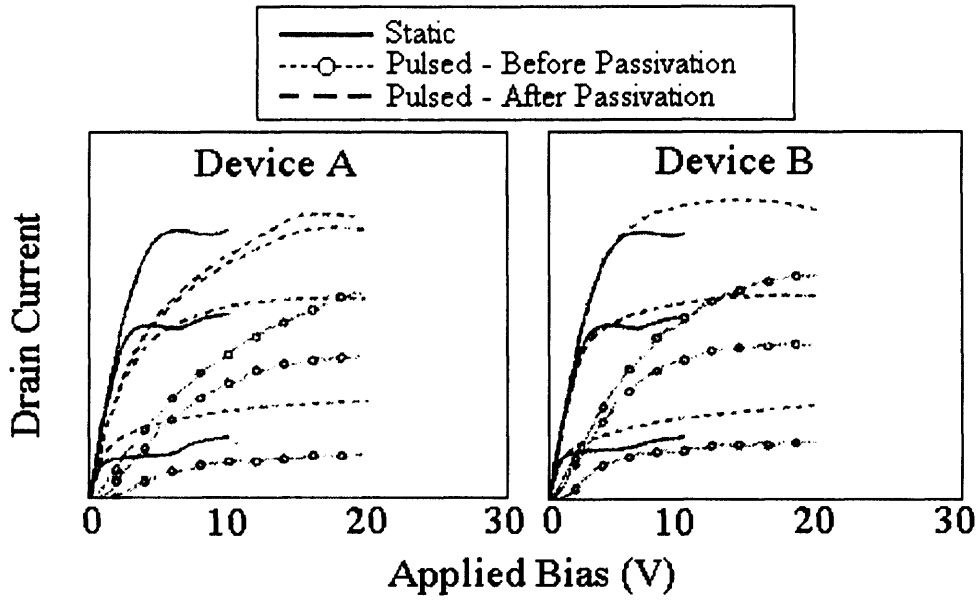

Figure 2-17 Pulsed and static I-V curves showing the effect of passivation on two different devices [25].

2.3.4 Transient effects

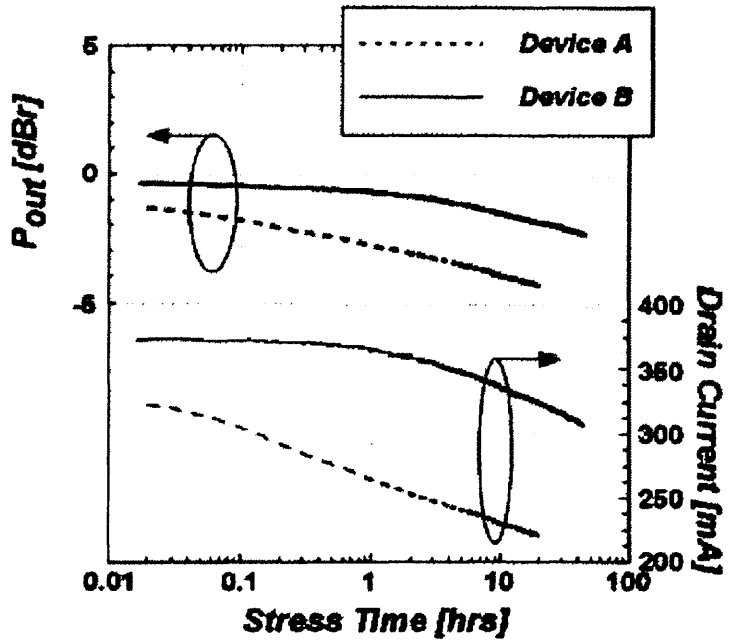

Figure 2-18 Time dependence of the output power and drain current of an AlGaN/GaN HEMT at 10GHz 3dB into compression V_{DS} = 20V [25].

GaN device output power has been shown to degrade over time (see Figure 2-18). This degradation over time is known as power drift if the change is recoverable or power slump if the reduction is permanent [25]. In GaAs, power slump was thought to be due to either electron trapping in the silicon nitride passivation layer or the creation of traps due to hot electron effects [25]. In GaAs, material improvements, passivation, surface pre-treatment and optimising channel and doping geometry to reduce the gate-drain electric field [25], all reduce power slump.

2.4 Summary

The III-nitrides have a variety of properties which allow the fabrication of high power, high efficiency, high linearity microwave transistors that are rugged enough to work in hostile environments such as space or next to high temperature fixtures [49]. Due to the difficulty of doping the III-nitrides p-type, unipolar n-type, and particularly heterostructure field effect transistors, are considered the most promising type of device. The formation physics of the two dimensional electron gas in III-nitride devices is different to that of III-V based devices as it relies on strain and polarisation in the materials. Despite their attractive properties, III-nitride devices exhibit various problems that mar their performance due to traps caused either by a poor material quality or due to the fact that 2-DEG formation leaves empty states at the surface that can be filled by electrons from the gate.

3 Properties of gallium nitride

3.1 Crystal structure of wurtzite gallium nitride

The wurtzite (WZ) structure, shown in Figure 3-1 consists of two interpenetrating hexagonal close packed lattices displaced from each other along the [0001] direction (For an explanation of the Miller-Bravais indices used in hexagonal crystals see Appendix A). Crystals of the wurtzite polytype are characterised by the lattice parameters a, c, and a dimensionless cell internal structure parameter u. For the idealised WZ structure $c/a = \sqrt{(8/3)}$, $u = 3/8$ and all the bonds are the same length.

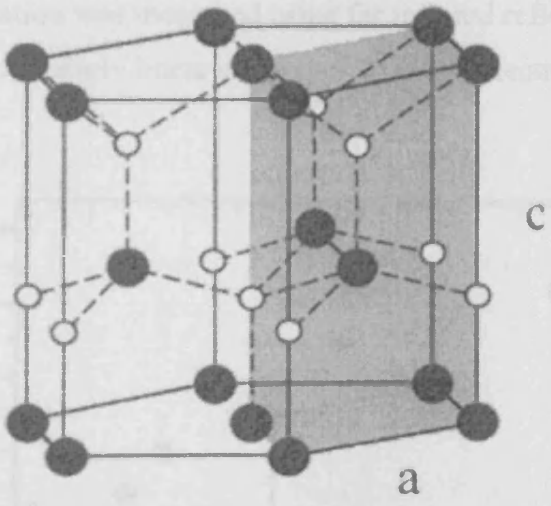

Figure 3-1 Picture of the WZ GaN crystal structure showing the lattice parameters a and c

Gallium Nitride has a thermodynamically stable phase with a structure close to the ideal WZ structure. Each one of the two hexagonal close packed lattices consists entirely of one species, either Ga or N. Four N or Ga atoms surround each Ga or N atom. In an ideal wurtzite crystal the nearest neighbour atoms have a tetrahedral arrangement. At room temperature and pressure, powder diffraction gives GaN lattice parameters of $a = 3.186$ Å, $c = 5.178$ Å and $c/a = 1.625$ [50]. Other values of lattice parameters for GaN bulk crystals and epitaxial layers measured using x-ray diffraction are given in [51 & 52]. WZ GaN has a density of ~ 6.15 g/cm^3 [53] and undergoes

a phase transition to the rock salt polytype at pressures of approximately 47 GPa for bulk crystals [54].

3.1.1 Variation of wurtzite GaN lattice parameters with charge carrier concentration, temperature and pressure

Factors that affect the size of the lattice include the electron density in the material, chemical composition (stoichiometry and impurity concentration) [55], external stresses and temperature [56].

The lattice constant variation with free electron concentration is shown in Figure 3-2 for various films. The lattice constants were measured using x-ray diffraction and the free electron concentration was measured using far infrared reflectivity. Both lattice constants have a approximately linear dependence on free electron concentration.

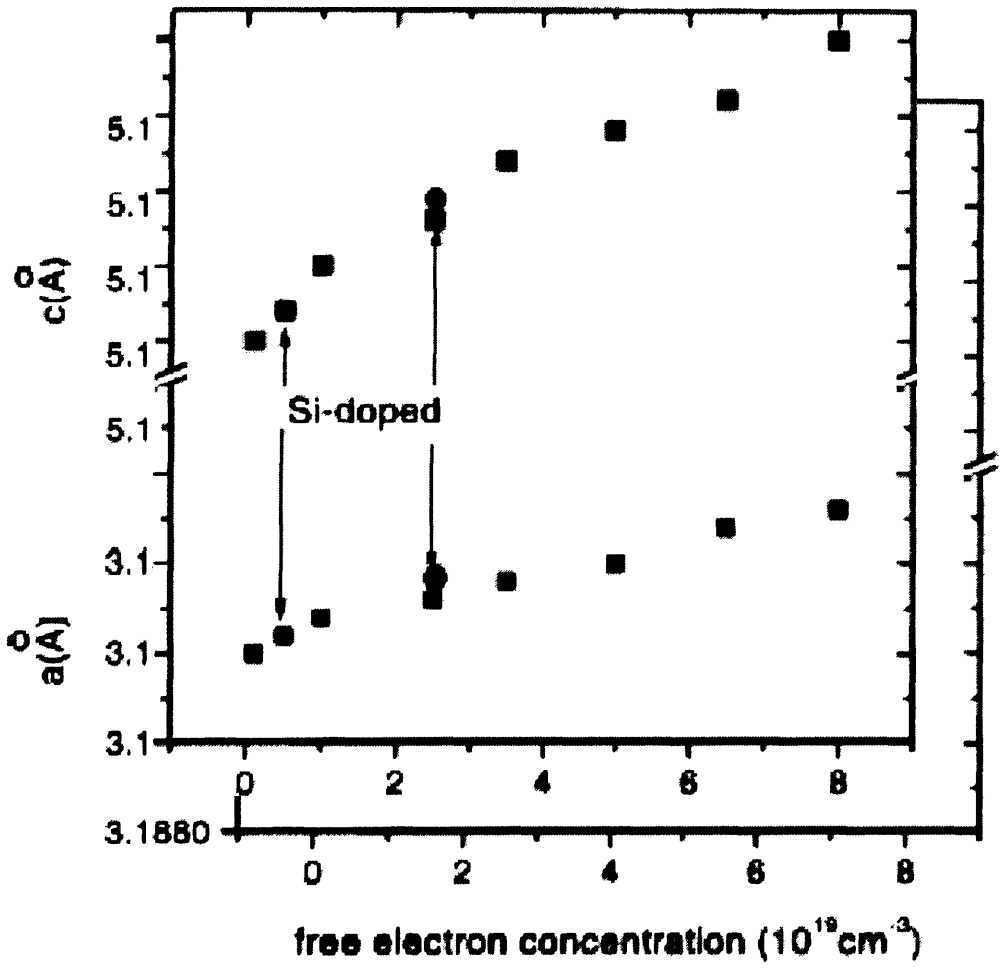

Figure 3-2 Variation of GaN lattice parameters with free electron concentration [57]

The lattice parameters in Figure 3-2 marked Si-doped were taken from silicon (Si) doped material and there are two data points for these samples: the lower results include a calculated correction for the perturbing effect of the silicon on the lattice. The larger results are the as-measured lattice parameters.

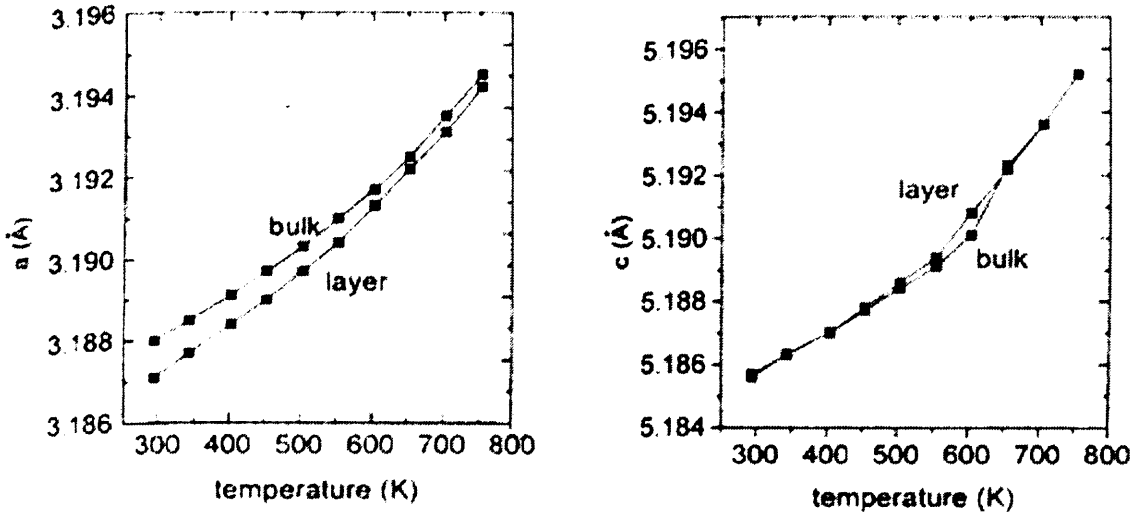

Figure 3-3 Temperature dependence of WZ GaN lattice constants *a* and *c* for bulk crystals and heteroepitaxial layers on sapphire [52].

The temperature dependences of the lattice parameters *a* and *c* are shown in Figure 3-3 for both bulk GaN crystal and MBE grown GaN on (0001) Sapphire [52]. The bulk crystals have a very high crystal quality, exhibiting x-ray rocking curves with full width of half maxima (FWHM) of ~ 30 arcsec (compared to ~15 arcsec for a perfect crystal and 1-2 arcmin for heteroepitaxially grown GaN substrates [52 & 58]). As shown in Figure 3-3, *c* for a bulk crystal and a heteroepitaxial film has a similar temperature dependence; this is because, in this case, growth was on the (0001) plane of sapphire, so that the film is free to expand and contract along the c-axis in the same way as the bulk crystal. However, the movement of heteroepitaxial layers parallel to the substrate is constrained by the substrate. Figure 3-4 shows how aluminium nitride (AlN) aligns with the surface of (0001) sapphire.

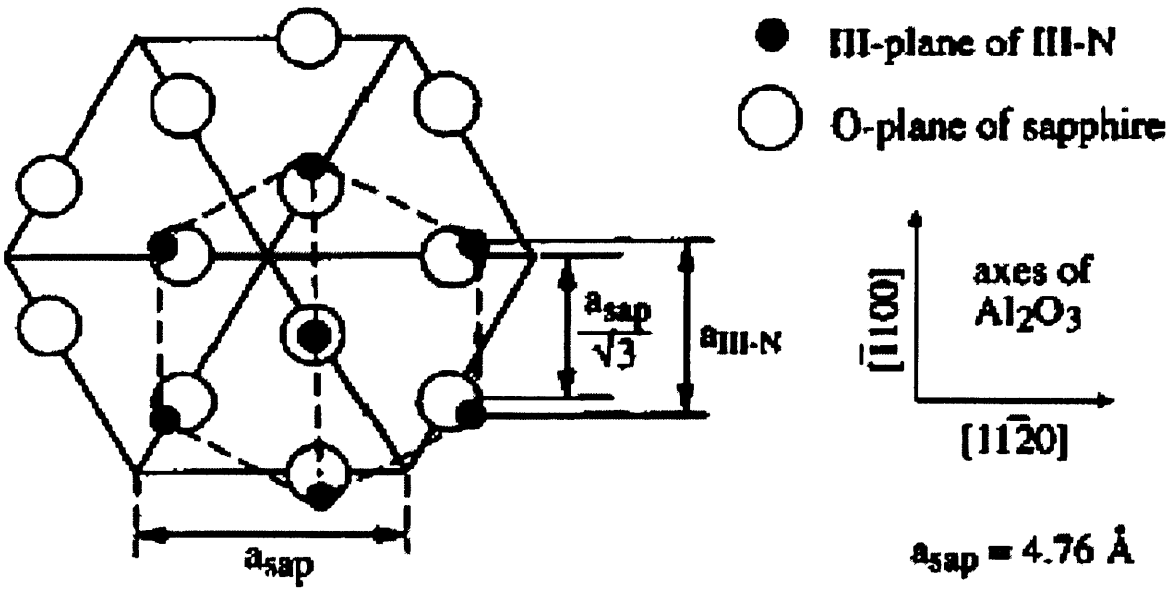

Figure 3-4 Schematic representation of the (0001) plane atomic arrangement in the case of (0001) AlN film grown on (0001) sapphire

Heteroeptitaxial materials may be grown using a two-stage growth, whereby a primary layer is grown onto a substrate at a low temperature and then a secondary high temperature layer is grown on this primary layer. For growth of GaN secondary layers, primary layers of GaN, AlN and InN have been used, though the first two are used more commonly than the third. Providing the primary layer is thick enough and the mismatch with the substrate great enough, at the high temperatures of the secondary growth (> 600°C) sufficient misfit dislocations are generated in the primary layer to leave the GaN layer unstrained by the substrate, and the layer is lattice matched with the substrate [59]. As the layer is allowed to cool the sapphire substrate contracts more than the GaN layer due to its higher thermal expansion coefficients. As the atoms in the film retain their positions relative to the atoms in the substrate, the layer of atoms parallel to the substrate experience a compressive biaxial strain and dislocations maybe produced to reduce the strain [52 & 60]. An equation for a layer's critical thickness i.e. the thickness before any stress in the layer is relieved by the generation of misfit dislocations is given in [59] though experimental agreement with the theory depends on the quality of the layer.

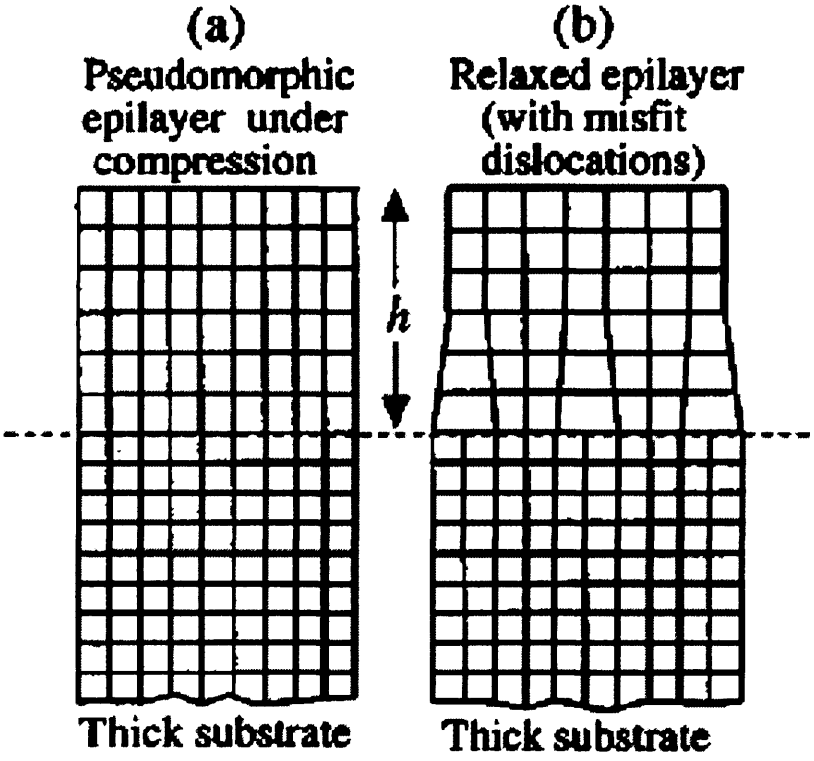

Figure 3-5 Structure of an epilayer under biaxial compression: (a) pseudomorphic and (b) relaxed with misfit dislocations.

Figure 3-5 illustrates a layer with a lattice constant greater than its substrate, with a thickness (a) below, and (b) above the critical thickness. Below the critical thickness the layer is strained by the misfit strain and the layer is latticed matched to the substrate (called a pseudomorphic layer). Above the critical thickness the strain is relieved by the creation of misfit dislocations.

3.2 Thermal properties of wurzite gallium nitride

3.2.1 Melting Point, Specific Heat and the Debye Temperature

The melting point of GaN is given as 2800 K [61]. This value was calculated theoretically because, as is indicated in Figure 3-6, the equilibrium pressure of nitrogen over GaN is very high at temperatures near the melting temperatures, i.e GaN will dissociate before melting unless high pressures are maintained around the sample. The nitrogen over-pressure at 2800 K is experimentally found to be > 4GPa

and is extrapolated to a value of ~ 4.5GPa in [61] and references therein. This means that bulk crystals grown by conventional methods such as Czochralski and Bridgeman are impossible and has meant that most epitaxial growth of GaN has been performed heteroepitaxially on foreign substrates such as Al_2O_3 and SiC.

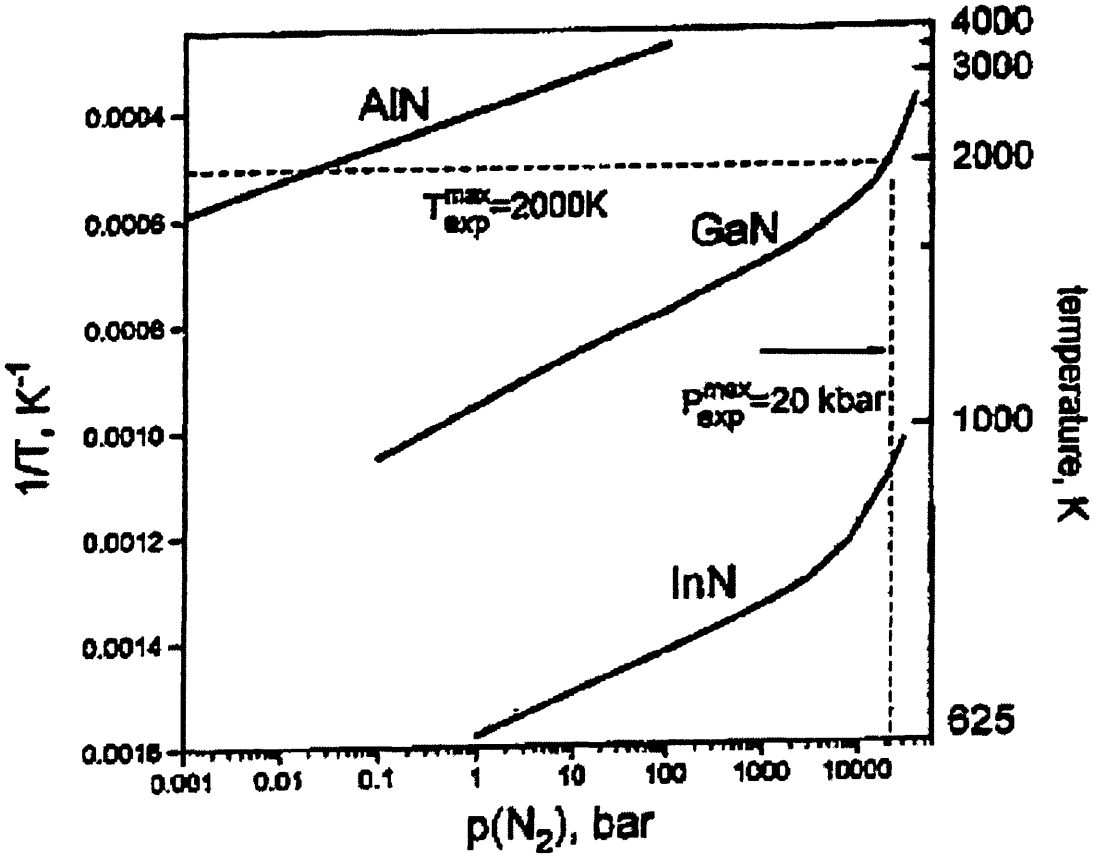

Figure 3-6 Temperature dependence of the equilibrium N_2 pressure over III-nitrides [62].

A graph of the temperature dependence of the specific heat of gallium nitride at constant pressure is shown in Figure 3-7. As can be seen there is a poor match between the experimental data and the calculated dependence. The Debye temperature at 0K was calculated from the results as 570 K. This result is in good agreement with the value of 600 K calculated by [63] and more recently the value of 586 K calculated in [64]. However values of the Debye temperature as high as 700 and 830 K have been stated in the literature [65 & 66].

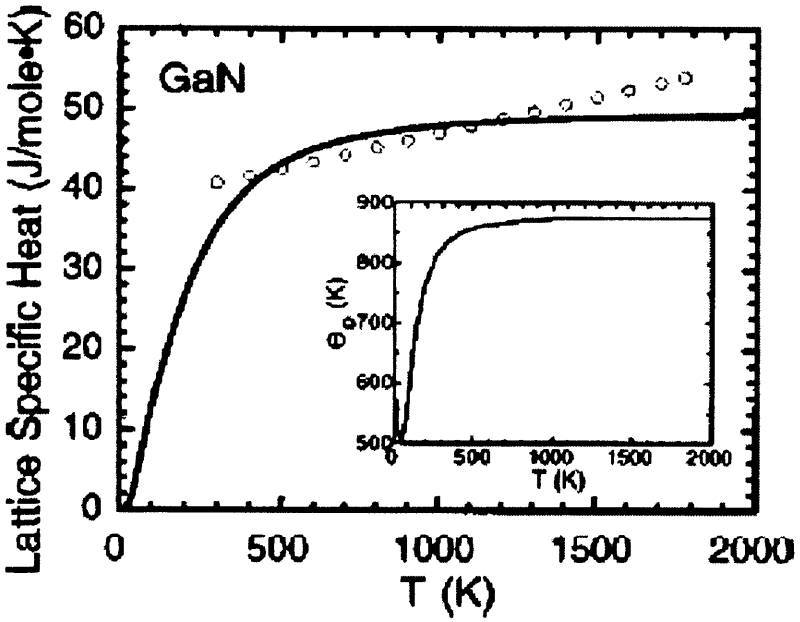

Figure 3-7. Dependence of α-GaN specific heat capacity on temperature, solid line calculated data and red circles experimental data [67]. The calculated temperature dependence of the Debye temperature is also shown as an inset.

3.2.2 Thermal Conductivity

The thermal conductivity κ of GaN has a theoretical limit of 4.1 W/cm K [66 & 68] which is close to that of SiC. However at present all real GaN samples have thermal conductivities lower than the ideal value. Films grown by hydride vapour phase epixtaxy (HVPE) have given values of 1.3 W/cm K [69] and more recently 1.95 W/cm K [70]. Lateral epitaxial overgrowth (LEO) films have been grown with regions with thermal conductivities of $2.00 < \kappa < 2.10$ W/cm K [71]. Crystal imperfections in real films such as lattice defects, dislocations, impurities and the inclusion of the less abundant isotopes of Ga or N, ^{71}Ga substituting ^{69}Ga and ^{15}N substituting ^{14}N * explain the discrepancy between the theoretical and experimental results [68, 72].

---

* ^{71}Ga, ^{69}Ga, ^{15}N and ^{14}N are the only naturally occurring isotopes of Ga and N respectively, though Ga has 23 radioisotopes and N 10. The natural abundance of the naturally occurring isotopes are ^{69}Ga: 60.108(6)%, ^{71}Ga: 39.892(6)%, ^{14}N: 99.634(9)% and ^{15}N: 0.366(9)%.

The variation of thermal conductivity with film thickness is shown in Figure 3-8. The increase of thermal conductivity with increasing film thickness is due to the increase in crystal perfection associated with the increase in film thickness [70 & 73].

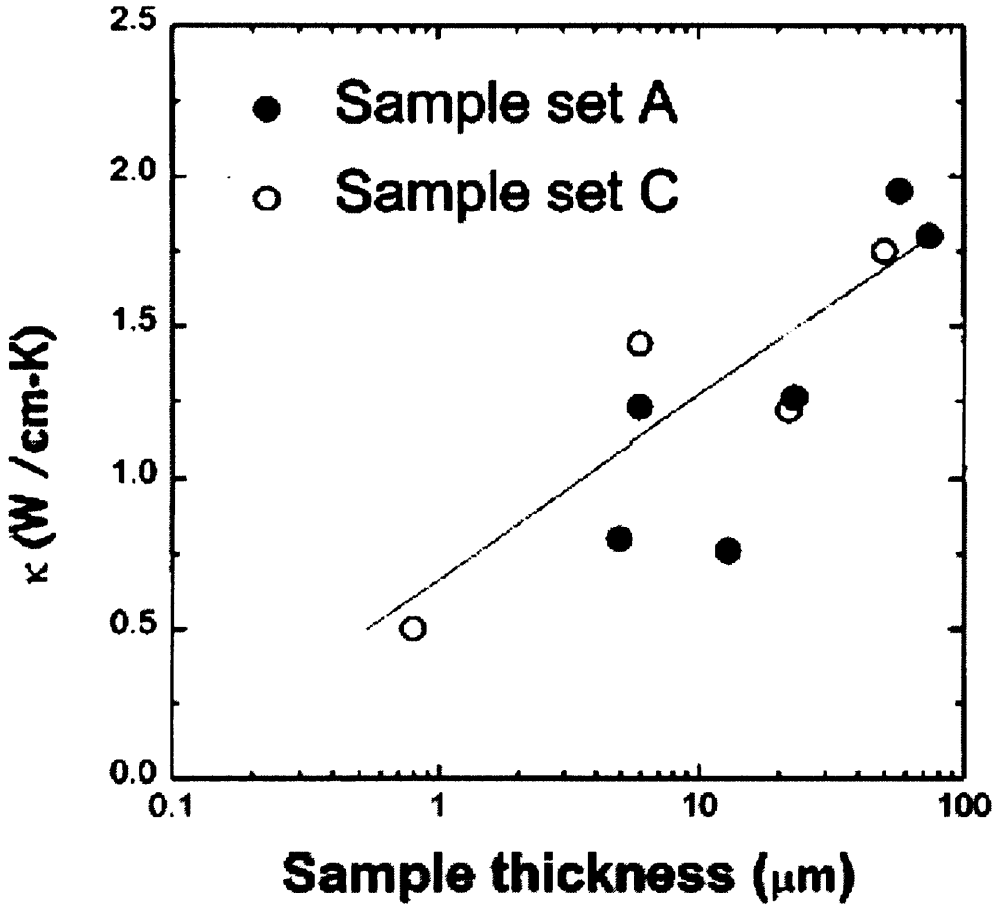

Figure 3-8 Dependence of thermal conductivity on the thickness of samples grown by HVPE on c-plane sapphire [70].

Figure 3-9 shows the dependence of the thermal conductivity of HVPE grown films on free electron concentration measured by either the Hall effect n_H or by micro-Raman techniques n_R. The films have either varying thickness (A1-A6) or a 10μm fixed thickness (B1-B7). The decrease in thermal conductivity with increasing electron concentration is due to the increased phonon scattering from free electrons and impurities that is much larger than the increase due to the electronic component of κ [70].

Figure 3-10 shows the variation of thermal conductivity with temperature [69]. The thermal conductivity peaks at a characteristic temperature T_{ch} of ~ 200 K for GaN.

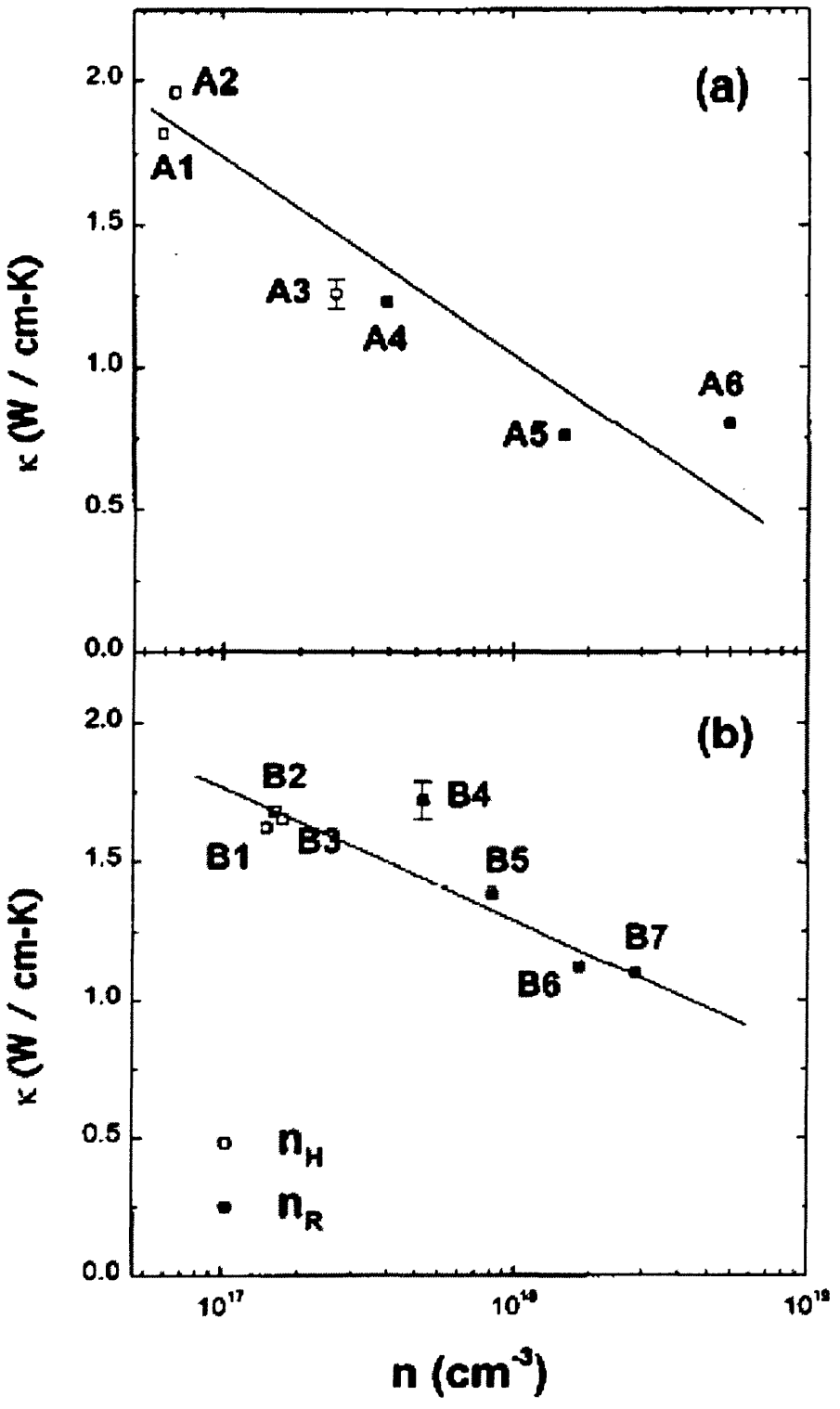

Figure 3-9. Thermal conductivity as a function of electron concentration determined from either the Hall effect or micro-Raman measurements [70].

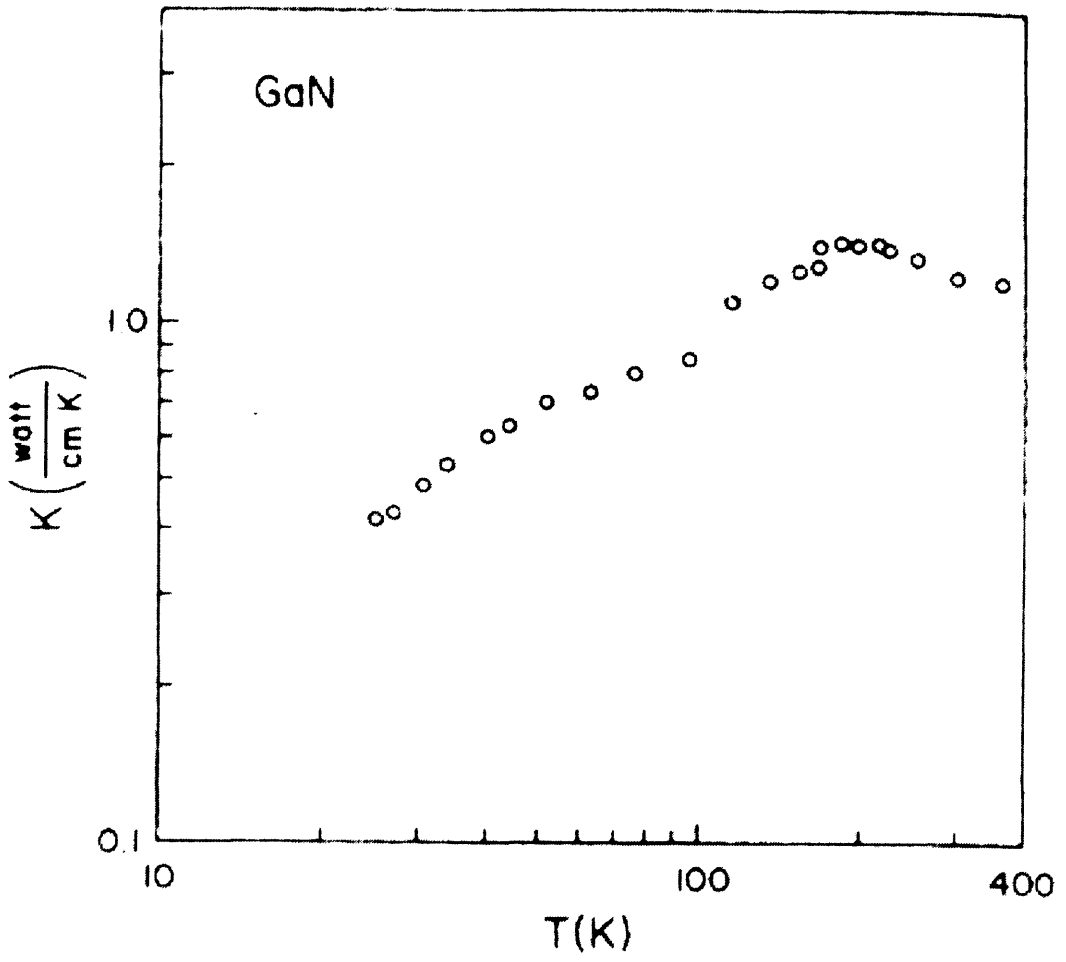

Figure 3-10 Temperature dependence of thermal conductivity for WZ GaN.

3.2.3 Thermal Expansion

Figure 3-11 and Figure 3-12 show respectively the thermal expansion coefficients in the *c* and *a* crystal directions at temperatures ranging from 294-753 K for GaN bulk crystals (grown from solution of nitrogen in liquid gallium in 15kbar nitrogen gas ambient), GaN epitaxial layers (grown by MBE on sapphire substrates) and sapphire substrates.

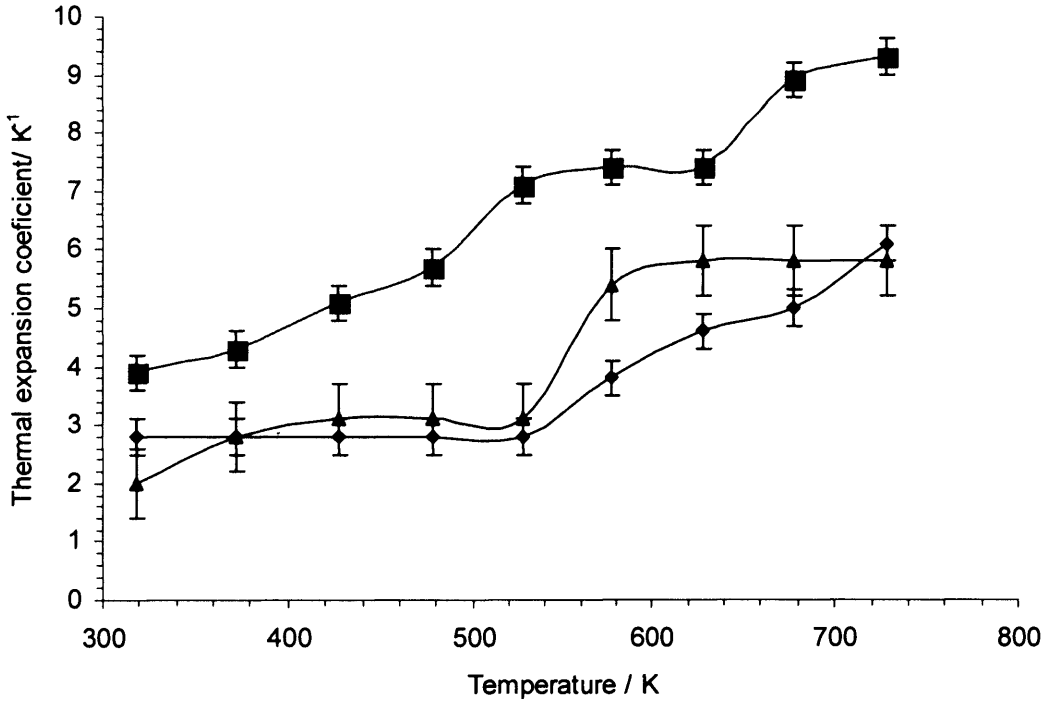

Figure 3-11. Dependence of α_c on temperature for GaN wurtzite bulk (circles), GaN heteroepitaxial layers (triangles) and a sapphire substrate (circles).

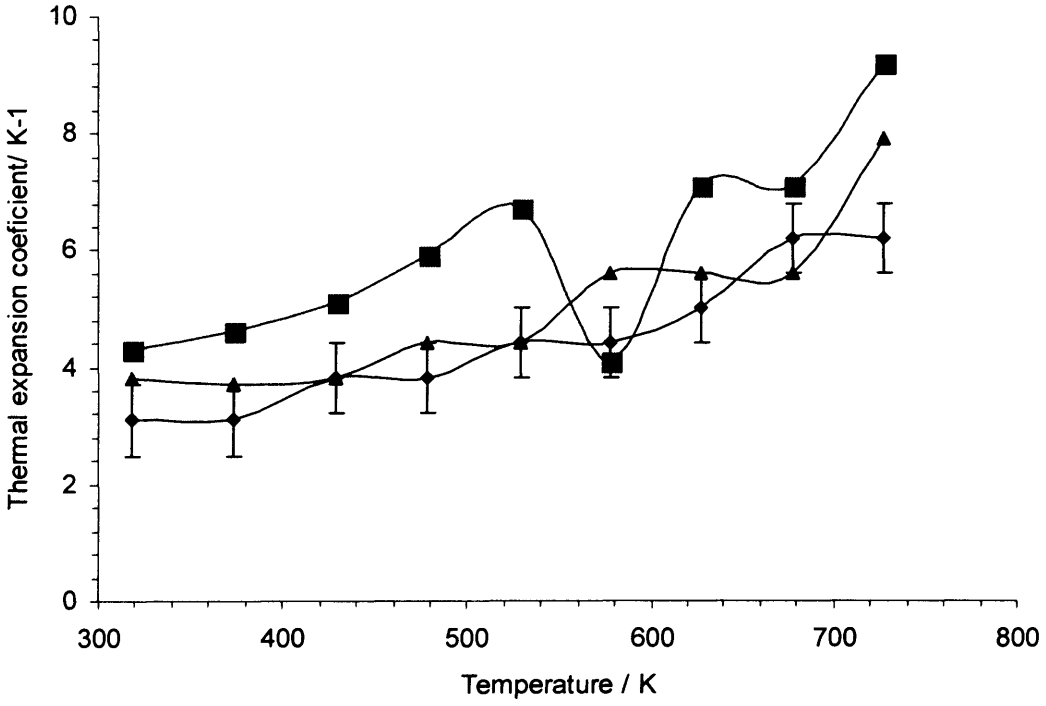

Figure 3-12. Dependence of α_a on temperature for GaN wurtzite bulk (circles), GaN heteroepitaxial layers (triangles) and a sapphire substrate (squares).

As may be seen in Figure 3-11 and Figure 3-12 the thermal expansion coefficients in the *c* and *a* directions of the GaN bulk and heteroepitaxial layer have similar values for the entire temperature range. Figure 3-3 shows the behaviour of the lattice constants of bulk and heteroepitaxial layers as they are heated; the lattice constant *a* is modified by the effect of the substrate, whereas *c* remains almost identical to the bulk crystal.

3.3 Band diagram and related parameters of wurtzite gallium nitride

The band diagram of wurtzite GaN calculated by the full-potential linearised augmented plane wave (FLAPW) method within the local density approximation (LDA) is shown in Figure 3-13 [74 & 75]. The first brillouin zone of wurtzite, Figure 3-14, shows the symmetry points and lines at and along which the energy dispersion of Figure 3-13 (a) is calculated.

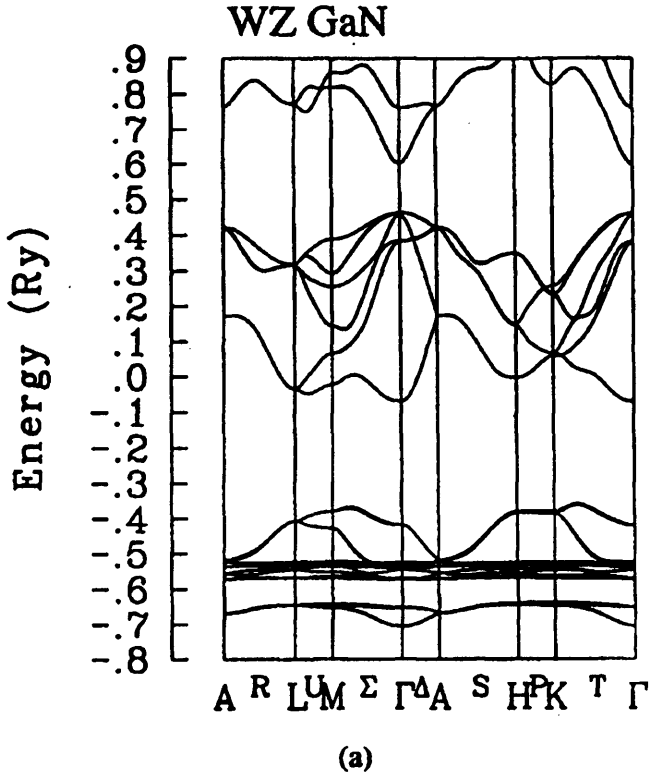

Figure 3-13 Wurzite GaN band structure calculated by the full-potential linearized augmented plane wave method [74 & 75].

Band structures with features unlike those shown in Figure 3-13 have been published, see for examples [76,77 & 78]. The first principles FLAPW band structure in Figure 3-13 is chosen above the other diagrams as it is a first principles calculation and it gives eigenvalue energies at the $L^{c}_{1,3}$ and Γ^{c}_{3} points (see Figure 3-15) of the correct order as given by the average of results given in [77] see Table 3-2. The minimum between the L and M points (along the U line) is in approximately the correct position (as given in [79]) with energy below that of the Γ^{c}_{3} point as predicted by [80]. Both diagrams also have the features common to most other band structures for the wurtzite polytype such as a direct band gap.

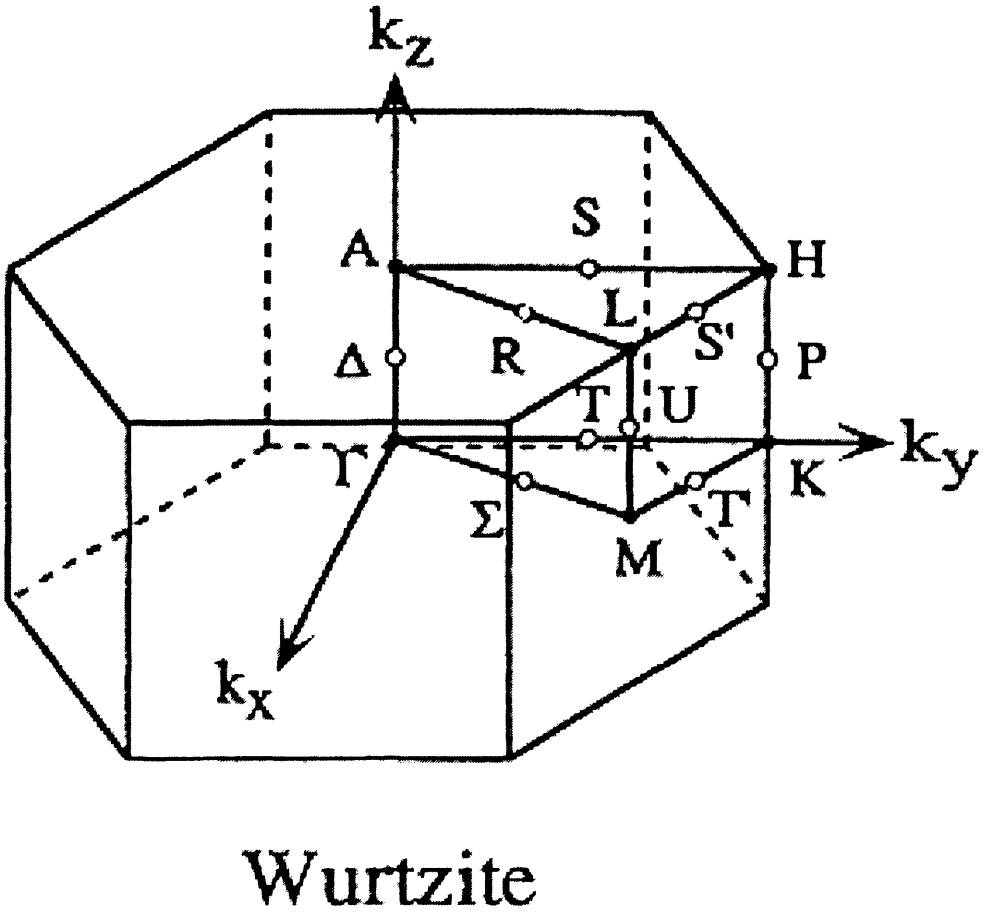

Figure 3-14 Wurtzite's first brillouin zone

The WZ band structure shown in Figure 3-13 consists of four regions, three valence regions between -0.8 and +0.5 Ryd (1Ryd ≈ 13.606 eV) and a conduction region

above approximately +0.6 Ryd. The electronic states that are attributed to each region are given in Table 3-1 starting from the lowest energy band between -0.70 and -0.65 Ryd and continuing up towards the conduction band [75].

Occupied Energy Interval (Ryd)	Electronic States
-0.70 to -0.65	Mostly N 2s but upper sides hybridised with Ga 3d
-0.55 to -0.38	Lower energy part Ga 3d upper energy part hybridised Ga 3d and N 2s
-0.1 to 0.5	N 2s, 2p and Ga 4s, 4p.
Conduction band near Γ_1 minimum	N s and Ga s states

Table 3-1 Electronic states attributed to regions of the WZ GaN band structure.

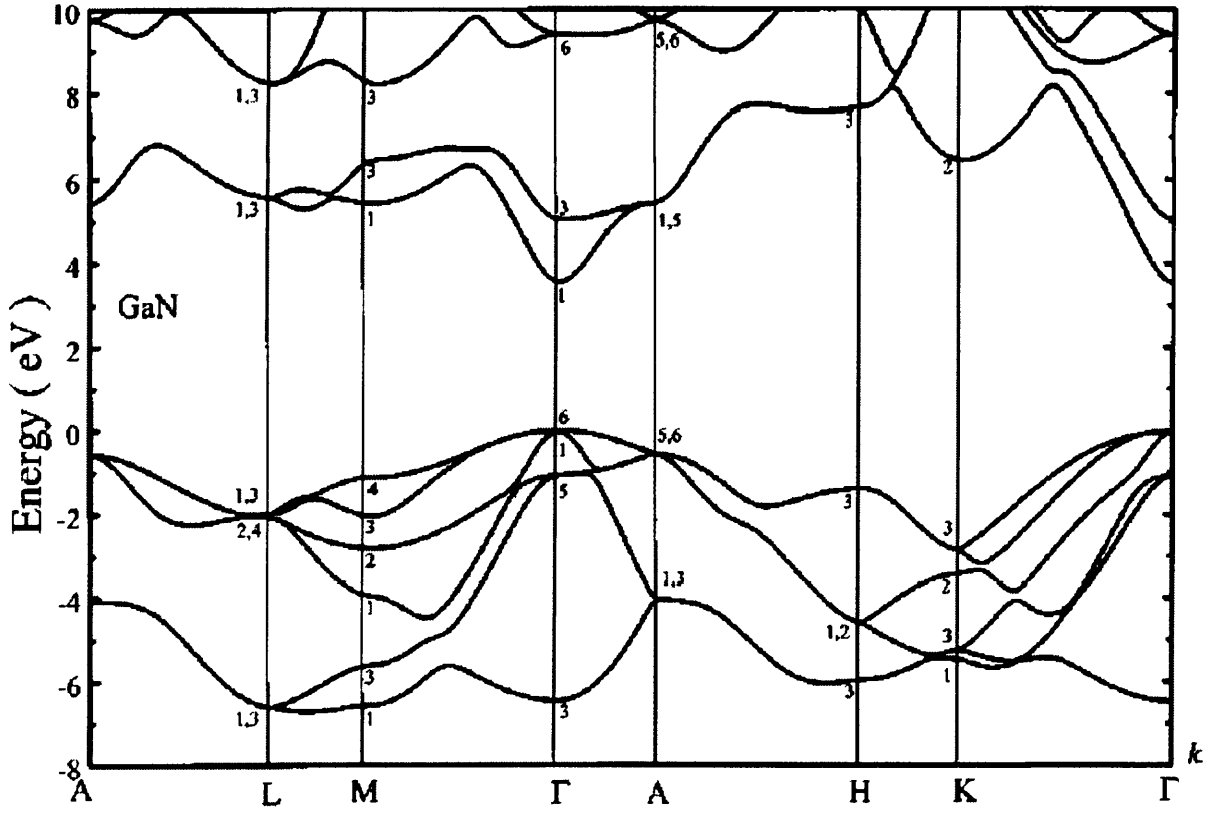

Figure 3-15 WZ energy band labelled with brillouin zone symmetry points (after [77]).

Conduction Band Point	Energy above VBM (eV)	Energy above CBM (eV)
Γ^c_3	5.12	1.68
K^c_2	6.31	2.87
M^c_1	5.88	3.01
$A^c_{1,5}$	5.46	2.02
H^c_3	7.57	4.13
$L^c_{1,3}$	5.44	2.00

Table 3-2 Table of the energy of various wurtzite GaN conduction band points with respect to Γ^v_6 the valence band maximum at the Γ point.

As is expected for a calculation performed in the Local Density Approximation, the magnitude of the energy gap given by the FLAPW method is too small. The correct magnitude is found through utilization of a quasi-particle correction using the GW approximation [76]. The experimentally determined room temperature Γ point energy gap for WZ GaN is 3.43 – 3.44 eV, [81].

Table 3-2 shows the energy eigenvalues of significant points of WZ GaN's conduction band relative to the Γ point valence band maximum Γ^v_6. These energies are taken as the mean of the entirely theoretical data presented in [77], where a more comprehensive list of band point and transitions energies from several studies may be found.

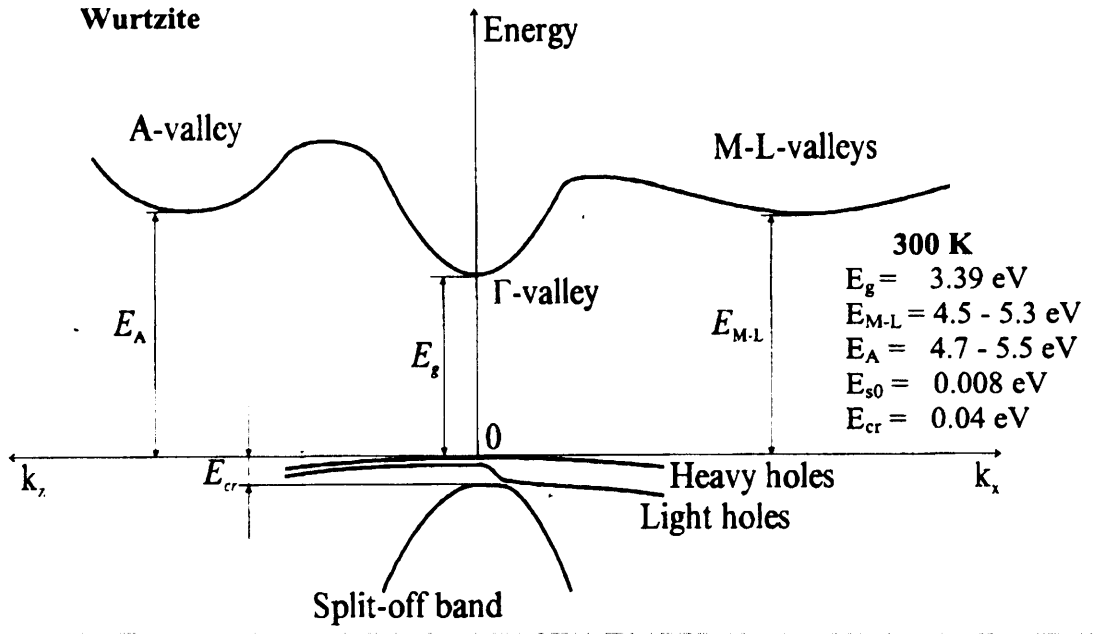

Figure 3-16 Band structure of wurtzite GaN showing important conduction band minima and valence band maxima [100].

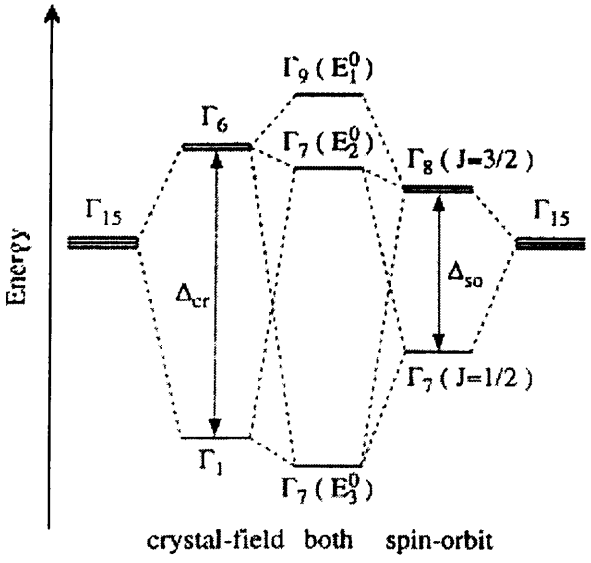

Figure 3-17 Valence band splitting at the Γ point due to the effects of the crystal-field (symmetry) and spin orbit coupling [74].

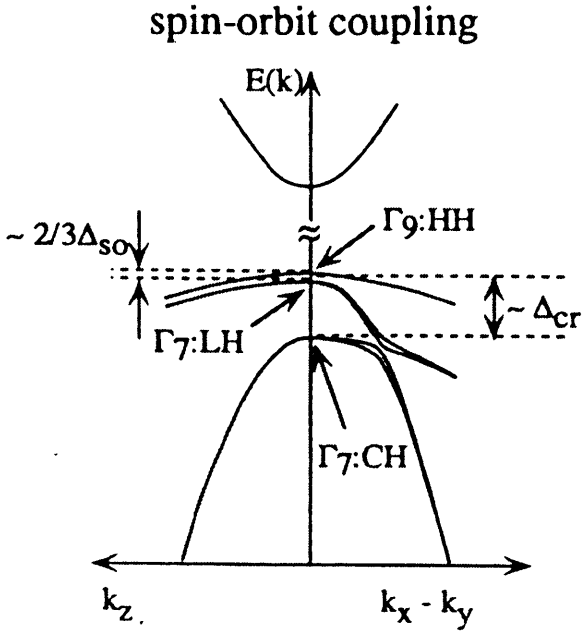

Figure 3-18 Diagram showing the upper valence band of wurtzite GaN near the direct band gap [74]

Figure 3-16 shows a schematic of the WZ GaN band structure. An important detail is the splitting of the Γ point valence band maximum (VBM) into three sub-bands due to crystal field and spin orbit coupling. The crystal field splitting depends on the kind of material, the ratio of lattice constants and the internal parameter u. Figure 3-17 shows the effects of crystal field and spin orbit coupling and crystal field and spin orbit coupling combined on the Γ_{15} point [74]. The three sub-bands caused by crystal field and spin orbit coupling are labelled, Γ_9, Γ_7 and Γ_7. Sometimes Γ_7 and Γ_7 are given symbols such as $\Gamma^{(1)}_{7v}$ and $\Gamma^{(2)}_{7v}$ to distinguish the upper and lower Γ_7 sub-bands respectively. The Γ conduction band is then labelled Γ_{7c}. The sub-bands are also labelled heavy hole (HH), light hole (LH) and crystal-field split off (CH) as shown in Figure 3-16 and Figure 3-18. Γ_9 band holes have a large mass in all k directions whereas the upper Γ_7 band holes are light in the k_x-k_y direction and heavy in the k_z direction and vice versa for the lower Γ_7 band [74 & 82].

The energies of the valence subbands' maxima relative to Γ_{15} are given in [83] (after [84]). At low temperatures photoluminescence and reflection spectra exhibit absorption or emission lines due to free exciton transitions between the Γ_{7c} conduction band and the

three valence subbands. From these transitions, and a knowledge of the exciton binding energy, Δ_{cr} and Δ_{so} can be determined [85]. Values for Δ_{cr} and Δ_{so} have been determined by a number of separate studies and the values indicative of their variety are shown in Table 3-3 [86]. The values recommended by reference [87] due to a recent convergence of values are Δ_{cr} = 10 meV and Δ_{so} = 17 meV.

Δ_{cr} (=Δ_1) (meV)	Δ_{so} (=$3\Delta_2$=$3\Delta_3$) (meV)
22	11
72.9	15.6
10.0±0.1	17.6±0.1[a]
22	15

Table 3-3 Values of the crystal –field splitting Δ_{cr} and spin-orbit splitting Δ_{so} in wurtzite GaN [86]

3.3.1 Charge Carrier Effective Mass

The Γ point conduction band minimum in wurtzite GaN is very nearly isotropic with negligible anisotropy; a parabolic relation of the form

$$E_c(k) \approx E_g + \frac{\hbar^2 k^2}{2m_e^*} \quad \text{..... Equation 3-1}$$

closely models the energy distribution, where m^*_e is the average electron effective mass around the conduction band maximum and k is the wave number [88]. The first Γ point conduction band electron effective mass recommended in [87] for wurtzite GaN is 0.20 m_0.

The wurtzite Γ point valence band maximum hole effective masses are not known with as much certainty as the electron effective mass due to the valence band's non-parabolicity and the close proximity of the three valence subbands. The value recommended in [89] is m_0 taken from the theoretical work by Suzuki et al. [90];

however, the more recent review by similar authors showed an increasing number of experimental results with values lower than this. In their more recent review, Vurgaftman and Meyer did not recommend a value for the hole mass but instead recommended a set of parameters for use in a detailed band structure calculation from which the hole behaviour may be predicted [87].

Γ^c_3	m_e/m_0
$\Gamma \rightarrow M\ (m^{\perp})$	0.2856
$\Gamma \rightarrow K\ (m^{\perp})$	0.2856
$\Gamma \rightarrow A\ (m^{\parallel})$	3.6227

Table 3-4 Electron effective masses at Γ^c_3 in various brillouin zone directions.

K^c_2	m_e/m_0
$K \rightarrow \Gamma$	0.7673
$K \rightarrow M$	0.7719
$K \rightarrow H$	0.4357

Table 3-5 Electron effective masses at K^c_2 in various brillouin zone directions.

M-L CBM	m_e/m_0
$\Gamma - H$	3.0375
$K - H$	0.3158
M	0.3858
L	0.3858

Table 3-6 Electron effective masses at the M – L conduction band minimum between the M and L points. The effective masses are given for several directions in the brillouin zone. [87]

The effective masses along various directions in the brillouin zone for three of the wurtzite satellite valleys are given in Table 3-4 to Table 3-6. Electrons in the conduction band at the Γ^c_3 point have effective masses nearly isotropic in the basal plane, with a mass much larger in a direction perpendicular to the basal plane. Large differences between the effective mass components are also apparent for the valley between the L and M points.

3.3.2 Temperature Dependence

The equations normally used to fit the temperature dependence of the energy gap in semiconductors are Varshni's formula and a Bose-Einstein model. Varshni's formula is[91]

$$E_{Vg}(T) = E_g(0) - \frac{\alpha_V T^2}{(\beta + T)} \quad \text{Equation 3-2}$$

and the Bose-Einstein model is

$$E_{Bg}(T) = E(0) - \frac{\alpha_B \Theta_B}{\exp\left(\Theta_B / T\right) - 1} \quad \text{Equation 3-3}$$

β (which has no true physical meaning) is meant to have the same order of magnitude as the Debye temperature (as has been demonstrated for GaAs [92 & 93]). α_V and α_B give the magnitude of the limiting slope as $T \rightarrow \infty$

$$\alpha \equiv \left(-\frac{d\left(E_g(T)\right)}{d(T)} \right)\Bigg|_{T \rightarrow \infty} \quad \text{Equation 3-4}$$

and Θ_B represents an effective phonon temperature

$$\Theta_B = \frac{\hbar\omega_{eff}}{k_B} \quad \text{Equation 3-5}$$

Experimental technique	$\alpha/10^{-4}$ eV/K	β (K)
Photoluminescence of *FX* (A)	5.0	400
FX (B)	5.2	450
Photoluminescence excitation	−5.08	−996
Photoluminescence of donor Bound exciton	7.2	600
Absorption of epilayer	9.39	772
Absorption of bulk sample	10.8	745
Photoreflection of *FX* (A)	8.32	835.6
FX (B)	10.9	1194
FX (C)	2.92	3698.9
Absorption of *FX* (A)	11.8	1414
Absorption	8.73	830
Reflectance of *FX* (A)	12.8	1190
FX (B)	12.9	1280
FX (C)	6.6	840
Absorption of MOCVD sample	5.66	737.9
Absorption of MBE sample	11.56	1187.4
Spectroscopic ellipsometry	8.58	700(fixed)
	6.06	800(fixed)
Reflectance of zinc-blende GaN	6.697	600
Thermomodulation	5.9	600

Table 3-7 Varshni coefficients for WZ GaN [94]

Varshni's equation is empirical and ad hoc. The temperature dependence of the band gap of WZ GaN seems to show a large variance, as indicated by the large spread in the values of coefficients α_V and β determined from fits to experimental data Table 3-7. The strain in the layers and the dependence of strain on temperature, the growth temperature, the ratio of film-to-substrate thickness, crystallographic orientation of the substrate, cooling procedure and the use of buffer layers has been cited as a reason for the large variation of Varshni parameters reported in the literature, [92]. Pässler [95] recently pointed out that the wide variation is also partly caused by a combination of the use of inadequate models such as Varshni's equation and the Bose-Einstein model to characterize the temperature dependence of films. The lack of data at high temperatures and the lack of precise data in pertinent regions also affect the precision of the reported results.

Pässler developed a model with a greater physical basis:

$$E_g(T) = E_g(0) - \frac{\alpha\Theta}{2}\left(\sqrt[4]{1+\frac{\pi^2}{6}\left(\frac{2T}{\Theta}\right)^2+\left(\frac{2T}{\Theta}\right)^4}-1\right) \quad \text{Equation 3-6}$$

which led the range of values of the characterising parameters α and Θ taken from results in the literature to be reduced by a factor of ten. The model suggested should be used more often in the future. From the data given in [95] values for α and Θ of 6.53 and 612 are determined by averaging the results of the two studies that extend the data to higher temperature regions.

In [87] Varshni coefficients are determined by averaging the values from a large number of studies. These average values are $\alpha_V = 0.909$ meV/°K and $\beta = 830$ °K.

3.3.3 Strain Dependence

Two low temperature (10°K) WZ GaN photoluminescence spectra are shown in Figure 3-19 for layers grown on (0001) 6H-SiC and sapphire. The dominant of both spectra peak (labelled BX) are attributed to excitons bound to donors. The peaks labelled FX^A and FX^B are free exciton transitions from the Γ_{7c} to the Γ_{9v} and $\Gamma^{(1)}_{7v}$ subbands, respectively. The transitions from Γ_{7c} to Γ_{9v}, $\Gamma^{(1)}_{7v}$ and $\Gamma^{(2)}_{7v}$ are often called the A, B and C transitions, respectively, and the excitons which result from these transitions the A, B and C excitons. The reason for the shift in the exciton spectrum shown in Figure 3-19 is the strain in the layers. The dependence of the exciton transition energies on strain is shown in Figure 3-20 [96].

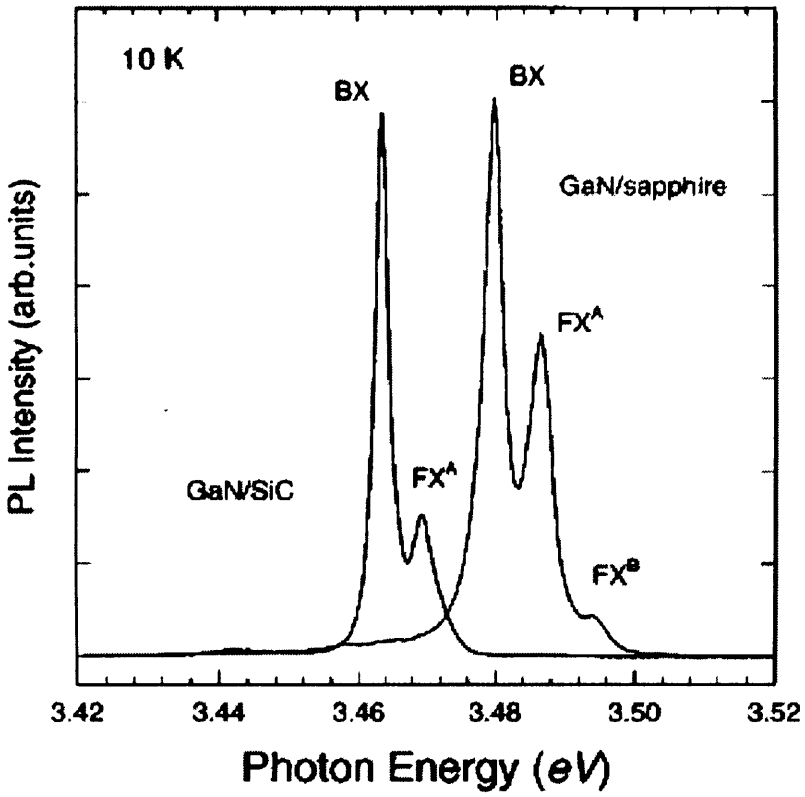

Figure 3-19 Photo luminescence of 3.7μm GaN film on Al_2O_3 and 4.2μm GaN film on 6H-SiC both films grown by MOCVD[96].

Figure 3-21 shows the temperature dependence of the A free exciton transition peak energy for GaN films grown on various substrates. The difference between the different layers is attributed to the different strain in each layer [97]. Strain in the layers is caused by lattice mismatch and the difference in thermal expansion coefficient between the layers and the substrates (sapphire 7.5x 10^{-6} K^{-1} GaN 5.6x10^{-6} K^{-1} and 6H SiC 4.2 x10^{-6} K^{-1}) with the difference in thermal expansion contributing the most to the observed strain [96]. Hence films grown on Al_2O_3 have a compressive strain and those grown on 6H SiC have a tensile strain. The reduction in the difference as temperature increases is attributed to the reduction in strain (Figure 3-22).

The difference between the thick HCVD grown layer and the homoepitaxial layer in Figure 3-21 is harder to explain as both layers should be relatively strain free. One possible cause is a difference in the free carrier concentration in the layers, the so-called Burstein-Moss effect [93].

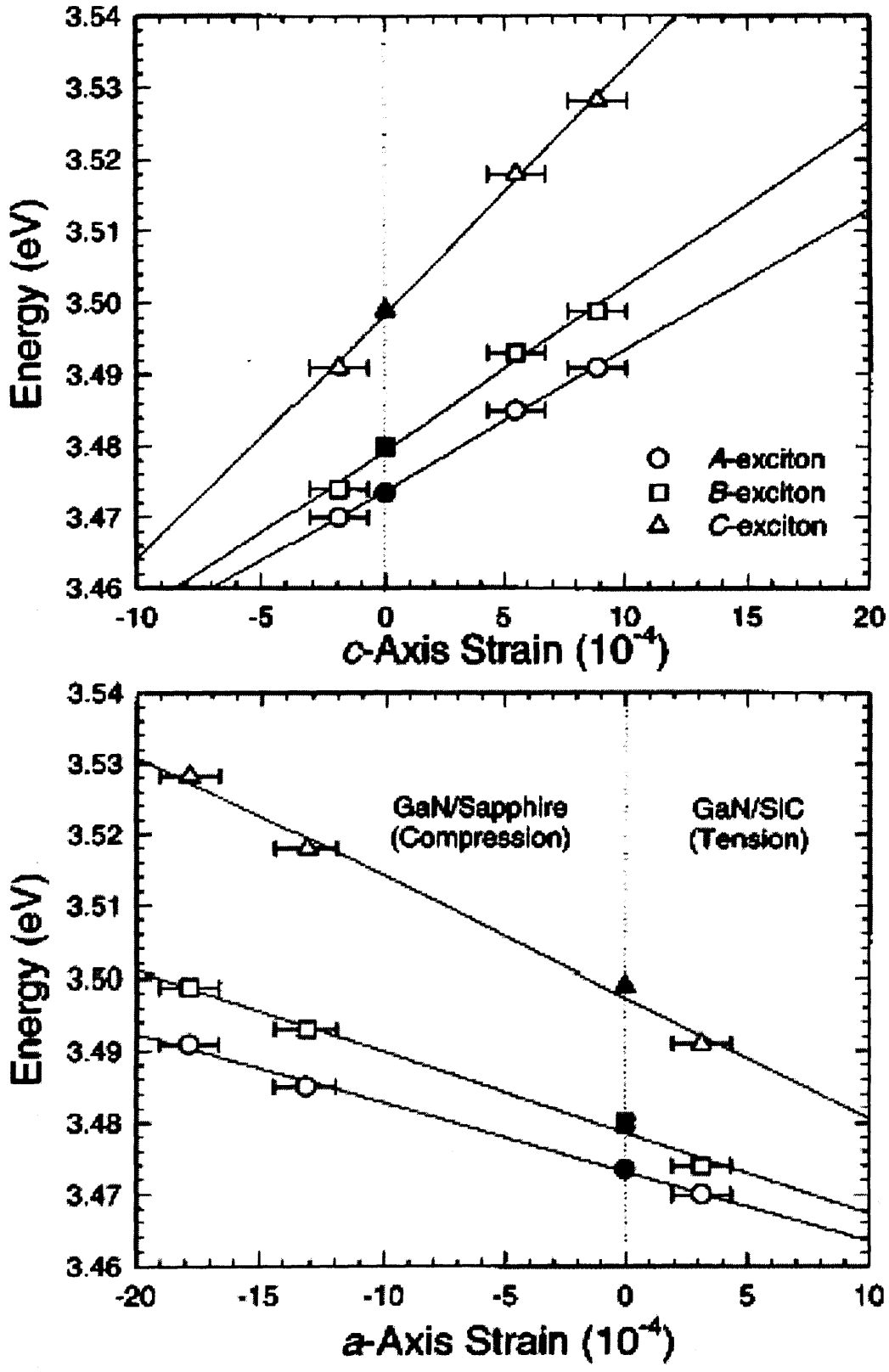

Figure 3-20 The dependence of exciton transition energies on strain on the layer; solid lines are best linear fits [96].

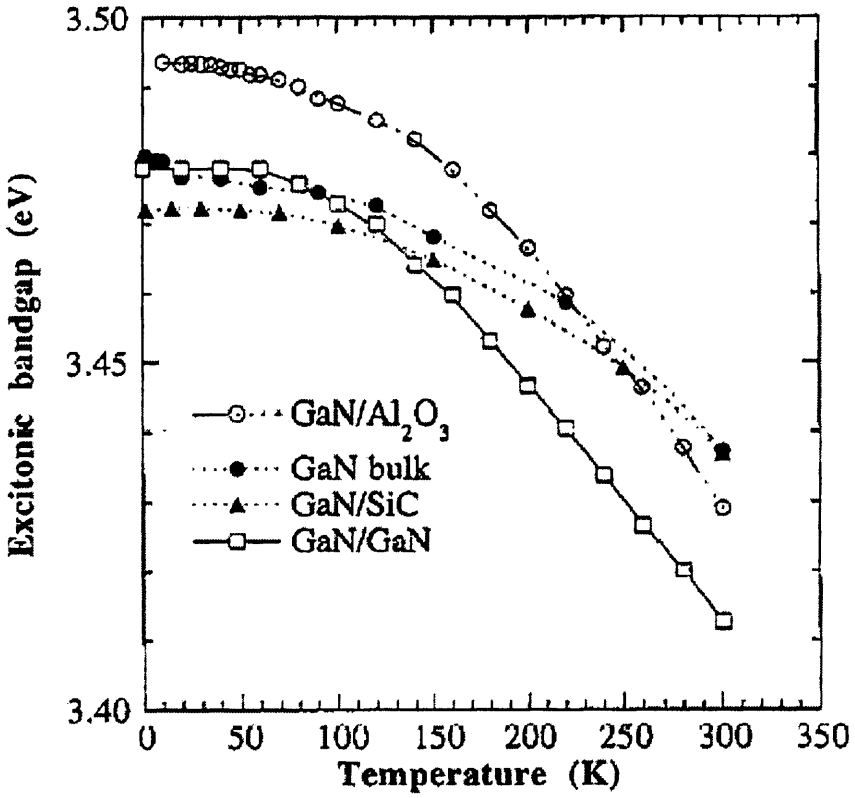

Figure 3-21 Exciton energy temperature dependence determined by photoluminescence studies in different samples the free exciton energy is closely related to the band gap. Open circles and squares and filled triangles: MOCVD grown. Filled circles: thick HCVD grown [97].

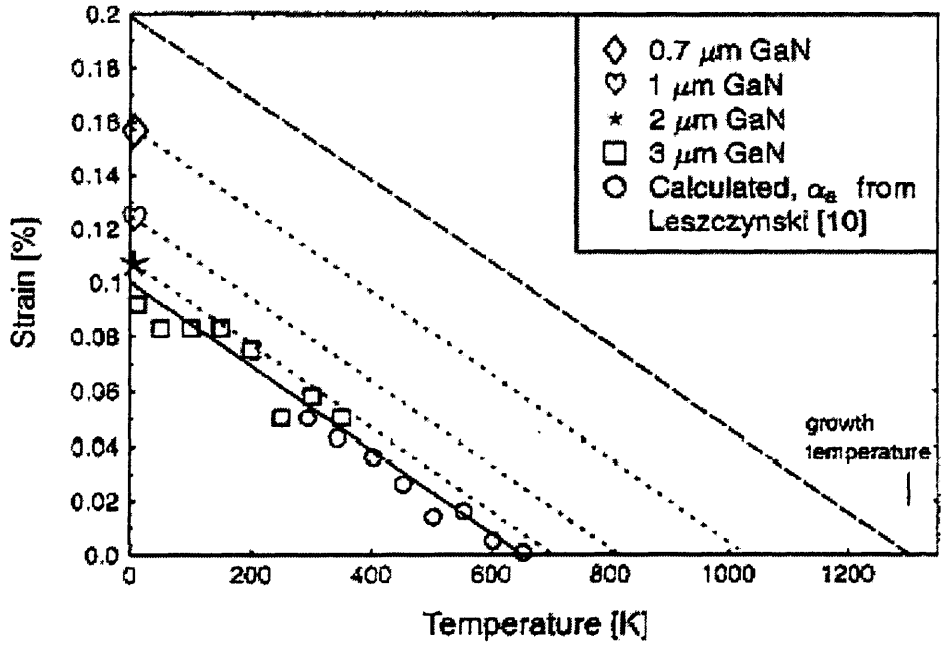

Figure 3-22 Dependence of strain on the temperature of various heteroepitaxial layers [98]

The effect of strain on the valence band structure of WZ GaN is shown schematically in Figure 3-23 [74] along with indications of the difference between axial and biaxial strain (hydrostatic strain is when the strain acts equally in all directions).

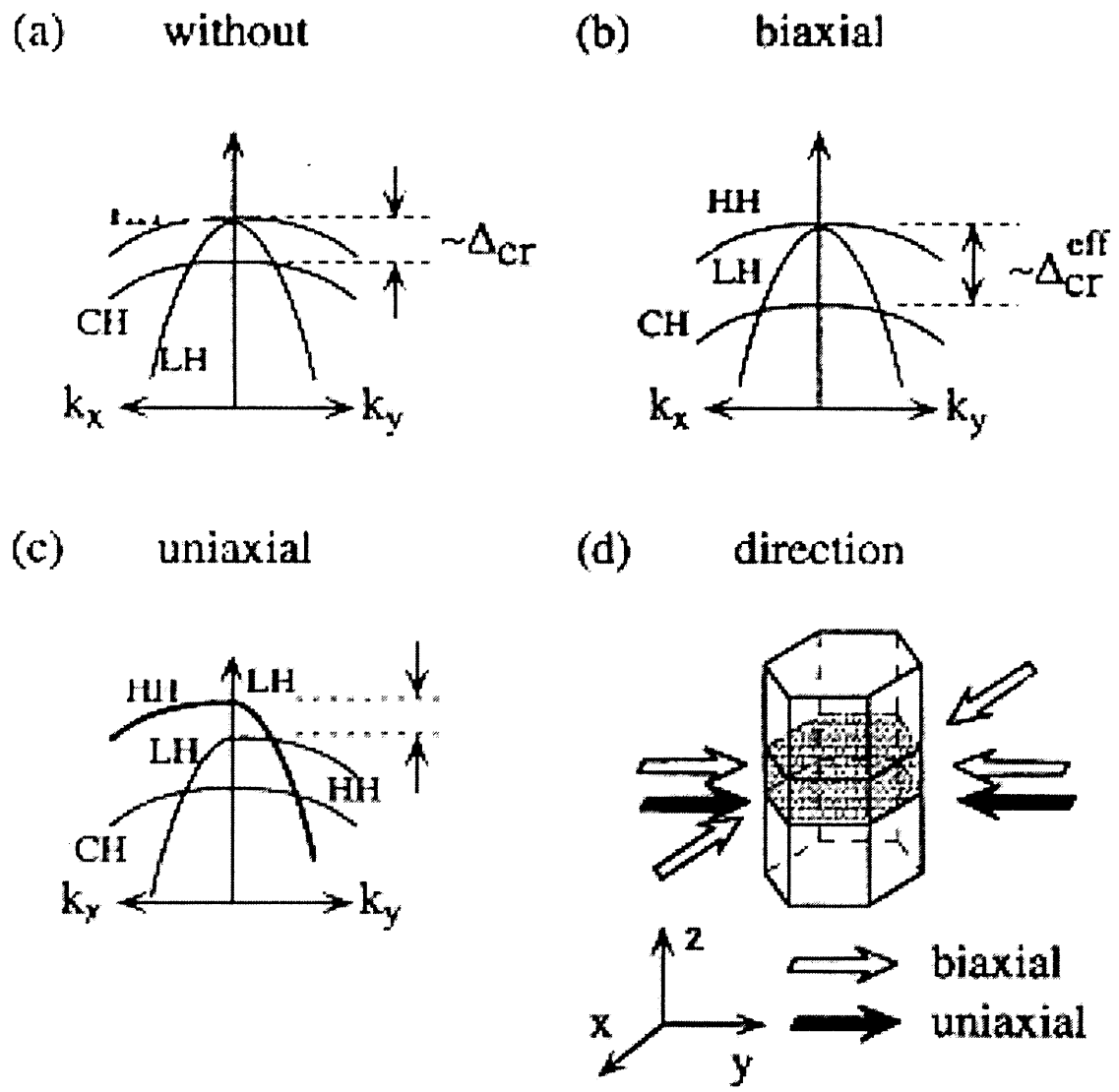

Figure 3-23 Schematic band structure in the k_x-k_y plane near the valence band maximum of WZ GaN [74].

3.3.4 Dopant ionisation energies

The approximate ionisation energy of some WZ GaN dopants are given in Table 3-8[99,100,101,102,103,104 & 105].

Donors, Ionization Energy (E_c- E_i) (meV)		
Impurity of Defect	Ga Site	N Site
Si	~ 28	
V_N (N vacancy)		40
C	110-140	
Mg		260
O		~ 29
S		48 ± 10
Te		50 ± 20
Acceptors, Ionization Energy (E_i- E_v) (meV)		
V_{Ga}	140	
Si		190
Mg	140-210	
Zn	210-340	
Be	150-700	
Li	750	
C		890
Ga		590-1090
Ca	169	

Table 3-8 Table of the energy required to ionize some intrinsic and extrinsic impurities used to dope GaN

3.4 Mechanical properties of wurtzite gallium nitride

3.4.1 Young's modulus, Poisson's ratio, Hardness, Fracture Toughness, Elastic Moduli, Poisson's Coefficient and the Bulk Modulus.

The Young's modulus of a material is defined as the initial stress divided by the initial strain for a tensile stress acting in one direction only with the sides of the material unbound Figure 3-24. In this situation Poisson's ratio is defined as (δw/w)/(δl/l) (see Figure 3-24 [106]).

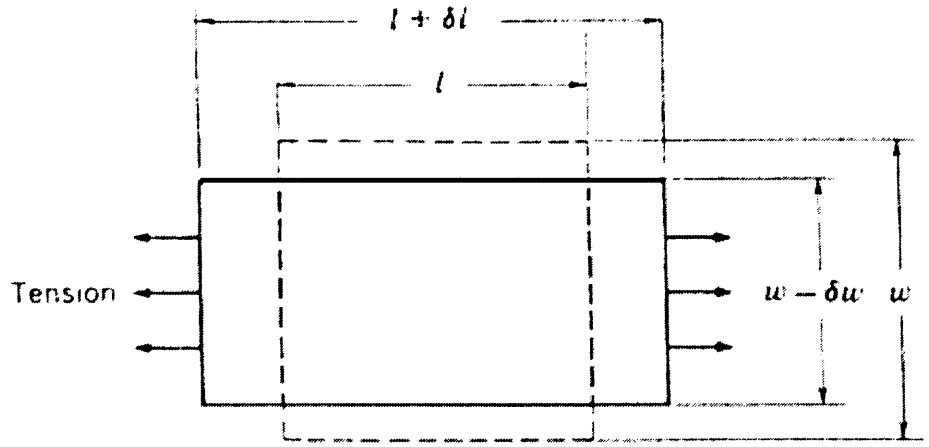

Figure 3-24 Schematic illustrating the meaning of the Poisson ratio.

Values of Young's modulus are reported in [107,108,109 & 110]. All these studies use nano-indentation to determine hardness and Young's modulus. The value recommended for Young's modulus is 295 ± 3 GPa from [110]. The merit of this study is that it was performed on bulk GaN and thus avoided the effects of the substrate and the large numbers of crystal defects associated with heteroepitaxial layers of GaN [110]. The recommended value of true hardness, 30 GPa, is also determined from [110]. The value from this study is preferred as it was performed on bulk GaN with the associated bonuses of that material and it utilizes the nano-indentation technique which has high accuracy compared to conventional Vickers micro-hardness testing [110].

The fracture toughness of WZ bulk GaN, a parameter characterizing the materials resistance to failure under load, is given as 0.79 ± 0.1 MPa $m^{1/2}$ [111].

The elastic moduli of a material relate the stress and strain in a material when Hooke's law is still applicable [106]. Many values of the elastic moduli have been published (see for examples [112 & 113]). The recommended values are those given by Polian et al. These are C_{11} = 390 GPa, C_{12} = 145 GPa, C_{13} = 106 GPa, C_{33} = 398 GPa, and C_{44} = 105 GPa. The zero pressure bulk modulus calculated with these values from the equation

$$B_0 = \frac{(C_{11}+C_{12})C_{33}-2C_{13}^2}{C_{11}+C_{12}+2C_{33}-4C_{13}} \quad \text{Equation 3-7}$$

is 210 ± 10 GPa. These values agree well (though not completely) with other experiments performed on epitaxially grown GaN [113 & 114]. It is assumed that the difference in values is due to the difference in quality of the material. The measurements of Polian et al, [115], were performed on high quality bulk crystals grown by high temperature, high pressure solution of nitrogen into liquid Ga, hence their measurements are likely to be more indicative of the true GaN material properties as opposed to the defect ridden epitaxial layers.

Poisson's ratio was determined as ν = 0.23 ± 0.06 in [116], in agreement with the value of 0.25 quoted in [110]. The high uncertainty in the former value is due to the presence of both hydrostatic and biaxial strain in epitaxial layers, the hydrostatic strain due to the effect of point defects and the biaxial strain due to the lattice constant and thermal expansion coefficient mismatch between the substrate and film [116]. Hydrostatic strain is when the strain acts in all directions equally whereas biaxial acts in two directions only. Using a Poisson's ratio of 0.23, values for the bulk modulus (B_0) and Young's modulus were calculated as 200 and 290 GPa, respectively [116].

The bulk modulus, which relates hydrostatic pressure to changes in volume, has been determined recently for GaN powder as 202.4 GPa. This value agrees well with theory (~200 GPa) and with the value determined from measurements on GaN bulk

crystals 207 ± 3 GPa [116]. The recommended value is 207 ± 3 GPa, concurrent with the value predicted by the elastic moduli of [115] and close to the values predicted in [116]. Because of the discrepancies between the values of the bulk modulus and Young's modulus predicted using a value of Poisson's ratio of 0.23, the recommended value for Poisson's coefficient is 0.25.

3.5 Electrical properties of gallium nitride

3.5.1 Unintentional Doping

As grown GaN is un-intentionally doped n-type [117]. When GaN was first grown for electronic applications the free electron concentration was much higher 1 x 10^{19} – 1 x 10^{20} cm^{-3} than in films grown today ~ 1 x 10^{16} cm^{-3}. The unintentional donors were initially thought to be native defects as the amount of impurities measured by secondary ion mass spectroscopy (SIMS) was smaller than the electron concentration (n) by several orders of magnitude [118 & 119].

In 1969 Maruska and Tietjen suggested the nitrogen vacancy (V_N) as the active defect [118] and theoretical studies predicted V_N as a shallow donor[120, 121 & 122]. However the calculated formation energies of various defects indicated that V_N was less likely to form than silicon on a gallium site (Si_{Ga}) and oxygen on a nitrogen site (O_N), both of which are also donor impurities. [120, 123 & 124].

Zhang et al. [125] claimed evidence for V_N being the dominant donor when the Hall carrier concentration was < 10^{17} cm^{-3}. Other evidence for V_N is the increase of sample resistivity with increasing nitrogen flux exhibited by MBE grown films [126,127 & 128]. Logically the amount of nitrogen vacancies should decrease as the nitrogen flux increases; however, the amount of oxygen in the film should also increase since contamination of the nitrogen source particularly ammonia is thought to be a major source of oxygen contamination [129]. Other lesser sources of oxygen are desorbtion of water from the chamber walls or oxygen from the chamber quartz [127 & 130]. The above argument is not conclusive, however, as the increase of nitrogen flux and reduction of

nitrogen vacancies could mean fewer sites where O_N can form. Also there could also be a corresponding increase in gallium site vacancies (V_{Ga}) or nitrogen interstitials (N_I) (a triple and single acceptor respectively) as the nitrogen flux is increased [120, 121 & 122]. These acceptors would act to compensate any donors, reducing the material's resistivity [127].

D.C Look et al. [131] have irradiated GaN with high-energy electrons and argued that nitrogen vacancy – nitrogen interstitial (V_N-N_I) Frenkel pairs are formed during the irradiation. From variable temperature Hall effect measurements (VTHEM) it was deduced that V_N has an activation-energy of 64 ± 10 meV. This is the only semi-direct observation of nitrogen vacancies and the only experimental evaluation of the ionization energy of the nitrogen vacancy. If the donor energy of V_N is in the region of 64 meV it makes it less likely that V_N is the principal dopant of unintentionally doped GaN [131 & 117].

Oxygen exhibits a very characteristic behaviour in nitrides. In GaN, it behaves as a shallow donor, but when the band gap is increased (either under hydrostatic pressure, or by alloying with AlN), the oxygen undergoes a transition to a deep centre (a so-called *DX* centre). In this new configuration, shown in Figure 3-25, oxygen is a deep acceptor and compensates the material. Note that the oxygen atom (shown moving 0.9 Å in Figure 3-25) moves away from its normal-substitutional site by almost one angstrom. Perlin et al. thought that the reduction in carrier concentration exhibited by GaN films at high pressure was due to the conduction-band-resonant V_N energy level predicted by theory [121 & 122] crossing the conduction band maximum (CBM) into the forbidden energy gap at high pressures [132]; however, later they attributed the same behaviour to oxygen impurities that have a DX like behaviour [133 & 134]. The similar behaviour of unintentionally doped and oxygen doped materials when put under pressure has been taken as proof of the oxygen as the unintentional donor [135]. Other lesser evidence suggesting oxygen as the dominant donor is given in [136, 137 138 & 129].

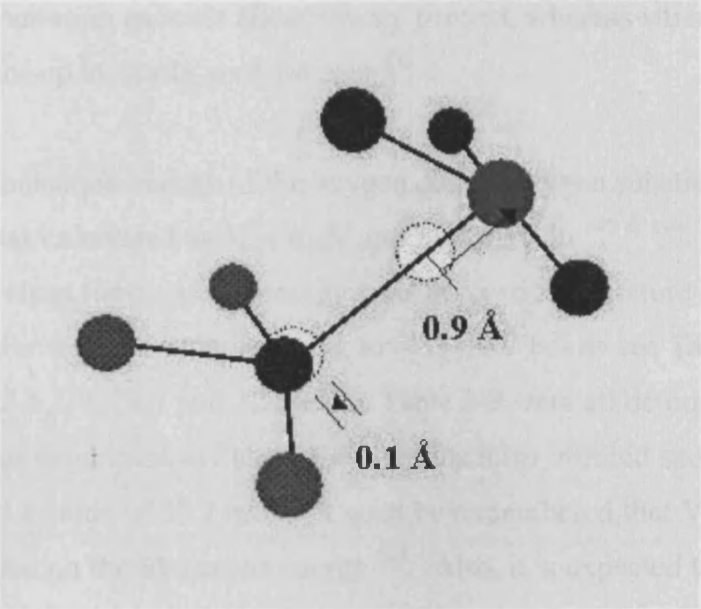

Figure 3-25 Illustration of the formation of the DX centre in GaN (see main text above) [139]

$E_C - E_D$ / meV	Room temperature Free carrier concentration / cm^{-3}	Technique	Reference
23.5 ± 1	> 1 x 10^{17}	VTHEM	136
- 40 ± 10	1 x 10^{19}	EXTR	140 & 133
10	5 x 10^{17}	VTHEM	137
4	1.5 x 10^{18}	VTHEM	
Degenerate	6 x 10^{18} – 4 x 10^{19}	VTHEM	
32 ± 5	~ 1.5 x 10^{18}	VTHEM	138
29	5 x 10^{17}	VTHEM	141
28.7	≤ 5 x 10^{16}	VTHEM	142
31.1	< 1 x 10^{17}	IT	143 and 146
33.2 ± 1	~ 1 x 10^{17}	FTIR	144

Table 3-9 Experimentally observed oxygen activation energies (E_C-E_D) from various studies measured by EXTR: Extrapolation of level-pressure graph, IT: infrared transmission, VTHEM: variable temperature hall effect measurements and FTIR: Fourier transform infrared spectroscopy.

Interestingly enough silicon is shown not to undergo any changes up to a pressure of 27GPa [133]. These results mean that oxygen becomes a deep level in AlGaN when the

aluminium concentration exceeds about twenty percent, whereas silicon will behave as a shallow donor up to nearly sixty percent [133].

The theoretical ionisation energy of the oxygen donor (oxygen substituted for nitrogen (O_N)) was calculated as 32.4 meV and 31.4 meV in [145 & 146]. Experiments give a range of values for oxygen's energy level at room temperature and pressure, from ~ 40meV above the conduction band, to ~ 33 meV below see Table 3-9. The values of 4,10, 23.5, 29, 28.7 and 32 meV in Table 3-9 were all determined by VTHEM, whereas experimenters using Fourier transform infrared spectroscopy (FTIR) measured a value of 33.2 meV. It must be remembered that VTHEM gives only a lower bound on the ionization energy [144]. Also, it is expected that the optical energy required to activate a donor will be $\geq$ 15% greater than the thermal energy [144]. This would mean that all the results, with the exception of those of reference [137], agree. Also at high donor concentrations the ionisation energy is expected to fall [147] and eventually the donor band will merge with the conduction band at a density of 1 x 10^{18} cm^{-3} - 6 x 10^{18} cm^{-3} [148, 126] (and references). This effect is clearly shown by the samples in [143] (see Table 3-9).

The reason for the discrepancy between the results of references [143 & 144] (i.e. samples with carrier concentrations of 1.5 x 10^{18} have ionization energies of 4 and 32 $\pm$ 5 in separate films) is unclear. VTHEM has been stated to give possibly inaccurate readings [144] possibly due to an uncertain r_H value [149 & 141]. Other effects include free carrier screening, which may reduce the activation energy, compensating acceptor affects and the affect of strain [145].

Si_{Ga} was also put forward to explain the measured conductivity of as grown GaN, though less evidence to support this has been presented [150 & 131]. Silicon as an unintentional donor could come from any quartz used in the chamber, contamination of the gallium precursor, or contamination of the chamber from previous growth runs. Silicon is the most commonly used intentional n-type dopant. The theoretical value of its ionisation energy is 30.8 meV; other transition energies are given in [145]. Experimental values for silicon's ionisation level are shown in Table 3-10. The value of 29meV has been questioned [143]. Jayapalan et al.[152] have shown that their results are consistent with the VTHEM results of Götz et al.[150].

$E_C - E_D$ (meV)	Room temperature free carrier concentration (cm^{-3})	Technique	Reference
30.18 ± 0.1	~ 1 x 10^{17}	FTIR	[144]
12-17	~ 6 x 10^{17} – 1 x 10^{17}	VTHEM	[150]
29	~ 1 x 10^{17}	EIT	[151]
22	Unspecified	LTP	[152]
17	~ 2 x 10^{17}	VTHEM	[141]

Table 3-10 Experimentally observed silicon activation energies (E_C – CBM energy, E_D – Oxygen donor energy, EIT extrapolated infrared transmission, LTP low temperature photoluminescence).

3.5.2 Electron mobility

Figure 3-26 shows the mobility temperature dependence for a freestanding, thick HVPE film, i.e. where the film was originally grown heteroepitaxially on a substrate (here c-plane sapphire) and, post growth, removed from the substrate to give a quasi-bulk GaN wafer [153].

The mobility temperature curve is well modelled by contributions to scattering from only piezoelectric scattering, polar optical phonon scattering, acoustic mode deformation potential scattering and ionized impurity scattering. At high temperatures polar optical phonon scattering is the dominant scattering mechanism and at low temperatures scattering from ionized impurities is the limiting scattering mechanism. The fact that only these four scattering mechanisms need to be considered to model the mobility-temperature dependence is an indication of the high quality of the films and of their freestanding nature. Similar high quality freestanding films have been grown by Huang et al. [154]. The Hall mobility-temperature curves for their samples are a close match to the one shown in Figure 3-26.

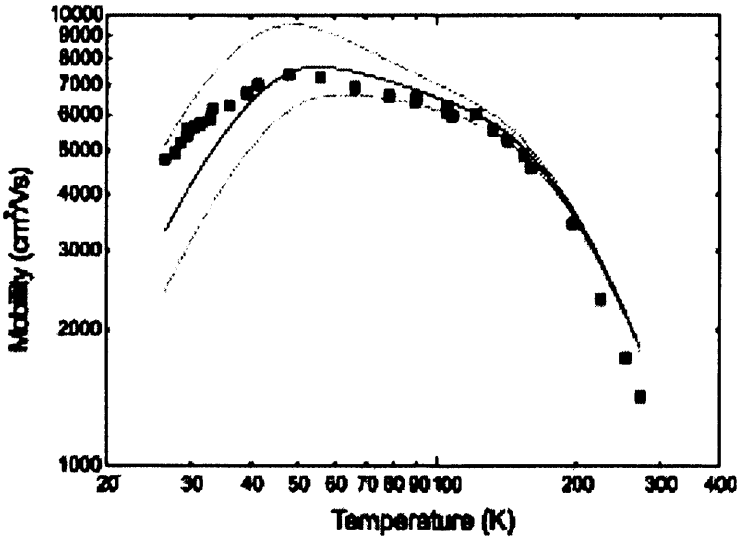

Figure 3-26 Hall mobility dependence on temperature for free-standing 200μm thick n-type GaN grown by HVPE originally on c-plane sapphire substrate [154]

In n-type films of lesser quality other scattering and conduction mechanisms have to be included to model the Hall effect measurement results. These other mechanisms include scattering from nitrogen vacancies [155], scattering from regions of cubic phase in WZ films[156], scattering from dislocations [157,158,159 & 160], scattering at grain boundaries in some MBE grown layers [161], phonon assisted impurity band conduction [162,163 & 164] and conduction in a degenerate layer next to the substrate in films grown by both hydride vapour phase epitaxy (HVPE) [165,166, 167 & 168] and metal organic chemical vapour deposition MOCVD [169, 170 & 171]. Deep traps can also be an issue (see [172]).

An example of the mobility-temperature curves found for less perfect crystals is shown in Figure 3-27, where μ_{meas} is the as measured mobility and μ_c and μ_d are the predicted mobilities of electrons within the conduction and impurity sub-bands of the sample, respectively. As can be seen, the sample shows a very different temperature dependence with a peak in mobility at approximately 200 °K and a drop off of mobility as the temperature decreases. Also the peak mobility is over ten times less than that in the freestanding sample at the same temperature.

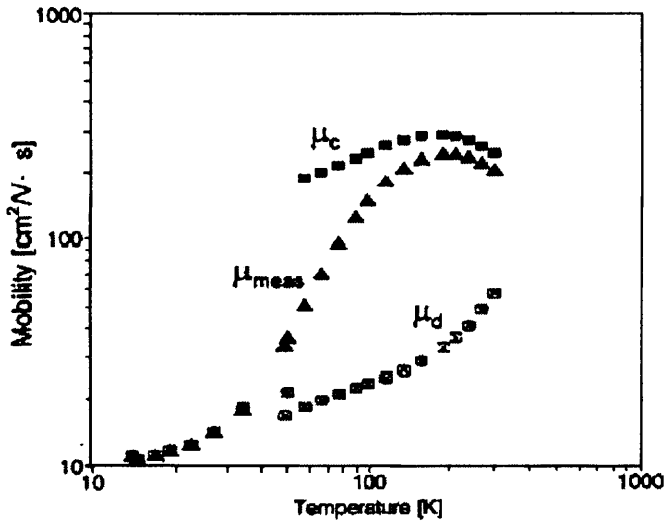

Figure 3-27 Temperature dependence of electron mobility in a film that clearly exhibits impurity band conduction at low temperatures [175].

Figure 3-28 shows the dependence of the room temperature mobility of ECR-MBE grown films on free carrier concentration and dislocation density. The films were grown on a low temperature GaN buffer layer on c-plane (0001) sapphire substrates with a nitridation step prior to growth of the buffer layer [157]. Varying the amount of silicon included in the layer during growth varied the carrier concentration; varying the nitridation time and the buffer layer thickness varied the dislocation density.

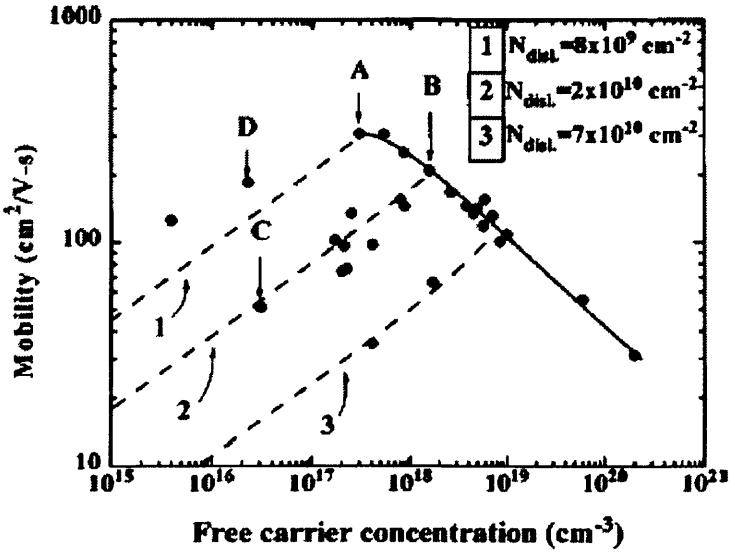

Figure 3-28 Dependence of mobility on free carrier concentration [157]

At high free carrier concentrations the mobility of the samples of Figure 3-28 can be seen to have a linear dependence, as would be expected if ionized impurity scattering were the dominant scattering mechanism [157 & 158]. At lower free carrier concentration the linear dependence breaks down. In papers [157 & 158] the cause for this is cited as the effects of dislocations. Dislocations introduce acceptor states along their length which accept free electrons and thus when ionized create a space charge along the length of the dislocation which acts to scatter electrons [166]. At high free carrier concentrations the charge of the ionized dislocation is screened and their effect is minimized. A similar effect has been observed in MOCVD films [157].

3.5.3 Electron Drift Velocity

Figure 3-29 [173] and Figure 3-30 [174] show the dependence of MOCVD grown GaN electron drift velocity on electric field strength, where the velocity-field characteristic was determined by the conductivity technique and time of flight technique, respectively. The conductivity technique gives a better match to theoretical peak velocities but does not show well the saturation at high voltages. The time of flight technique shows the opposite with a clear saturation at an electric field greater than 225 kV/cm but no obvious peak and a lower velocity at all fields. The voltage range in the conductivity technique experiments was limited by breakdown of the structure under test. In both experiments imperfect films were cited as a cause for the disagreement between theory and experiment. In the conductivity experiment the disagreement between theory and experiment in the pre-peak portion of the curve was specifically attributed to defect ridden material. Also in the time of flight experiment it was suggested that a reduction of the separation between the two lowest CBMs at the Γ point from 2 eV to 0.34 eV (in agreement with the results of ballistic-electron emission spectroscopy) would bring experiment and theory into closer agreement [175]. The difference between the band structure found in real GaN films and that predicted by theory is explained by the effect of strain on the band structure [176]. However even with the inclusion of the correction of the band gap the results still show a large discrepancy see (Figure 3-31).

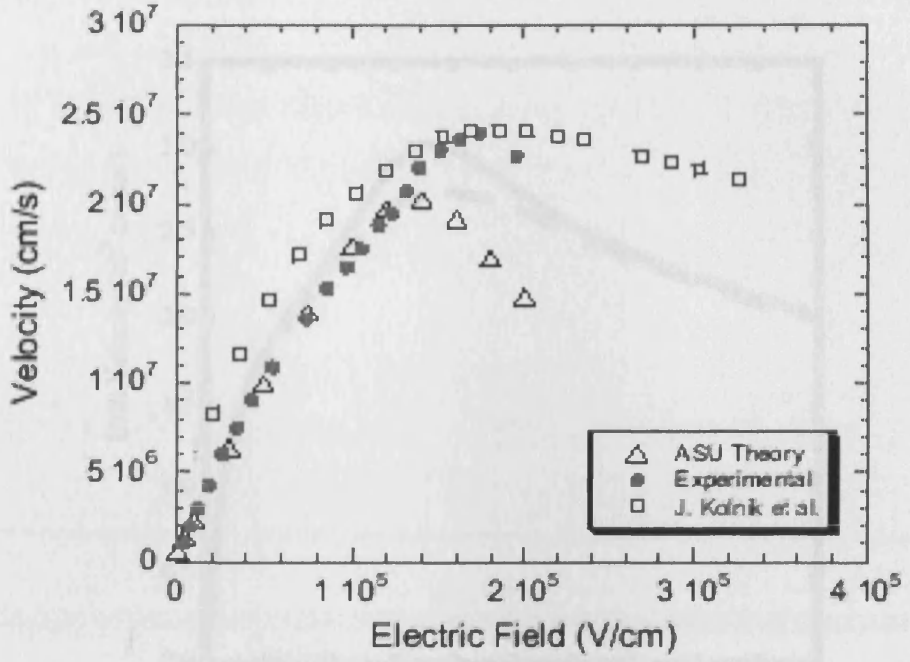

Figure 3-29 Electron velocity-field characteristic for WZ GaN determined by conductivity technique [173]

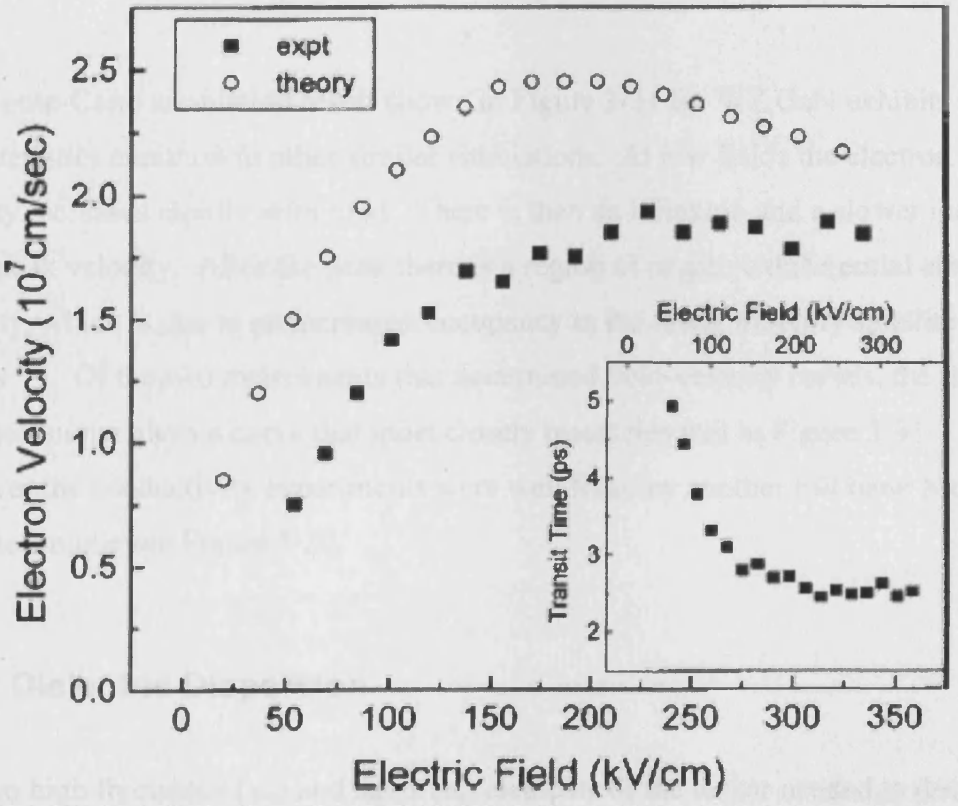

Figure 3-30 Electron velocity-field characteristic for WZ GaN determined by time of flight technique [174]

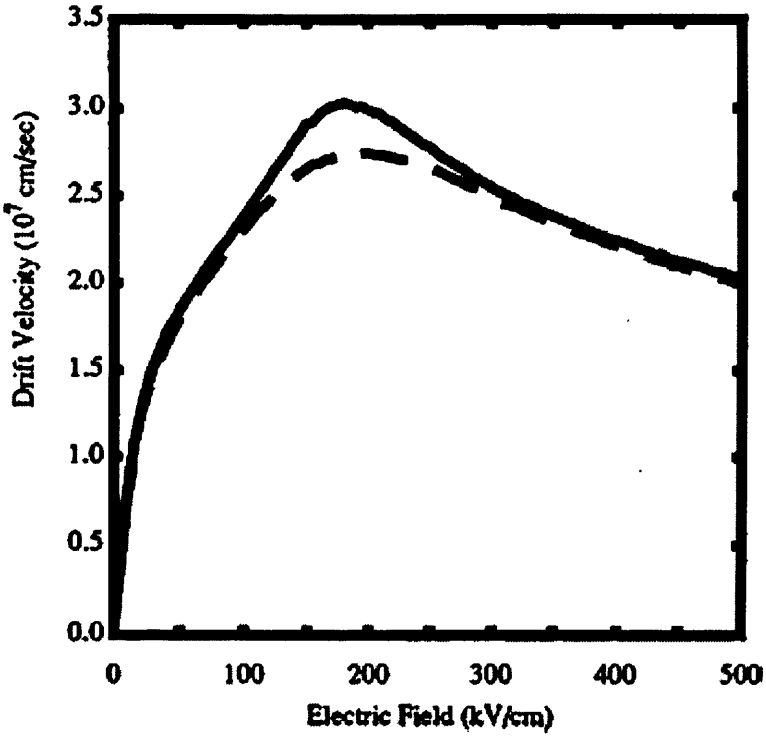

Figure 3-31 Calculated velocity dependence on electric field with (solid line) ~ 2eV and (dashed line) ~ 0.34 eV separation between the two Γ conduction bands.

The Monte-Carlo simulation result shown in Figure 3-31 for WZ GaN exhibits several characteristics common to other similar simulations. At low fields the electron velocity increases rapidly with field. There is then an inflexion and a slower increase to the peak velocity. After the peak there is a region of negative differential electron mobility, which is due to an increased occupancy in the lower mobility satellite valleys [177]. Of the two experiments that determined field-velocity curves, the time of flight technique gives a curve that most closely resembles that in Figure 3-31. However the conductivity experiments were well fitted by another full band Monte-Carlo technique see Figure 3-29.

3.5.4 Dielectric Dispersion

The two high frequency (ε_∞) and static (ε_s) elements of the tensor needed to describe the dielectric dispersion for wurtzite GaN due to the lattice interactions with electic fields incident parallel to the *c* axis (extraordinary $\varepsilon_{zz} = \varepsilon_\parallel$) and perpendicular to it

(ordinary $\varepsilon_{xx} = \varepsilon_{yy} = \varepsilon_{\perp}$), found by two theoretical [178 & 179] and three experimental studies are shown in Table 3-11. The arithmetic mean of the results is given in the bottom row of the table. The experimental results quoted are all referred to in [178] but are here quoted separately again to aid commentary.

Referenced Article	$(\varepsilon_\infty)_{xx}$	$(\varepsilon_\infty)_{zz}$	$(\varepsilon_s)_{xx}$	$(\varepsilon_s)_{zz}$
[178]	5.2	5.39	9.24	10.35
[180]	5.29	5.29	9.28	10.2
[179]	5.21	5.41	9.25	10.34
Mean Results	5.23	5.36	9.26	10.3

Table 3-11 Table of the dielectric constant tensor elements for wurtzite GaN.

The dielectric constants from both [178 & 179] were calculated using the Lyddane-Sachs-Teller relationship (Equation 3-8 where α is either x or z) once the longitudinal and transverse optical phonon frequencies at the zone centre (ω^2_{LO} and ω^2_{TO}, respectively), and the high-frequency dielectric tensor (ε_∞) had been calculated ab initio within the framework of density-functional perturbation theory. The workers in [180] used a similar method, but with optical phonon frequencies determined by Gaussian and/or Lorentzian fits to Raman spectra and single values for $(\varepsilon_\infty)_{xx}$ and $(\varepsilon_\infty)_{zz}$ determined in infrared experiments performed by them, but not documented.

$$\frac{(\varepsilon_s)_{\alpha\alpha}}{(\varepsilon_\infty)_{\alpha\alpha}} = \frac{\omega^2_{LO}(\alpha)}{\omega^2_{TO}(\alpha)} \quad \text{Equation 3-8}$$

3.6 Summary

Various properties of wurtzite gallium nitride are presented. At the time this was written almost all gallium nitride was of the wurtzite type though cubic gallium nitride was also being studied. The values chosen were selected after a wide ranging search of the relevant literature, as representing the most representative values

available at the time. The reliance of data taken from gallium nitride grown by compression of gallium and nitrogen at high temperature rather than on data taken from films grown epitaxially on foreign substrates means that the data is as close to a theoretically pure crystal as will probably ever be possible; and hence should not need revision as the crystal quality of the epitaxial films improves.

4 Dielectric resonance method of conductivity measurement

4.1 Introduction

When a wafer of semiconductor is grown it is necessary to characterise it before any work is carried out on it ensuring that no time is wasted working on an inadequate wafer and aiding interpretation of results; furthermore if the wafer shows conduction less than would be expected from the suppliers specification, it may be sent back to the supplier before it is damaged. It is of course advantageous if the method used to measure the conductivity of a wafer is simple, cheap, easily put into practice, requires no prior knowledge of working with the material involved, does not affect the material in any way (i.e. the material is left unchanged by the technique) and it is applicable to all materials.

The most commonly used non-destructive method of measuring the conductivity of a semiconductor is the four-point probe method; this method is relatively simple, cheap, easily put into practice and is non-destructive; however, this method relies on the semiconductor being either sufficiently thick or conductive to conduct enough current to allow both a voltage and current measurement to be taken.

For thin, micron-thick epilayers the most often used method of measuring the sheet resistance or conductivity of the wafer are TLM measurements or Van de Pauw Hall Effect measurements, both these suffer from the fact that a working process (cleaving, photoresist patterning, etching, ohmic contact deposition) must already be in place for the material, as well as facilities to take the measurements. Also, any processing of the wafer might affect the conductivity of the sample, leading to erroneous measurements.

What would be ideal would be a method of measuring the conductivity of a thin epilayer structure without having to process the wafer, a method like the four-point

probe method but applicable to very thin films. In this chapter a simple and non-destructive method of measuring the conductivity of a thin film, that does not require the wafer to be processed in any way is described.

Because the bandwidth of the resonant peak of a resonant system is proportional to the energy stored in the resonant system divided by the power lost from it, introducing an additional method of power loss to the system causes the bandwidth of the system's resonant peak to increase. A small dielectric puck of high dielectric constant may be made to resonate at microwave frequencies and the resonance in this case is an electro-magnetical resonance and the resonant energy stored in the system is transferred between the electric and magnetic fields. If a conductive wafer is placed into such a resonant system, the bandwidth of the resonant peak widens due to I^2R ohmic losses. As is shown later in the chapter because the electric fields generated by the dielectric resonance are confined very close to the dielectric the electric field through the wafer varies as the dielectric is moved to and from the surface of the wafer. Calculations based around the fields in the cavity and in the wafer as a function of distance from the wafer (calculated with a suitable numerical field solver) can be fitted to the experimentally observed variation of the bandwidth of the resonant peak as a function of distance from the semiconductor wafer. This fit can be used to yield a value of the conductivity of the wafer.

The first part of this chapter gives in more detail the theory behind the experimental method including modes in dielectric resonators and the use of discrete component circuits to model such resonant cavities. Later, the experimental apparatus and method that was used are described and finally the results that were taken from one of the gallium nitride wafers that were bought for the purposes of this project are given. The conductivity value obtained is compared with the result expected and the method is discussed.

4.2 Theory

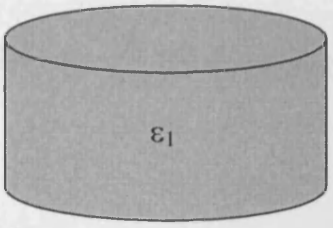

Figure 4-1 Schematic showing a cylindrical dielectric puck of dielectric constant ε_1 surrounded by air with a dielectric constant approximately equal to ε_0

In cylindrical co-ordinates Maxwell's equations may be written [181]

$$-\frac{\partial H_\phi}{\partial z} - \frac{1}{c}\cdot\frac{\partial E_r}{\partial t} = 0 \quad \text{Equation 4-1}$$

$$\frac{1}{r}\cdot\frac{\partial}{\partial r}(r\cdot H_\phi) - \frac{1}{c}\cdot\frac{\partial E_r}{\partial t} = 0 \quad \text{Equation 4-2}$$

$$\frac{\partial E_r}{\partial z} - \frac{\partial E_z}{\partial r} + \frac{1}{c}\cdot\frac{\partial H_\phi}{\partial t} = 0 \quad \text{Equation 4-3}$$

$$\frac{1}{r}\cdot\frac{\partial}{\partial r}(r\cdot E_r) + \frac{\partial E_z}{\partial z} = 0 \quad \text{Equation 4-4}$$

and

$$-\frac{\partial E_\phi}{\partial z} - \frac{1}{c}\cdot\frac{\partial}{\partial t}\cdot(-H_r) = 0 \quad \text{Equation 4-5}$$

$$\frac{1}{r}\cdot\frac{\partial}{\partial r}(r\cdot E_{\phi})-\frac{1}{c}\cdot\frac{\partial}{\partial t}\cdot(-H_r)=0 \quad \text{Equation 4-6}$$

$$\frac{\partial}{\partial z}\cdot(-H_r)-\frac{\partial}{\partial r}\cdot(-H_z)+\frac{1}{c}\cdot\frac{\partial E_{\phi}}{\partial t}=0 \quad \text{Equation 4-7}$$

$$\frac{1}{r}\cdot\frac{\partial}{\partial r}(-r\cdot H_r)+\frac{\partial}{\partial z}\cdot(-H_z)=0 \quad \text{Equation 4-8}$$

As may be seen the first set of equations has only a ϕ component of the magnetic field and only z and r components of the electric field. Similarly the second set of equations only has only a ϕ component of the electric field and only z and r components of the magnetic field. The solutions of these equations which, for the case of a cylindrical dielectric resonator such as that shown in Figure 4-1 must be found numerically, are the transverse magnetic (TM) and transverse electric (TE) modes of the resonator respectively. In the case of TM modes the magnetic field is always transverse to the z axis and in the case of the TE modes it is the electric field that is transverse to the z-axis. These are not the only solutions to the Maxwell equations for a dielectric resonator: hybrid modes that are neither TM or TE do exist. Furthermore, in the case of a cylindrical dielectric placed concentrically in a cylindrical cavity or in free space it is possible to classify the TM and TE modes as $TM_{m,n,p}$ and $TE_{m,n,p}$ modes where the m specifies the azimuthal variation given by either $\cos(m\phi)$ or $\sin(m\phi)$ and n and p refer to the number of field extrema within the DR in the radial and axial directions respectively [182].

One of the numerical field solvers that may be used to solve for the electric and magnetic fields of resonant cavity problems is Superfish which, uses finite element modelling (FEM) [183]. Superfish calculates electric and magnetic fields and the resonant frequency of the resonant mode closest to the initial conditions. Superfish creates a fine mesh of points within the geometry of the given problem and solves for the fields at these points. In its natural state Poisson Superfish will solve for the TM modes of the problem given to it; this is because the Superfish program had as a

principle application the modelling of particle accelerators which require the electric field to have an axial or z component (see Figure 4-2). However, due to the symmetry in the electric and magnetic field vectors described in Maxwell's equations it is relatively simple to transform the data for the TM mode output by Superfish into data pertinent to TE modes. In cylindrical co-ordinates Superfish will report values of E_r and E_z in MV/m and H_ϕ in A/m. To convert these field components to the corresponding fields for the TE mode H_r, H_z and E_ϕ the following three equations must be applied [184].

$$E_\varphi\left[\frac{MV}{m}\right] = (Z \times 10^{-6}) \cdot H_\phi\left[\frac{A}{m}\right]$$

$$H_r\left[\frac{A}{m}\right] = (-\frac{10^{-6}}{Z}) \cdot E_r\left[\frac{MV}{m}\right] \quad \text{.....Equations 4-9}$$

$$H_z\left[\frac{A}{m}\right] = (-\frac{10^{-6}}{Z}) \cdot E_z\left[\frac{MV}{m}\right]$$

where Z is the dielectric material's impedance given by

$$Z = \sqrt{\frac{\mu}{\varepsilon}}$$

In the absence of any material $\mu = \mu_0$ and $\varepsilon = \varepsilon_0$ and Z becomes the impedance of free space Z_0 equal to approximately 376.7Ω. Different boundary conditions also need to be applied to the TM and TE mode problems and the material properties must also be changed i.e. the relative permittivity and permeability of all the materials in the problem definition need to be reversed. Also care has to be taken with the other results calculated by Superfish from the data e.g. in the graphical output of the field lines generated by WSFplot (part of the Superfish program package) the lines of constant E_z or rH_ϕ have to be understood as lines of constant H_z and rE_ϕ respectively.

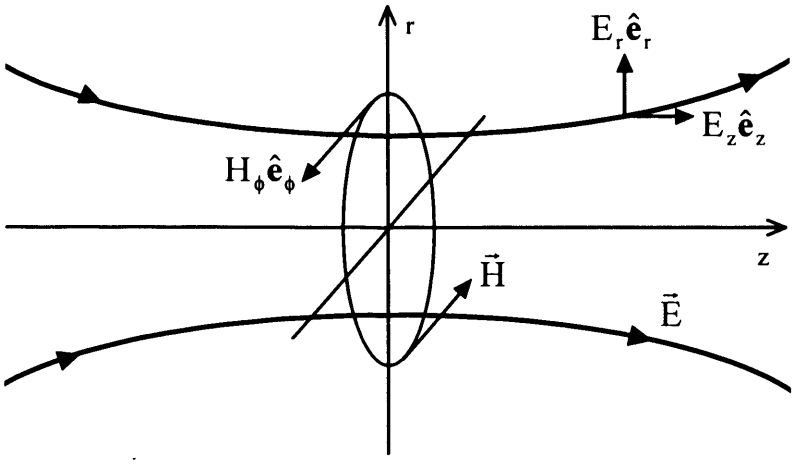

Figure 4-2 Schematic showing the field lines in a cylindrically symmetric cavity resonating in a TM mode. For a TE mode the electric and magnetic fields are interchanged and their directions are reversed. The magnetic field lines are out of the plane of the paper above the z axis and into the paper below the z axis.[184].

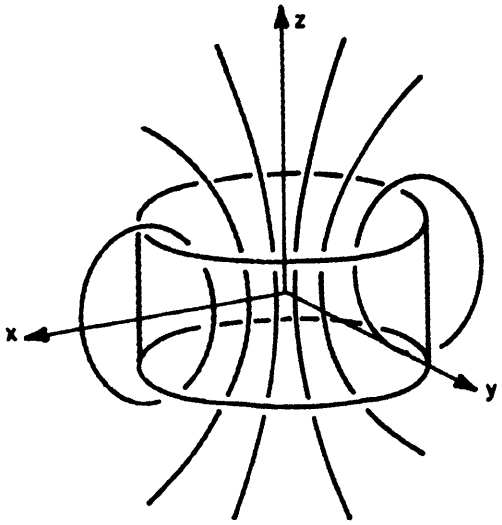

Figure 4-3 Schematic of the magnetic field lines of the TE_{011} mode

When resonating the electric field is much greater within the dielectric than outside, with the electric field magnitude reducing exponentially with distance from the dielectric (see Superfish graphical output in Appendix B). A schematic of the magnetic field lines of a dielectric resonator resonating in the TE_{011} mode is shown in Figure 4-3. The TE_{011} mode is utilised as it is a high Q mode [185]; also, in the case of the dielectric used in the experiments the resonant frequency of the TE_{011} mode was well clear of the cavity resonances. As may be seen the magnetic field lines of the TE_{011} mode are similar to those of a coil of wire. From this analogy it should be

possible, experimentally, to couple e-m energy to the TE_{011} mode of the resonator by passing an oscillating current through a coil positioned so as to have the greatest amount of flux linkage with the mode as possible; the more flux linkage between the coil and the mode, the greater the excitation of the mode. In this respect the dielectric resonator resonating in the TE_{011} mode is analogous to the discrete resonant circuit shown in Figure 4-4 where the dielectric is represented by a LRC resonant circuit with M_1 the coupling coefficient between the resonant mode and the excitation source.

If there were no losses from a resonating system then the system would carry on resonating forever; however, no resonant system will resonate *ad infinitum* if whatever system is driving it to resonate is removed. The time that the system takes to stop resonating once the driving system is removed is quantified by its Q. A general definition of Q is

$$Q = \frac{\omega_0 (\textit{time averaged energy stored in system})}{\textit{energy loss per second from system}} \quad \text{.....Equation 4-10}$$

where ω_0 is the resonant angular frequency of the system equal to $2\pi f_0$ where f_0 is the resonant frequency of the system [185].

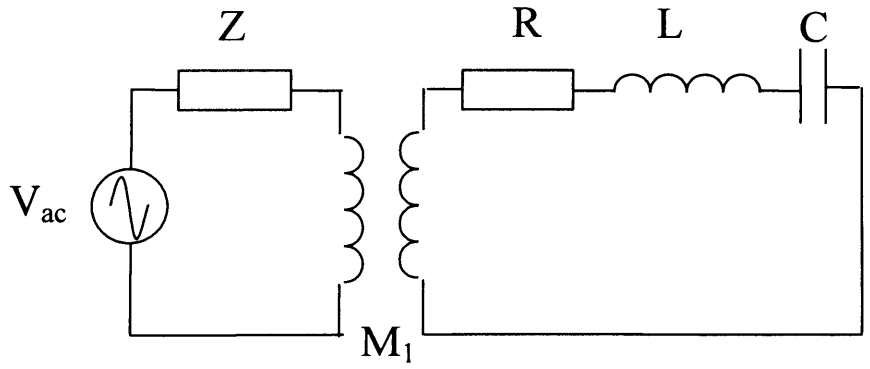

Figure 4-4 Circuit diagram of the discrete element circuit analogous to coupling to a mode of a dielectric resonator with a coaxial cable loop.

If the dielectric resonator is depicted as in Figure 4-4 neglecting the coupling to the voltage source then the resonator may be analysed as in [186] and we learn that impedance of the system is at a minimum when it is purely resistive and more importantly that

$$Q = \frac{f_0}{\Delta f} \quad \text{.....Equation 4-11}$$

or that the Q of the system is equal to the resonant frequency divided by the FWHM bandwidth. In other words, if it were possible to measure the FWHM bandwidth (bandwidth) and resonant frequency of the resonant peak then the Q of the system would be quantifiable.

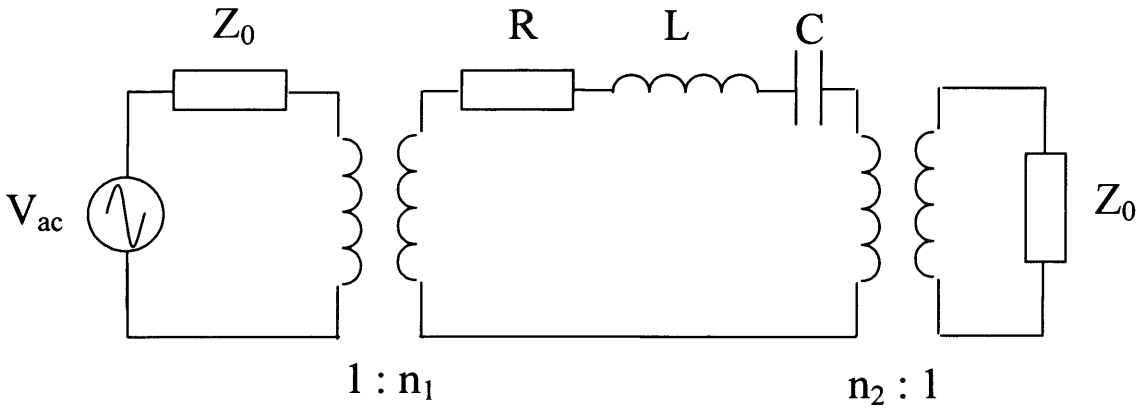

Figure 4-5 Equivalent circuit of a dielectric resonator coupled to a voltage source and to a resistive load by two loops [187].

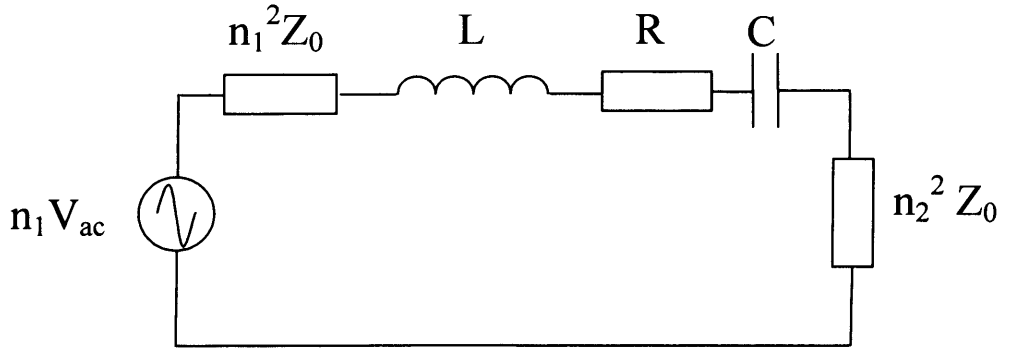

Figure 4-6 Equivalent of Figure 4-5 with the transformers taken into consideration and removed.

In order to measure the bandwidth of a dielectric resonator (excited by a loop), another loop may be coupled to the resonant mode of the dielectric. In this case the equivalent circuit of the system is shown in Figure 4-5 where Z_0 is the impedance of the transmission line system. Transforming the resistances and the voltage source gives Figure 4-6. From standard circuit theory it may be shown that the Q of an LRC circuit (the equivalent of the dielectric) is

$$Q_u = \frac{\omega_0 \cdot L}{R} \quad \text{Equation 4-12}$$

where Q_u stands for unloaded Q. From the equivalent circuit of Figure 4-6 it is easily seen that when the dielectric resonator is coupled to a power source and to a load then the Q becomes Equation 4-13.

$$Q_L = \frac{\omega_0 \cdot L}{R + n_1^2 \cdot R_d + n_2^2 \cdot R_L} \quad \text{Equation 4-13}$$

where Q_L is the loaded Q. The difference between these two Q factors is that the second contains losses due to the power source and load whereas the first is the Q due only the LRC circuit or its equivalent, the dielectric resonator. The first is called the unloaded Q and the second the loaded Q; it is always the loaded Q that is measured and if the unloaded Q is required this must be extracted. For a transmission line supplying power to a load impedance such as a cavity or dielectric resonator unless the load is matched to the impedance of the transmission line (usually 50Ω) the incident wave carried by the transmission line will be both reflected and transmitted at the junction between the transmission line and the load. This case is shown diagramatically in Figure 4-7.

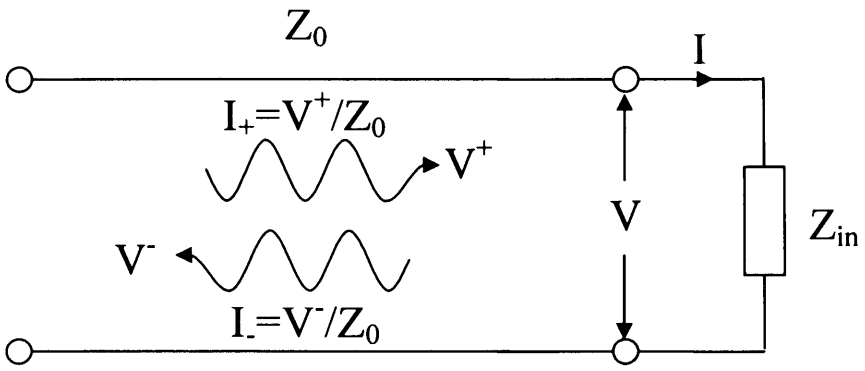

Figure 4-7 Diagram of transmission line with impedance Z_0 supplying power to a load of impedance Z_{in}.

The voltages generated by the incident and reflected wave interfere constructively at the interface and the currents generated at the interface interfere destructively. From this we may say that

$$V^+ + V^- = V \quad \text{Equation 4-14}$$

and

$$V^+ - V^- = I \cdot Z_0 \quad \text{Equation 4-15}$$

or that

$$2V^+ = I(Z_{in} + Z_0) \quad \text{Equation 4-16}$$

Hence the equivalent circuit of Figure 4-7 is Figure 4-8; note that the voltage driving the equivalent circuit of Figure 4-8 is twice the voltage generated by the source in Figure 4-7.

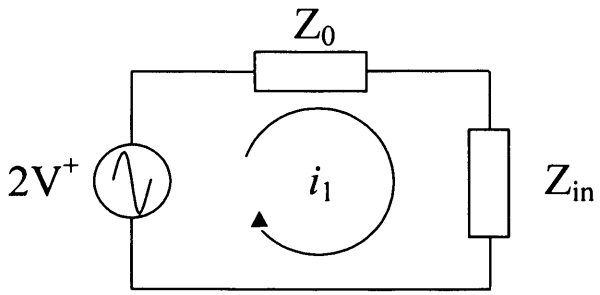

Figure 4-8 Equivalent circuit for a transmission line of impedance Z_0 supplying power to an impedance Z_{in}, V^+ is the voltage generated by the source.

The equivalent circuit of the two port coupled resonator circuit at resonance is shown in Figure 4-9.

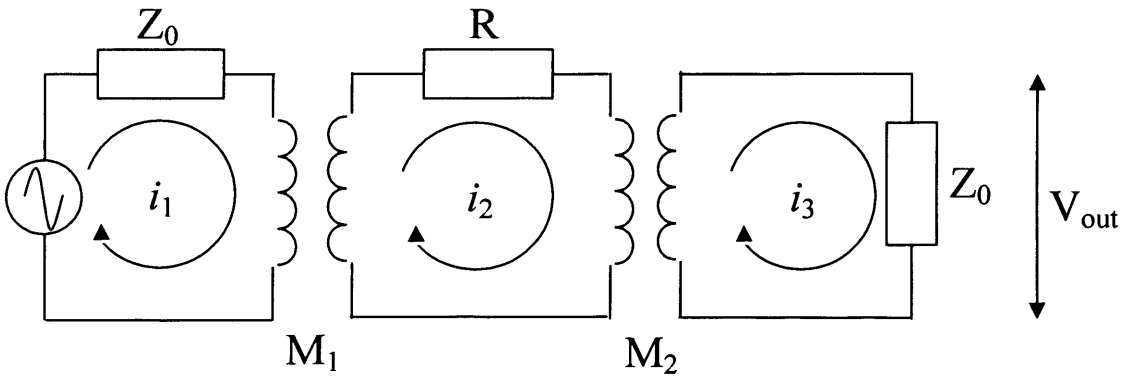

Figure 4-9 Equivalent circuit of full 2-port resonator circuit at resonance, M_1 and M_2 are the mutual inductance coupling the resonator to the external circuitry and Z_0 is normally 50Ω.

Analysis of the circuit shown in Figure 4-9 with the Kirchoff laws leads to Equation 4-17 at resonance (i.e. $\omega = \omega_0$)

$$\frac{V_{out}}{V^+} = S_{21} = \frac{2 \cdot \sqrt{g_1 \cdot g_2}}{1 + g_1 + g_2} \quad \text{.....Equation 4-17}$$

where

$$g_1 = \frac{\omega^2 \cdot M_1^2}{R \cdot Z_0} \quad and \quad g_2 = \frac{\omega^2 \cdot M_2^2}{R \cdot Z_0} \qquad \text{Equation 4-18}$$

are the coupling coefficients to and from the resonator and S_{21} is one of the circuit's scattering parameters, its voltage transmission coefficient [188]. Assuming symmetrical coupling i.e. ($g_1 = g_2 = g$) Equation 4-17 gives

$$2g = \frac{S_{21}}{1 - S_{21}} \qquad \text{Equation 4-19}$$

since

$$\frac{1}{Q_L} = \frac{1}{Q_u} + \frac{1}{Q_{e1}} + \frac{1}{Q_{e2}} \qquad \text{Equation 4-20}$$

and

$$Q_{e1} = \frac{Q_u}{g_1} \quad and \quad Q_{e2} = \frac{Q_u}{g_2} \qquad \text{Equation 4-21}$$

$$\frac{1}{Q_L} = \frac{1}{Q_u} + 2g\frac{1}{Q_u} \qquad \text{Equation 4-22}$$

and hence

$$Q_u = \frac{Q_L}{1 - S_{21}} \qquad \text{Equation 4-23}$$

i.e. a knowledge of S_{21} allows the unloaded Q of a resonant circuit to be calculated. S_{21} itself may be found from the insertion loss measured by a Network Analyser as

$$S_{21} = 10^{\frac{-|IL|}{20}} \quad \text{.....Equation 4-24}$$

where IL is the insertion loss [188].

As may be seen from Equation 4-10 the Q of a resonant peak (and hence the bandwidth) is proportional to the power lost from the system, the greater the power lost the lower the Q and the greater the bandwidth.

In the case of a dielectric resonator in free space, power is lost from the system due to damping in the dielectric itself and due to radiation of energy into free space. Although nothing can be done about the first loss mechanism (providing the dielectric material is given), the loss of energy through radiation can be made negligible by enclosing the dielectric resonator in a metal cavity. Although the enclosure of the dielectric in a cavity introduces another loss mechanism due to conduction in the metal walls of the cavity, because the losses due to radiation are very much greater than the losses due to conduction in the cavity walls, the net effect is a dramatic increase in the Q of the resonant peak. If the metal cavity is cylindrically symmetric then the only other way in which the resonant peak will be changed by the enclosure in a cavity is that the resonant frequency of the modes will shift. The exact resonant frequency shift will depend on the shape and type of dielectric and the size of the cavity. The resonant frequency shift is due to the containment (squashing) of the e-m fields into the cavity.

From the above, if the dielectric is resonating in a TE mode there will be an azimuthal electric field in a region surrounding the dielectric. If a semiconductor wafer is introduced near to the resonator as shown in Figure 4-10 then the azimuthal electric field will excite a current in the wafer.

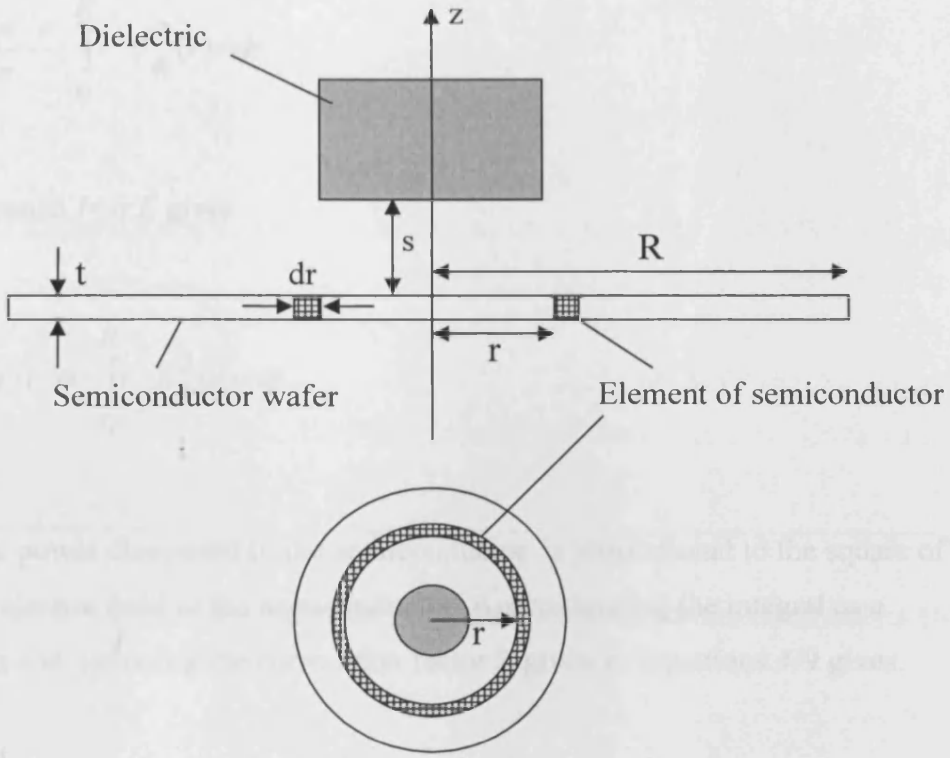

Figure 4-10 Schematic showing how a cylindrical dielectric puck and a circular semiconductor wafer may be juxtaposed in order for the azimuthal fields of a TE mode to excite conduction and therefore I^2R losses in the semiconductor. Above, as viewed from the side, below as viewed from above.

The power lost when a current flows in an element of semiconductor volume

$$dV = 2\pi \cdot t \cdot r \cdot dr$$

(see Figure 4-10) is

$$dP = \frac{J_\phi^2}{\sigma} \cdot dV$$

where J_ϕ is the azimuthal current density and σ is the conductivity of the semiconductor. Intergrating this expression for the entire semiconductor wafer and expressing explicitly the dependence on r we have

$$P_{tot} = \frac{2 \cdot \pi \cdot t}{\sigma} \cdot \int_0^R r \cdot J_\phi^2(r) \cdot dr$$

which, because $J=\sigma.E$ gives

$$P_{ds} = 2 \cdot \pi \cdot t \cdot \sigma \cdot \int_0^R r \cdot E_\phi^2(r) \cdot dr$$

i.e. that the power dissipated in the semiconductor is proportional to the square of the azimuthal electric field in the semiconductor. Approximating the integral as a summation and including the conversion factor Z given in Equations 4-9 gives.

$$P_{ds} = 2 \cdot \pi \cdot t \cdot \sigma \cdot \sum_0^R r \cdot Z \times 10^{-6} \cdot H_\phi^2(r) \cdot \Delta r \quad \text{.....Equation 4-25}$$

Where Δr is the width of an actual element of semiconductor and H_ϕ^2 is the azimuthal electric field calculated by Superfish. From Equation 4-11 and the general definition of Q the bandwidth of the resonant peak of a dielectric resonator excited in a metal cavity close to a semiconductor wafer may be written

$$\Delta f(s) = \frac{P_{ds}(s) + P_{dc} + P_{ds}}{2\pi \cdot U} \quad \text{.....Equation 4-26}$$

where the dependence of the power dissipated in the semiconductor P_{ds} and hence the dependence of *frequency* bandwidth Δf on the separation between the dielectric and the semiconductor s is shown explicitly. P_{dc} and P_{ds} are respectively the power dissipated by conduction in the walls of the metal container and the power dissipated in the dielectric itself; U is the energy stored in the entire system which at resonance is equal to [182]

$$U = \sum_{i=1}^{n} \frac{\varepsilon_i}{4} \cdot \int_{V_i} |E_i|^2 dV_i$$ **Equation 4-27**

where the summation is over all the materials in the resonant system and ε_i is the dielectric constant of each material. On inclusion of the conversion factor given in Equations 4-9, Equation 4-27 becomes

$$U = \sum_{i=1}^{n} \left[\frac{\mu_0 \cdot \mu_i}{4} \times 10^{-12} \cdot \sum_{V_i} H_\phi^2 \cdot \Delta V \right]$$

which, if all the materials have a relative permeability of one becomes

$$U = \frac{\mu_0}{4} \times 10^{-12} \cdot \sum_{V} H_\phi^2 \cdot \Delta V$$ **Equation 4-28**

where the sum is over the entire volume of the cavity

Every component of Equation 4-25 except the conductivity of the wafer may be measured, or calculated from the fields attained computationally be Superfish. Substituting Equation 4-25 and Equation 4-28 into Equation 4-26 and simplifying gives

$$\Delta f(s) = \sigma \cdot g(s) + c$$ **Equation 4-29**

where

$$g(s) = \frac{8 \cdot \pi \cdot t \cdot Z \times 10^6 \cdot \sum_{0}^{R} r \cdot H_\phi^2(r) \cdot \Delta r}{\mu_0 \cdot \sum_{V} H_\phi^2 \cdot \Delta V}$$

and

$$c = \frac{P_{dc} + P_{ds}}{2\pi \cdot U}$$

is well approximated as a constant.

g(s) may be calculated from the fields calculated by Superfish if a program is used to perform the relevant summations etc. The conductivity of a semiconductor may be determined from the fit of the *g(s)* function to the experimentally determined variation of bandwidth with dielectric-semiconductor separation if σ and c are used as fitting parameters. Programs were written with Mathcad to perform the analysis of the Superfish data and to fit the function g(s) to the experimental data found in the manner detailed below. Details of these codes and also further details of the Superfish program set may be found in Appendix B.

4.3 Experimental method

The cavity used in these experiments was machined from copper and consisted of three parts, a base, a middle and a lid that slotted together (see Figure 4-4-11). The position of the three parts was fixed relative to each other via a pin-hole mechanism. The semiconductor wafer was placed on a ledge in the base Figure 4-4-11. A approximately two centimetre separation between the ledge on which the wafer rested and the top and bottom of the cavity was affected in order to reduce the reduction in Q caused by conduction in the cavity walls. Four holes were drilled through the cavity walls of the middle section of the cavity in order to introduce two antennae into the cavity approximately adjacent to the dielectric at all heights above the wafer. The antennae were used to couple a network analyser to the resonant system. The antennae were fabricated from semi-rigid co-axial cable as described in Appendix B.

The resonant frequency of the TE_{01} mode of the dielectric resonator was first approximated using the formula [182]

$$fGHz = \frac{34}{a \cdot \sqrt{\varepsilon_r}} \cdot \left(\frac{a}{L} + 3.45 \right)$$

where a is the radius of the dielectric in mm, L is the length of the dielectric in mm and ε_r is the relative permittivity of the dielectric; this gave a value of 2.94 GHz, this was used as an initial guess value for the Superfish simulation.

In the experiments the dielectric was placed on a tube of quartz that was placed approximately in the centre of the wafer's surface; the height of the dielectric above the wafer was varied by varying the length of the tube of quartz; the heights used were 6, 9, 12, 15 and 18mm as specified by the manufacturer, Pikem. An HP 8753E network analyser was used to measure the bandwidth, peak frequency and loaded Q of the resonant peak and the insertion loss associated with the resonance. The dielectric resonator was a titanium dioxide (rutile) cylindrical puck with a diameter of 10.5 mm and a length of 4.3 mm as measured with a metal vernier calliper with a digital read-out. As designed the inside dimensions of the cavity were a diameter of 53 mm above the ledge and 49mm below it and a total height of 51mm, the ledge was 24 mm above the base of the cavity. The gallium nitride wafer used in the experiments was 3.3 μm thick and was grown on an 60 μm thick sapphire substrate. A photograph of the apparatus including the disassembled copper cavity, the ad hoc fabricated loop antennas, one of the quartz stands and the dielectric is given in Figure 4-12.

For each measurement at each height the apparatus was disassembled and reassembled five times and each time a new measurement of the measured parameters was taken.

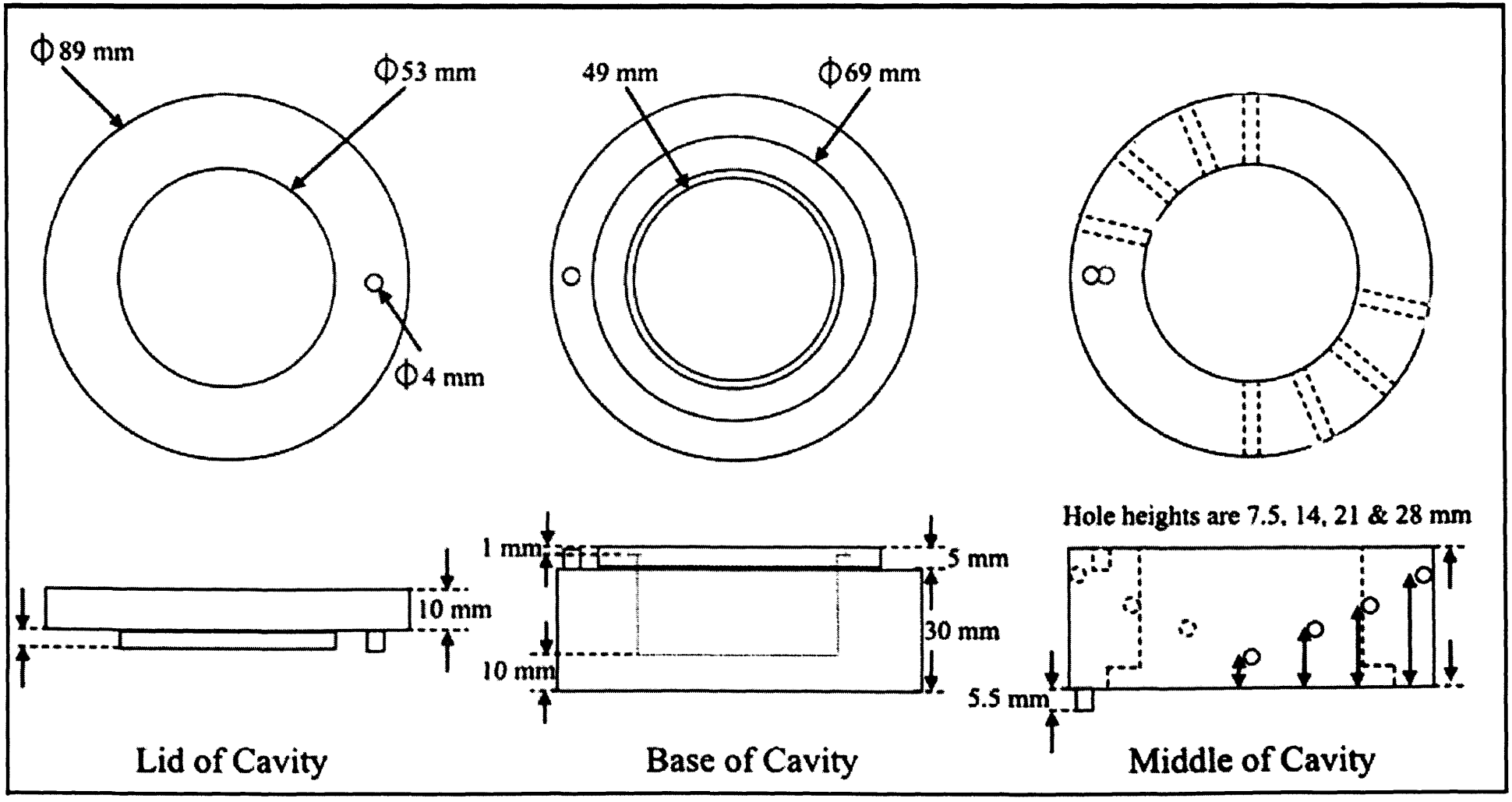

Figure 4-4-11 Schematic of the copper cavity used in the conductivity measurement experiments, the diagrams are to scale.

Figure 4-12 Photograph of some of the experimental apparatus used for the measurement of the conductivity of a semiconductor by the method described in this chapter.

The dielectric constant of the titanium dioxide dielectric resonator was used as a fitting parameter to fit the calculated value of the resonant frequency to that of the experimentally determined resonant frequency the best fit integer value was 106 similar to the value of 107 at 4.5GHz quoted for rutile titanium dioxide in the literature [189]. The value used for the relative permittivity of the gallium nitride was 9.32 (an average from the results of [190 191 & 192]), the value for the relative permittivity of quartz was 4.5 [193 & 194]; and the value of the relative permittivity of sapphire was 9.418 [195]. The dielectric resonator used was kindly supplied by Professor Neil Alford of Southbank University.

4.4 Results

The experimental results taken following the method outlined in the Experimental Method section are shown in Table 4-1. Table 4-2 allows for a comparison between the resonant frequency calculated using Superfish and the averages of the experimentally determined resonant frequencies. The *g(h)* values calculated from the Superfish fields were fit with an exponential equation using another Mathcad program

Figure 4-13; this exponential equation was in turn fitted to the unloaded bandwidths calculated from the experimental data; the fitting parameters for this fit were the conductivity of the wafer and the bandwidth of the resonant peak with the wafer at an infinite distance from the dielectric i.e. removed from the cavity Figure 4-14. From the fit to the unloaded bandwidth the conductivity of the gallium nitride was determined to be 63 S/m and the bandwidth of the resonant peak with the wafer removed 0.17 MHz; this compares to an experimentally determined bandwidth of 0.26 MHz. The sheet resistance of the GaN layer is found by dividing its bulk resistivity (0.015873 Ωm) by the thickness of the layer (3.3 μm). This gives a sheet resistance of 4810 Ω/□.

h/mm	IL/dB	BW/MHz	f_p/MHz	Q_L
6	-56.1	13.7	2998.9	218
	-57.9	13.5	2999.1	222
	-60.7	13.3	2998.9	226
	-59.3	13.9	2998.7	216
	-52.6	14.6	2997.9	206
9	-54.6	5.6	3001.1	535
	-52.3	5.6	3001.1	535
	-53.3	5.6	3001.1	532
	-53.9	5.6	3001.1	535
	-53.6	5.6	3001.2	530
12	-48.8	2.6	3004.7	1174
	-48.5	2.55	3004.7	1180
	-49.9	2.54	3004.6	1182
	-47.8	2.52	3004.6	1195
	-48.7	2.52	3004.7	1195
15	-38.8	1.222	3014.1	2465
	-48.9	1.193	3014.4	2530
	-45.7	1.203	3014.4	2502
	-46	1.179	3014.3	2550
	-43.9	1.177	3014.4	2555
18	-51.0	0.634	3045.9	4813
	-51.4	0.640	3046.0	4759
	-47.24	0.653	3046.0	4670
	-58.43	0.623	3046.1	4800
	-56.23	0.623	3046.0	4810

Table 4-1 Table of results for the conductivity measurement of a gallium nitride wafer.

Stand height / mm	Experimental average resonant frequency / MHz	Resonant frequency calculated by Superfish / MHz
6	2999	2997
9	3001	2998
12	3005	3002
15	3014	3011
18	3046	3041

Table 4-2 Table allowing for the comparison between the experimentally determined system resonant frequency and that calculated by Superfish.

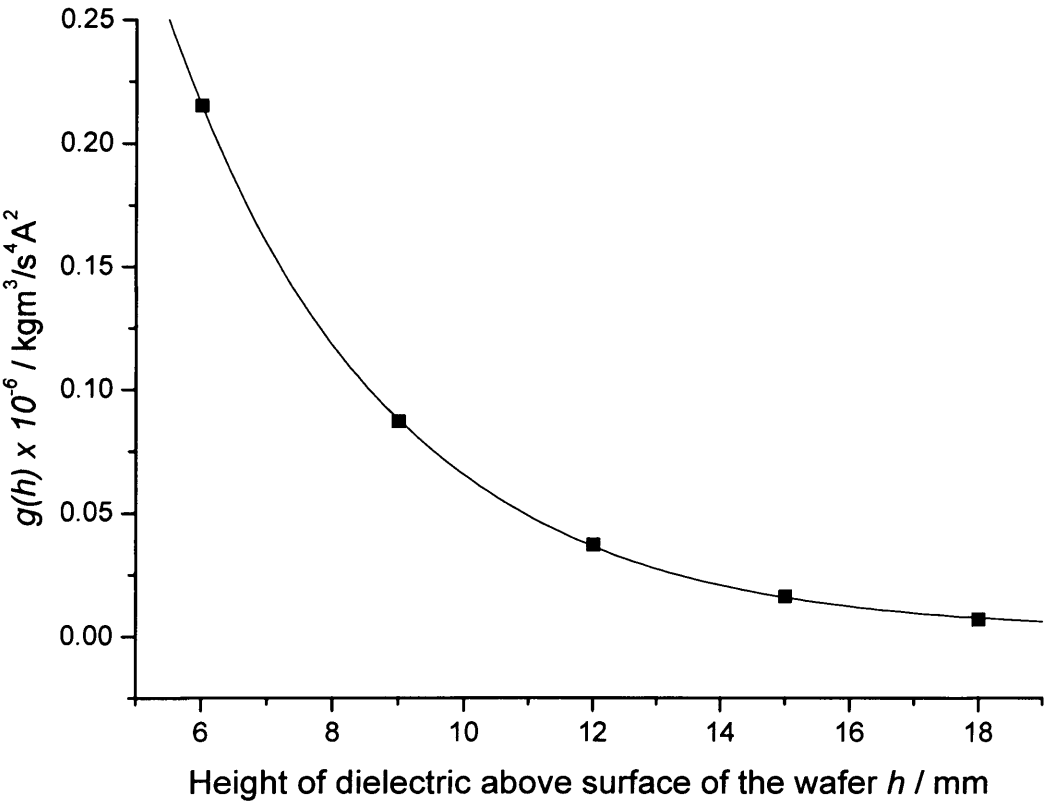

Figure 4-13 The exponential equation shown fitted to $g(h)x10^{-6}$ is used to fit the experimental determined bandwidth (MHz) as an approximation to $g(h)$

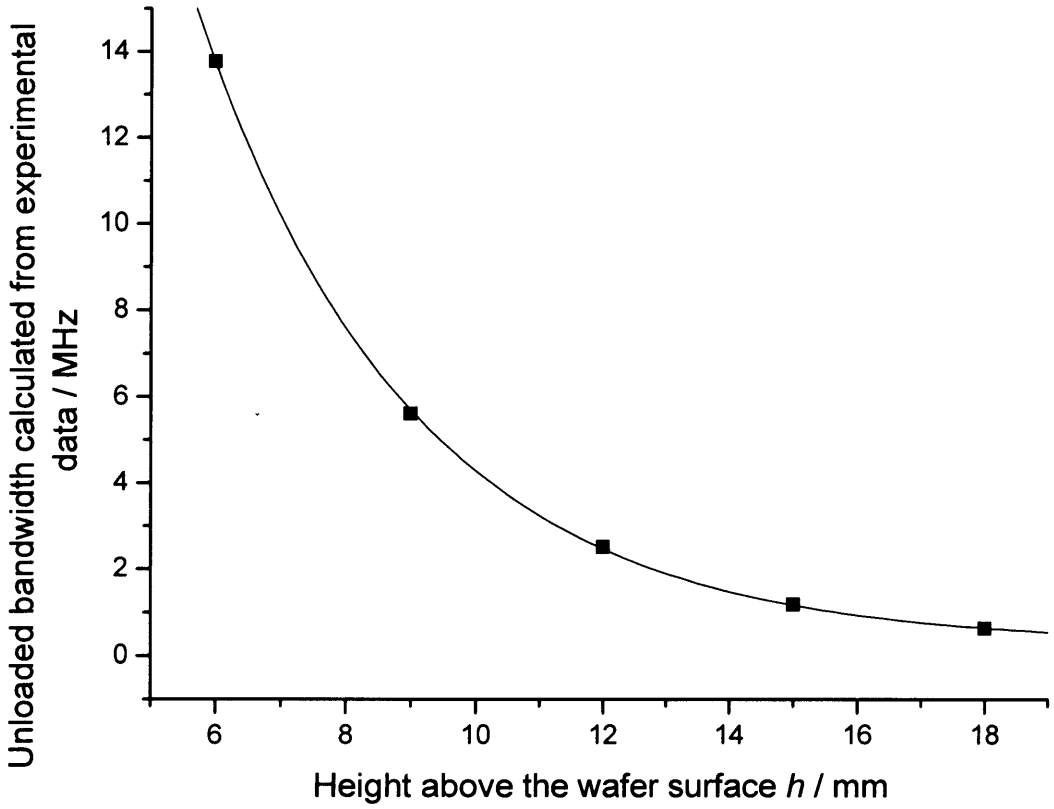

Figure 4-14 The exponential curve shown in Figure 4-13 fitted to the unloaded bandwidth of the resonant peak calculated from experiment. It is from this fit that the conductivity is deduced.

4.5 Discussion

The gallium nitride wafer used in this experiment had a supplier quoted free carrier density of 1-5x10^{16} cm^{-3}. Values for the mobility of gallium nitride seen in the literature at the time ranged between 50 $cm^2V^{-1}s^{-1}$ and 900 $cm^2V^{-1}s^{-1}$; these values led us to expect the conductivity of the gallium nitride to fall within 8 and 720 Sm^{-1}; this is in agreement with the value measured using our resonance perturbation technique and leads to a mobility for the wafer of between approximately 79 and 395 $cm^2V^{-1}s^{-1}$ dependent on the actual carrier concentration.

The above resonance perturbation method is only applicable when the fields in the experiment are well modelled by Superfish. Because Superfish does not take into account the affect of conduction in the wafer on the strength and distribution of the

fields within the cavity conduction in the wafer must not perturb the fields greatly from the zero conduction case. This is the case when the conducting layer is thin or when the material is highly resistive. These are both cases when the four point probe method, commonly used for similar non-destructive conductivity measurements, is impracticable.

A thin and degenerate, low-mobility interface layer has been observed in GaN [196, 197, 198, 199 & 200]. The resonance perturbation method of conductivity measurement assumes that conduction is homogenous throughout the conducting region. For the case of two conducting layers of equal radius the volume that conducts is given by

$$V = \pi R^2 (t_1 + t_2).$$

Providing the thickness of the film is much less than the skin depth of the material the power dissipated is given by

$$P = \left[\sigma_1 \pi R^2 t_1 + \sigma_2 \pi R^2 t_2 \right] E^2$$

which may be written as

$$P = \sigma_{eff} \pi R^2 (t_1 + t_2)$$

where σ_{eff} is the conductivity measured using the techniques described here. σ_{eff} may be written as

$$\sigma_{eff} = \sigma_1 \left(\frac{t_1}{t_1 + t_2} \right) + \sigma_2 \left(\frac{t_2}{t_1 + t_2} \right).$$

If there was an interface layer in our sample similar to that written about in the literature: a thickness of approximately 0.2μm, with a carrier density and mobility of respectively $1x10^{20}cm^{-3}$ and $50cm^2V^{-1}s^{-1}$ then the conductivity of the gallium nitride layer becomes negative; from this we assume that there is either no layer in our wafers or that it has a character significantly different to that written about in the literature. Whatever the character of the interface layer, if it existed, it would give an unrealistically high value of the conductivity.

In the above it was noted that for the method to give an accurate value for the conductivity conduction had to be uniform throughout the wafer, such as when the material to be measured was composed of two layers of differing conductivity. Another reason that the conductivity would not be accurately measured was if the magnitude of the electric field changed significantly through the thickness of the material; this would happen if the thickness of the material were not very much less than the skin depth of the material; fortunately for materials with a small skin depth the four point probe method is usually applicable.

The fit of the theoretical variation of bandwidth with distance from the wafer to the experimental variation is very good and the uncertainty in the experimental measurement calculated from the standard deviation of the five sets of measurements taken at each height was at most 3.4% of the mean measurement, though was typically closer to 1%. The peak frequency variation with distance from the wafer observed in the experiment was well modelled by that calculated by Superfish and the dielectric constant used to fit the calculated resonant frequencies to the experimental ones was in good agreement with the literature value.

In the above method, with the computational resources available it was impossible to reduce the size of the mesh sufficiently to allow the actual situation to be modelled without dimensional approximations, that is to say that dimensions less than one hundred microns caused Superfish to crash. Because of this the wafer (sapphire substrate plus gallium nitride epilayer) was approximated as being 100μm thick and have a relative permittivity of sapphire and the titanium dioxide puck was approximated as having a diameter of 5.3mm. Although one hundred microns is

approximately thirty percent greater than the actual width of the wafer it is still much thinner than the distance between points at which the field is calculated. The only limit on the spacing of the points at which the fields are calculated is the memory available to store the calculated data and the time available to make the calculations.

4.6 Conclusion

A method of measuring the conductivity of a thin film of semiconductor was demonstrated, which relied on the perturbation that the introduction of a conductor near a resonating dielectric had on the resonant peak of the dielectric, i.e. the bandwidth increase caused by the ohmic power dissipation in the wafer. Because at resonance the electric field exhibits an exponential reduction in magnitude with distance ventured outside the dielectric, there is a clear variation in the bandwidth of the resonant peak as the dielectric is moved to and from the wafer, this variation is caused by the increase and decrease of the electric field magnitude in the wafer and hence a corresponding increase and decrease in current flow and hence power dissipation. A Poisson equation solver, Superfish, was used to calculate the fields within the cavity. These fields were used to calculate a curve that could be fitted to the experimentally observed bandwidth-height variation with the conductivity of the wafer as a fitting parameter. The curve to be fitted to the experimental data was calculated from the Superfish fields with a Mathcad program which is given in the Appendix B. The method was applied to the measurement of the conductivity of a gallium nitride wafer for which the four-point probe method did not yield results. The measurement of the conductivity using the resonant-peak perturbation technique yielded a result within the expected range of values calculated from a combination of manufacturer's data and literature values.

5 Inductively coupled plasma etching of gallium nitride

5.1 Introduction

In order to fabricate various semiconductor based devices and technologies, it commonly occurs with the state of the art of semiconductor processing that the semiconductor has to be etched. Etching can be used to form mesas for laser facets, to electrically isolate devices from each other on integrated circuits such as computer processors, to allow backside grounding with via holes (holes that run straight through the semiconductor to a grounded electrode on the backside of the wafer), gate recess etches, gate pad-source-drain isolation etc. Etching is also invaluable in carving the intricate shapes and features that give form to MEMS and lab-on-chips.

The methods of etching semiconductors can broadly be split into two groups, wet and dry etching. Wet etching involves the chemical reaction between a liquid chemical and the semiconductor, preferably at room temperature though also at elevated temperatures. Dry etching is the etching of the semiconductor in a plasma, ion beam, laser beam etc. A plasma, the fourth stage of matter, is a gas where some of the gas atoms have been ionised. Ionisation can take place when the gas is heated to a very high temperature, as is the case in most natural plasmas, or when electric fields accelerate the small population of electrons that exists naturally in a gas (due to UV or cosmic ray ionisation etc) to energies where collisions with the gas causes further ionisation.

By creating an electric field, attractive to ions, in a direction perpendicular to the face of the semiconductor, ions present in the plasma may be accelerated into the surface of the semiconductor (for an explanation of how this is accomplished see the section on dc bias in [201]). Because ion bombardment increases the etch rate in the vertical direction away from the surface but not the horizontal direction parallel to the surface plasma etching etches in the vertical direction away from the surface much quicker than in the horizontal direction allowing deep narrow features to be formed (this

effect may further be increased by using a gas which forms a polymer on the side walls of the etched material). Wet chemical etching on the other hand has no preferred etch direction and hence etches in all directions at the same speed. An etch which etches in a vertical direction into the semiconductor much quicker than in the horizontal direction parallel to the semiconductor surface is called an anisotropic etch; an etch which etches in all directions at the same speed, i.e. no preferential direction, is called an isotropic etch.

Anisotropic etching is required when the feature needs to be as deep as possible but also as thin as possible. This is the case for device isolation on computer processors where the devices must be well isolated from each but at the same time must take up as little space as possible. Dry etching is also required when the material is very resistant to wet chemical etching, such as is the case with gallium nitride. On the other hand plasma etching, due to its physical nature, damages the surface of the semiconductor so it is disadvantageous when such surface damage will affect the performance of the device such as is the case for gate recess etches where damage to the surface may cause excessive gate leakage. Dry etching is also expensive, with all but the simplest single gas barrel ashers costing several hundred thousands of pounds to buy and install, thousands of pounds to maintain each year and large amounts of power to run.

In both wet and dry etching, a mask is normally used to cover the areas that are required to be un-etched with the areas to be etched left exposed. The mask protects the underlying area from the plasma or wet chemicals; however, wet chemical etches will etch underneath any mask at approximately the same rate as they etch into the material. On the other hand it is normally much easier to get a high selectivity between the mask and the material with a wet etch than with a dry etch due to the fact that the ion bombardment of the plasma will etch any material no matter how un-reactive it is with the gas used. Selectivity is the term used for the ratio of the etch rate of two materials in the same chemical or plasma. Hence if silicon etches one hundred times faster in a particular plasma than its silicon dioxide mask then the plasma is said to give a selectivity of one hundred to one of silicon to silicon dioxide.

The plasma reactors used for plasma etching come in several varieties, the most common are reactive ion etchers (RIEs), electron cyclotron resonance reactors (ECRs), and inductively coupled plasmas (ICPs). RIEs are capacitively coupled plasmas i.e. the plasma is formed by placing a gas between two plates of metal (or one electrode and the grounded chamber as is normally the case) and using RF power applied to one of the plates to accelerate electrons and ions and form a plasma. Electron cyclotron resonance uses a cyclotron to produce a plasma. ICPs use the electric field generated by a time varying current in a coil to sustain a plasma though, as is shown below, it is the potential difference between the two ends of the coil that initiates the plasma when only a coil is used. ICPs have several advantages over RIEs and ECRs; ICPs generate plasmas with a higher plasma density (number of ions per unit volume in the plasma) than RIEs and have a simpler apparatus than ECRs and avoid the microwave frequencies and large electro magnets used in ECRs. For a more detailed discussion of the different plasma generators see [202].

As the plasma generator that was used in all the processing for this thesis was an ICP plasma generator, in the first part of the chapter a more detailed look at the origins and operation of this type of plasma generator is given. In the second part of the chapter a thorough review of the literature concerning the etching of gallium nitride in chlorine based plasmas, in ICPs, is presented, along with some theory concerning etching in plasma reactors. In the last part of the thesis the results taken on two ICP reactors are presented and discussed.

5.2 Introduction to and origin of inductively coupled plasmas

Plasmas can be used to etch any material and are frequently used to etch semiconductors when a high aspect ratio (depth of feature compared to area of feature) is needed such as is the case with trench isolation of devices in integrated circuits [203] or for via etches for backside grounding. Another reason that plasma etching might be used is for etching hard materials that do not etch easily in wet chemical etches such as HF acid etc. such as is the case for gallium nitride.

The reason that plasma etches give a high aspect ratio and can be used to etch hard material is due to the fact that plasma ions can be given a momentum by the use of electric fields and used to bombard the surface of the semiconductor, where they increase the speed of the chemical reactions occurring there (the gas species used to excite the plasma in is usually chosen so as to react with the material and form volatile etch products e.g. F with Si to form SiF_4). In practice, because the electric field is arranged to be perpendicular to the semiconductor surface, ions arrive at the surface of the semiconductor travelling near perpendicularly to it. This increases dramatically the rate that chemical reactions occur at the bottom of the features (and hence the vertical etch rate) without increasing at all the lateral etch rate. This ion assisted chemical etching is also the reason that materials that do not etch at all in chemical etchants can be etched by a plasma, though in the limit of no chemical reaction whatsoever the etch is entirely physical (due only to ion bombardment).

Several sorts of plasma generator are widely used to generate the plasmas used to etch semiconductors; however they can be split broadly into two sorts. The first sort uses only one mechanism to generate both the plasma and the electric field used to accelerate the ions (the dc bias). The second sort uses one mechanism to generate the plasma and a second mechanism to generate the dc bias.

Of the first sort reactive ion etcher (RIE) systems are the most well known. These systems use an RF field between two plates, or between a plate and the plasma/chamber system to generate a plasma. At low pressures (less than a torr) the RF field causes electrons that are already present in the chamber to be accelerated into the field plate (or the field plate covering if, as normal, there is one) and the chamber ceiling generating secondary electrons. These electrons keep on liberating further electrons from the chamber ceiling and the RF plate and will also ionise some of the gas atoms if the chamber is filled with a gas. These ions will be accelerated by the electric field and bombard the field plate as before hence leading to ion assisted chemical etching if the gas is reactive. RIE etching has the disadvantage in that as the number of atoms ionised increases the discharge resistance decreases and the electrostatic potential drop across the discharge must also decrease; this means that the ionising affect of the capacitive coupled RF energy on the plasma is limited. Also

it is impossible to get a highly ionised gas without having a high dc bias as the power source for the generation of both is the same.

The second sort of plasma generator relies on two mechanisms: the first is the same as the RIE system described and is used to generate the voltage that accelerates the ions from the plasma into the semiconductor (and to start the plasma in certain cases as we shall see), the second is used to generate the plasma. Of the second type of generator the following are common: inductively coupled plasma generators (ICPs), electron cyclotron resonance generators (ECRs) and helical wave generators. Of these three ECRs have a slightly higher plasma density (number of ions generated per unit volume) though they all generate plasma densities two to three orders of magnitude higher than RIE plasmas. However, ICPs benefit from a simple design (partly due to the use of RF rather than microwave frequencies) and the ability to place the source very close to the sample. The rest of this section contains a brief history of ICPs with an explanation of how they work.

The electromotive force generated by a time varying current in a solenoid can be considered to consist of two components. An electrostatic component, E_l, due to the potential difference between the two ends of the coil, and an azimuthal or angular component E_θ due to the time variation of magnetic flux within the coil.

The first plasma initiated by a time varying current in a cylindrical solenoid (helix) (similar to the helical configuration of today's ICPs, see figure 1(a)) was documented in 1884 by Hittorf. Hittorf and J.J Thomson [204 & 205] were both convinced that the plasma was initiated and sustained by electron neutral collisions, with electrons accelerated primarily by the azimuthal electromagnetic EMF. Thomson attempted to model plasma initiation with this in mind [205].

Many people disagreed that the discharge was initiated by the induced EMF and some believed that the electrostatic electric field was the primary cause of the plasma discharge. Townsend and Donaldson in 1928 [206] were the first to point out that the axial electrostatic field in a solenoid would have a greater magnitude (approximately thirty times greater according to their calculations) than the azimuthal electromagnetic

field. They thus argued that the plasma could not be sustained by the induced electric field but instead the electrostatic field must be the primary discharge mechanism. Indeed they even conducted experiments with two different coil configurations that gave evidence to suggest that the discharge was maintained primarily by the electrostatic field.

MacKinnon in 1929 [207] noticed that plasma discharge consisted of two distinct phases (E- and H-modes). The first mode, the E-mode, which consisted of a diffuse glow that filled the entire chamber, was produced by low frequency excitation of the solenoid. The H-mode was reached by increasing the excitation frequency past a certain threshold value at certain pressures. Past the threshold a ring-like region of intense luminosity was formed in a limited portion of space surrounded by the coil. This plasmoid (as the bright region was termed [207]) was normally so bright that that the diffuse glow that filled the container before the transition could no longer be observed. Plasma diagnostics showed that within the plasmoid region the plasma density was approximately two orders of magnitude higher than in the surrounding diffuse, capacitively coupled, region ($\sim 10^{12} cm^{-3}$ cf $10^{10} cm^{-3}$) [208]. MacKinnon [207] conducted experiments that showed that the E-mode of the discharge (the mode studied by Townsend and Donaldson) was almost certainly generated by the electrostatic component of the EMF, as Townsend and Donaldson had shown. He also gave evidence that the H-mode (ring) discharges, those studied by Thomson and Hittorf, were of electromagnetic origin.

Experiments were carried out by Yarnold in 1932 [209] that showed that the electric field required to initiate a discharge into the E-mode was only slightly influenced by the induced electomagnetic field. Furthermore, using electrostatic shields, Yarnold confirmed that it was much more difficult to initiate a plasma when it is shielded from the electrostatic field. Other shielding experiments were carried out separately by Cabannes, and Kubota [210]. Hence it can be assumed that initialisation of the discharge is achieved almost solely by capacitive effects.

Experiments were performed in 1947 by Gill and von Engel to probe the initialisation of HF plasmas between two parallel plates. Experiments they conducted showed that at pressures of the order of 10^{-3} torr the electric field needed to initialise the plasma

was independent of gas type and dependent on the wavelength of the current generator in a universal manner [211]. The fact that the current through the solenoid was independent of the gas used and that at pressures of the order of 10^{-3} torr the mean free path of electrons was greater or approximately equal to the dimensions of the container suggested that the multiplication of the few electrons naturally present in the chamber could not be due to collisions within the gas. Instead it was suggested that secondary emission after collisions with the end walls was the dominant mechanism for electron multiplication, at least when only a small number of electrons were present. The theory expounded by Gill and von Engel was extended by Francis and von Engel in 1953 [212]. Gill and von Engel continued their work with gases at higher pressures, where it was found that the nature of the gas became important.

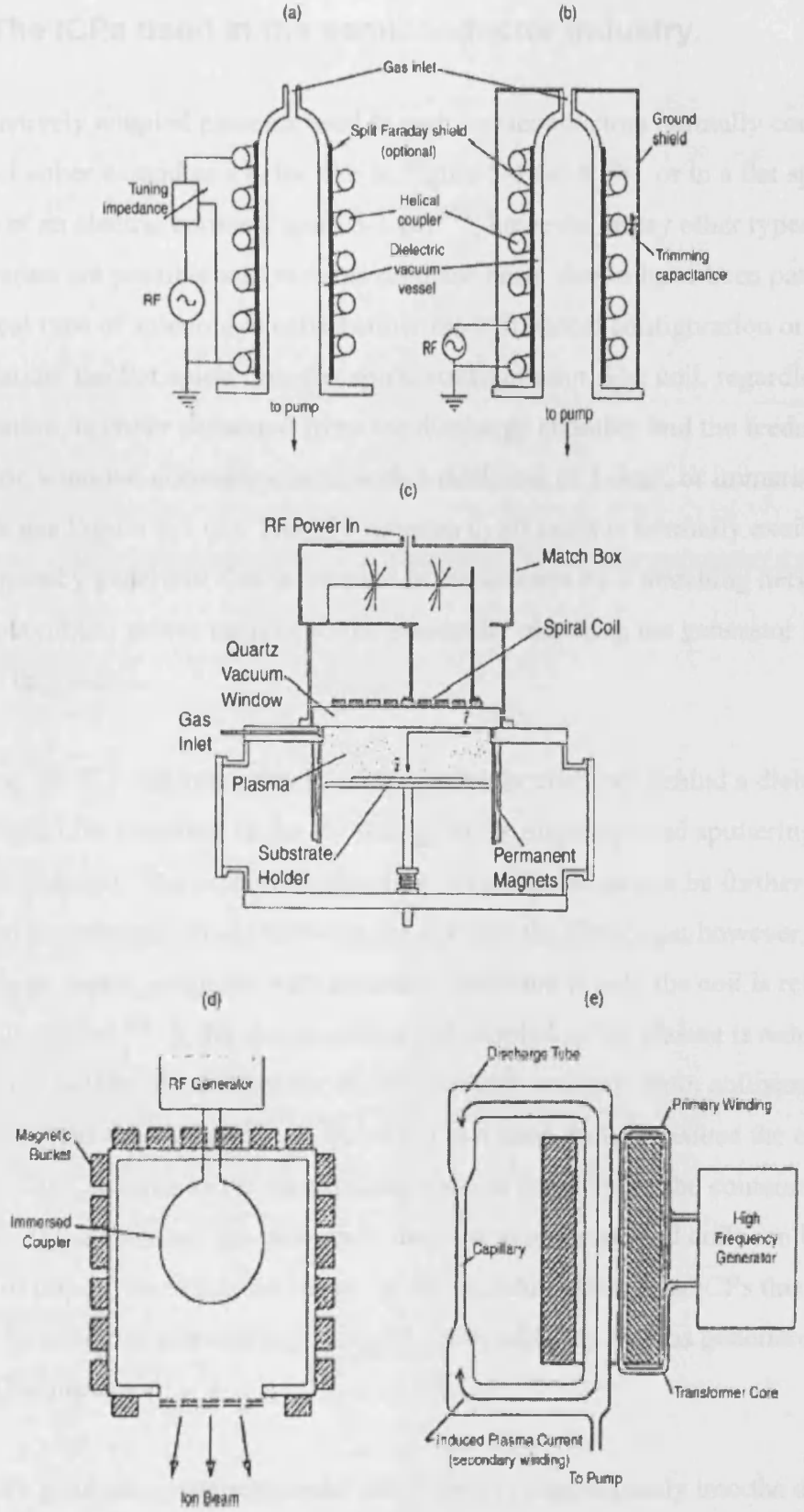

Figure 5-1. Diagrams of various ICP reactors: (a) helical coupler, (b) helical resonator, (c) spiral coupler, (d) immersed coupler and (e) transformer-coupled plasma. The Faraday shield devices ((a) and (b)) avoid capacitive coupling from the coil to the plasma. The permanent magnets ((c) and (d)) confine the plasma, enhance uniformity and increase plasma density. [213]

5.2.1 The ICPs used in the semiconductor industry.

The inductively coupled plasmas used to etch semiconductors normally consist of a metal coil either wound as a helix like in Figure 5-1 (a) & (b), or in a flat spiral like the hobs of an electric cooker Figure 5-1 (c) [214]; however, many other types of coil configuration are possible and variants on these basic shapes have been patented [215]. The helical type of solenoid is called either the cylindrical configuration or the helical configuration, the flat spiral type the spiral configuration. The coil, regardless of configuration, is either separated from the discharge chamber and the feedstock gas by a dielectric window, normally quartz with a thickness of 1-3cm, or immersed in the feedstock gas Figure 5-1 (d). The ICP antenna in all cases is normally excited by a radio frequency generator that is coupled to the antenna by a matching network which enables maximum power transfer to the plasma by matching the generator impedance to that of the plasma.

By placing the ICP antenna outside of the discharge chamber behind a dielectric screen, capacitive coupling of the RF energy to the discharge and sputtering of the antenna is reduced. The capacitive coupling to the discharge can be further reduced by placing an electrostatic shield between the coil and the discharge; however, too much shielding can create problems with discharge initiation if only the coil is relied on to start the discharge [216]. If the electrostatic field coupled to the plasma is reduced too greatly there will be insufficient secondary electron emission from collisions with the container to start the plasma [211]. In general it is a good thing to reduce the capacitive coupling of the antenna as the electrostatic lines of force bisect the container [206] and sputtering of the chamber (or antenna in the case of an immersed coil) can lead to the addition of impurities to the discharge. In the Oxford Instruments ICPs this problem is resolved by using the capacitively coupled wafer table-top dc bias generator to initialise the plasma.

Spiral ICPs generate a magnetic field which decays exponentially into the discharge over a skin depth of approximately 2.5cm for a discharge with a plasma density of ~ $10^{11}cm^{-1}$. As the electric field generated by electromagnetic induction for this coil

configuration is only 4-8Vcm^{-1} [213] a wafer can be placed in close proximity to the coil without the coil fields affecting the wafer processing. The loss of efficiency experienced by the remote sources is thus avoided and the plasma flux and ion bombardment energy at the wafer can be closely controlled. Furthermore the low aspect geometry of the chamber (Radius of chamber>>length of chamber) that the spiral coil configuration enables means that that less plasma flux is coupled to the walls for a unit flux of ions to the wafer. One of the advantages of the ICP design is the high uniformity of plasma density over large areas. The uniformity can be improved and the ion density increased using magnetic fields in ICP design [217 & 218].

The ICP system should in principle be easily scaleable to larger dimensions and can thus continue to supply a highly uniform, high density plasma source as the wafer size increases; however, it has been noted in the literature that the ICP does not scale to very large dimensions as when the wavelength of excitation becomes equivalent to the length of the coil standing wave affects become noticeable; hence, alternative technologies must be utilised [219] or the conventional singular coil ICP design may be modified by using multiple coils to sustain a larger volume discharge [220].

5.3 *Inductively coupled chlorine based plasma etching of gallium nitride*

Table 5-1 shows some of the plasmas, based on chlorine (Cl_2), that researchers have used to etch gallium nitride (GaN) and the other III-nitrides. Table 5-1 also shows the number of studies conducted with a particular chemistry. As may be seen researchers have studied chlorine-argon (Cl_2/Ar) based plasmas the most, followed by chlorine and boron trichloride (Cl_2/ BCl_3) based plasmas.

Plasma Chemsitry	Cl_2/BCl_3	Cl_2/Ar	Cl_2/N_2
Number of Studies	6	18	4
References	221, 222, 223, 224, 225 & 226	221, 227, 228, 229, 230,231, 232, 233, 234, 235, 236, 237, 238, 239, 240, 241, 242 & 243	237, 238, 242 & 244

Plasma Chemistry	Cl_2/HBr	Cl_2	$Cl_2/CH_4/H_2/Ar$	$Cl_2/BCl_3/Ar$	$Cl_2/N_2/Ar$
Number of Studies	1	3	3	2	2
References	241	241, 255 & 245	255, 246 & 247	248 & 249	240 & 243

Plasma Chemistry	Cl_2/CH_4	Cl_2/Xe	$Cl_2/SF_6/Ar$	$Cl_2/Ar/O_2$	Cl_2/H_2
Number of Studies	1	1	3	3	4
References	255	233	240, 243 & 250	251, 252 & 253	237, 242, 254 & 255

Plasma Chemistry	$Cl_2/H_2/Ar$	$Cl_2/BCl_3/Kr$	Cl_2/He
Number of Studies	5	1	1
References	240, 243, 255, 250 & 256	224	233

Table 5-1 showing the number of etch studies conducted for a particular Cl_2 based plasma chemistry.

5.3.1 Gallium nitride etch rate as a function of percent chlorine in the feedstock gas

Lee et al. in their study [221] used Cl_2/Ar and BCl_3/Cl_2 plasmas generated by a custom built, planar coil inductively coupled plasma generator (ICP); they observed peaks in etch rates at ninety percent Cl_2 in both Cl_2/Ar and Cl_2/BCl_3 plasmas at pressure of both ten and thirty mtorr (Figure 5-2). Similar results to those of Lee et al. were found by Kim et al. using the same apparatus at approximately 10 mtorr, with the same dc bias (-120V) but with only 400W supplied to the coil.

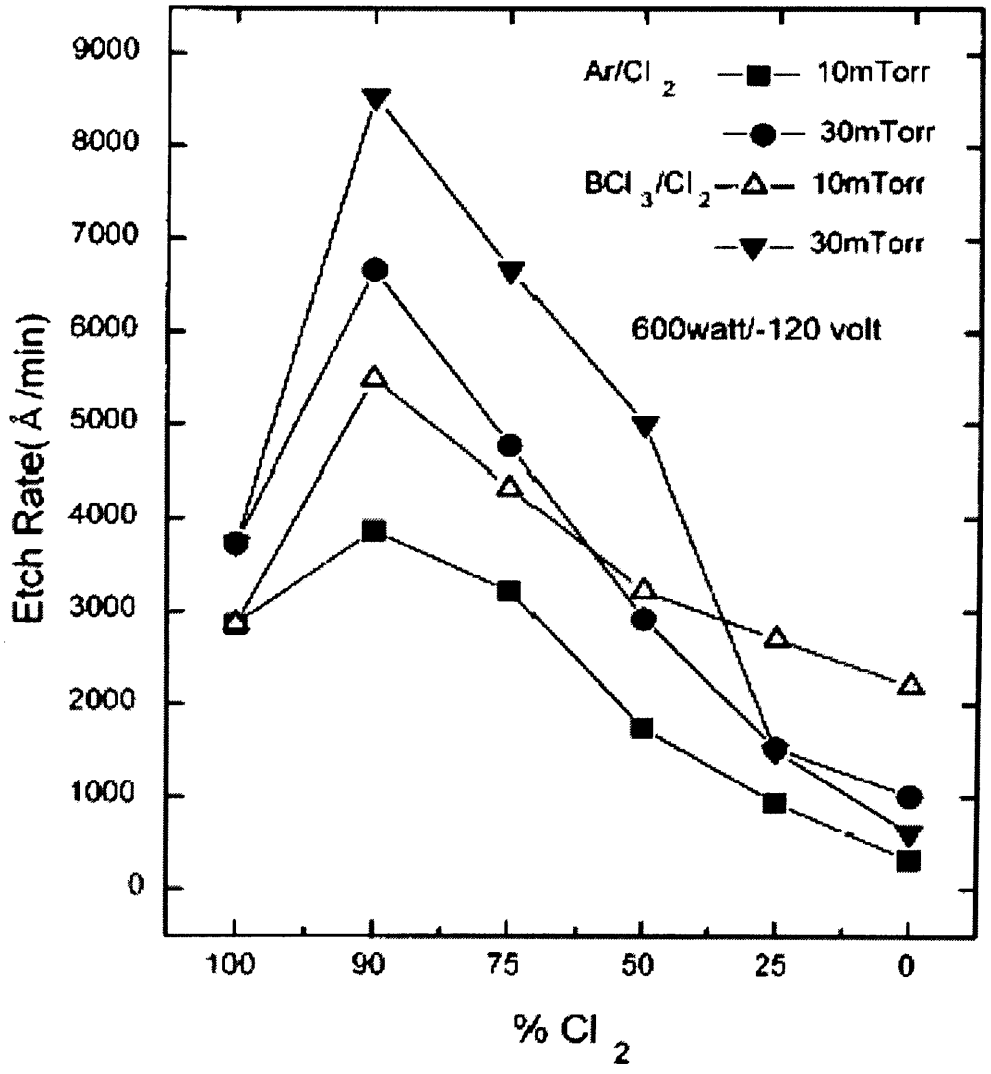

Figure 5-2 The dependence of GaN etch rate on percent Cl_2 in Cl_2/Ar and Cl_2/BCl_3 plasmas. Plasma conditions were 600W ICP power -120V DC bias and substrate temperature of 70°C. Other parameters are as shown [221].

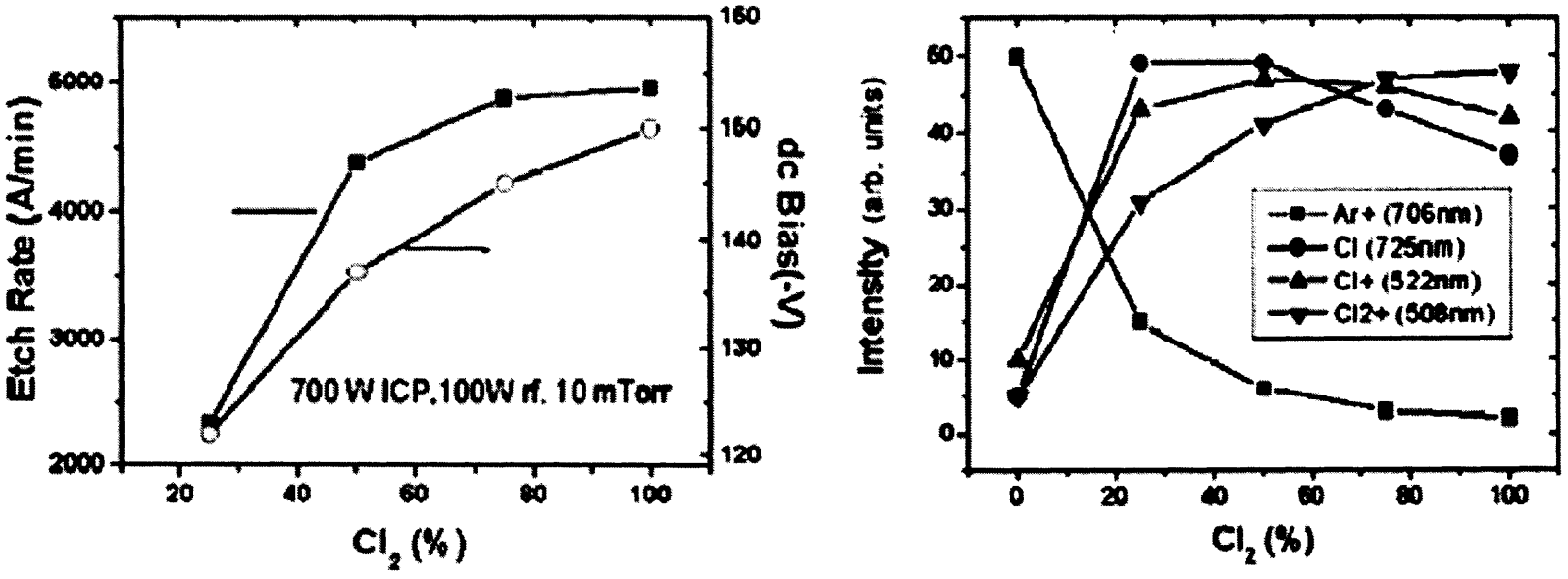

Figure 5-3 Etch rate of InGaN-MQWs and plasma composition as a function of percent chlorine in the plasma. 700W was supplied to the coil and 100W supplied to the RF chuck. The total gas flow rate was 40sccm and the pressure and temperature were held constant at 10mTorr and 25°C respectively. [228]

Figure 5-3 shows the dependence of the etch rate of InGaN multi quantum wells and the intensity of various plasma species (MQWs) on the mixture of gases in the plasmas of Park et al. [228]. Although at first sight the variation of the etch rate in Figure 5-3 seems to be different to those observed by Lee et al. and Kim et al. (Figure 5-2 and Figure 5-7) this is not certain as Park et al. avoid plasmas with approximately ninety percent Cl_2, the percentage at which the characteristic peak is observed; however, they do observe an increase in etch rate with increasing Cl_2 content, something that is common to all three studies.

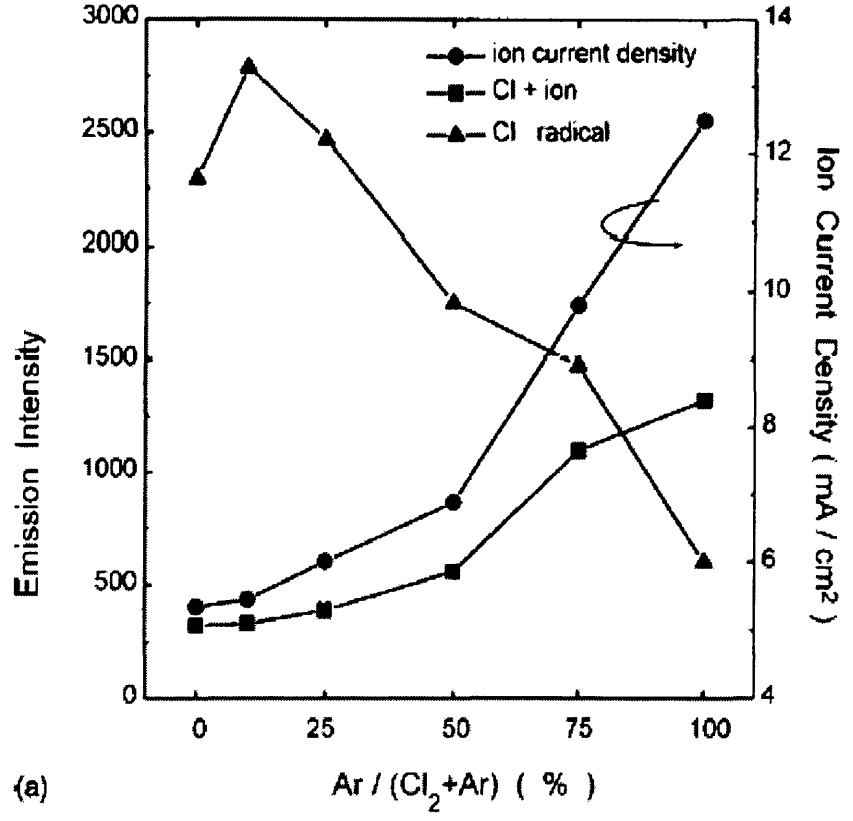

Figure 5-4 Radical, radical ion and plasma density as a function of percentage of Ar in a Cl_2/Ar plasma measured by OES and Langmuir probe. Plasma parameters were 600W power to the coil, -120V dc bias and 70°C wafer temperature all at 30mTorr [221].

Various studies [221, 222, 223, 224 & 228] have used diagnostic techniques such as spectroscopy and Langmuir probes to determine the relative amounts of various substances in the plasmas they used to etch their GaN samples. From the analysis of the optical emission spectra (OES) of Lee et al. [221] (Figure 5-4) it is possible to conclude that the etch rate is dependent on the Cl radical intensity as the variation of

the etch rate of the Cl_2/Ar plasma with $\%Cl_2$ is very similar to the variation of Cl radical and they both peak at approximately 90% Cl_2 (compare Figure 5-2 with Figure 5-4). The Cl_2/BCl_3 plasma from the same study does not show such a good correlation between the etch rate and Cl radical density, though the two graphs are similar and from this study it is possible to conclude from the data presented that the etch rate was limited by availability of Cl radical.

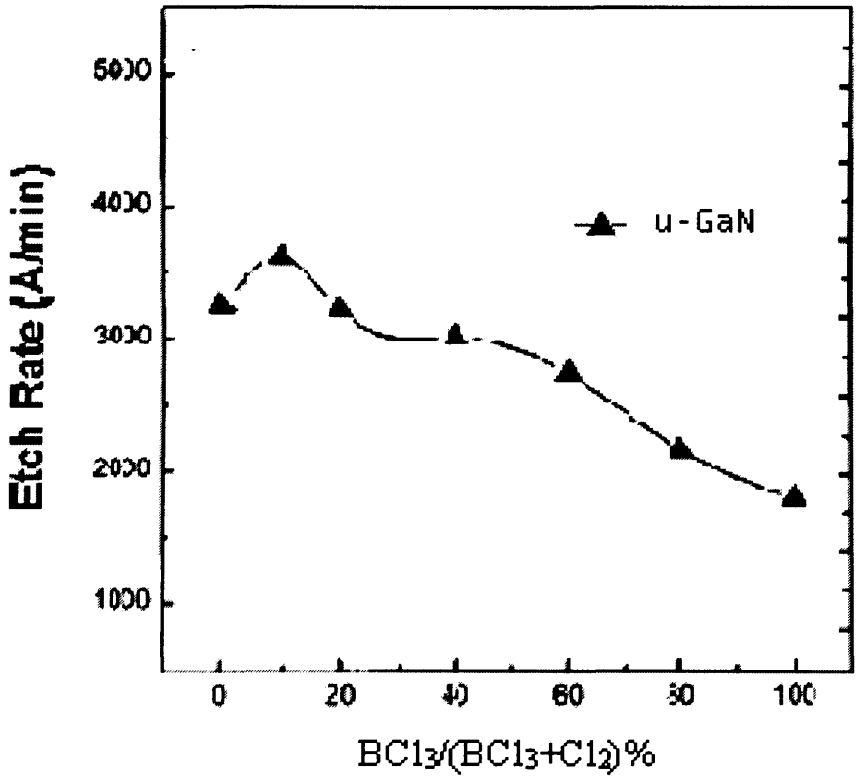

Figure 5-5 GaN etch rate of a Cl_2/BCl_3 plasma as a function of $\%BCl_3$. Other parameters were 600W coil power -120V dc bias, 10mtorr of pressure and 70°C table temperature [224].

In another study by Lee et al. the etch rate was studied as a function of $\%BCl_3$ in a 10mtorr plasma with 600W of power supplied to the coil and -200V dc bias at a temperature of 70°C. They used quadropole mass spectrometry (QMS) to measure the plasma constituents. The etch rate results are shown in Figure 5-5. The variation in the QMS output for the plasma constituents measured as a function of $\%BCl_3$ is shown in Figure 5-6, the ionic species being shown in the top graph and the neutral species mainly in the bottom graph. There seems to be no obvious correlation between any

single plasma element with the ion saturation current and the Cl radical density showing the closest relation to the observed variation in etch rate. There is a peak in the etch rate at 90% Cl_2 and the ion density drops quite sharply once the %BCl_3 is increased past 20%.

One reason (possibly the reason) for the peak in the etch rate with a small amount of BCl_3 added to the plasma is given in [257] to be because BCl_3 is highly electron deficient and hence the reaction

$$BCl_3^* + Cl_2 \rightarrow BCl_4 + Cl^+$$

where the * denotes and excited species and the reaction involves the transferral of an electron is favourable and leads to a higher Cl radical-ion density that would be found with just pure chlorine.

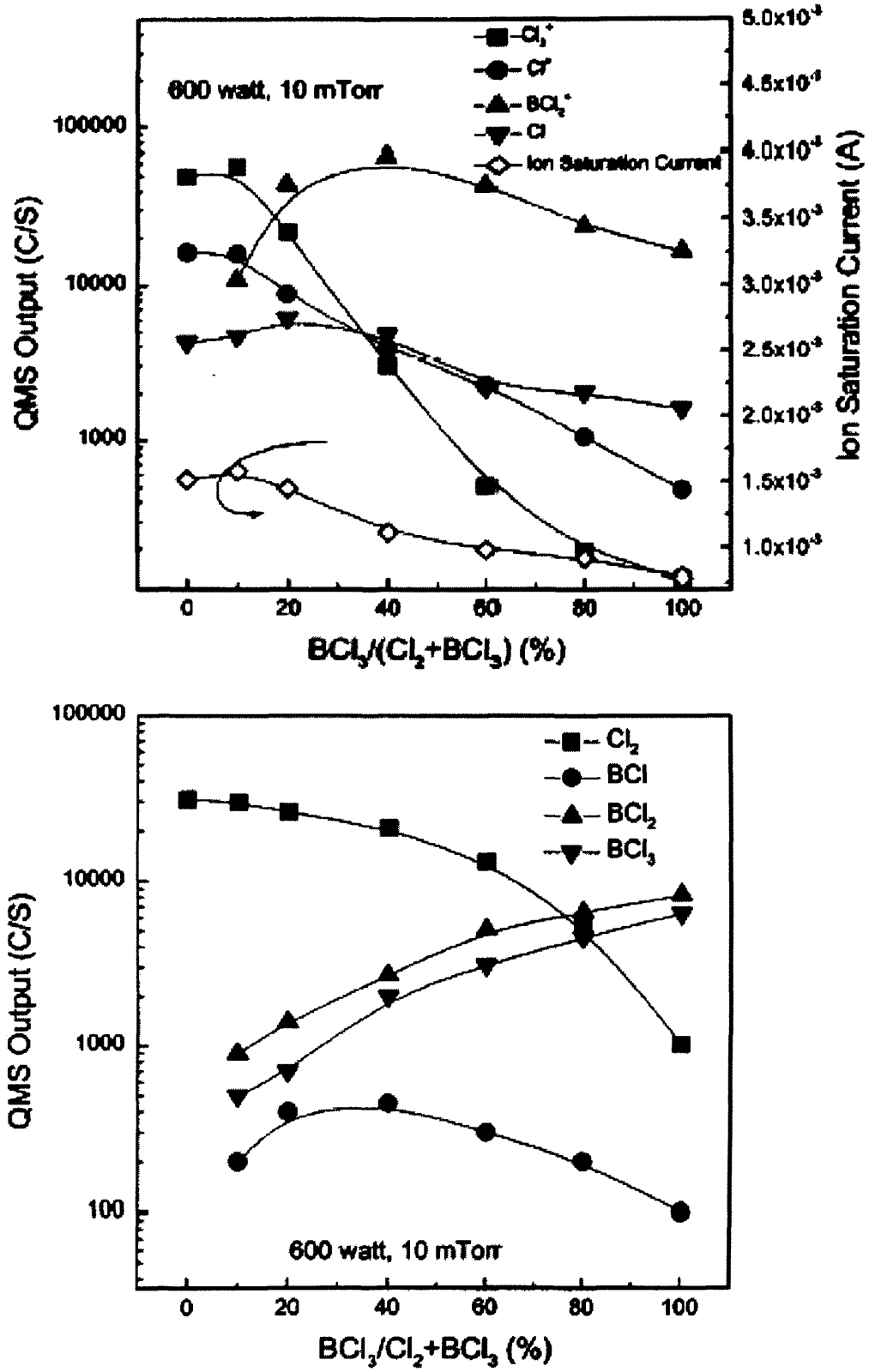

Figure 5-6 Plasma constituents of a Cl_2/BCl_3 plasma as a function of $\%BCl_3$. Other parameters were a pressure of 10mtorr, -120V dc bias, 600W coil power and a table temperature of 70°C [224].

5.3.2 Gallium nitride etch rate as a function of temperature

Kim et al. also looked at the variation in the etch rate of GaN with the temperature of the sample and their results are shown in Figure 5-7. As may be seen the etch rate increases monotonically with temperature from a temperature of 3°C to a temperature of 70°C. The fact that the etch rate is increased much more by increasing temperature when there is a high percentage of chlorine (% Cl_2) in the plasma suggests that the increase in etch rate with the increase in temperature is due to an increased reaction rate, most likely due to increased desorbtion of the not-so-volatile etch products though possibly due to an increased reaction rate at the surface. From [266], at high temperatures we expect more of the etch product to be GaCl; whereas, at lower temperatures we expect the higher number chlorides $GaCl_2$ and $GaCl_3$ to become more predominant, similarly with AsCl, $AsCl_2$ and $AsCl_3$ and therefore presumably NCl, NCl_2 and NCl_3.

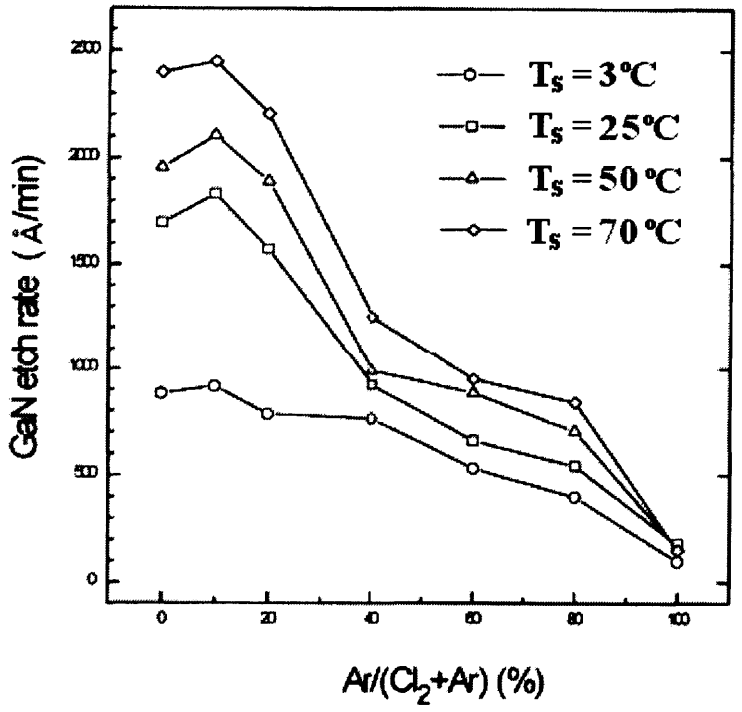

Figure 5-7 Etch rate of GaN in a Cl_2/Ar plasma as a function of the gas ratio and wafer temperature for Cl_2/Ar plasma at ~10mTorr, 400W ICP and -120V dc bias [232].

At equilibrium between a gas and a solid a certain amount of gas molecules or atoms will be absorbed on the solid surface; Equation 5-1 gives the equilibrium fraction of the wafer surface on which gas phase molecules are absorbed at the interface between the surface and a gas consisting of only one type of molecule. [258]

$$\theta_A = \frac{\kappa \cdot n_A}{1 + \kappa \cdot n_A} \quad \text{Equation 5-1}$$

Here n_A is the equilibrium gas phase volume density of absorbing molecules and κ is an equilibrium constant given by Equation 5-2. In Equation 5-2, R is the gas constant, T is the temperature of the surface in Kelvin, G^0_{desor} is the standard Gibbs free energy of desorbtion and n^0 is the gas-phase density at standard temperature and pressure (Loschmidt's number). Figure 5-8 shows a graph of θ_A against $\kappa \cdot n_A$. θ_A has a value of one when $\kappa \cdot n_A$ equals infinity.

$$\kappa = \frac{1}{n^0} \exp\left(\frac{G^0_{desor}}{RT}\right) \quad \text{Equation 5-2}$$

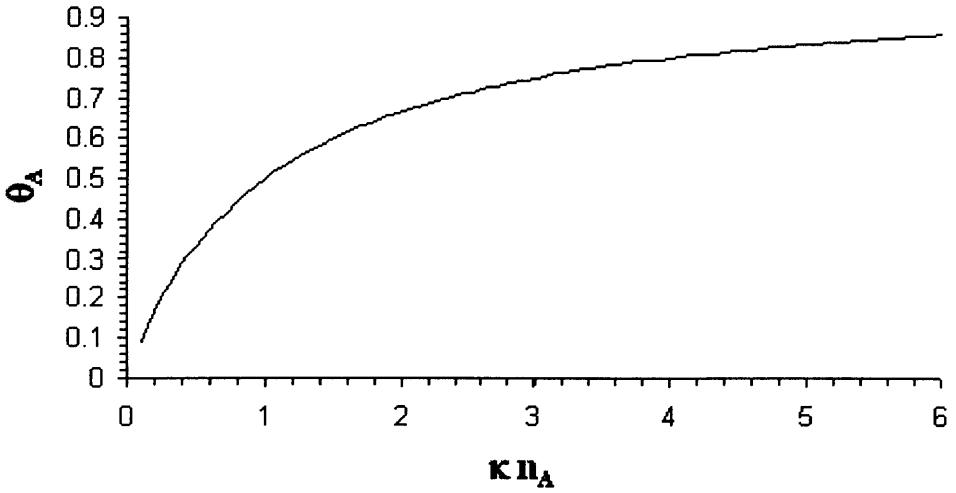

Figure 5-8 The Langmuir isotherm [258]

From this it may be seen that at high temperatures (low $\kappa \cdot n_A$) the surface is not covered well and from this it is expected that at high temperatures the etch rate will decrease, as it does for silicon etching using XeF_2 gas [258].

5.3.3 Gallium nitride etch rate as a function of pressure

In the study of Kim et al. [223] the authors examine the effect of pressure on the etch rate of GaN using pure Cl_2, $90\%Cl_2/10\%BCl_3$, $50\%Cl_2/50\%BCl_3$ and pure BCl_3 plasmas. They used quadropole mass spectrometry (QMS), optical emission spectroscopy (OES) and Langmuir probes to discover the effect of pressure on the relative amounts of different substances in pure Cl_2 and $90\%Cl_2/10\%BCl_3$ plasmas. Their study showed no direct correlation between any of the individual plasma constituents and the etch rate of GaN see Figure 5-9, though the etch rate increased with increasing Cl and Cl_2 density as the ion density decreased and seems only to decrease when the ion density is reduced past a certain level.

The variation of various plasma constituents as a function of pressure in a $90\%Cl_2/10\%BCl_3$ plasma is shown in Figure 5-10 (a) and (b). From comparison of these two graphs (Figure 5-10 (a) and (b)) with the etch rate of the $90\%Cl_2/10\%BCl_3$ shown in Figure 5-9 (a) it can be seen that the etch rate seems to correlate to the concentrations of ions with the peak in the more abundant ions, i.e. BCl+, BCl_2+, BCl_3+ and Cl_2+, countering the drop in the less abundant ions Cl+ and B+. The neutral density increases monotonically with pressure though the Cl radical density remains approximately constant between 30 and 40 mtorr and even seems to drop slightly.

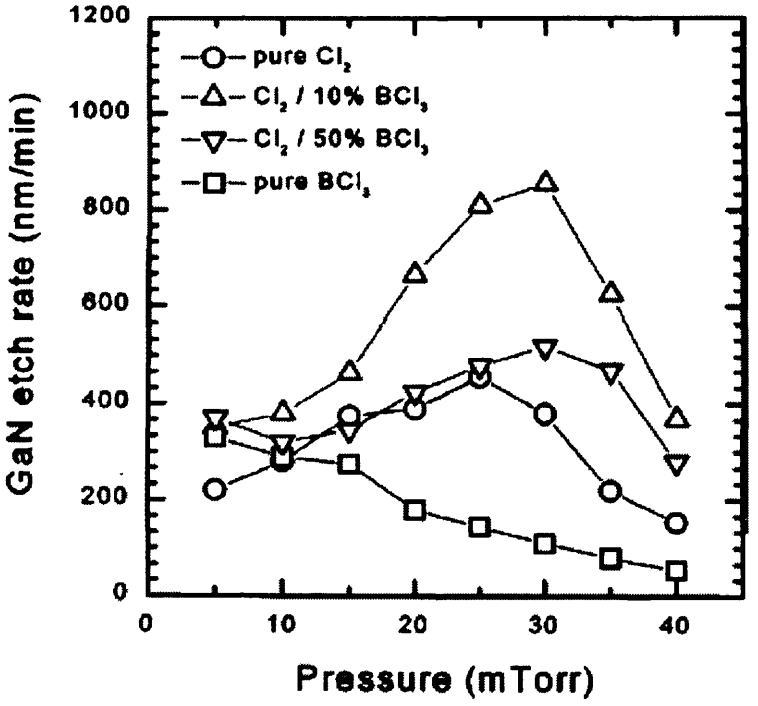

(a)

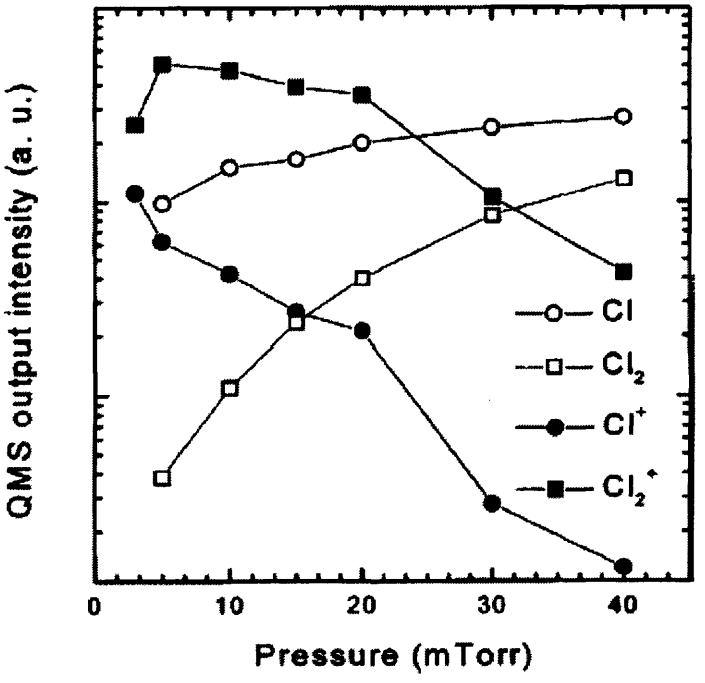

(b)

Figure 5-9 (a) Etch rate variation with pressure observed for various chlorine and boron trichloride plasma chemistries. (b) The relative abundances of plasma constituents observed in a pure chlorine plasma. The power to the coil was 600W, the table temperature was 70°C and the dc bias was -120V. [223]

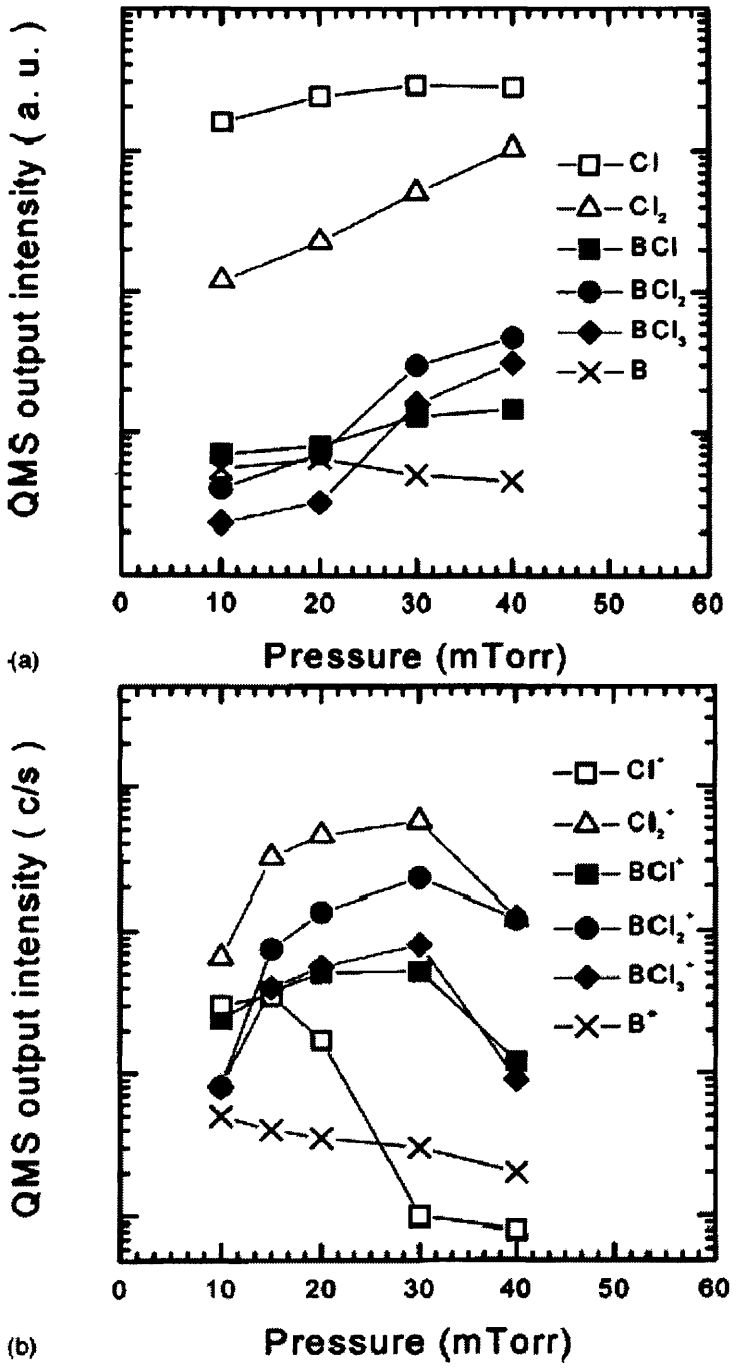

Figure 5-10 QMS output intensities of various plasma components in a 90% Cl_2/ 10% BCl_3 plasma (a) neutral species and (b) ionic species. The plasma conditions were 600W coil power, 70°C table temperature and -120V dc bias [223].

H. S. Kim et al. [222] have published a study which contained, among other things, the etch rate of GaN as a function of pressure in a 70%Cl_2/30%BCl_3 plasma at 600W coil power, -120V dc bias and 70°C table temperature, see Figure 5-11. Figure 5-12 is the graph of the plasma constituents measured in the same plasmas.

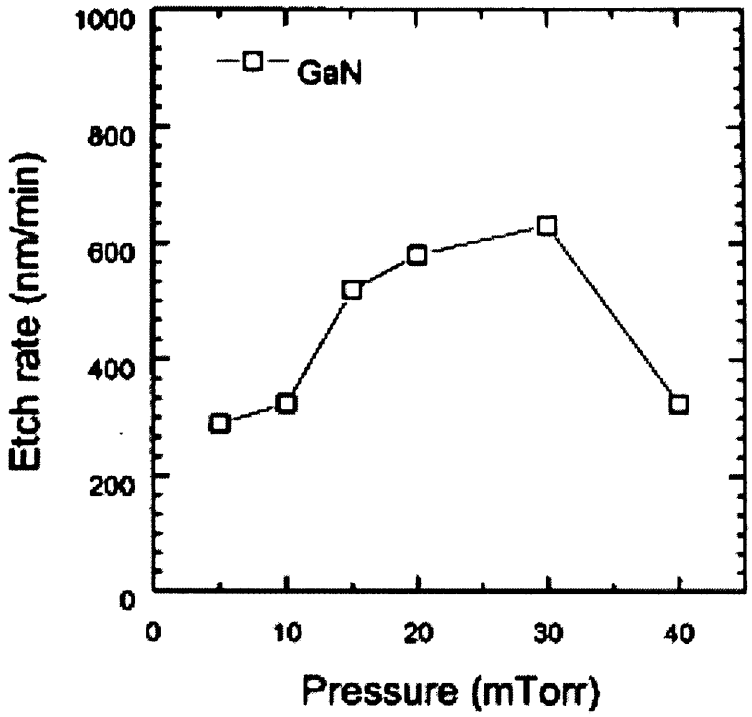

Figure 5-11 Etch rate as a function of pressure in a 70%Cl_2, 30%BCl_3 plasma, 600W coil power,-120V dc bias and a table temperature of 70°C [222].

The results of Figure 5-11 and Figure 5-12 are very similar to those of Figure 5-10, indeed the only difference is that the results of Figure 5-10 were taken with a plasma of 90%Cl_2 and 10% BCl_3 whereas the results of Figure 5-12 are for a plasma composed of 70%Cl_2 and 30% BCl_3. From Figure 5-9(a) and Figure 5-11 it is possible to see that at 600W power to the coil and -120V dc bias the highest etch rate found with a Cl_2/BCl_3 plasma at 30 mtorr is for a plasma with 10% BCl_3 content.

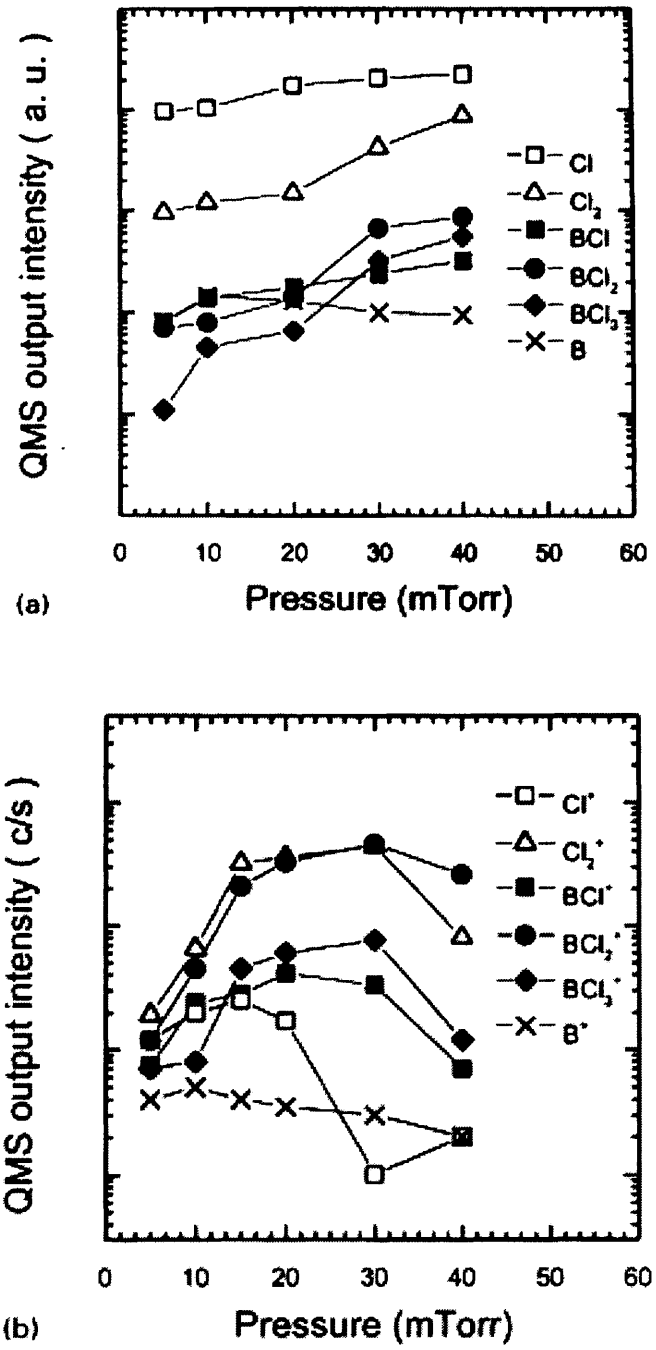

Figure 5-12 Figure showing the relative intensities of various plasma constituents in a 70%Cl_2/30%BCl_3 plasma as a function of pressure. Other parameters were 600W coil power, -120V dc bias and 70°C table temperature [222].

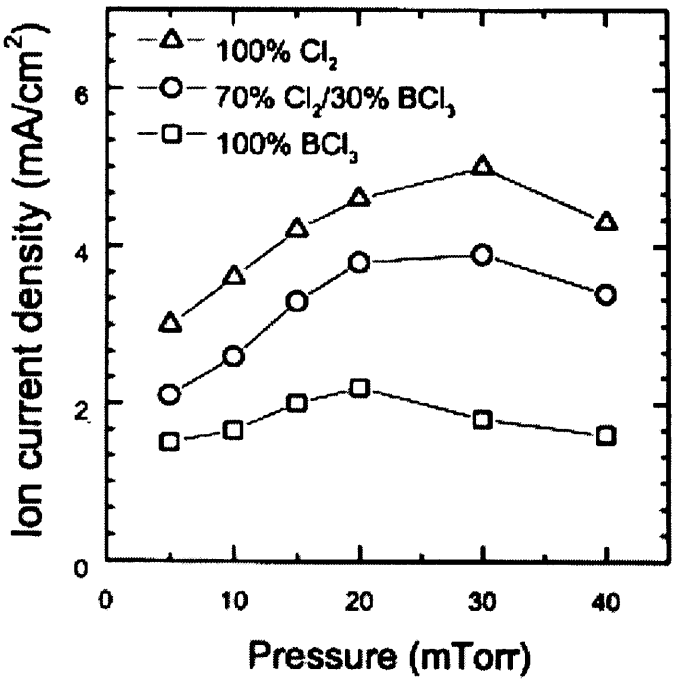

Figure 5-13 Ion current density as a function of pressure in plasmas excited by 600W to the coil, with a dc bias of -120V and table temperature of 70°C. The plasma chemistries are recorded in the figure [222].

Figure 5-13 shows the ion current density as a function of pressure for plasmas including the one detailed in Figure 5-11 and Figure 5-12. For this plasma as well as for the plasma detailed in Figure 5-10 the etch rate correlates weakly to the total ion current density. This would seem to imply that the ion density limits the etch rate; however, the ion current density is highest for the pure Cl_2 of the results shown whereas the 70% Cl_2, 30% BCl_3 plasma has the highest etch rate of the three. This could implies that although the ion density is also important, other factors such as the type of ion, the neutral density in the plasma, or the removal of oxygen and water from the chamber by the BCl_3 helps to significantly increase the etch rate.

Park et al. in their study [228] conclude that at lower pressures the etch rate is limited by the availability of neutral molecules to react with the GaN surface and hence the etch rate increases with pressure. However, above 10mTorr (ninety percent Cl_2) the etch rate decreases as the etch rate is limited by the ion flux; i.e. the rate that new Cl-GaN reaction sites are created by the breaking of GaN bonds or the desorbtion of fully or

partially formed etch products. The dependence on the number of ions is not completely unexpected as the etch rate limiting step of tough material such as GaN is thought to be the rate that bonds are broken allowing chemical reactions to form etch products [233] (it is after all the resistance of the GaN to wet chemical etching that has meant other etch methods such as dry etching have had to be used to pattern it). Ions also help desorb etch products and also help dissociate molecules bound weakly to the surface.

5.3.4 Gallium nitride etch rate as a function of RF power (dc bias)

The etch rate in almost every case monotonically increases with the increase in dc bias or RF power. Studies where the etch rate increased when the dc bias or RF power was increased include [225, 228, 230, 233, 234, 236 & 244] whereas only [222] shows a decrease at the higher powers though [225, 234 & 244] all show a decrease in the rate of increase at higher dc bias. This decrease in the rate of increase as RF power is increased was discovered for with the ICP 380 and is discussed with the results below.

5.3.5 Gallium nitride etch rate as a function of ICP power

The variation of the etch rate as a function of ICP power fits broadly into two categories. The first is a monotonic increase as the ICP power is increased, presumably due to an increase in the Cl radical density and the ion density. A good example of this variation is shown in Figure 5-14, which also shows the variation in some ion densities and in the Cl radical density. Other studies that exhibit similar behaviour are [222, 228, 230, 236, 241 & 244] though admittedly it is common to see the rate of increase slow as the power is increased. A reason for the slow down could be the decrease in the dc bias that accompanies the increase in the plasma density. The

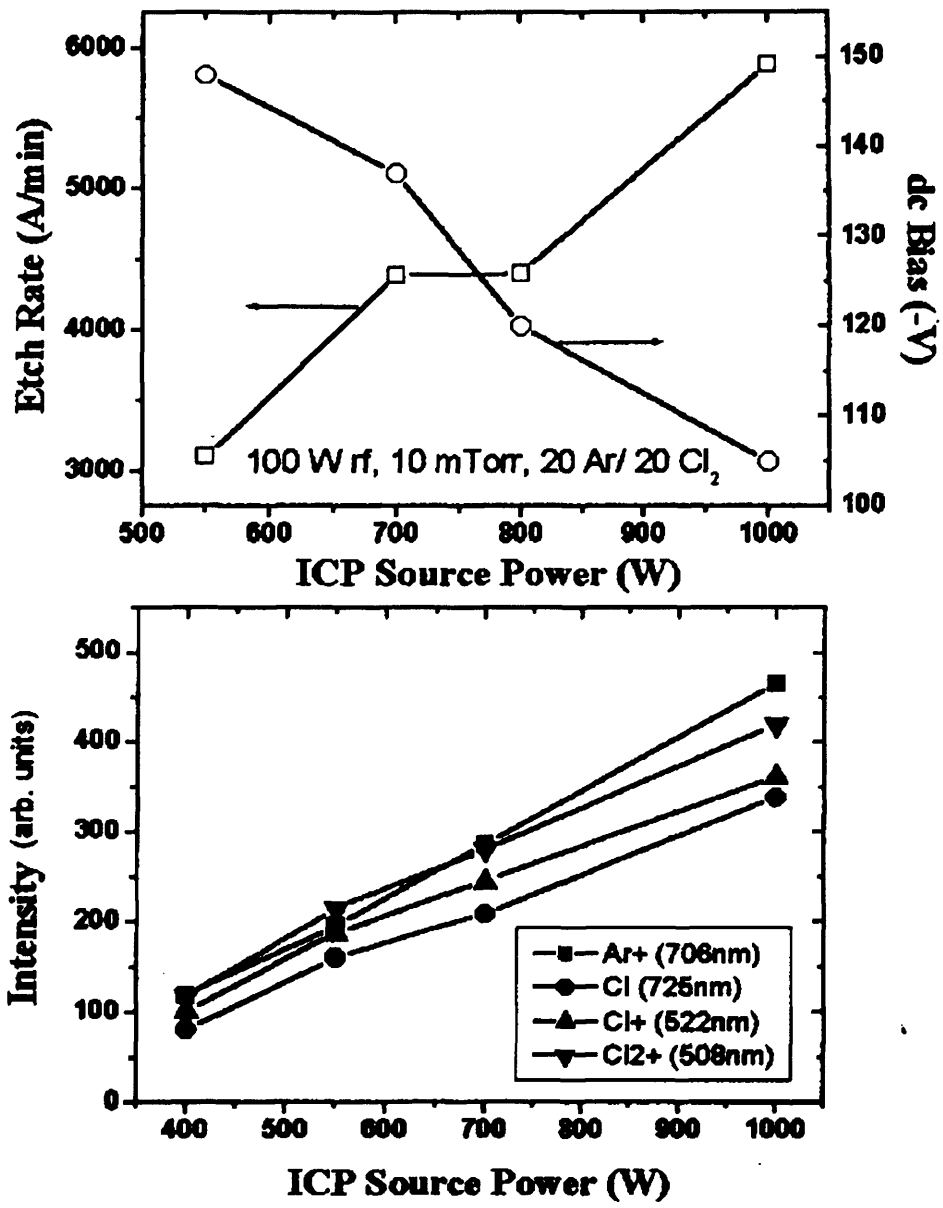

Figure 5-14 Monotonically increasing etch rate as a function of ICP power commonly found in the literature (left), the increase in the ion density and the Cl radical density (right) both indicate why the etch rate of the etch increases as a function of ICP power. The other plasma parameters are shown underneath the left-hand graph [228].

decrease in dc bias with increasing ICP power is shown in the upper graph of Figure 5-14.

The second type of variation commonly found in the literature is where the decrease in the rate of increase of the etch rate at higher powers actually becomes a decrease in

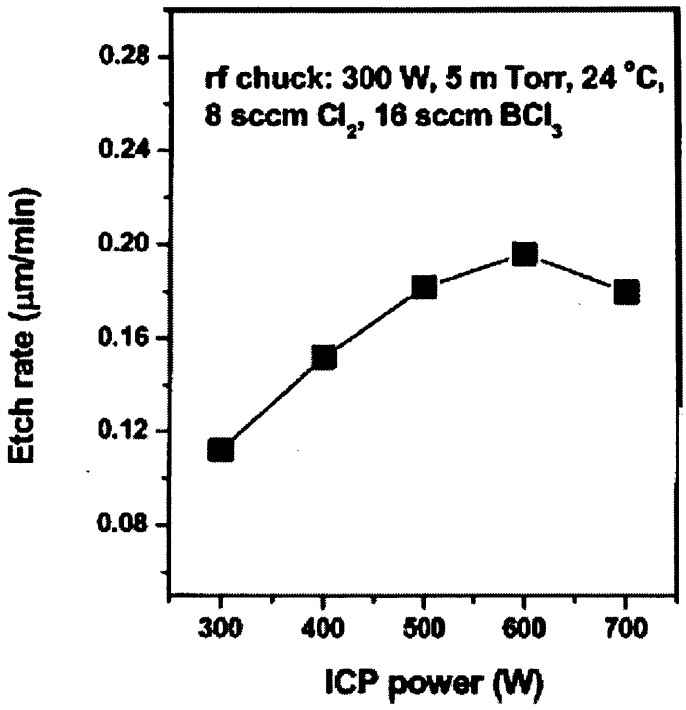

Figure 5-15 Variation in etch rate as a function of ICP power for a plasma with parameters shown in the figure. Of note is the decrease in the etch rate at 700W ICP power [225].

the etch rate at higher powers. An example of this behaviour is shown in Figure 5-15. Other examples may be found in [227, 231, 233, 238 & 242]. This behaviour is just an extension of the slowdown in the increase of the rate and is presumably caused by the same mechanism.

5.3.6 Theoretical considerations

The dc bias voltage drop will give the same amount of energy to all ions, of the same charge, regardless of their mass. This is due to the fact that a potential difference indicates the energy drop per unit charge across it. As the energy due to thermal energy and the Bohm pre-sheath [214] is small (less than approximately 4eV) almost all the ion's energy comes from the dc biases, the dc bias being normally larger than the bond energy of GaN (8.92 eV/atom), AlN (11.52 eV/atom) and InN (7.72 eV/atom) [240]

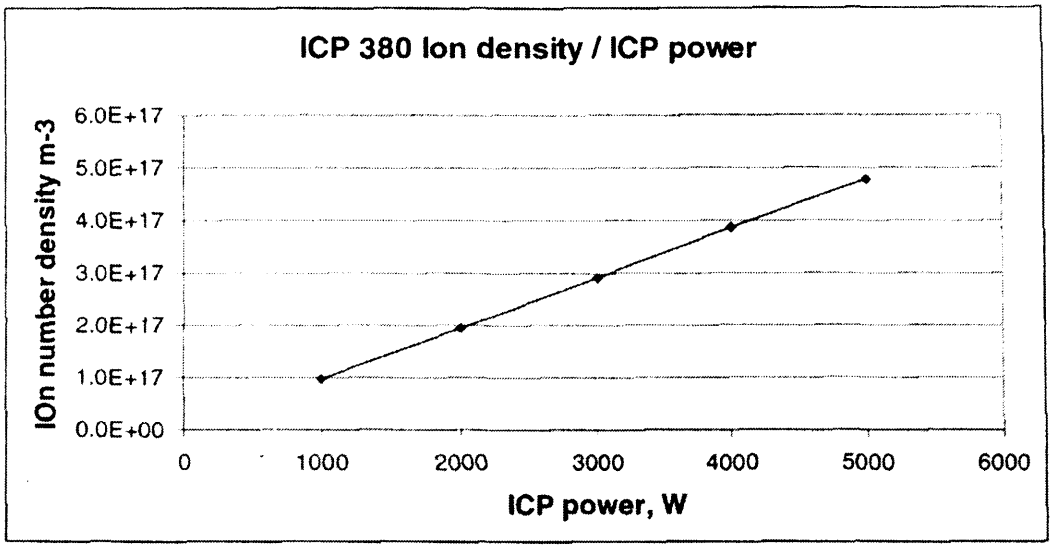

Figure 5-16 Ion current density at the wafer versus ICP power for pure Ar plasma in an Oxford Instruments ICP 380 measured with a Langmuir probe at -30V [259].

Figure 5-16 displays plasma density data for an Argon plasma generated in an Oxford instruments ICP 380. The data was taken in Argon gas at 1 mTorr, with RF power applied only to the ICP source. A dc bias power was applied to the lower electrode at -30 V dc to measure the ion current. This was converted to plasma density using plane Langmuir probe theory. For a coil power of 1000W, the density is approximately $1x10^{11}$ cm^{-3}.

From [260] the number of atoms in 1 cm^3 of GaN is $8.9x10^{22}$; hence from this the number of atoms in various thicknesses of 1cm^2 of GaN may be approximated simply as the thickness of the layer in centimetres multiplied by $8.9x10^{22}$; hence, a layer 1 nm=$1x10^{-9}$m=$1x10^{-7}$cm thick corresponds to $8.9x10^{15}$ atoms. A moderate ICP etch should only affect approximately the top 1 nm of GaN, though any damage might penetrate much further than that [261]. Hence, the plasma needs to supply energy of the order of 10^{17} eV (~ number of atoms in 1 nm multiplied by the bond energy/atom) in order to break the bonds of the first 1 nm of a 1cm^2 sample of GaN, and thus reliably provide sites for chemical reactions.

The energy of an ion incident on the substrate is approximately equal to the dc bias divided by π if the frequency of the ac signal generating the bias is greater than

approximately 10 MHz (see [262]). The frequency of the most RF generators used in plasma generators 13.56MHz. Another factor that we should consider is due to the mass transfer between the surface and the ion. The angle averaged energy accommodation coefficient is given by Equation 5-3 [263]

$$\alpha = \frac{4\mu}{3(\mu+1)^2} \quad \text{Equation 5-3}$$

where μ is the mass of the ion divided by the mass of the solid atom. The energy accommodation coefficient for the gases commonly used to etch the III-nitrides are shown in Table 5-2.

Ion	Appoximate relative atomic mass	μ to Ga %	μ to N %
Cl_2^+	70	33	19
BCl_3^+	115	31	13
Cl^+	35	30	27
BCl^+	45	32	24
Ar^+	40	31	26
N_2^+	28	27	30
N^+	14	19	33
H^+	1	2	8
CH_3^+	15	19	33
CH_4^+	16	20	33

Table 5-2 Showing the energy accommodation coefficients for ions striking Ga and N atoms, for various ions, commonly used to etch GaN.

As may be seen from Table 5-2, the greatest amount of energy that is transferred in this simple model is approximately a third of that of the ion. This model is for interactions between atoms modelled to behave similarly to solid billiard balls and does not account for reactions that occur at the surface, such as those likely between

the Cl+ radical ion or the Cl_2+ molecule and the surface. With these extra considerations due to the alternating nature of the dc bias and the inefficient transfer of energy to the substrate, the energy of a molecule incident onto the substrate surface is less than the dc bias by approximately an order of magnitude.

A plasma density of $1x10^{11}$ ions/cm^3 corresponds to approximately 2 mA/cm^2 of current, or approximately $1x10^{16}$/cm^2 singly charged particles per second incident on the substrate; hence, for a 1cm^2 sample, if only singularly ionised ions are assumed and if the flux to the substrate is approximately $1x10^{16}$ ions/s, to break all the bonds in the top 1 nm of a 1 cm^2 GaN sample a dc bias of the order of 100V is required.

The above reasoning may be written as Equation 5-4, where B is the bond-strength per atom, N is the density of atoms in the sample, V is the area of the sample multiplied by 1 nm, Γ is the ion flux to the substrate (determined by a planar langmuir probe) and α is the mass transfer factor introduced above; $\pi(f)$ is equal to π if the frequency of the signal generating the dc bias is greater than 10MHz but is lower if the frequency is lower [262]. The transfer of energy into the breaking of bonds will not be totally efficient so an efficiency factor is added and the dc bias is thus given by Equation 5-5, where Λ is a constant of proportionality related to the efficiency with which bonds are broken.

$$optimum\ dc\ bias \propto \frac{B\ N\ V}{\Gamma\ \alpha\ \pi(f)} \quad \text{.....Equation 5-4}$$

$$optimum\ dc\ bias = \Lambda\ \frac{B\ N\ V}{\Gamma\ \alpha\ \pi(f)} \quad \text{.....Equation 5-5}$$

The effect of dc bias on the desorbtion of the GaCl etch product is shown in Figure 5-17 [232], where the OES signal is normalised by the zero bias signal. As may be seen, more GaCl, Ga and N_2 are desorbed from the surface of the GaN as the dc bias is increased to 60V, after which the rate increases more slowly; the top graph is for a 100% Cl_2 plasma and the bottom graph for a 100% Ar plasma. The other plasma parameters were an ICP power of 400W and a pressure of 10 mtorr.

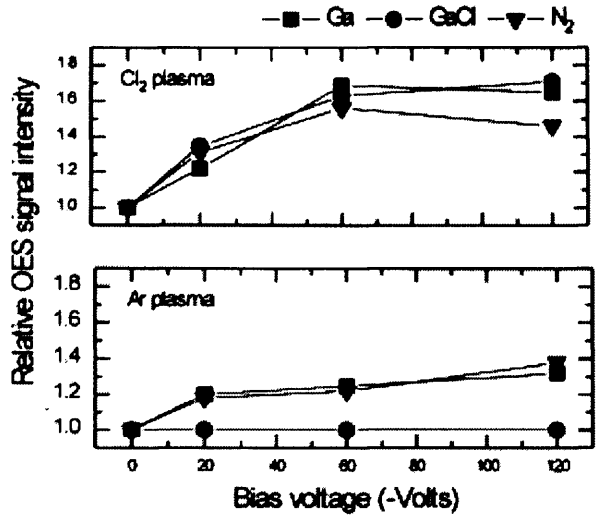

Figure 5-17 Optical emission spectra from GaN etching by 100% Cl_2 and by Ar. The OES signal is shown relative to the spectra from a sample etched with zero dc bias [232].

Following [264], the fraction of the feedstock gas that is utilised in etching a substrate U (the utilisation factor) is given by Equation 5-6; where N is the number of atoms contained in 1cm x 1cm x 1Å volume of substrate, n is the number of gas atoms in a standard cubic centimetre per minute (sccm), A_s is the area of the substrate, E is the etch rate of the substrate in Å/min and Q is the flow rate in standard cubic centimetres per minute.

$$U = \frac{N}{n} \cdot \frac{A_s \cdot E}{Q} \quad \text{.....Equation 5-6}$$

For GaN, N is 8.9×10^{14} cm^{-2} $Å^{-1}$ and n is given in [264] as 2.69×10^{19} molecules/min. In [264] Chapman and Minikiewicz state that a high utilisation factor at low flow rates is caused by an insufficient supply of gas to feed reactions with the substrate. Using Equation 5-6 it is found that, for a $1cm^2$ sample of GaN such as those commonly used in research, the utilisation factor is small. A value of approximately 0.5 for the utilisation factor is reached when the etch rate is set to 15000 Å min-1 (higher than any values reported in the literature) and the flow rate is 1 sccm. For higher flow rates

and lower etch rates U is much lower than 0.5, as is shown in Figure 5-18 and Figure 5-19.

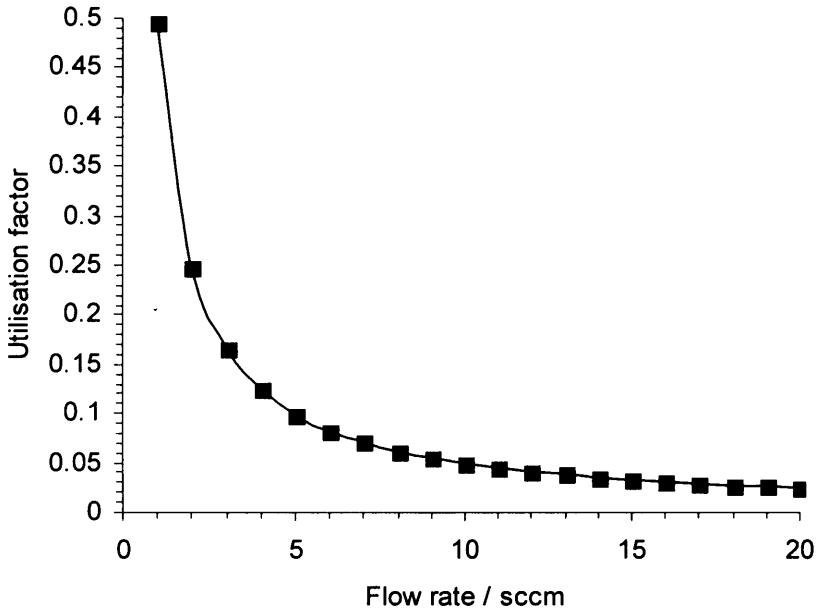

Figure 5-18 Utilisation factor as a function of flow rate as calculated from Equation 5-6 with the sample area 1cm^2 and the etch rate 15000 Å min^{-1}.

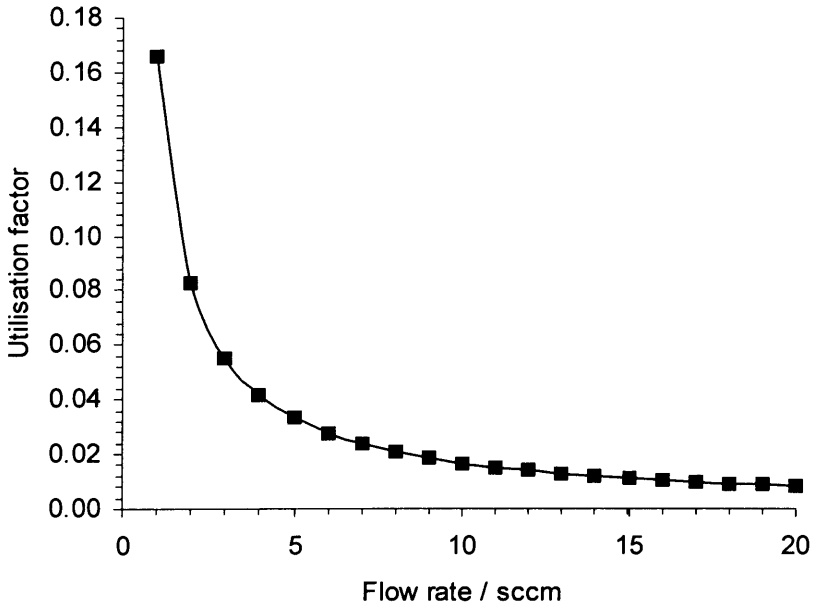

Figure 5-19 Utilisation factor as a function of flow rate as calculated from Equation 5-6 with the sample area 1cm^2 and the etch rate 5000 Å min^{-1}.

In [264] Chapman and Minikiewicz define a low flow region where any variation of the rate has a large effect on the etch rate (due to the relative scarcity of etchants) and a high flow region where a change in the flow rate has little effect due to the over supply of etch gases. From Figure 5-18 and Figure 5-19 it is possible to conclude that a flow rate of 10 sccm should be sufficient for $1cm^2$ samples; however, in this model reactions with the sidewalls of the chamber are ignored or assumed negligible. In large reactors, like the Oxford Instruments ICP range, this assumption is less likely to be valid though conditioning the chamber with an appropriate plasma before the etch will help to make it more so. Experimentally there should be a region where there is an insufficient supply of etchants to sustain the etch and a region at higher flows where little variation is observed, such as was the case in [234] where little variation with flow was exhibited between flows of 15 and 60 sccm.

Also in [264] Chapman and Minkiewicz give Equation 5-7, describing the probability that an active species will react with the substrate before being pumped away in the high flow region, where the symbols are the same as for Equation 5-6 except Q is now in units of millitorr litres per second (1sccm = 12.7 mtorr l/s), *c- bar* is the mean speed of the reactive species, R_s is the probability of reaction per incident active species and P is the pressure in torr.

$$\alpha = \frac{1}{1 + \frac{4Q}{c \cdot P \cdot R_s \cdot A_s}} \quad \text{Equation 5-7}$$

From Equation 5-7 we may see that the probability that an active species reacts with the substrate before being pumped away is reduced by increasing the flow rate and by decreasing the pressure.

From [265] the maximum possible value of the trapping probability is given as Equation 5-8

$$\xi_M = 1 - \exp\left[-\frac{2.4 \cdot \mu^*}{1 - 0.4 \cdot \mu^* + (\mu^*)^2} \cdot \left(\frac{D}{kT_g} - \frac{T_s}{T_g} \right) \right] \quad \text{Equation 5-8}$$

where D represents the depth of a potential well that traps the gas at the surface of the material, T_g and T_s are the temperatures of the gas and the solid, respectively, and μ^* is the ratio of the masses of the gas and solid atoms as shown in Equation 5-9. However, due to the scarcity of data about the adsorbtion and desorbtion of chlorine to GaN there was no way of calculating the required quantities.

$$\mu^* = \frac{M_g}{M_s} \quad \text{Equation 5-9}$$

The best way of estimating D was from data related to the adsorbtion and desorbtion of chlorine on GaAs, for which the state of the art is far more advanced. Using an average of the barrier heights calculated in [266] the depth of a potential well is calculated is 0.044eV and the calculated trapping probability as a function of substrate temperature for adsorbtion to nitrogen (N) is shown in Figure 5-20 for a gas at room temperature. The graph for adsorbtion to Ga looks very similar to that for adsorbtion to N. From these graphs we see that a gas atom impinging on a substrate at room temperature will stick to it approximately 50% of the time.

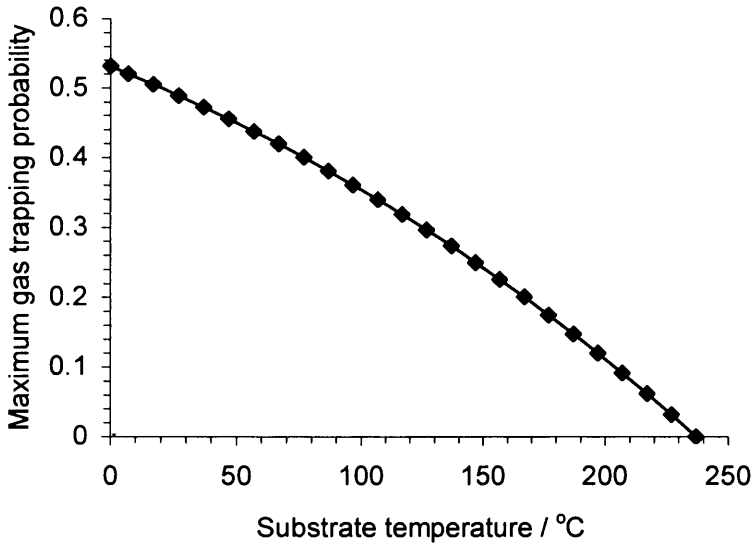

Figure 5-20 Variation of the maximum trapping probability of a Cl atom to a N atom on a GaN surface as a function of temperature calculated from Equation 5-8.

Using a value for R_s in Equation 5-7 of 0.5 and a mean gas molecule velocity of 30000 cm/s, the probability that an active species will react with a $1cm^2$ sample of GaN before being pumped away for flow rates of 5, 10 and 15 sccm and pressures from 1 to 20 mtorr, calculated with Equation 5-7, are shown in Figure 5-21.

Obviously if the probability of a reaction occurring is less than 0.5 the probability that an etchant will react with the surface before being pumped away is reduced. This effect is shown in Figure 5-22 as a function of pressure for a flow rate of 10 sccm.

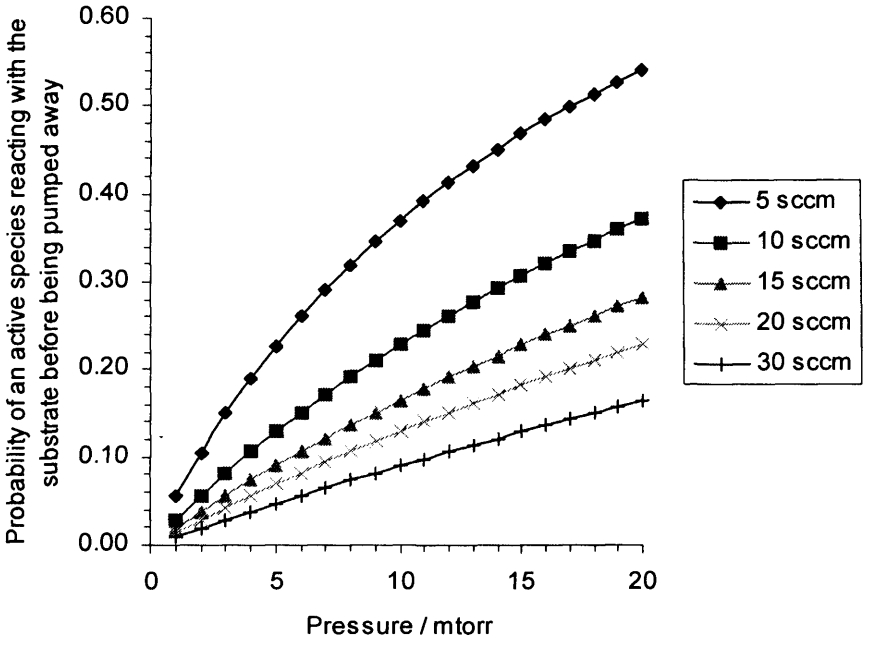

Figure 5-21 Probability that an active molecule will react with the substrate before being pumped away as a function of pressure for five flow rates as calculated with Equation 5-7. The mean speed of a molecule was taken as 30000 cm/s and the probability of a gas particle incident on the surface reacting with the substrate as 0.5.

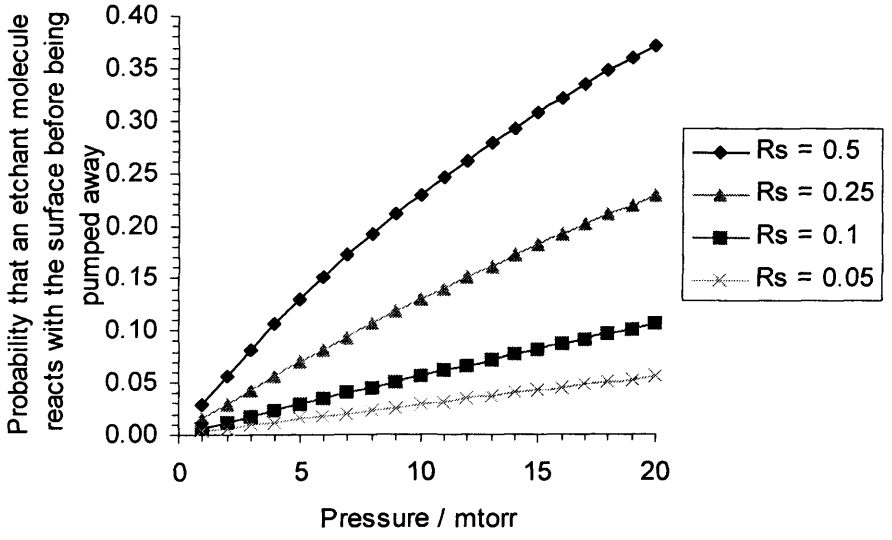

Figure 5-22 Graph showing the effect of decreasing the probability of an impinging etchant molecule reacting with the substrate (Rs) on the probability that an etchant will react with the substrate before being pumped away, (the flow rate is set at 10 sccm the other parameters are the same as before).

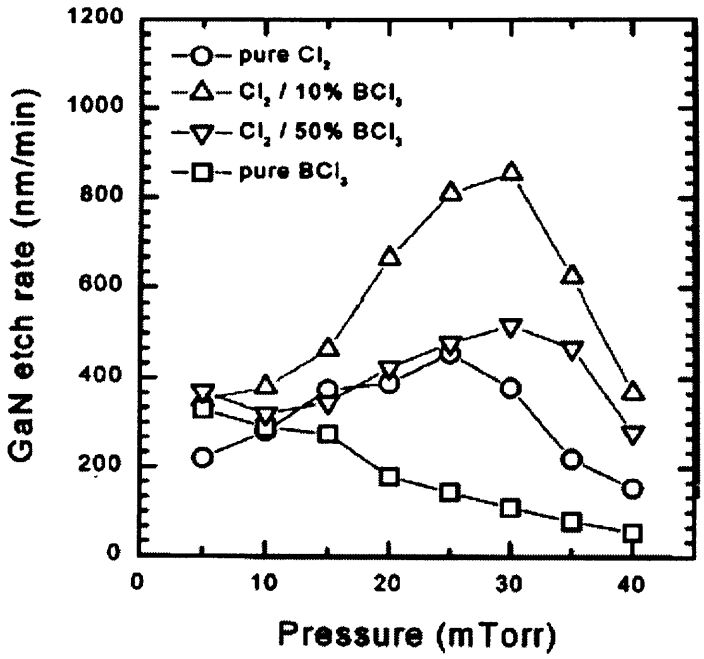

Figure 5-23 Variation of GaN etch rate as a function of pressure for various inductively coupled plasmas.

From Figure 5-23 we see that there is, in all the plasmas shown, an initial increase in the etch rate as the pressure is increased followed by a decrease at higher pressures. The mechanism for the decrease at higher pressures is the decrease in the plasma density normally attributed to the increased frequency of recombination between ions and electrons at higher pressures.

	GaCl	$GaCl_2$	$GaCl_3$	NCl_3
Heat of Formation (kJ/mol)	-84	-260	-448	-229
Boiling Point (°C)		535	~206	71
Melting Point (°C)		172	~77	-40

Table 5-3 The heat of formation, boiling and melting points of several of the important etch products from chlorine etching of GaN [267].

The heats of formation of some of the different Ga and N chlorides, as well as their melting and boiling points, are shown in Table 5-3. As may be seen the heat of formation decreases (becomes more negative) as the chlorine number increases indicating an increasing exothermic reaction. Also the boiling and melting points of

the gallium chlorides decreases as the chlorine to gallium ratio increases and one must guess a similar behaviour for the nitrogen chlorides.

In [268] Winters gives several steps for an etch to proceed and illustrates these steps with the etching of silicon with CF_3. These steps are shown below but with chlorine etching of GaN given as an example instead.

1. Adsorbtion (nondissociative and dissociative):

$$Cl_2(gas) + GaN \rightarrow Cl_2(ads) + GaN$$

$$Cl_2(gas) + GaN \rightarrow 2Cl(ads) + GaN$$

2. Formation of product molecule:

$$xCl + Ga \rightarrow GaCl_x(ads) \ (x=1,2 \text{ or } 3)$$

$$xCl + N \rightarrow NCl_x(ads) \ (x=1,2 \text{ or } 3)$$

3. Desorbtion of product molecule:

$$GaCl_x(ads) \rightarrow GaCl_x(gas)$$

$$NCl_x(ads) \rightarrow NCl_x(gas)$$

Winters also includes a step for desorbtion of any residue, in the case of CF_3 etching of Si, the carbon residue. This may be relevant for plasmas containing large amounts of BCl_3. Winters, carries on to state that any of the above steps may be rate limiting. It would therefore be good to know whether chlorine reacts with the GaN surface at room temperature and pressure to form chlorides with either nitrogen or gallium without the need for ion bombardment to break any bonds. If a spontaneous reaction between chlorine and GaN does occur at the GaN surface then it is almost certainly the desorbtion of the product molecule rather than its formation that is the rate limiting step of the GaN etch. The temperature dependence of the etch (Figure 5-7) could either be due to the temperature changing the rate at which chlorine reacts with GaN to form an etch product, or it could be due to the increase rate that the etch products evaporate from the surface.

Because GaN does not etch well in wet chemical etchants and because GaAs has a higher etch rate than GaN (GaAs has similar etch products but a lower bond strength than GaN), it was thought that it was the strong bond strength of GaN that limited the etch rate of GaN. The implication for etching with chlorine is that the Ga and N atoms prefer to bond to one another rather than to Chlorine. The standard heat of formation of stoichiometric GaN is given in [269] as -157 ± 16 kJ/mol, in agreement with several other values from the literature. This value compared with the values for the gallium chlorides in Table 5-3 indicates that the reaction of Ga with N is more favourable than that of Ga with Cl but is less favourable than the reaction of Ga+yCl to form $GaCl_y$ where y is 2 or 3. The differences in the heats of formation of the GaN and GaCl is about 73 kJ/mol or 1eV per molecule.

5.3.7 Sidewall profiles and etch damage

The SEM images in [221] etched at 30mtorr do not show obvious signs of under cutting as might be expected, and in fact exhibit the opposite with acute angled sidewalls. However, much better profiles have been achieved at lower pressures (see Figure 5-25 and Figure 5-26. The etch rate for Figure 5-25(b) was ~ 3800 Å/min, for Figure 5-26(b) it was ~ 2400 Å/min).

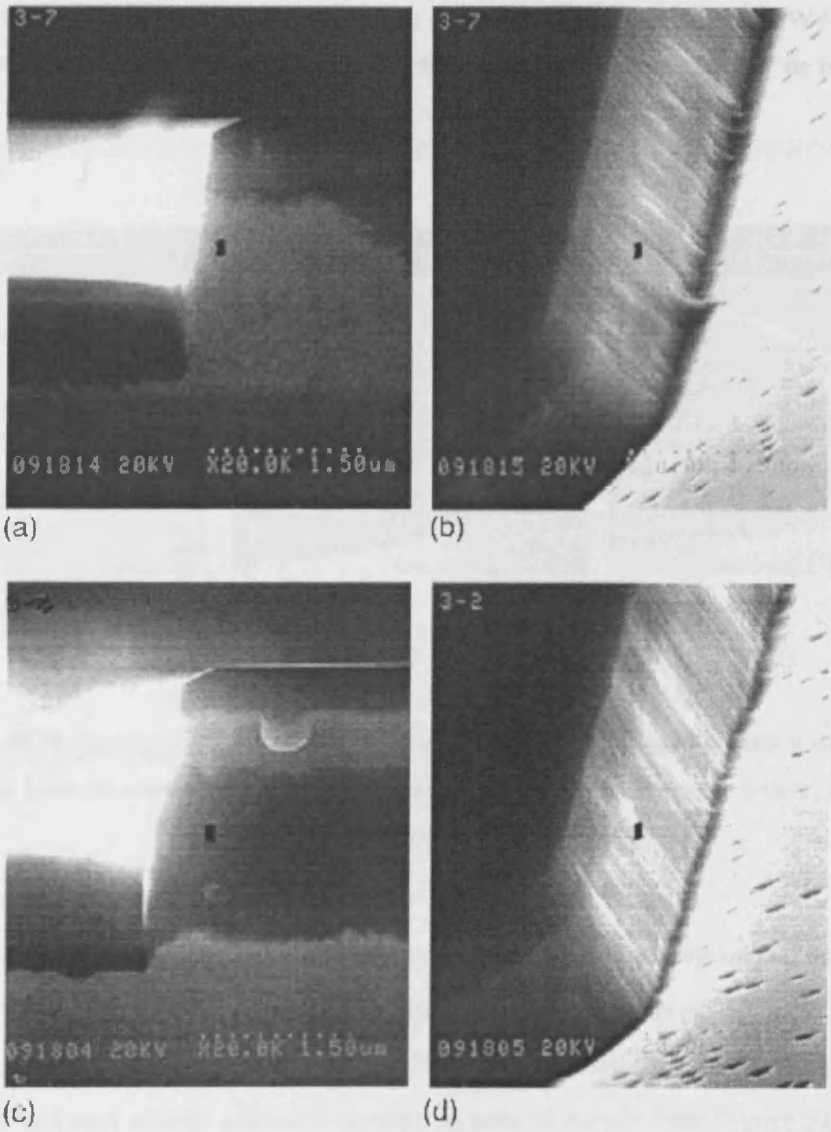

Figure 5-24 SEMs of SiO_2 masked GaN etched in ((a) & (b)) Cl_2/Ar plasmas at 30mtorr, 70°C, 10% Ar, -120V dc bias and 600W power to the coil, and ((c) & (d)) Cl_2/BCl_3 plasmas at 30mtorr, 70°C, 10% BCl_3, -120V dc bias and 600W power to the coil [221].

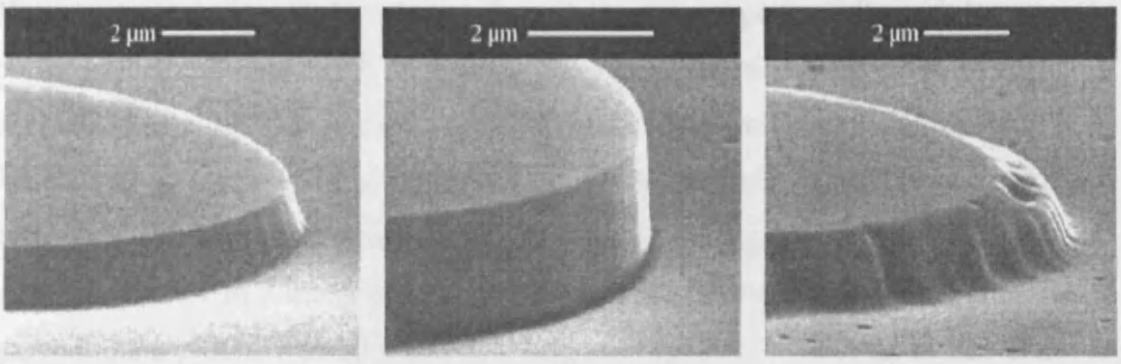

(a) (b) (c)

Figure 5-25 SEM micrographs for GaN etched at (a) 250, (b) 500, and (c) 1000W ICP source power. ICP etch conditions were 32 sccm Cl_2, 8 sccm BCl_3, 5 sccm Ar, -100 V dc bias, and 2 mTorr pressure [270].

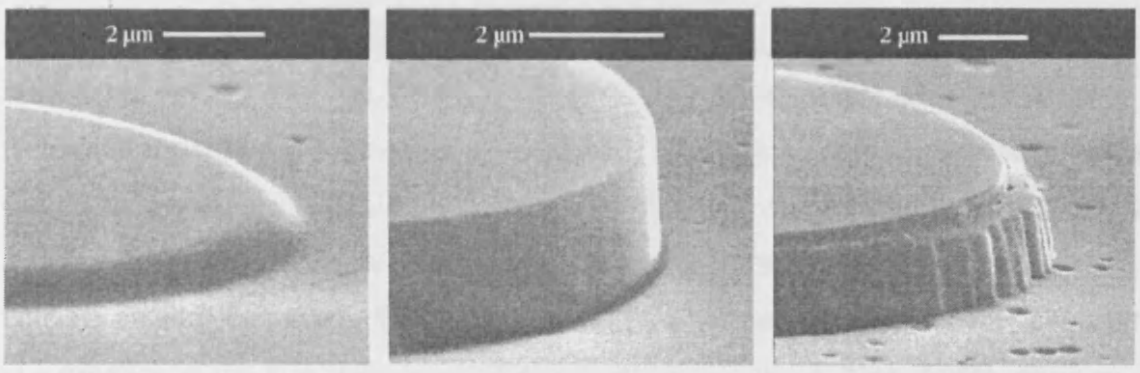

(a) (b) (c)

Figure 5-26 SEM micrographs for GaN etched at (a) -50, (b) -150, and (c) -300 V dc bias. ICP etch conditions were 32 sccm Cl_2, 8 sccm BCl_3, 5 sccm Ar, 500 W ICP source power, and 2 mTorr pressure [270].

The study from which the SEM micrographs (Figure 5-25 and Figure 5-26) are taken investigated the affects that mesa etch conditions had on the reverse bias leakage of p-i-n junction diodes at -30V. In this study Schottky contacts were deposited first and then mesa etched and ohmic contacts deposited after the etch (see Figure 5-27). Their results show that the reverse leakage current of the diodes increased by approximately two orders of magnitude when the dc bias used in the mesa etch was increased to -350V dc bias from -250V. The value at -250V was equivalent to the value at -25V.

The reverse leakage current increased approximately exponentially with increasing power to the coil from 100W to 1000W, whereas it remained approximately unchanged as a function of $\%Cl_2$ in the plasma (500W coil power, -100V dc bias, 2mtorr and 40 sccm total flow rate). As a function of pressure, the reverse leakage current dropped approximately two orders of magnitude when the pressure was increased from 1 to 2 mtorr and remained at the lower level up to the highest measurement pressure of 10mtorr. Annealing of damaged diodes up to 500°C did not improve the reverse leakage current and annealing at 600°C was found to increase the leakage current.

In their study of plasma-induced damage to Schottky diodes on n-GaN [271], Khan et al. deposited ohmic contacts, etched the surface with a Cl_2/Ar plasma rinsed the surface with 1:1 $HCl:H_2O$, and then deposited Ni/Au Schottky contacts. They found that changing the ICP coil power from 100 to 500W had little affect on the barrier height, breakdown voltage (the voltage at which the leakage current reached 1mA), ideality factor and forward turn-on voltage; this was at a dc bias of -100V a pressure of 3mtorr and a total gas flow rate of 20sccm (70% Cl_2). The etch rate for all powers was always less than 1500 Å/min. The above four factors, Schottky barrier height, breakdown voltage, ideality factor and forward turn-on voltage, all remained essentially constant as a function of the etch duration (300W coil power, -100V dc bias, 3mtorr pressure, 70% Cl_2 and 20sccm total flow rate). For a plasma with 300W coil power at a pressure of 3mtorr, 20 sccm 70% Cl_2, the Schottky barrier height, breakdown voltage, ideality factor and forward turn-on voltage all drop as a function of dc bias, as shown in Figure 5-28.

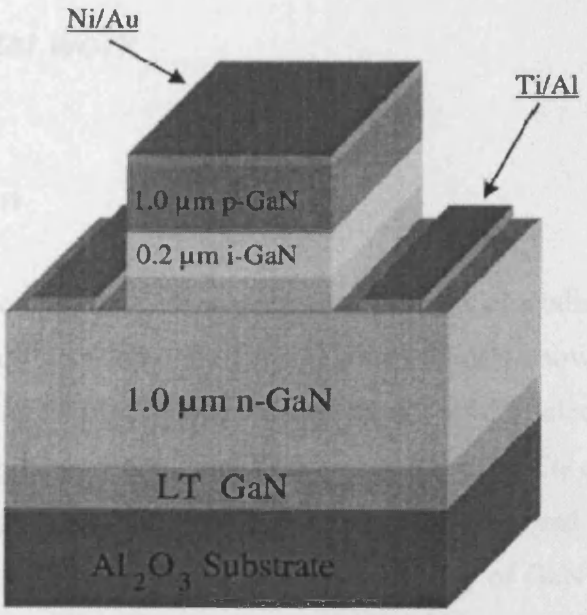

Figure 5-27 Schematic of the mesa isolated p-i-n diode used in the study of ICP damage by Shul et al. [270].

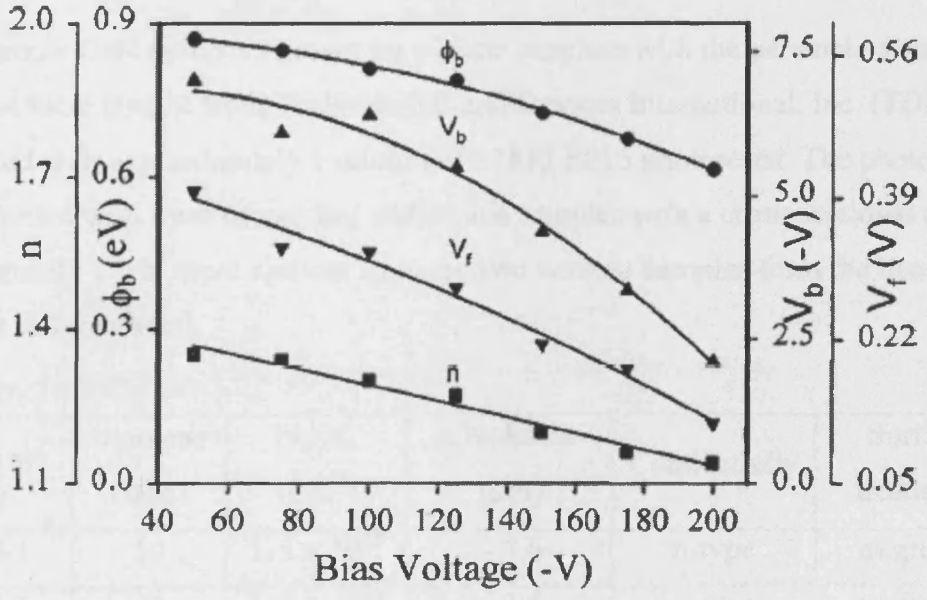

Figure 5-28 Graph showing the deterioration in (from top) Schottky barrier height, breakdown voltage, forward turn on voltage and ideality factor of Ni/Au Schottky diodes when the dc bias of the inductively coupled plasma used to etch the surface beneath the contact is varied [271].

5.4 Experimental work

5.4.1 Introduction

The motivation for the experiment was the perceived lack of studies of the selectivity of gallium nitride (GaN) to photoresist (PR). To the author's knowledge before the work reported here there was only one published study of the selectivity of GaN to PR in an inductively coupled plasma etcher (ICP) using the BCl_3/Cl_2 chemistry [272], and this was in a magnetised ICP. In this study we used an orthogonal experimental design to optimise the etch rate of GaN and the selectivity of GaN to PR in BCl_2/Cl_2 based plasmas.

5.4.2 Experiment

Two wurtzite GaN epilayers grown on c-plane sapphire with the parameters shown in Table 5-4 were bought from Technologies and Devices International, Inc. (TDI Inc.) and coated with approximately 1 micron of S1813 SP15 photoresist. The photoresist was patterned with lines of varying widths and samples with a cross-sectional area of approximately 1 cm^2 were cleaved from the two wafers. Samples from the two wafers were not differentiated.

Sample N°	Diameter (mm)	N_d-N_a (cm^{-3})	Thickness (μm)	Conductivity	Surface treatment
AP-15-1	50	1-5 x 10^{16}	~ 3.6	n-type	as grown
AP-19-1	50	1-5 x 10^{16}	~ 3.5	n-type	as grown

Table 5-4 Parameters of the two GaN on sapphire wafers used in this etch study.

The experiment was performed in an Oxford Instruments System100 with ICP 180 at the Oxford Instruments Plasma Technology site in Yatton. A schematic of the Oxford Instruments Plasma Technology ICP 180 generator is shown in Figure 5-29. 13.56 MHz power supplies delivered power to both excite the plasma and generate dc bias.

Before the first etch was performed the chamber was conditioned with a plasma that was the same as the first etch plasma, run for fifteen minutes. Before each etch an argon based pre-etch was used to de-scum and remove any oxides from the surface. The parameters for the pre-etch are shown in Table 5-5.

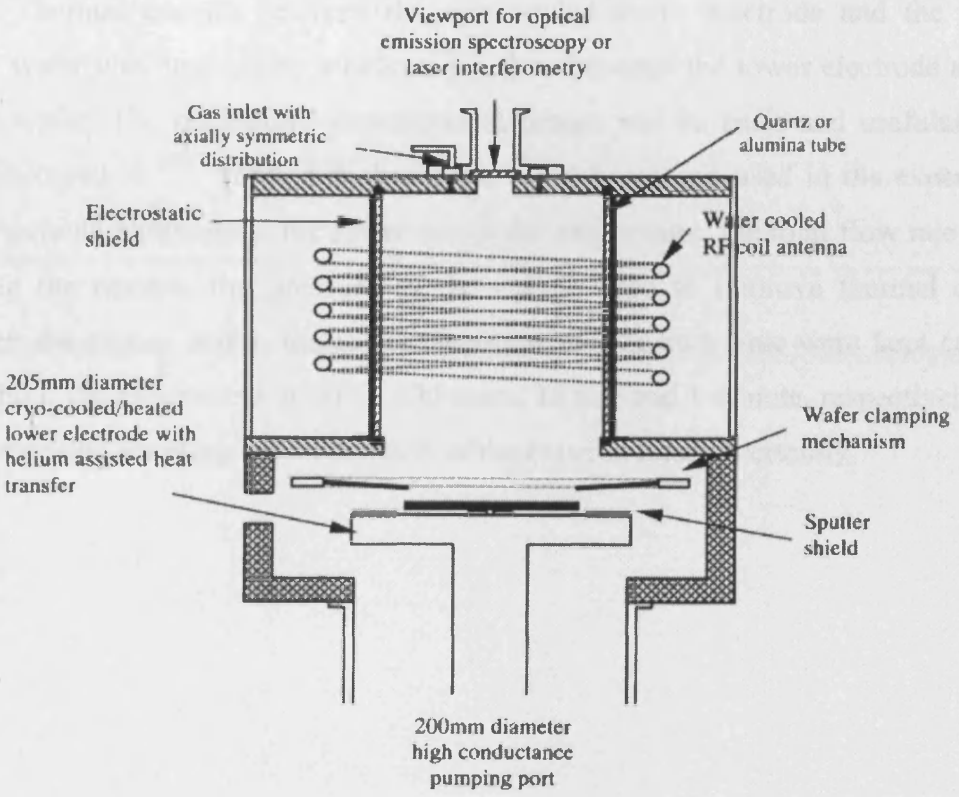

Figure 5-29 Schematic of the Oxford Instruments Plasma Technology ICP 180 Source [273]

flow rate (sccm)	ICP Power (W)	RF Power (W)	Pressure (mtorr)	Temp (°C)	He pressure (torr)	Time (sec)
50	500	125	10	10	15	30

Table 5-5 Parameters for the Ar pre-etch used to de-scum the wafer surface and remove any native oxide before the BCl_3/Cl_2 etch.

The thickness of the PR on each sample was measured at Oxford Instruments using a nanospectrometer made by Nanometrics before each etch. After each etch the etch depth was measured in several places across the sample with the PR still in place using a Sloan Dektak, the PR was then removed with acetone and the etch depth re-

measured. From these measurements we calculated the etch rate and the selectivity of GaN to PR i.e. the etch depth of the GaN divided by the etch depth of the PR.

In order to etch the samples, they were attached to a silicon carrier wafer with silicon based wafer grease, which improved the thermal contact between the sample and the wafer. Thermal contact between the cyro-cooled lower electrode and the silicon carrier wafer was ensured by a helium gas flow between the lower electrode and the carrier wafer. The orthogonal experimental design and its basis and usefulness are well discussed in [274]. Table 5-6 shows the variable settings used in the experiment. Other variable parameters: the lower electrode temperature, the total flow rate of gas entering the reactor, the pressure of the helium used to improve thermal contact between the carrier wafer, the lower electrode and the etch time were kept constant throughout the experiment at 10°C, 100 sccm, 15 torr and 1 minute, respectively. Run 2 was repeated enabling the calculation of the experimental uncertainty.

DC bias (-V)	Selectivity GaN:PR	PR Etch rate (nm/min)	Original PR thickness (nm)	PR thickness after etch (nm)	GaN Etch rate (nm/min)	Pressure (mtorr)	% Cl_2	ICP Power (W)	RF Power (W)	Run
270	1.00	115	700	585	115	5	25	500	75	1
270	0.46	195	800	605	90	10	50	600	75	2
270	0.85	130	700	570	110	15	75	700	75	3
320	0.73	110	770	660	80	15	50	500	100	4
270	0.79	330	780	450	260	5	75	600	100	5
315	0.57	115	700	585	65	10	25	700	100	6
350	0.58	190	740	550	110	10	75	500	125	7
360	0.20	50	700	650	10	15	25	600	125	8
327	0.59	488	800	312	286	5	50	700	125	9
270	0.69	160	820	660	110	10	50	600	75	Rpt 2

Table 5-6 Each run is a set of parameters that constitute one etch with one set of results resulting from each run.

5.4.3 Experimental Results with the ICP 180

From [274] the average of the results gained at each variable setting e.g. RF power at 75 W may be plotted in order to see the affect of varying a parameter, here RF power, on any measurable outputs. The dependence of the GaN etch rate, PR etch rate, dc bias, and selectivity output averages on RF power, ICP power, pressure and $\%Cl_2$ are plotted in Figure 5-30 to Figure 5-33. The lines shown in these graphs are there as a guide to the eye only. The uncertainties calculated using Equation 5-10 and the results from Run 2 and its repeat are ± 10% for etch rate, ± 20% for the selectivity and ± 2% for the dc bias. In the graphs shown here the uncertainty is shown as ± 10% for the etch rate ± 20% for the selectivity and ± 2% for the dc bias. A major source of this uncertainty is believed to be the Dektak measurements, the reason for the large uncertainty was the small depths etched in the one minute etch time. Because the features etched were very small, the roughness of the surface and of the photoresist was significant compared to the depth of the feature making accurate measurement of depths difficult. Larger depths would be facilitated by a longer etch time but this etch time is limited by the selectivity of the etch to gallium nitride over photoresist and the photoresist thickness.

$$\text{Uncertainty} = \frac{\text{highest result - lowest result}}{\text{highest result + lowest result}} \quad \text{.....Equation 5-10}$$

As shown in Figure 5-30 our results showed that as RF power was increased from 75W to 100W the etch rate of GaN increased but then showed no significant increase when the RF power was increased from 100W to 125W, this was despite the monotonic increase in dc bias that was observed as the RF power was increased. The etch rate of the photoresist increased as the RF power increased. The difference between the etch rate of the GaN and the etch rate of the PR led the selectivity of GaN to PR remain the same within experimental uncertainty and then decrease when the RF power was increased to 125W.

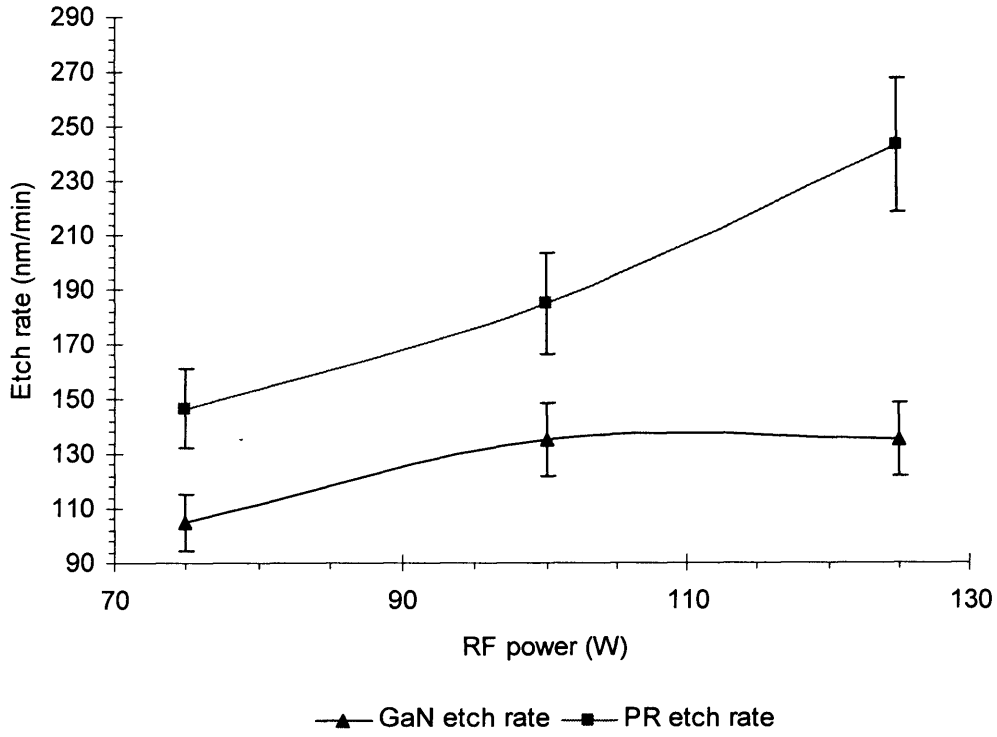

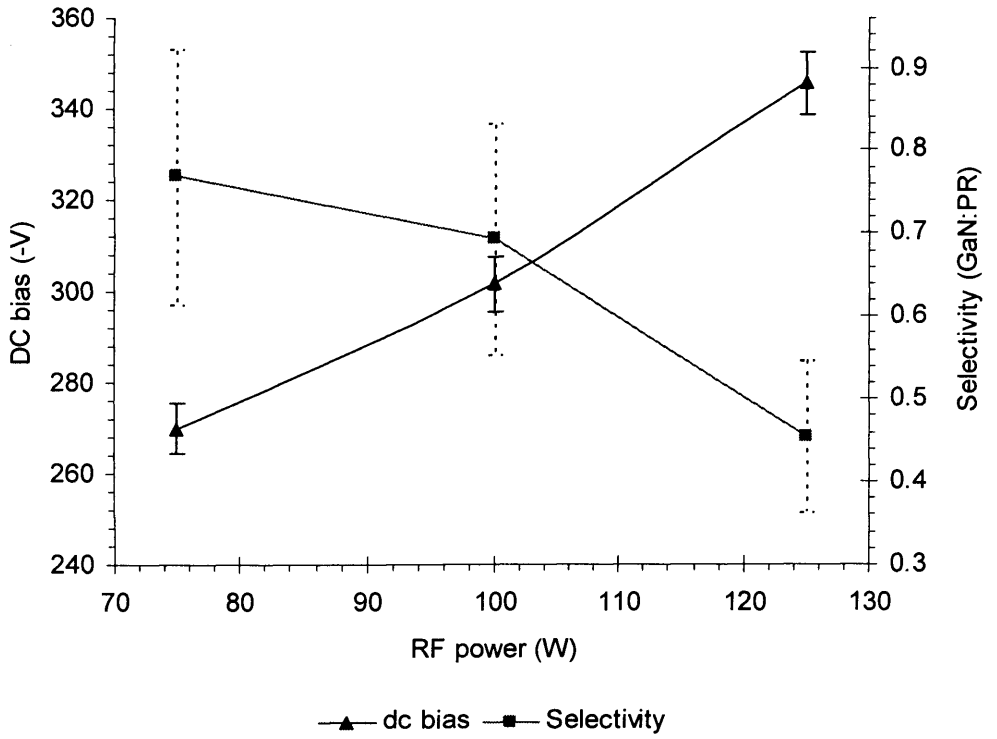

Figure 5-30 Top, GaN etch rate and PR etch rate as a function of RF power; below, the dc bias and selectivity for the same runs; the uncertainty shown for the etch rates, selectivity and dc bias is ± 10%, ±20% and ±2%, respectively.

As shown in Figure 5-30 the etch rate of GaN did not increase monotonically with RF power as would be expected from previous results published in the literature, other results taken with the ICP180 when the other variables were held constant (see Section 5.4.4) and the etch rate variation of the photoresist seen in the same graph. This could be due to the increase in dc bias having less effect at higher values once a certain threshold is passed; also, there could be a linear variation that is obscured by the large experimental uncertainty associated with the data coupled with the small variation of the GaN etch rate over the range of these variables.

When one looks at the original results more closely, one can see that the reason for the plateau in the average etch rate shown is the abnormally low etch rate of run 8 where the other parameters were 600W ICP, 25% Cl_2, 15mtorr (125W RF power). This could have been a mistake, except that the result was re-taken and a result similar to that shown discovered; so what could be the cause for the low etch rate? On studying the results further we see that run 8 is the only run to have the combination of 25% Cl_2 and 15mtorr pressure. As is seen in Figure 5-32 and Figure 5-33, 25% Cl_2 and 15 mtorr pressure both led to low etch rates. If one looks at those results where the %Cl_2 was 25% and examine how the etch rate varied as a function of pressure it is observed that at 15 mtorr the etch rate was 10 nm/min, at 10mtorr the etch rate was 65 nm/min and at 5 mtorr the etch rate was 115 nm/min. This was despite the fact that the last result had both the lowest RF and the lowest ICP power of the three results. Similarly if one looks at just the results with 15mtorr of pressure and vary the %Cl_2. At 25% Cl_2 the etch rate was 10 nm/min at 50% it increased to 80 nm/min and at 75% Cl_2 the etch rate increased to 110 nm/min; this was again despite some changes in RF and ICP power that we would expect would act against such a trend. Indeed if we look at the variation in the results as set out in Table 5-7 then it is clear that the higher results are confined to the top right hand corner (the result at 5 mtorr and 50% Cl_2 was made with 125W RF power and 700W ICP power, whereas the 5mtorr and 75% Cl_2 result was taken at 100 W RF and 600W ICP power). Similar behaviour is observed for the photoresist though with the effect less marked (see Table 5-8).

	25%	50%	75%
5 mtorr	115	286	260
10 mtorr	65	90	110
15 mtorr	10	80	110

Table 5-7 Showing the variation in the etch rate of gallium nitride observed when only pressure and $\%Cl_2$ are examined and the other variables discounted.

	25%	50%	75%
5 mtorr	115	488	330
10 mtorr	115	195	190
15 mtorr	50	110	130

Table 5-8 Showing the variation in photoresist observed when only pressure and $\%Cl_2$ are examined and the other variables discounted.

This effect is not caused by changes in the dc bias; as is made clear in Table 5-9 the dc bias does not exhibit any pattern of values.

	25%	50%	75%
5 mtorr	270	327	270
10 mtorr	315	270	350
15 mtorr	360	320	270

Table 5-9 Showing the variation in dc bias observed when only pressure and $\%Cl_2$ are examined and the other variables discounted.

So, in essence what the anomalous RF power result is telling us is that there is a strong underlying effect caused by the combination of $\%Cl_2$ and pressure that is stronger than the effect of RF power on the etch rate.

The above reasoning implies that the increase in etch rate must be due to something other than the ion flux to the wafer or the dc bias i.e. the effect must be of a chemical nature with a decrease in a certain reactive gas species caused by the combination of a low % Cl_2 and a high pressure (from Table 5-7 it seems that the decrease in pressure

or the increase in $\%Cl_2$ both independently act somewhat to mitigate the combined effect).

The above combination effect, due to the nature of the experiment, will have affected all the results and needs to be taken into consideration when analysing the rest of the results. In order to avoid such combination effects separation between the variable settings should be as large as possible in orthogonal design experiments; however, in this experiment where a high selectivity was desired, seeming to demand low powers, the choice of parameters was deliberately limited to values that were thought likely to give a high selectivity.

Figure 5-31 shows the etch rate of gallium nitride and photoresist, the selectivity and the dc bias varied as a function of ICP power. As may be seen, the etch rate of the photoresist increased linearly as a function of ICP power whereas the etch rate of GaN does not increase quite linearly, with the increase from 500 to 600W less than that from 600 to 700W. This non-linear behaviour is possibly caused by the anomalous run 8 as already commented on; such an adjustment to make the variation of the etch rate of GaN linear would require an increase in etch rate observed at 600W to 127 nm/min from 120 nm/min; such an increase would lead to the selectivity showing no variation within experimental uncertainty as a function of ICP power. Similarly if the GaN etch rate as a function of RF power is made to increase linearly the selectivity as a function of RF power seems to decrease linearly though truly this is obscured by the large experimental uncertainty. To get the GaN etch rate as a function of RF power to increase linearly, the etch rate must be increased by approximately 25 nm/min this is compared to only 7 nm/min for the ICP power. This seems to indicate that ICP power seems to act to mollify the effect of the combination of a high pressure and a low $\%Cl_2$.

The dc bias as a function of ICP power would be expected to show a monotonic decrease as the ICP power was increased, as may be seen in Figure 5-31 this is not observed and again this is assumed to be an artefact of the experimental design though again the uncertainty in the results would allow for a linear variation.

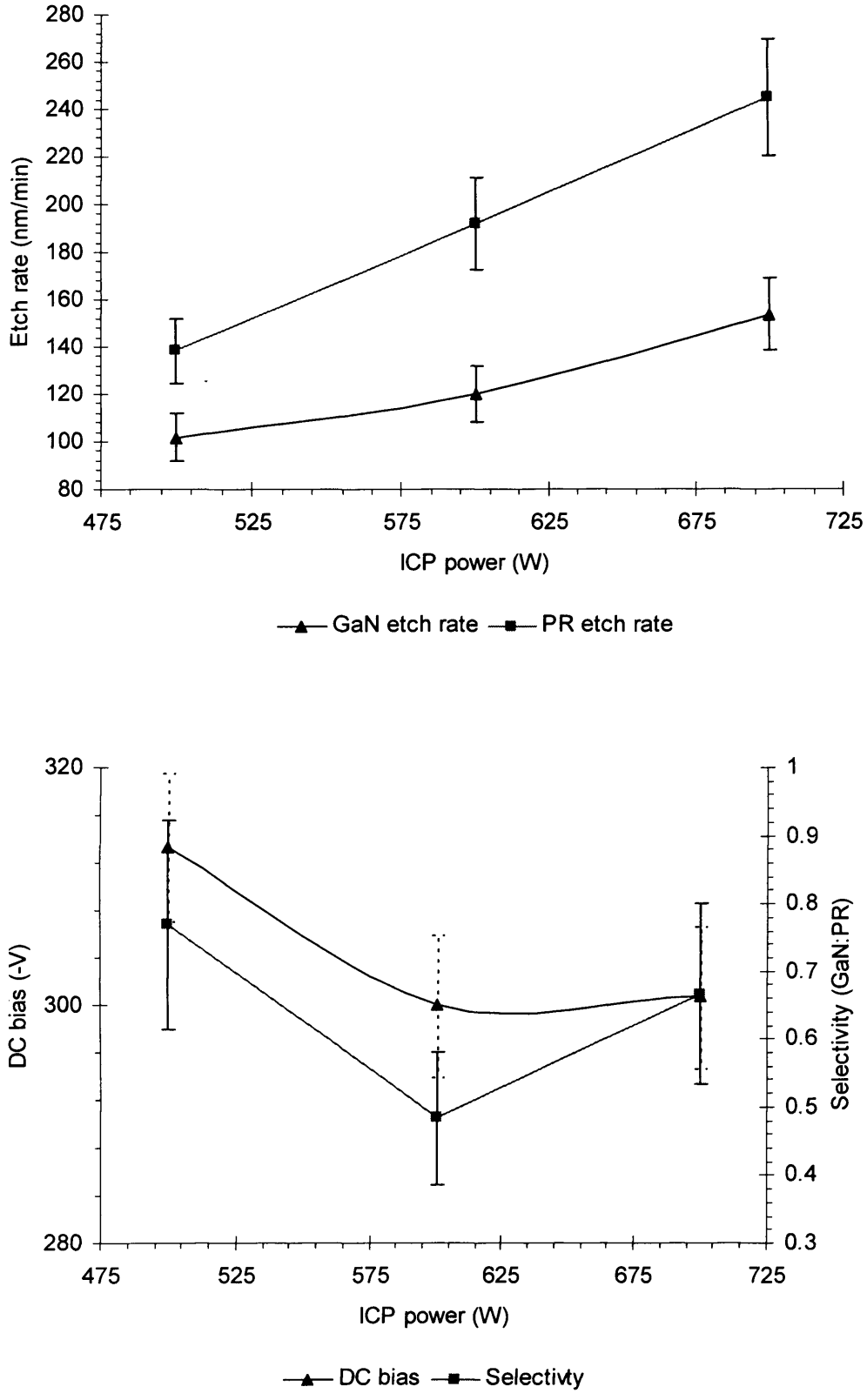

Figure 5-31 GaN and PR etch rate (top) and dc bias and selectivity (bottom) as a function of ICP power.

The variation of the etch rates and selectivity, as well as the dc bias as a function of pressure are given in Figure 5-32. The variation of the etch rates follows approximately the same trend being, oddly enough, approximately the inverse of the variation shown by the dc bias. As dc bias is inversely proportional to the flux to the wafer this would suggest that the flux to the wafer or the reaction or desorbtion of etch products at or from the surface respectively limits the etch rate in this case. However, in the graph of the etch rate of GaN as a function of pressure, it can be seen that the etch rate increases by approximately 140nm/min for a decrease in dc bias of approximately -20V (a pressure decrease from 10 to 5 mtorr). This increase in etch rate is much greater than any of the increases seen for RF or ICP power suggesting that the dc bias is not the only factor at work. From [201] at 1 mtorr the number of gas molecules in 1 micron cubed is approximately 35, it could be that at higher pressures, recombination of molecules limits the number of reactive radicals. Recombination of electrons and ions limits the ion numbers, and the decreased mean free path of atoms increases the number of collisions in the dc bias sheath causing a reduced efficacy of the power used generating the plasma and the dc bias. The increase in the etch rate as the pressure decreases was seen in other experiments (results from which are given below) and seems to be a valid, reproducible phenomenon in BCl_3/Cl_2 plasmas generated in Oxford Instrument ICPs; however, in the experiments shown below the increase was quasi-linear.

The variation of the measured parameters (GaN etch rate, dc bias etc.) as a function of $\%Cl_2$ is shown in Figure 5-33. The dc bias is seen to decrease linearly as the $\%Cl_2$ in the plasma is increased, this implies that the increase in the $\%Cl_2$ is increasing the ion flux to the substrate. This could be due to the slightly smaller ionisation energy of chlorine gas compared to boron tri-chloride gas molecules (11.5 cf 11.6 eV [275]) or due to the different cross sections or the fact that the more energy will be lost disassociating BCl_3 in BCl, BCl_2, B with little consequence for the etch. The etch rates of both the PR and the GaN, however, do not show linear behaviour with both etch rates increasing as the $\%Cl_2$ is increased, peaking or plateauing at 50%. This indicates that in this case it is chemical effects, such as the amount of Cl radical, rather than the dc bias or ion flux that are the dominant factors in determining the etch rate.

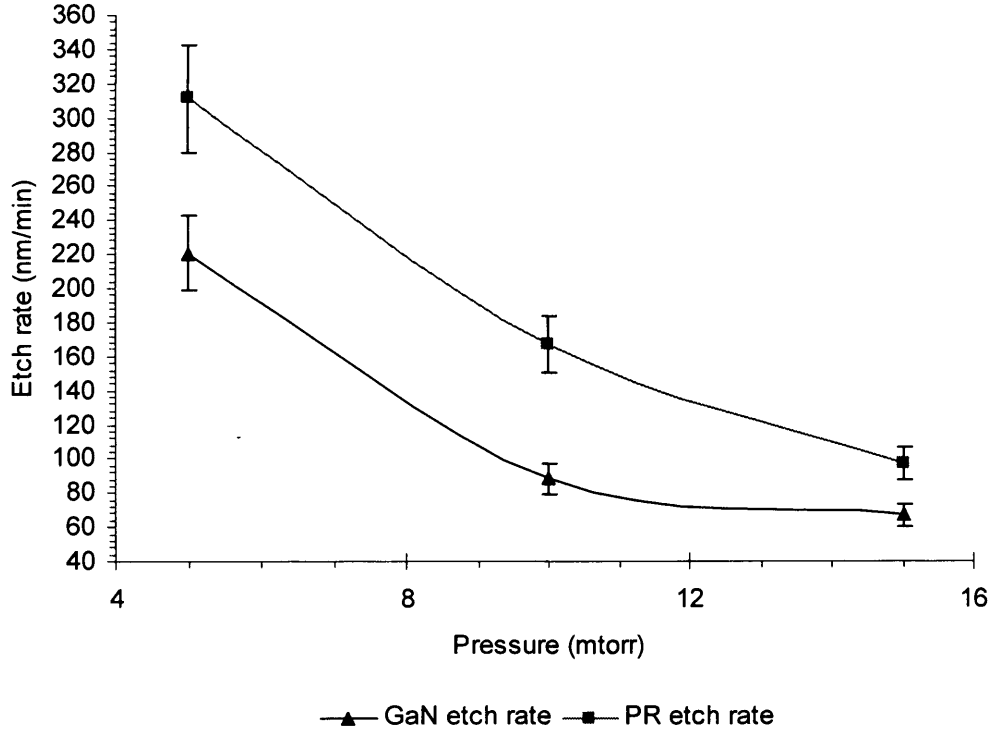

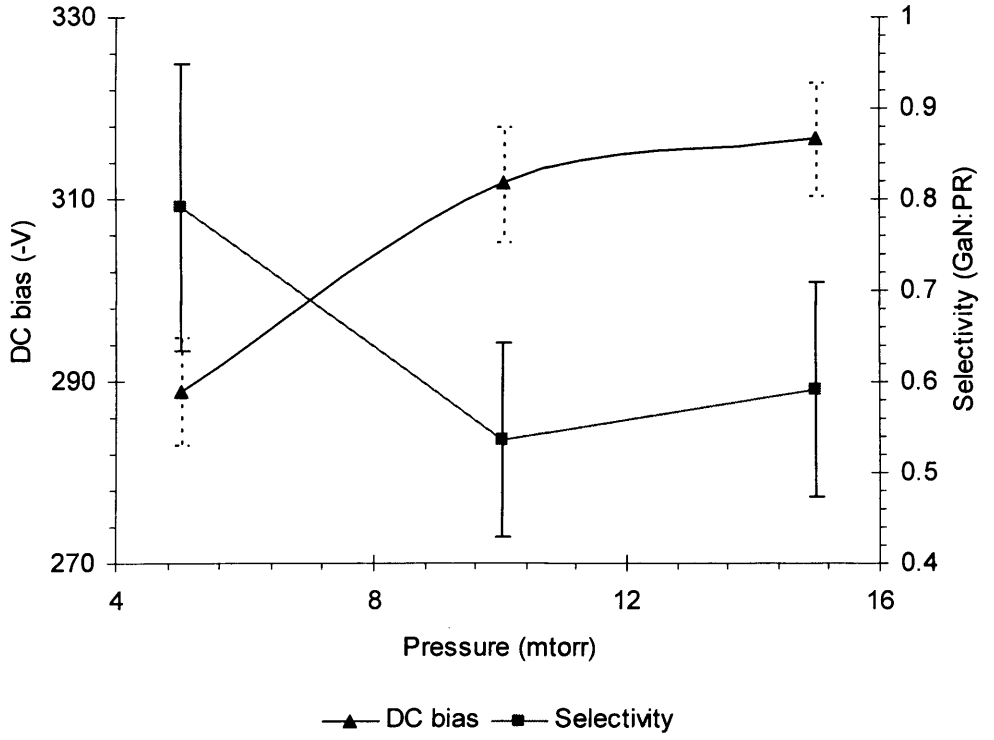

Figure 5-32 Graphs of the observed variation of the etch rate of GaN and PR as a function of pressure (top) and the dc bias and selectivity as a function of the same variable (bottom). Uncertainty is as in the other graphs of this experiment e.g. Figure 5-31.

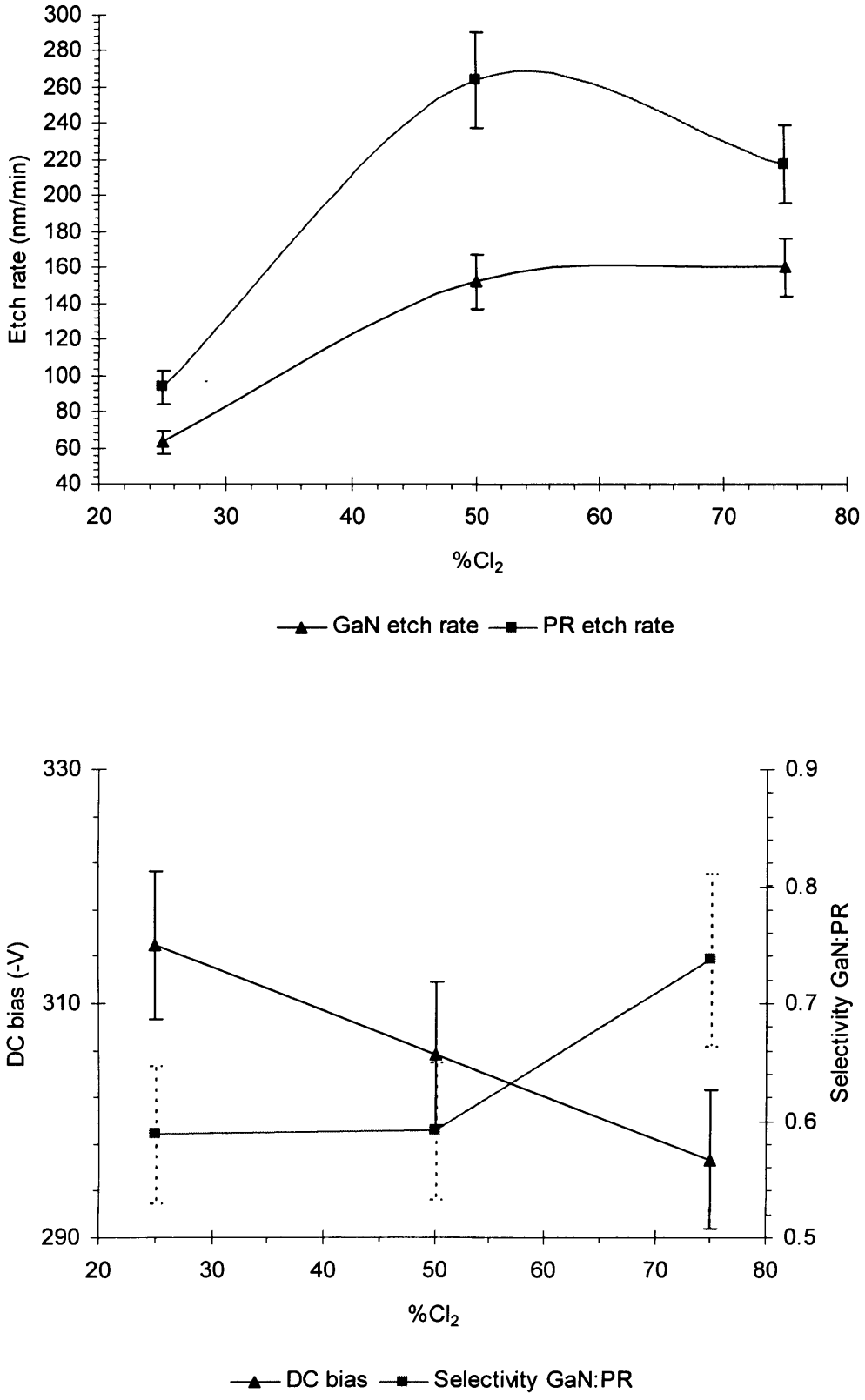

Figure 5-33 Selectivity and dc bias (bottom); PR and GaN etch rate (top) as a function of the $\%Cl_2$ in the feedstock gas used in the plasma, uncertainty is 10% for the etch rates, 20% for the selectivity and 2% for the dc bias.

Interestingly, in the other work presented below that investigated the efect of the $\%Cl_2$ on the etch rate of both GaN and PR an almost linear increase in the etch rates as the $\%\ Cl_2$ was increased was exhibited.

Addition of BCl_3 to a chlorine plasma has been shown to improve the anisotropy of the etch for GaP and GaAs [276]. This is thought to be due to BCl_3 forming a polymer on the surface of the material being etched, acting to inhibit the horizontal etch. In this same study, however, the addition of BCl_3 to a plasma used to etch GaN did not improve the anisotropy of the etch which was near perfect even without BCl_3 addition. This is thought to be due to the higher bond strength of GaN as compared to GaAs or GaP meaning that little etching occurs without an ion flux to break the bonds to allow etching.

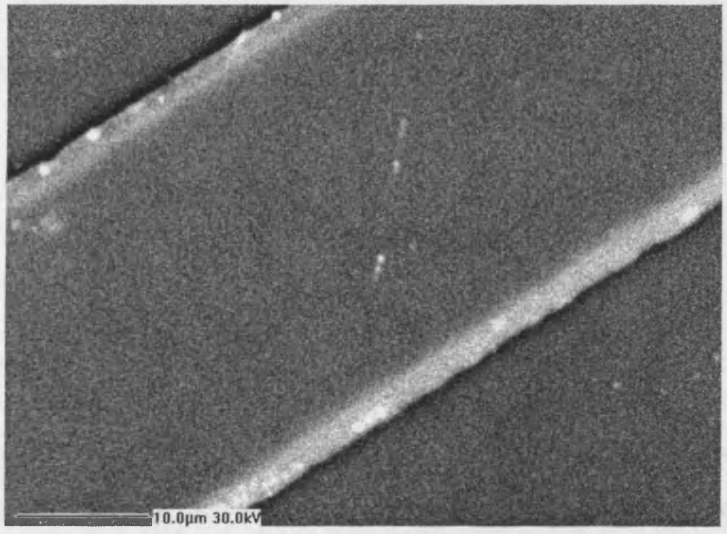

Figure 5-34 Image of the GaN surface etched with the optimised etch for two minutes.

Figure 5-34 shows an scanning electron microscope (SEM) image of the surface of the gallium nitride etched with an etch that was a combination of the parameters used to find the above trends in etch rate, selectivity and dc bias; this plasma was the optimum etch that was found following the method of Yin and Jillie [274] and gave an etch rate of 215 nm/min and the selectivity of GaN to PR of 0.81 both of which were above the expected values calculated from the non-optimised results. The parameter settings of the optimised etch was a RF power of 50W, an ICP power of 700W, a pressure of 10 mtorr and a $\%Cl_2$ or 75%. As may be seen, the side walls of the etch

were quite rough and far from vertical, this almost certainly due to the photoresist mask used to pattern the sample rather than any other factor. The SEM image in Figure 5-34 is of a sample that was etched for two minutes, all the other samples from which data was taken were etched for just one minute. As may be seen from Figure 5-34 the etch depth even after two minutes with one of the faster etches of which measurements were taken the etch depth is still quite shallow, it is this shallowness of the etches that is a major cause of the uncertainty in the results as at this depth Dektak measurements are plagued with signal noise that is a significant proportion of the actual etch depth, this of course implies that the slower etches have a larger uncertainty in their etch rate values than the faster ones.

5.4.4 Further Results

The plasmas observed with the orthogonal experimental design did not yield very high etch rates. Further experiments were performed to increase the etch rate of gallium nitride by increasing the RF power and ICP power while keeping the other parameters at their optimised values. The results of these two sets of experiments are shown in Figure 5-35 to Figure 5-38.

As can be seen, the etch rate of both gallium nitride and photoresist seemed to increase linearly with power applied both to the ICP coil and to the lower electrode, this is as would be expected. In the case of increased RIE power, the dc bias increased linearly and in the case of ICP power the dc bias decreased linearly again, as would be expected. Interestingly the selectivity in both cases remained constant within experimental error. It should be noted that because the etch depth in these etches was much greater, the uncertainty in the Dektak measurement is much reduced, hence, the uncertainties used here are smaller than those shown for the previous etches. To further increase the etch rate a single etch was performed with an ICP power of 1700W and an RF power of 225W (a d.c. bias of –465V) with the other parameters set to their optimum values. This etch gave an etch rate of 660 nm/min with a selectivity of 0.9 - much higher than would have been expected from the other results. Figure 5-39 shows an SEM image of the GaN etched with this higher power etch for a minute and a half.

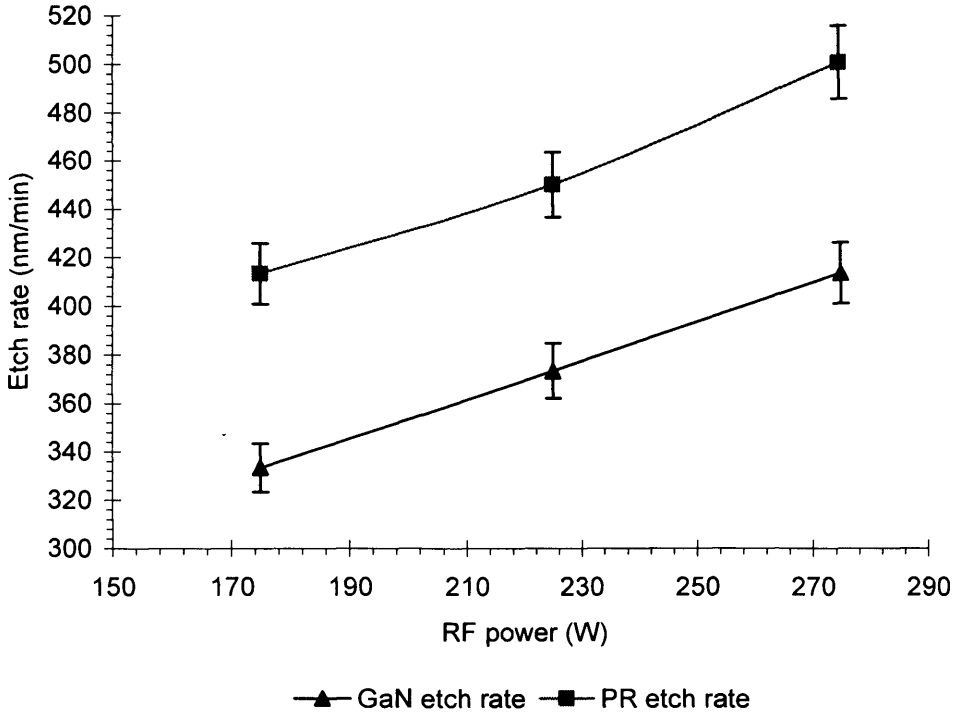

Figure 5-35 graph of the etch rate of gallium nitride and of photoresist (PR) as a function of RF power. Uncertainty is shown at ± 3%.

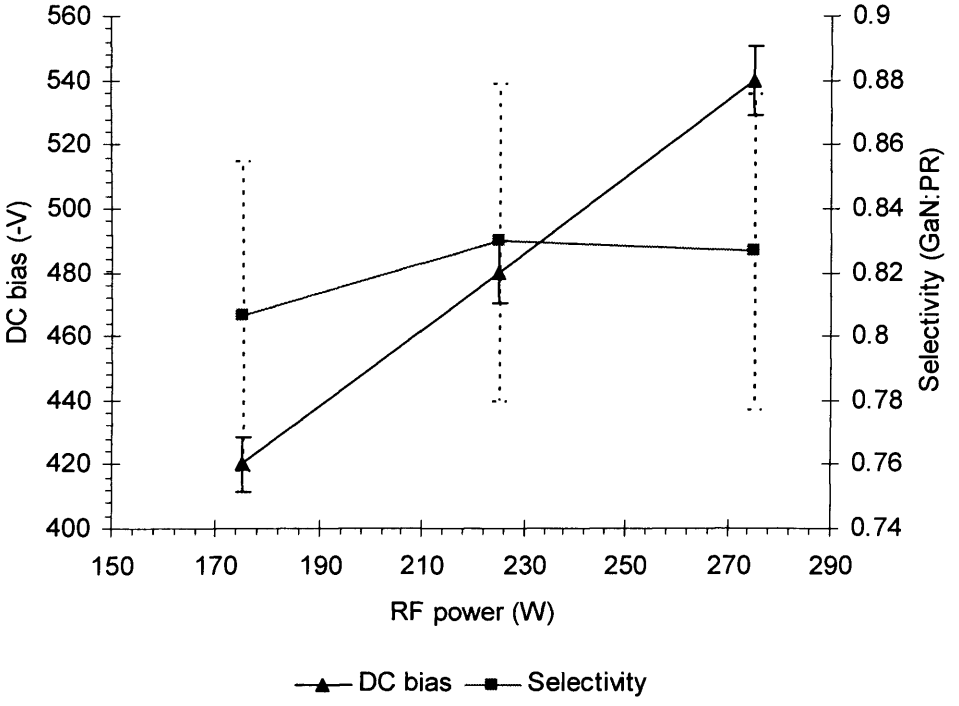

Figure 5-36 graph of the dependence of dc bias and selectivity of GaN over PR on RF power. Uncertainty is shown at ± 6% for the selectivity and ± 2% for the dc bias.

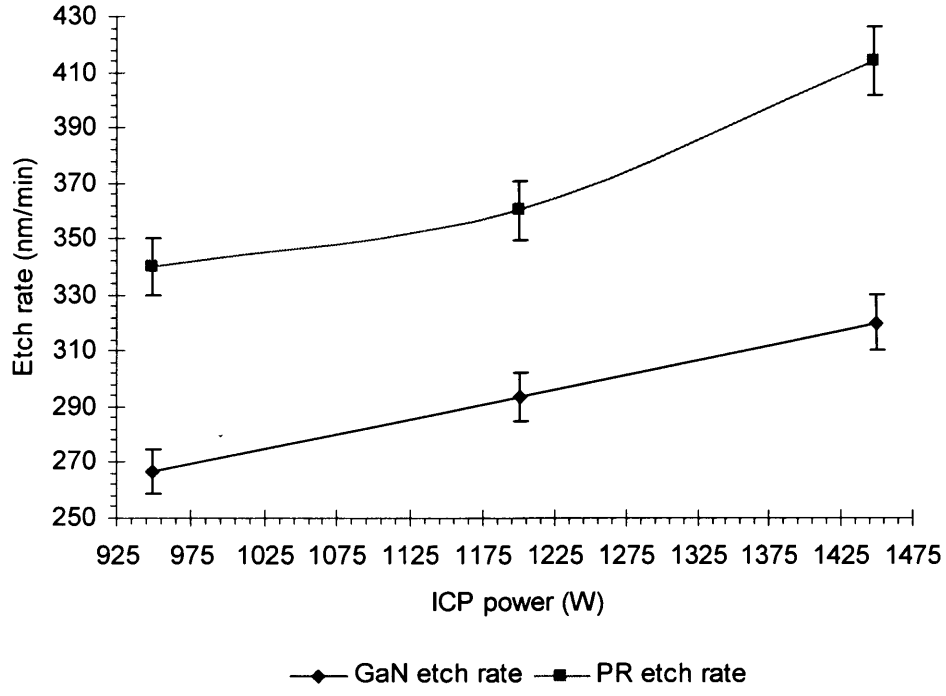

Figure 5-37 graph of the etch rates of gallium nitride and photoresist as a function of ICP power. Other factors were held constant; experimental uncertainty is shown at ± 3%.

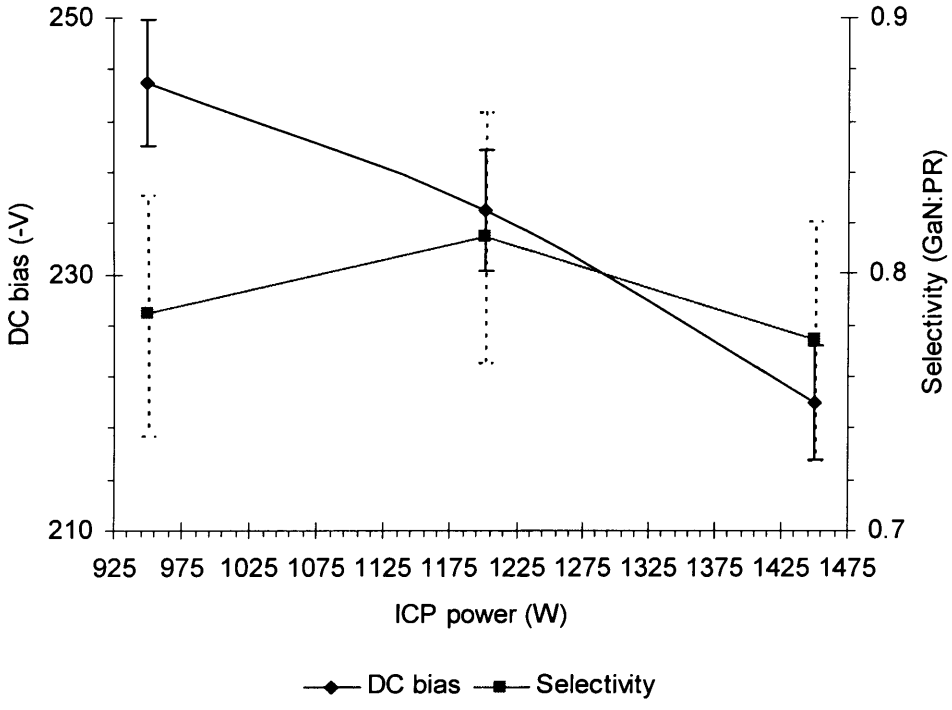

Figure 5-38 graph of selectivity of GaN over PR and dc bias as a function of RF power, flow rate, %Cl_2, pressure and table temperature were held constant at 75W, 100 sccm, 50%, 5 mtorr and 10°C, respectively. Uncertainty is shown at ± 6% for the selectivity and ± 2% for the dc bias

The roughness of the sidewalls is again attributed to mask roughness or striations caused by ions striking the photoresist sidewall.

Several stages were carried out differently between the original orthogonal experiment and these additional etches. Firstly, as the etches used higher power the need for the argon pre-etch was no longer as pressing and in fact, no argon pre-etch was used. A second difference was that a new photoresist was spun on and patterned for this second set of experiments in order to avoid any effects of photoresist degradation over time. It is believed that the procedure followed both times was the same; however, in the original experiment photoresist was spun onto the entire wafer whereas in the later experiments the photoresist was spun onto the approximately one centimetre-squared samples one at a time. There was a noticeable difference in the quality of the two masks, possibly due to the way they were handled during transit. The improved selectivity seen in the experiments could be due to the method used to pattern the samples or it could just be an effect of the higher powers used or the lack of argon pre-etch.

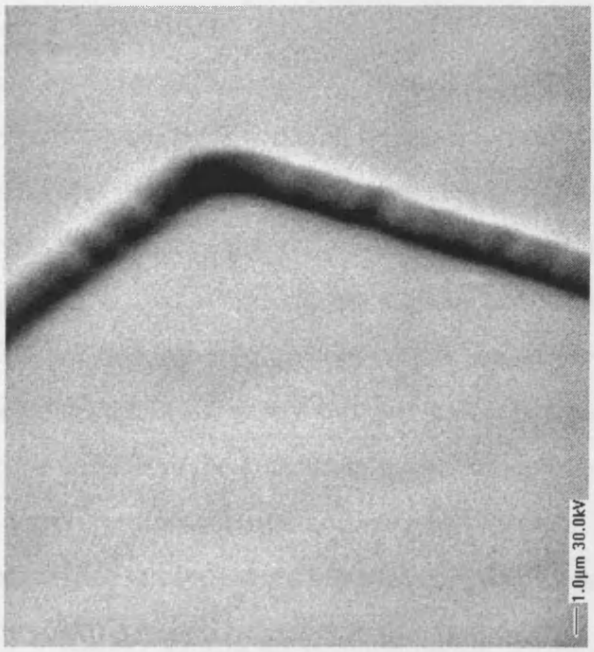

Figure 5-39 The pattern produced with the ICP380 parameters 50%Cl_2, 50% BCl_3, 5mtorr pressure, 100sccm total flow, 1700W ICP power and 225W RF power; table temperature was 10°C.

The orthogonal experimental design is well suited for systems like the ICP etcher where there is a vast parameter space where the result of varying one parameter is not necessarily independent of the level of another. Because of the way the effect of each variable is calculated when using the orthogonal experiment design i.e. from results taken without true control of the non-variable parameters. If a trend is seen, it is a trend that expands throughout a multi-parameter space rather than just a trend seen at a particular set of values. In this respect the orthogonal experimental design saves far more samples than it seems to at face value, as to gain such a picture of the trends over such a large parameter space with one dimensional searches would take vast numbers of samples. However, as has been noted above and in the paper by Yin and Jillie, by varying the other parameters whilst varying the variable whose effect is being studied, the effect of the variable can be diluted; hence, the strength of this method is also its weakness and it is very important that, with the orthogonal experimental design, a significant spacing is left between parameter settings so that combination effects do not obscure the true effect of varying a parameter. Even if such precautions are taken it will never be possible to be 100% certain of results which are statistically derived from other measurements.

The decision to use the orthogonal experimental design depends on the requirements of the data. If a multi-parameter space needs to be characterised as quickly as possible for global trends then, if it is possible to space parameter settings so that other factors are not likely to obscure the effect of the variables, then the orthogonal experimental design may be used providing that 100% accuracy of the results is not required. However, if results that are one hundred percent certain are required then the traditional one-dimensional searches, where one parameter is varied and all others held constant, should be used. It is the authors opinion that orthogonal experimental design is a powerful experimental technique when used correctly, the above data are flawed because the parameter settings were not spaced apart enough and the etch depth was too shallow making experimental uncertainty too large.

5.4.5 Comparison of the Results with the Literature

In the most directly comparable study (Lee et al. [272]) the best result measured was an etch rate of 400 nm/min with a selectivity of gallium nitride over photoresist of 2.1. This result was found at 100% BCl_3 using permanent and electro-magnets to condition the plasma. The best result they found without the use of magnets to condition the plasma was an etch rate of approximately 200 nm/min coupled with a selectivity of GaN to photoresist of approximately 1.4.

In their study Chang, Liu and Jeng [272] looked at the selectivity of GaN to nickel (Ni), silicon dioxide (SiO_2) and PR masks in $BCl_3/N_2/Ar$ plasma. Their best result for the GaN masked with PR coupled an etch rate of approximately 400 nm/min with a selectivity of 1.65; however, the selectivities for the Ni and SiO_2 were much greater, at best 15 and 5.6 respectively.

In their more recent study Kim et al [277] were able to couple an etch rate of 640 nm/min with a selectivity of 1.5 whilst maintaining reasonable etch anisotropy in an inductively coupled BCl_3/HBr plasma. In the other plasmas that Kim et al. investigated, Cl_2/HBr and HCl/HBr, the selectivity was always below 0.8. In their study Kim et al used a very high ICP power, 1600W, a moderate dc bias, –150V, a low temperature, 3°C, and a high flow rate of 100 sccm whilst pressures were maintained at approximately 10mtorr

5.4.6 Experimental results with the ICP 380

The above work on the ICP 180 had been undertaken in order try and develop an etch which yielded a high selectivity of GaN over PR. Further result were needed to characterise the etch rate of GaN and selectivity of GaN over PR of plasmas generated by the ICP 380 at Cardiff University. Due to the above problems that were encountered with the orthogonal experimental design it was decided that it would be better if reliable results were taken and the one-dimensional search methodology was adopted for these experiments.

To measure the etch rates of the gallium nitride and photoresist in this experiment a different method of measurement was used to that in the experiments with the ICP180. The ICP 380 was equipped with a laser interferometer that could be used to measure the etch rate of transparent films with the reflections from the top surface and any underlying material interfering destructively and constructively in varying amounts as the surface was etched closer to the underlying material. This variation of constructive and destructive interference is registered as a sinusoidal wave that progresses as the material is etched. If the thickness of the layer was known then one sample could be etched until the sinusoidal oscillation ended (a non-transparent material is reached) or the signal changed significantly (interface between two different transparent materials) and the total etch depth could then be divided by the number of oscillations observed to give the etch depth for each oscillation. Once the etch depth of each oscillation is known (it was 0.144 μm/osc for the GaN used here and 0.198 μm/osc for the photoresist) the time taken to etch from one peak to the next (one oscillation) could be measured (the time taken is actually recorded above the sine wave trace and correlated to the peak with a ruler) and used to calculate the etch rate of the plasma that is being used. In this way for a single sample many measurements can be taken (in this case the GaN used was over 3 microns thick and the entire set of sixteen results was taken on only two samples).

In order to calculate the etch depth per oscillation for the photoresist used, one quarter of a three inch silicon wafer was patterned with thick S1813 SP15 (~1.4 μm by using two 4000rpm spin-ons with 3min 97°C bakes after each spin-on). Samples of rectangular shape ~ 5mm by 8 mm were cleaved from this wafer and one patterned and used to measure the etch depth of the photoresist with the Dektak. Once the photoresist thickness was known the sample was etched until all the photoresist was removed which took eight minutes. The depth per oscillation was then calculated. The depth per oscillation for gallium nitride was found by patterning one sample with thick S1813 SP15 photoresist in the same way as the silicon; however in this case the above method yielded a photoresist thickness of greater than 1.6 μm. This sample was then etched for eight minutes and the etch depth measured by the Dektak; the measured etch depth was then divided by the number of oscillations recorded to find the depth per oscillation. All the samples were of approximately the same area though

the difficulty of cleaving GaN on sapphire substrates meant the equivalence was only approximate.

Once the depth per oscillation for the photoresist and the gallium nitride had been calculated for each set of etch parameters, enough of the material was etched to yield two clear peaks or troughs in the interference pattern for each plasma. The time taken to etch between the two peaks or troughs was measured and the etch rate calculated from the etch depth per oscillation for each plasma. In this set of experiments the etch rate was measured as a function of RF power, ICP power, % Cl_2 in the BCL_3/Cl_2 plasma, pressure and flow rate. As trends in the etch rate and selectivity were being sought, parameters were spread from the lowest levels used to the highest, four values of each parameter were used to give a better idea of any trend than the three values used in the ICP 180 study. The control values for this experiment were 175W RF power, 1250 W ICP power, 67% (0 dp) Cl_2, 15mtorr pressure and 24 sccm flow rate. When one of the parameters was varied, all the other parameters were held at their controlled values. Run-to-run uncertainty was calculated from a repeat of the measurement of the controlled plasma (all the parameters set at their control values). The the fourth and seventeenth etches for both the GaN and PR were controlled etches. The uncertainty for both the GaN and PR etch rates was found to be ±1%, which actually did not show up on the graphs. The uncertainty in the selectivity is shown as ±2%.

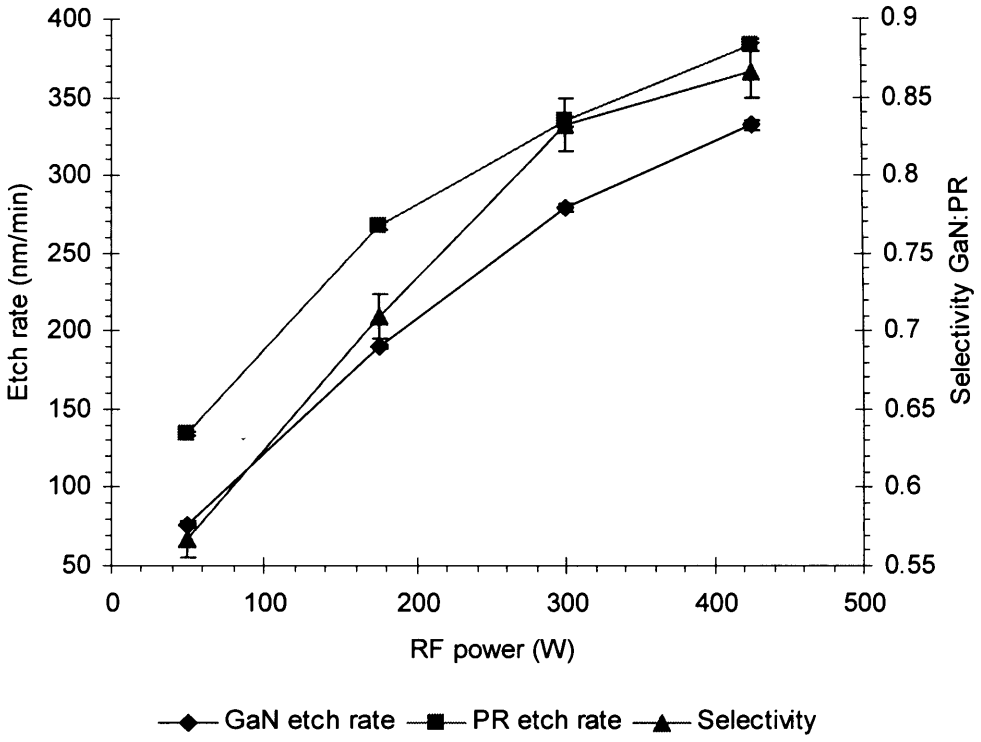

Figure 5-40 Graphs of the etch rate of GaN and PR and the selectivity of GaN over PR as a function of RF power

The results as a function of RF power are given in Figure 5-41, as can be seen the etch rates and selectivity follow the same basic pattern, increasing monotonically but with a slightly slower rate at higher powers than at lower powers. If it were not for the high precision of the data it would be tempting to say that the true, linear, nature of the results was obscured by experimental uncertainty; however, due to the small uncertainty in the results and the large range over which the results are taken this reduction in the rate of increase of the etch rates and selectivity as the etch rate is increased is assumed to be due to the decreased efficacy of the etch at higher powers, due to the increased power hampering as much as aiding the etch process by dislodging reactants or hindering reactions. It could thus be possible that if the RF was increased even further that a stage would be reached where the etch rates would start to decrease as the RF power was increased as the chemical component of the etch was no longer effective and the etch became predominantly physical (sputtering or chemical reactions alone yielding much slower etch rates than the combined action of both etch mechanisms). It was quite surprising that the selectivity increased as the

etch rate and RF power was increased, normally the opposite would be expected (as was found on the study with the ICP 180).

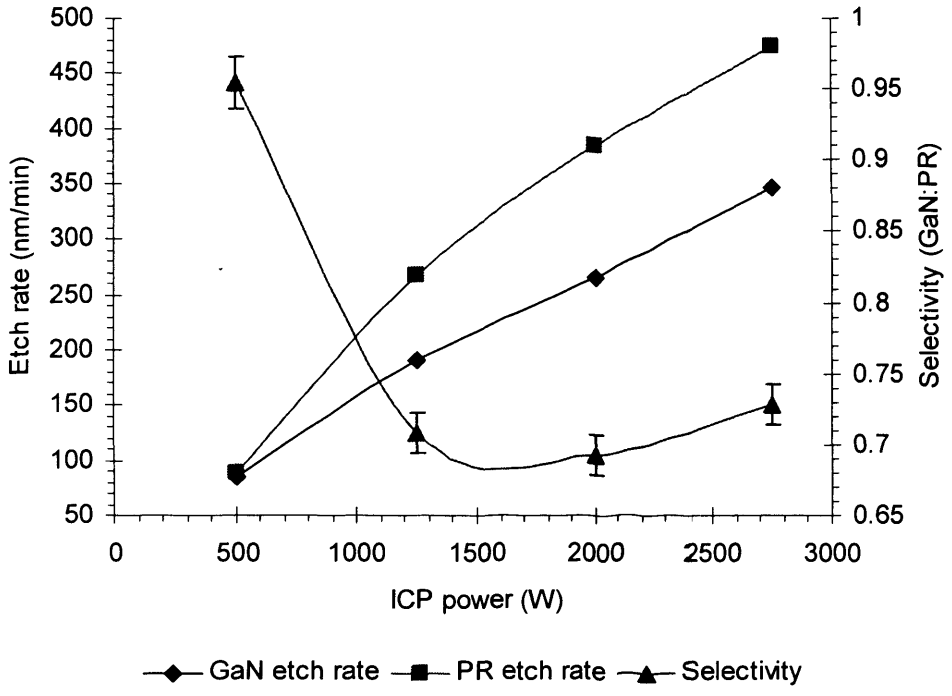

Figure 5-42 graph of the selectivity of GaN over PR and the etch rates of PR and GaN as a function of ICP power.

The effect of increasing the ICP power on the measured parameters is shown in Figure 5-42, as may be seen again the etch rates are seen increasing as a function of the power inputted to the coil; however this time the etch rate of the photoresist jumps from being near to that of the gallium nitrides at 500W to being higher at 1250 W, from this point on the etch rate of GaN and the PR increases at approximately the same rate, this is shown by the change in the selectivity which drops sharply from a high of over 0.9 to around 0.7 where it remains approximately constant as the ICP power is increased. This change in the selectivity or the rate at which the two materials are etched again can be attributed to the softness of the PR which responds to a much greater degree to the increase in the ICP power at lower powers than the tougher GaN which begins to respond in a manner equivalent to that of the PR at higher powers as seen.

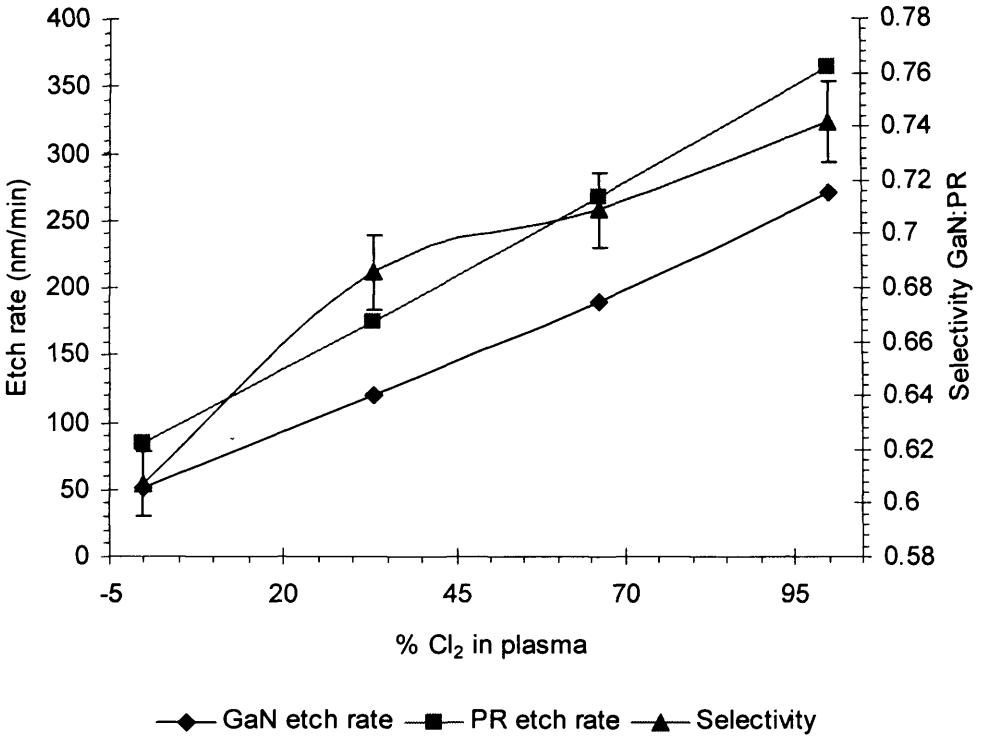

Figure 5-43 Etch rate of photoresist (PR) and gallium nitride (GaN) as a function of the $\%Cl_2$ in the plasma, the selectivity of GaN over PR (the etch rate of GaN ÷ the etch rate of the PR) is also shown

The dependence of the etch rates and selectivity on the $\%Cl_2$ in the plasma is given in Figure 5-43, the etch rate of both the photoresist and the gallium nitride increase as the percentage of chlorine in the feedstock gases is increased, the selectivity also increases as the $\%Cl_2$ is increased implying that the increase in the etch rate of the gallium nitride is slightly greater than the increase of the photoresist as a function of the $\%Cl_2$ in the plasma. The increase in etch rate will be due to a combination of the increased ion density as the $\%Cl_2$ is increased (as was seen in the study using the ICP 180) and also due to a increased amount of reactive chlorine radicals as was discussed above (see Section 5.3.1).

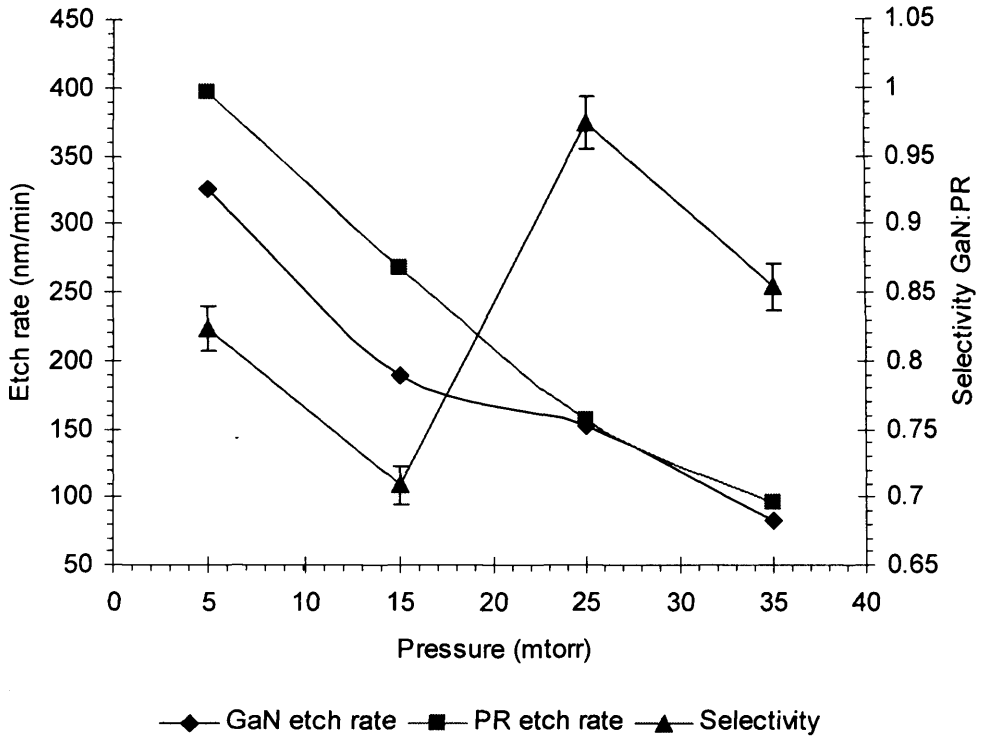

Figure 5-44 Gallium nitride and photoresist etch rates as a function of chamber pressure in an Oxford Instruments ICP 380, the selectivity of GaN over the photoresist is also shown.

The measured results as a function of pressure are shown in Figure 5-44, as was mentioned earlier the etch rate as a function of pressure shows broadly the same linear decrease as was noticed in the ICP 180 study, the reason for the increase in etch rate as the pressure is decreased has already been discussed in relation to the results of the study conducted with the ICP 180 and this reasoning will not be repeated here.

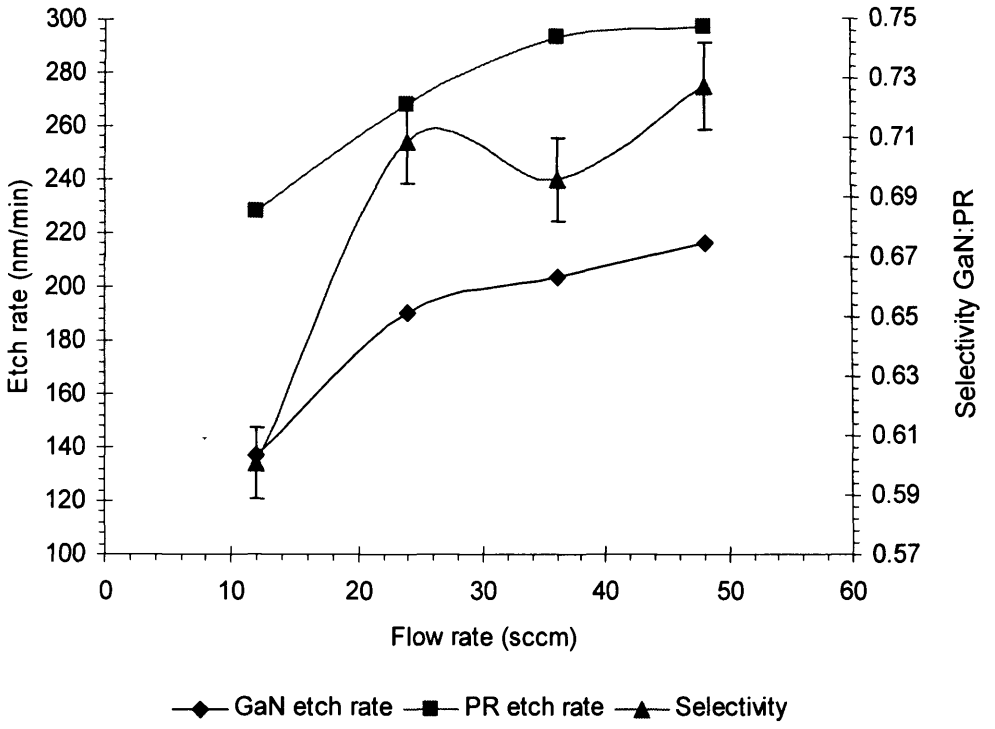

Figure 5-45 Graph showing the variation of the etch rate of gallium nitride, the variation of the etch rate of photoresisit (PR) and the variation of the selectivity of GaN over PR as a function of the flow rate of gases into and out of the plasma.

The dependency of the selectivity and the etch rates measured on the flow rate is presented in Figure 5-45. As may be seen there is an initially a large increase from a flow rate of twelve to a flow rate of twenty four sccm but then only a slight increase when the flow rate is increased to higher flow rates. This is approximately the behaviour predicted in [264] due to a lack of reactants at lower flow rates, which once past an equilibrium does not act to increase the etch rate. 12 sccm is quite a high flow rate to see such an effect and it could be due to the large size of the cavity of the ICP 380. Further results at lower flow rates would be needed to clarify this point as it could just be a dc bias or other plasma based effect.

5.4.7 Conclusions

In this chapter an orthogonal experimental design was used to examine the effects of varying the pressure, RF power, ICP power and $\%Cl_2$ of a BCl_3/Cl_2 plasma on GaN etch rate and the selectivity of GaN to PR. Unfortunately due to the choice of the parameters a strong combination effect was noticed that affected the results and made them unreliable. In orthogonal design experiments, care needs to be taken in choosing the variable settings used to ensure that the variable exerts a sufficient influence on the measured parameter to ensure that such combination effects do not override the effect of the variable that is being observed. From the orthogonal design and the later experiments to increase the etch rate, the effect of both the chemical and physical aspects of the plasma on the etch rate of gallium nitride are both clearly exhibited. Both these aspects are important in the etching of gallium nitride whereas much literature places a greater emphasis on the physical action of ion bombardment chiefly due to the slow etch rate of gallium nitride in wet chemical etches. The highest etch rate etch found in this study with an etch rate of 660 nm/min coupled with a selectivity of 0.9 a result that is comparable with the best results found in the literature. One dimensional search type etches performed in the ICP 380 system at Cardiff University yielded good results that showed clear trends in the etch rates and selectivity of gallium nitride and of gallium nitride over photoresist respectively. Due to the small uncertainty in these results, conclusions based on them were possible that would not otherwise have been so.

6 Microwave FET processing

6.1 Introduction

As mentioned above a few steps are required to make a basic working transistor, these include a good material on which to base the device, a mask set for isolating the device, defining the source and drain contacts and defining the gate contacts, a method for isolating the device, a good ohmic metallisation for the source and drain and a rectifying contact for the gate. In this chapter the steps that were taken to address the requirements of a working high frequency heterostructure field effect transistor are described. The material that was used to fabricate the devices was bought from *Nitronex* and was grown on silicon which made it both cheaper and easy to cleave.

Firstly in this chapter the mask pattern used for the fabrication of FETs is presented. Patterns made with this mask set were found to have rough sidewalls that were noticeable at high optical magnifications, this roughness was eventually concluded to be due to the roughness of the mask that was a print taken from a sub-master mask. It was decided that metals deposited by lift-off using these masks were sufficiently good for development work though for high quality devices a master or sub-master mask would be better.

As was mentioned before, isolation of the devices was achieved by etching of the material so that only a small region was left un-etched, this method is suited to HFET devices as the material becomes resistive once the 2-DEG is etched through requiring shallower etch depths. The etching was performed in the ICP380 for which a study of the etch rate of gallium nitride has already been presented. As will be shown, a problem with using an etch for isolation purposes is that the gate, source and drain metallisations must transcend the discontinuity between the etched materials and the un-etched materials, this can cause metal thinning which in turn can cause problems with the device performance. One solution to this problem is to use thicker metals;

here a method of melting photoresist leading to shallow sidewall gradients due to surface tension is found to work as well.

Several plasma etchings were used to etch the device mesa isolations. As is shown below all the etched material yielded a similar sheet resistance as measured using TLM patterns formed with various ohmic contacts. A slight correlation between the dc bias of these etches and the conductivity of the wafer is noticed, as long as the etch depth is kept reasonably low. The reason for this could be due to damage to the surface through the photoresist or strain relaxation in the layers.

Both ohmic and Schottky contacts are investigated. A good Schottky contact is presented and it is the authors view that with further efforts to treat the surface this contact could be made to exhibit state of the art parameters; however, as it is, it is a workable contact. No ohmic contact with a resistance of the required order of magnitude was discovered, some of the failure mechanisms for ohmic contacts are presented after the results of the TLM measurements taken with the contacts tried.

At the end of the chapter the best dc transistor characteristic that was gained during this work is presented. Due to a higher than expected sheet resistance after etching and poor ohmic contacts the transistor only exhibits a very low saturated drain-source current; however, or possibly because of the feeble current drain, the breakdown voltage of the FET is found to be near 90V.

6.1.1 The mask pattern used for processing.

The photolithography mask pattern used for the fabrication of microwave field-effect transistors (FETs) was designed by Peter Lomax, formerly a postgraduate student at Cardiff University, and fabricated by Align-right (now Photronics UK ltd). The mask set consisted of both a positive and negative mask. The masks were copies of a submaster retained by Align-right, both had clearly printed on them the words *HEMT Test Array 1* (HTA1). The *HTA1* mask set contained all the features necessary for the fabrication of a FET and these features and the FET fabrication process are reviewed here.

It was found during FET process development that a close contact between the mask and the photoresist was essential for good small feature pattern transfer and metal lift-off using the bi-layer photoresist method. This required complete removal of edge beads, something which is not strictly necessary with larger features. The mask *HTA1* contained features for the removal of edge beads shown schematically in Figure 6-1. These patterns allowed either a central square to be exposed while the edge beads were shadowed (for negative photoresist), or for the centre to be shadowed while the edge beads were exposed (positive photoresist). The inverse of the two patterns shown in Figure 6-1 was also available on the other mask in the set of two.

Figure 6-1 Schematic diagram of form of patterns used for edge bead removal, black regions indicate regions of chrome (opaque) and white regions clear glass, the inverse (black = white) of the patterns shown above was also available on the other mask.

The second pattern that was necessary in the fabrication of a FET was the pattern for the device mesa isolation. Device mesa isolation was used to ensure that current flow between the source and drain of the FET was limited to the region covered by the gate. Mesa isolation was achieved by patterning the sample and then etching the heterostructure until the 2-DEG was destroyed everywhere apart from where the photoresist protected the sample. A picture of the mesa patterns for a 100μm (two 50μm gates) gate width device and a 50μm (two 25μm gates) gate width device is shown in Figure 6-2. The dark squares in Figure 6-2 are where the photoresist would remain if the photoresist were positive as for the Shipley S1813 photoresist used here. As may be guessed correctly the vast majority of the sample is etched leaving only the small bits of sample underneath the photoresist un-etched and conductive.

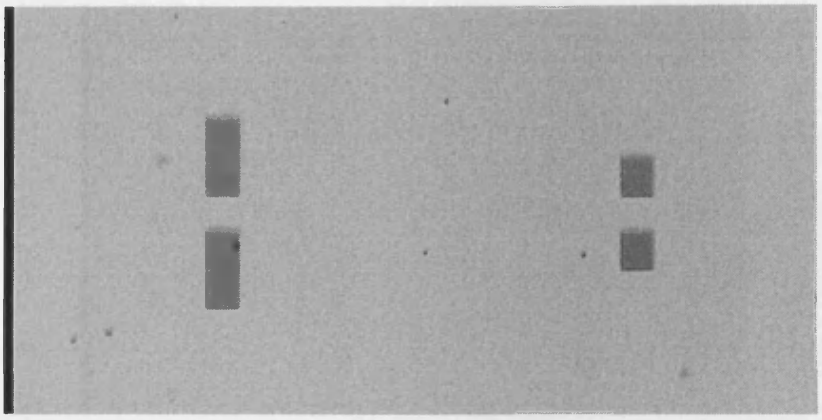

Figure 6-2 Picture taken through a microscope of the mesa isolation patterns for the 100μm (left) and 50μm (right) single gate devices.

After the mesa etch the ohmic contact pads for the source and drain were laid which, was because the ohmic contacts required a high temperature anneal whereas the gate metal needed no anneal. The through-microscope photo of the source-drain metallisation pattern for the two widths of gate available on this mask (100μm and 50μm) is shown in Figure 6-3. The cross at the bottom-centre of Figure 6-3 was the alignment mark that was supposed to be used to align the gates with the source-drain metallisation though in practice it was often difficult to see through the alignment mark while simultaneously keeping the sample free to move beneath the mask unless the photoresist on the sample was very flat. Apart from the 100μm and 50μm devices there was also a large part of the mask dedicated to FETs with larger gate widths (for higher powers), these larger devices had mesas similar to the smaller gate width devices. Almost all of a source-drain metallisation pattern for a 200μm gate width device is shown in Figure 6-4.

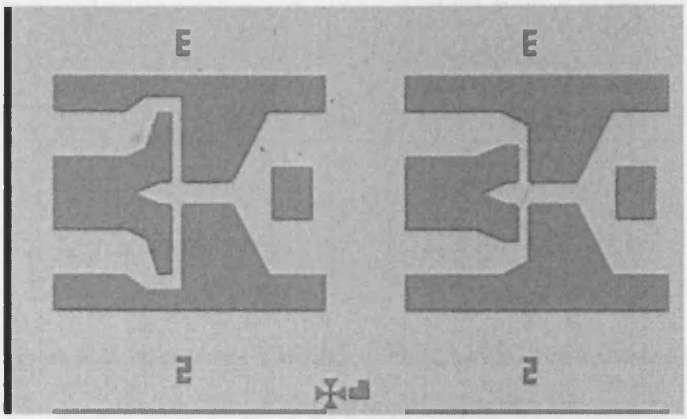

Figure 6-3 Microscope picture of the source-drain metallisation for a single gate 100μm gate width device (left) and a single gate 50μm gate width device (right).

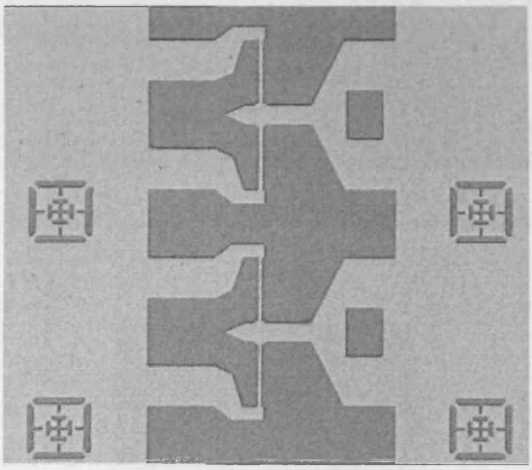

Figure 6-4 Source drain pads for a two gate device with alignment marks also shown.

After the deposition and anneal of the source-drain pads, the gate metal was deposited. The gates that could be defined by photolithography had a width of 50μm or 100μm and a length of either 2 or 4 microns (see Figure 6-5 and Figure 6-6 respectively). Apart from this there were, on the mask, several gate pads without gates that could be used in conjunction with an electron beam writer to gain access to other gate dimensions Figure 6-7.

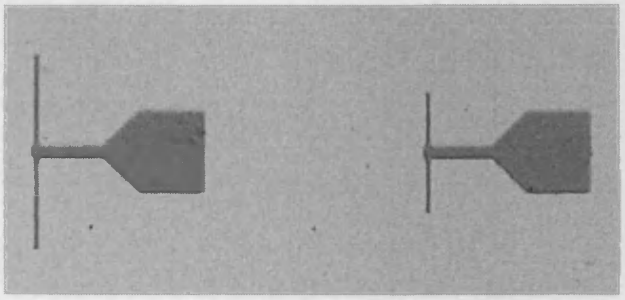

Figure 6-5 The two types of 2 micron gate length devices on the mask, on the left the 100μm wide device and on the right the 50μm device.

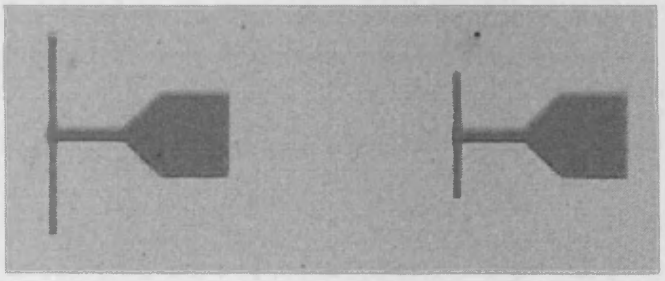

Figure 6-6 Through-microscope photograph of the two 4 micron gate length devices.

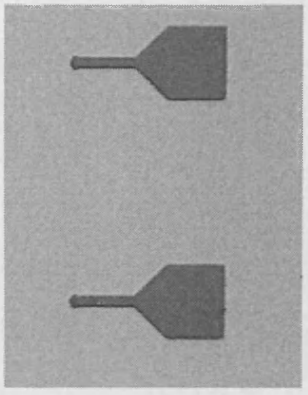

Figure 6-7 The gate pads without gates that would be used in conjunction with an electron beam writer.

Also available on the *HTA1* mask set were patterns for the test of ohmic contacts using the transfer length method (TLM). Those familiar with the TLM method will know that a mesa should be etched to ensure that current only flows in a restricted region and that contact regions must be formed with differing spaces between them on this mesa, those unfamiliar with the TLM are referred to [278] for a good description. The mesa mask pattern, in this case, looked similar to two rectangles as drawn in

Figure 6-8. A SEM micrograph of a TLM mesa may be found in the copy of the physics thesis by Mark Dineen held in the Trevithick library at Cardiff University.

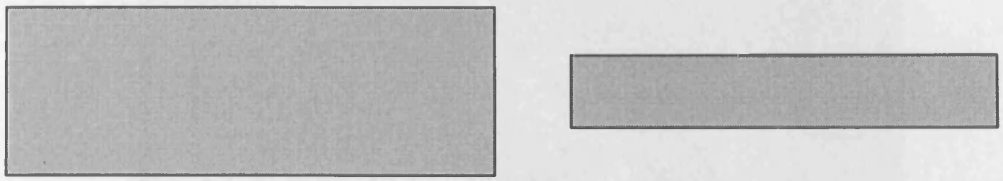

Figure 6-8 Schematic of the TLM mesa pattern of the mask *HEMT test array 1*.

The TLM metalisation patterns in this case were of two types, one that fit over the larger rectangle mesa, and one that fitted over the smaller rectangle mesa. These two patterns were similar, one just being smaller than the other and they are shown, respectively the larger and the smaller, in Figure 6-9 and Figure 6-10. It should be noted that the spacing between contacts is the same for both the large and small TLM contact patterns and that these spacings are 20, 10, 5 and 2 μm.

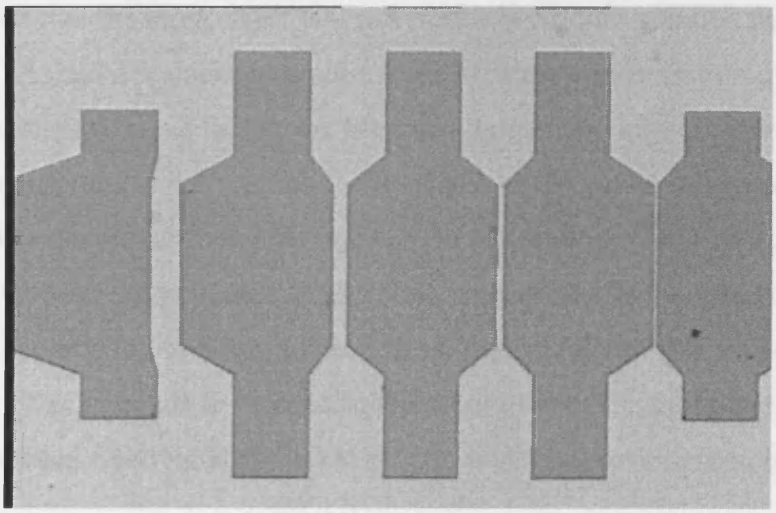

Figure 6-9 Larger TLM contact pattern with varying distances between pads.

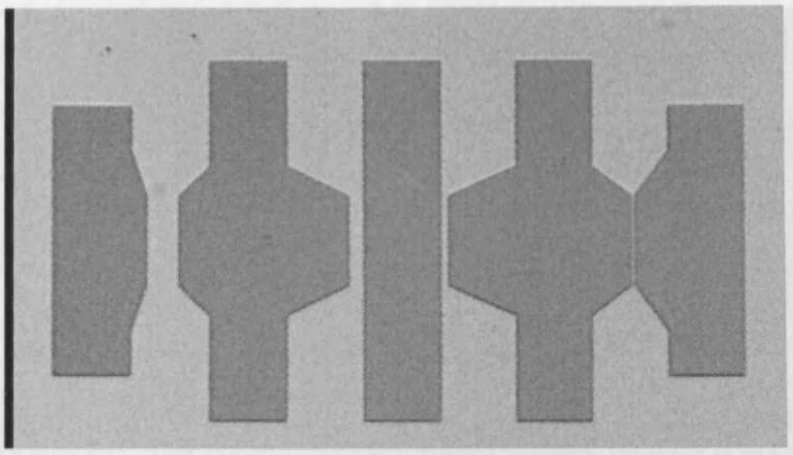

Figure 6-10 Smaller TLM contact pattern. The distances between pads are the same as those in the larger pattern.

6.2 Pattern definition

In preliminary fabrication steps it was noticed that some features had very rough sides with the roughness significant in comparison to the width of the transistor gates of the *HTA1* mask (see Figure 6-11). It was suggested that the length of the exposure time, or the concentration of the developer solution could cause this roughness [279]. It was also pointed out that the mask itself was not perfectly smooth and that the mask might be a factor [279]. As the developer was a 6:1 H_2O:2401 the concentration of the developer was removed as a factor; the literature accompanying the developer recommends a dilution of 4:1 for fine features; also, a developer with a concentration of 8:1 H_2O:2401 developer failed to improve the pattern roughness consistently. Furthermore, varying the exposure time had no consistent effect on the roughness, though over exposing led to larger feature sizes. Another factor that was considered was the effect of edge beads in increasing the separation of the mask and photoresist; however, edge bead removal again led to no consistent improvement in the roughness.

The mask was probably too rough to transfer good patterns. Comparison of the pattern given by the gate mask (which was particularly rough) with the pattern given by a part of the mask that was less rough seemed to indicate that the mask roughness was a considerable factor in the pattern roughness. However, occasionally good results such as those of Figure 6-12 were seen even with the rough mask.

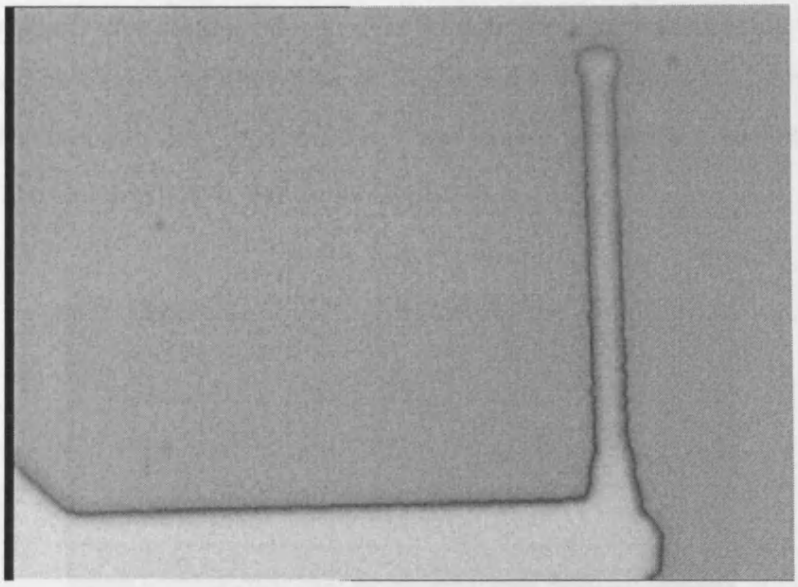

Figure 6-11 Example of the rough sidewalls that were routinely observed (this was for a 4s expose and 15s develop time). The gate width is fifty microns, slightly more than half of which is shown, the gate length is 2 microns.

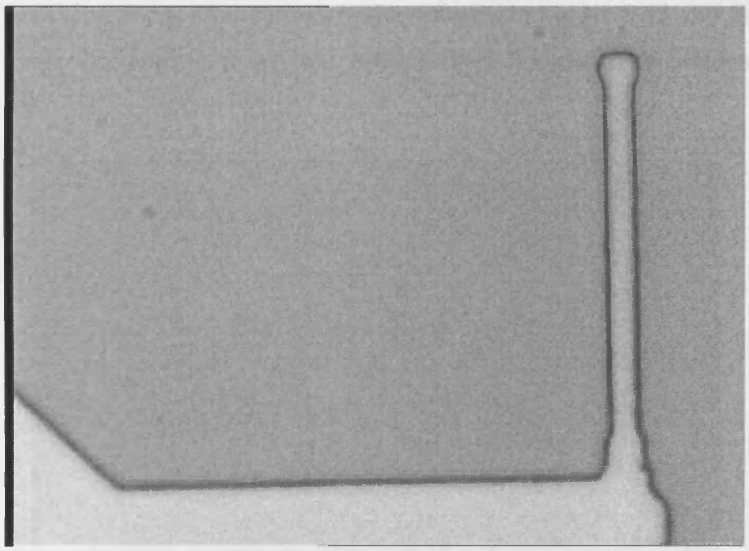

Figure 6-12 An example of the good results that were occasionally seen despite the mask roughness. The gate width is fifty microns, slightly more than half of which is shown, the gate length is 2 microns.

The mask pattern that was used to make the patterns shown in Figure 6-11 and Figure 6-12 is shown in Figure 6-13. To solve the problem of rough features it was suggested that a sub-master mask be bought. The masks in the clean room at the time were copies printed from a sub-master and it was believed that a sub-master would be much smoother. Such a mask would have cost in total next to £1000. Before a sub-master

mask was bought it was suggested that the metal patterns deposited using the masks we already had be examined after lift-off. Figure 6-14 shows the gate fabricated using the process described in the Appendix D. It was judged that such a feature would be sufficient though a sub-master would be desirable.

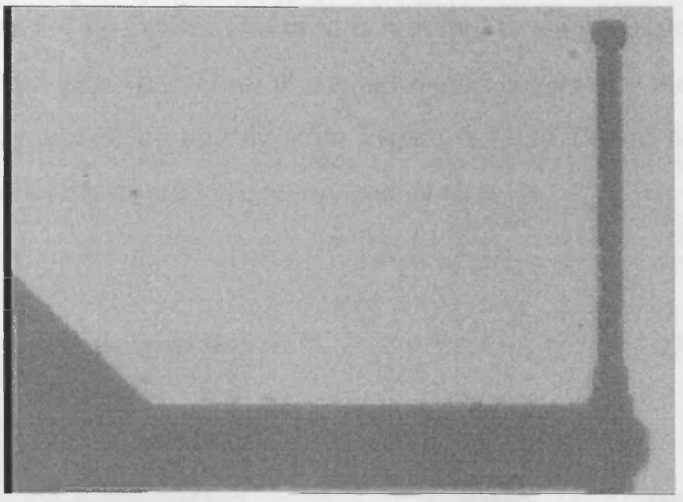

Figure 6-13 Microscope image of the mask pattern shown in Figure 6-11 and Figure 6-12. The gate width is fifty microns, slightly more than half of which is shown, the gate length is 2 microns.

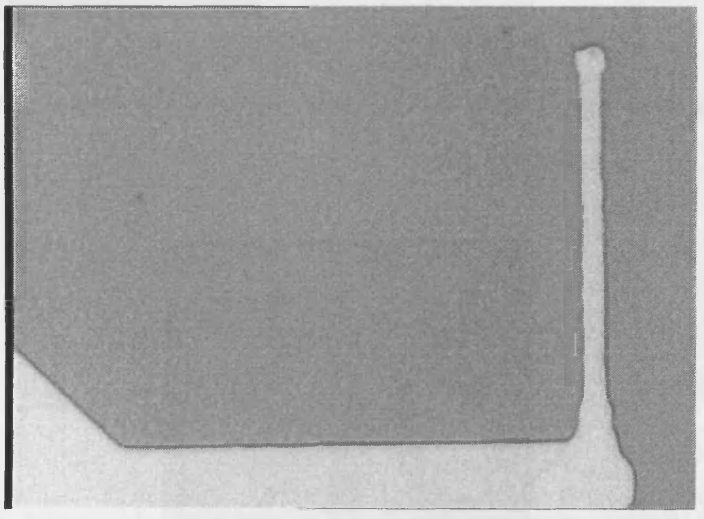

Figure 6-14 Through-microscope photograph of the gate metallisation post lift-off. The gate feature shown is the same as that in Figure 6-11 to Figure 6-13. The gate width is fifty microns, slightly more than half of which is shown, the gate length is 2 microns.

6.3 Photoresist flow bake to reduce mesa sidewal angle

A problem with the fabrication of heterostructure field effect transistors (HFETs) found previously [280] was that the mesa-isolation of the device by etching could cause the gate metal that passed over the mesa edge to thin, and sometimes even break completely (Figure 6-19). Device isolation is required to stop conduction between the source and drain and gate apart from in a small region covered by the gate fingers. As is shown in the sequence of figures from Figure 6-15 to Figure 6-17, Figure 6-18 shows a schematic of the layout of a completed device.

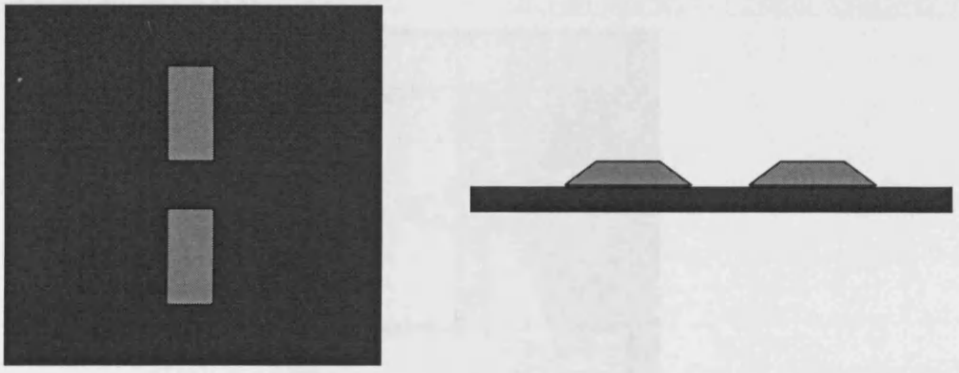

Figure 6-15 Schematic showing plan and side view of the device mesas once etched

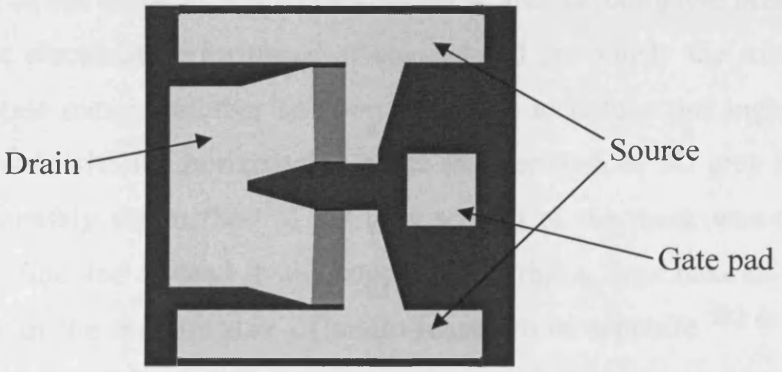

Figure 6-16 Rough schematic of what a single gate device looks like once the source drain pads have been deposited on the mesa.

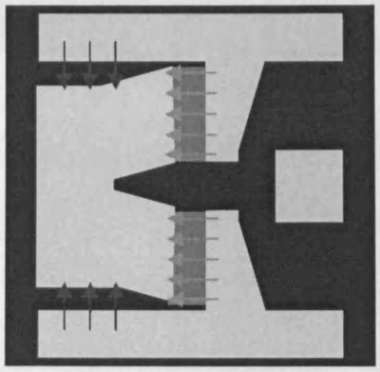

Figure 6-17 Schematic showing the allowed current paths over the mesas (green (lighter) arrows) and some of the previously allowed but now forbidden current paths (red (darker) arrows).

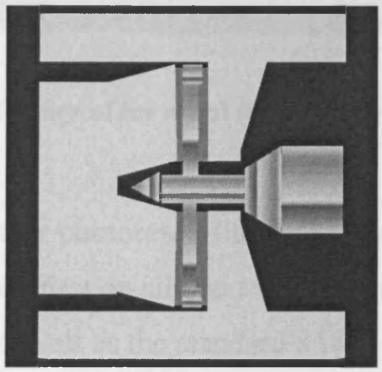

Figure 6-18 Schematic showing a completed device with device mesa, source, drain and gate.

Both the thinning of the metal as it traverses the mesa and the complete break caused problems with the electrical performance of devices and previously the solution was to use a thicker gate metal. Another solution would be to reduce the angle that the mesa sidewall makes with the horizontal in some manner such as 3D grey scaling of the resist. Unfortunately the method of 3D grey scaling of the mask was not easily practicable at the time and instead it was suggested [281] that a flow bake of the resist such as that used in the manufacture of micro-lenses from sapphire [282 & 283] might decrease the angle of the photoresist sidewall and that this pattern would be transferred into the etched material.

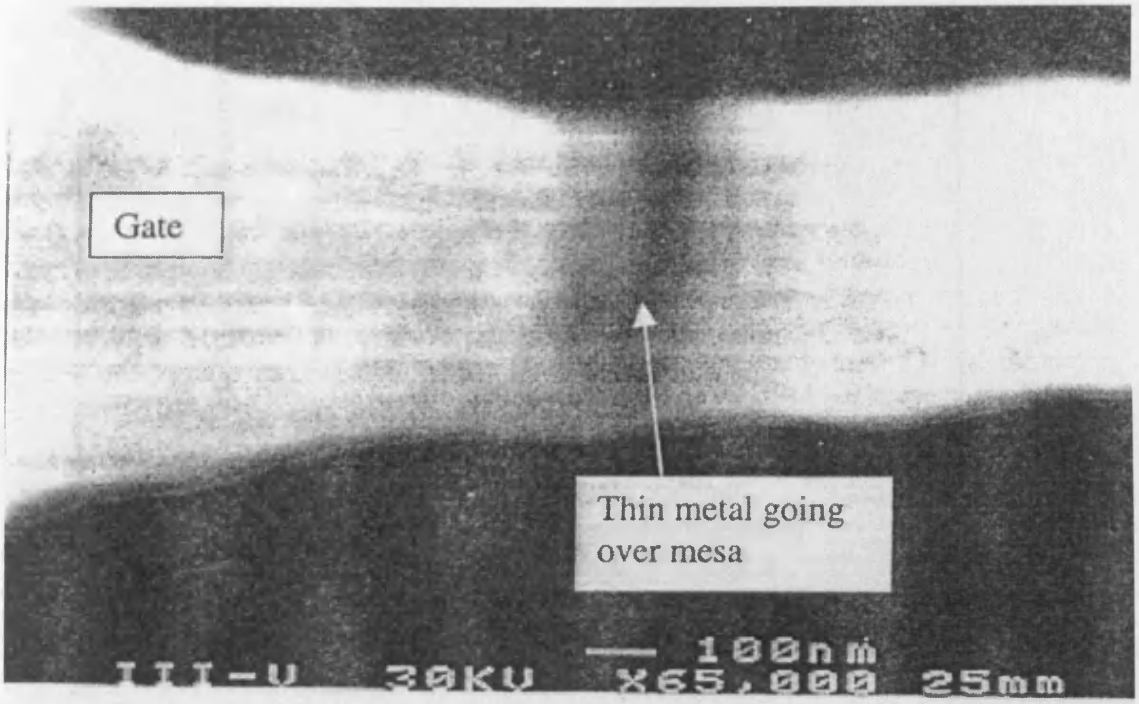

Figure 6-19 SEM image of the metal thinning over the mesa etch [280]

The experiments to test whether photoresist flow baking reduced the angle of the mesa sidewall were performed first on silicon to test the concept cheaply. Three samples were subjected to, as-well as the standard S1813 SP15 spin-on and pattern steps (see Appendix D), a bake at 180°C for 5, 10 and 15 minutes, respectively, after the develop step. The profile that was achieved after 5, 10 and 15 minutes of flow bake time was very similar. The profiles of a control and a flow baked sample, as measured with a Dektak profilometer, are shown in Figure 6-20 and Figure 6-21 respectively.

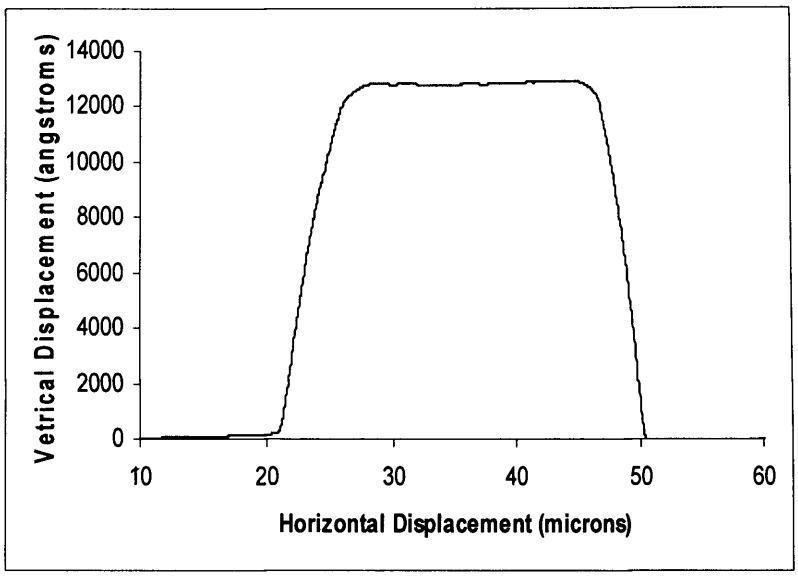

Figure 6-20 Profile of photoresist measured with Dektak profilometer without any flow bake

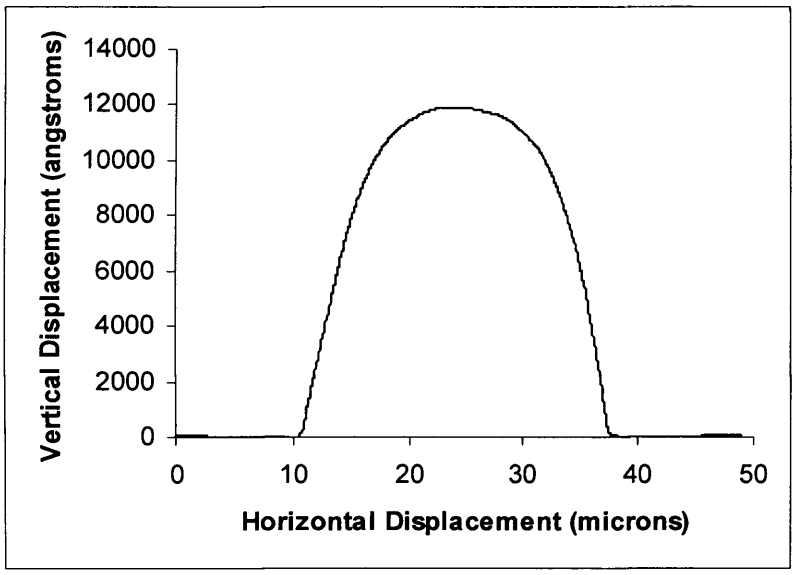

Figure 6-21 Profile of a 10 minute flow baked photoresist pattern analogous to the one shown in Figure 6-20.

In the results reported here specific mesa patterns were designated on the sample by a grid of letters and numbers so that the same patterns could be measured before and after the etch and compared.

The dimensions of the un-etched control sample and the etched samples that were measured are shown in Figure 6-22 (For details of the plasma used to etch the samples please see the Appendix D). The dimensions of the flow baked samples that were

measured before the photoresist was removed are shown in Figure 6-23. The reason for the two different sets of measurements is the difference in profile as shown in Figure 6-20 and Figure 6-21.

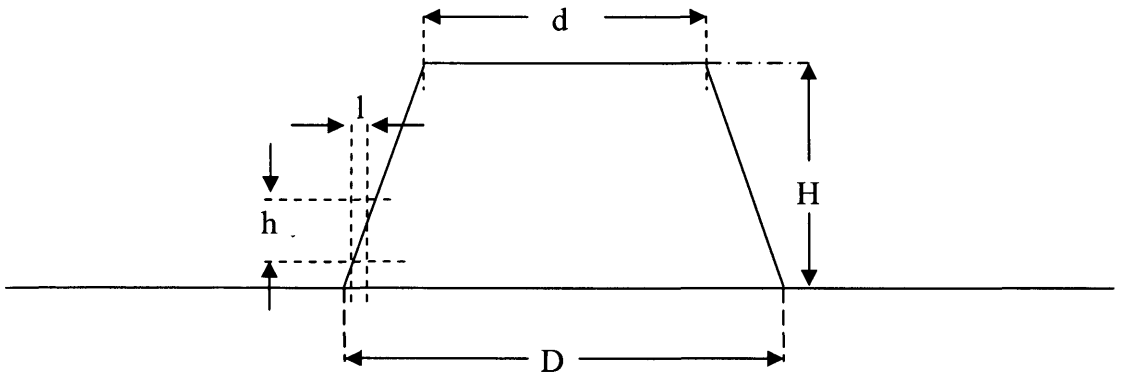

Figure 6-22 Schematic of the dimensions taken from the etched and control samples.

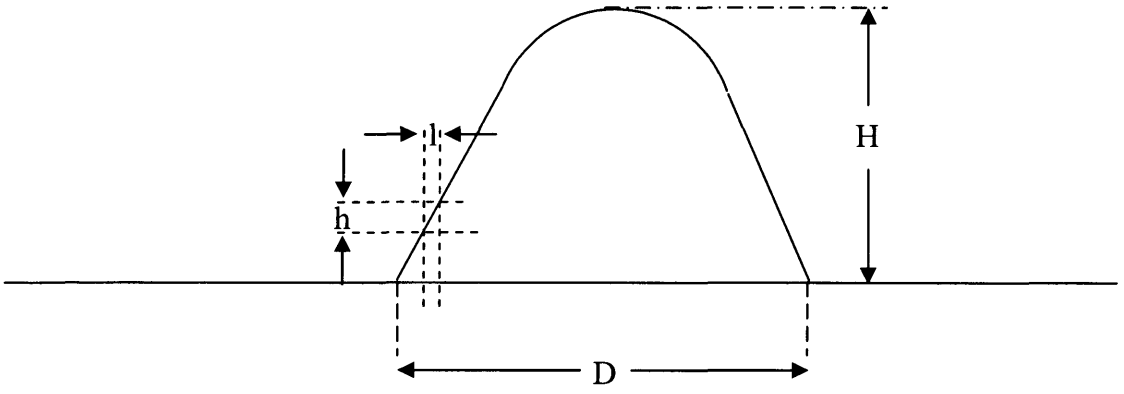

Figure 6-23 Schematic of the dimensions taken from the flow baked samples both before and after etching, before the photoresist was removed.

All of the measurements were taken using the Dektak surface profilometer at Cardiff University using a low speed, a scan length of 75 microns and a peak surface profile. This scan took 1500 measurements across the 75 microns and therefore had a resolution of 0.05 microns or 50 nm. In both cases *h* and *l* were used to calculate the sidewall angle and these dimensions were taken from as close as possible to the edge of the photoresist once the gradient had become approximately constant i.e. within 1 micron of it.

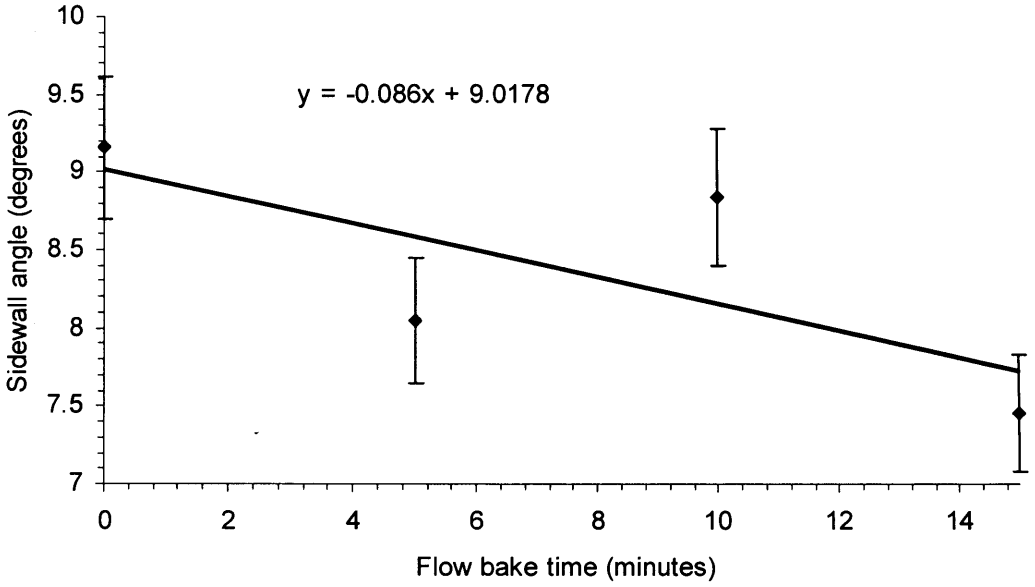

Figure 6-24 Graph of the effect of the flow bake time on the mesa sidewall angle, the line is a least squares fit to the data and the uncertainty shown is +/- 5%.

As Figure 6-24 shows, the flow bake did appear to decrease the sidewall angle as expected; however, the change was not much and in these experiments the sidewall angle was already very shallow, so indeed the problem would seem to be how to make the sidewalls steeper, not more shallow. If the trend shown in Figure 6-24 were to continue a flow bake of 45 minutes would reduce the sidewall angle to 5^{o} and a bake at $180^{o}C$ for 90 minutes would reduce the sidewall angle to 1^{o}. A photograph taken through a microscope of the mesa etched for 8 minutes with a 10 minute flow baked photoresist is shown in Figure 6-25. In Figure 6-25 the sloped sidewalls are clearly seen, though in actual mesa etches the etch depth would be much less than shown and hence the slope would be less noticeable.

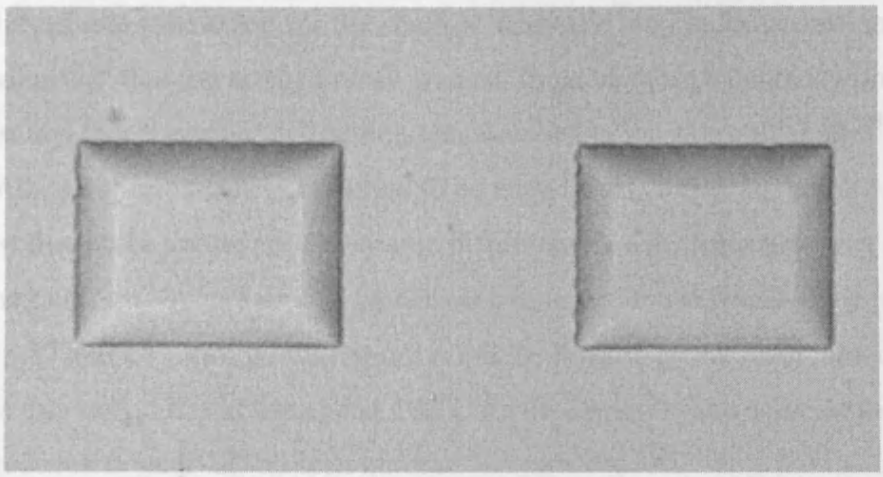

Figure 6-25 Eight minute etch of 10 minute flow baked photoresist. The sloping sidewall is clearly seen. The mesa pattern shown is for a 2 x 25 μm gate width device.

A fortunate side effect of the flow bake that was not predicted was the increase in etch selectivity caused by the flow bake that may be seen in Figure 6-26. There was an increase in selectivity from the control sample (0 minutes flow bake) to the 5 minute flow bake of approximately four times and this increased to approximately five times when the bake time was increased to 15 minutes. If the trend shown in Figure 6-26 were to continue the photoresist selectivity would be increased by an order of magnitude after a 40 minute bake at 180°C.

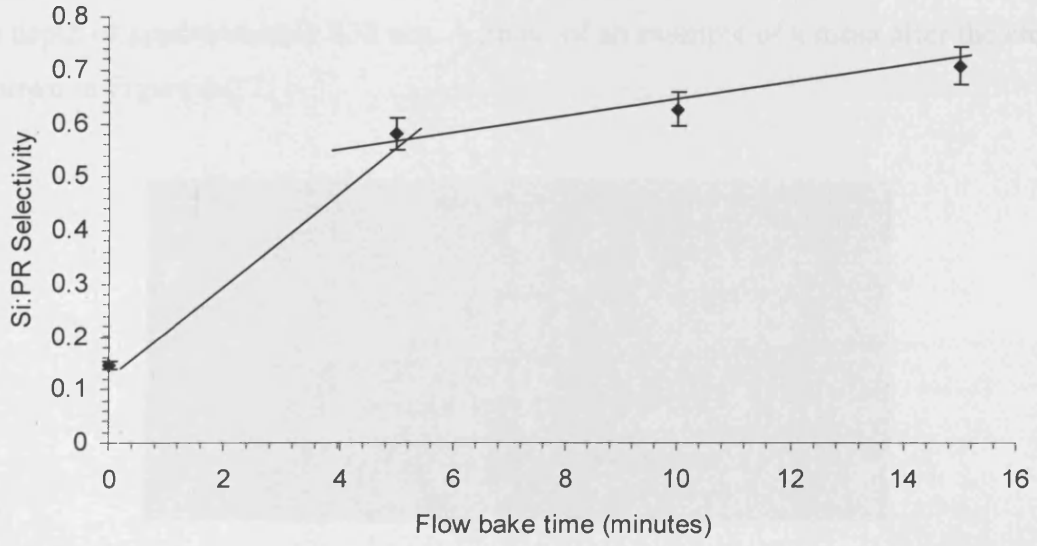

Figure 6-26 Graph of the selectivity of silicon over photoresist calculated by dividing their respective etch rates as a function of the bake time at 180°C. The lines were added by eye, by the author. Uncertainty is shown at +/- 5%.

It was believed that the reason for the shallow sidewalls seen in the control in the above studies was that the contact mask was not in good enough contact with the photoresist and that therefore diffraction was decreasing the sidewall slope [284]. The reason for the poor contact was assumed to be edge beads, which are beads of photoresist that build up the edge a sample if the sample does have a sloping edge to prevent the build up. Once the edge beads were removed the sidewall angle increased to between 20 and 25°, though this figure might be limited by the resolution of the Dektak. In this case, after annealing at 180°C for five minutes the angle of the sidewall reduced to near 12° as seen before.

Later studies showed that the resist could not be flow baked and then exposed and developed; if this were not the case a high selectivity could be coupled with a relatively steep sidewall. There is thus a compromise between the selectivity and sidewall angle with a high selectivity giving a lower sidewall angle.

To test whether the same effect would be exhibited on GaN, a sample was patterned with device mesas; the edge beads were reduced though not completely removed due to lack of time and the mesas once patterned were flow baked at 180°C for 5 minutes. The etch was performed in the same chemistry as before and the etch lasted for 2 minutes. The average angle of five measured mesa edges was 13° to 0 dp with a standard deviation of 0.5°. The etch rate of this etch was 88 nm/min, leading to an etch depth of approximately 438 nm. A photo of an example of a mesa after the etch is shown in Figure 6-27.

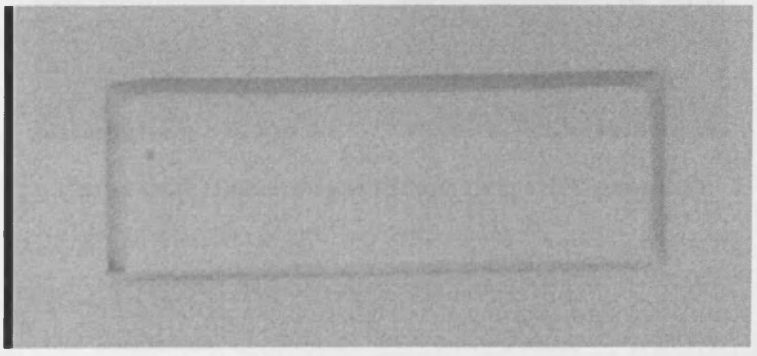

Figure 6-27 Through-microscope picture of the mesa etch with flow baked photoresist on GaN.

To confirm whether gate metal would cross the mesa edge without thinning, gate metal was deposited onto the mesa Figure 6-28, Figure 6-29 and Figure 6-30. As may be seen, for the gate metal that was used here namely (20/80 nm Ni/Au) there was no observable gate metal thinning.

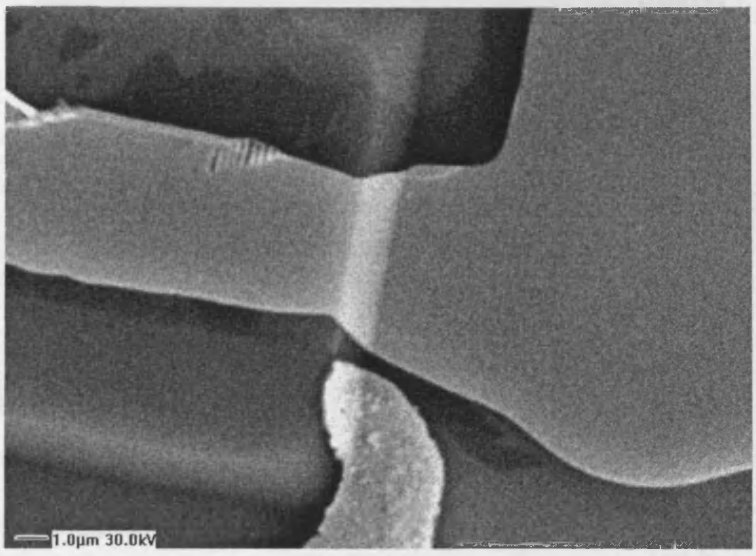

Figure 6-28 SEM image of the gate metal over the mesa

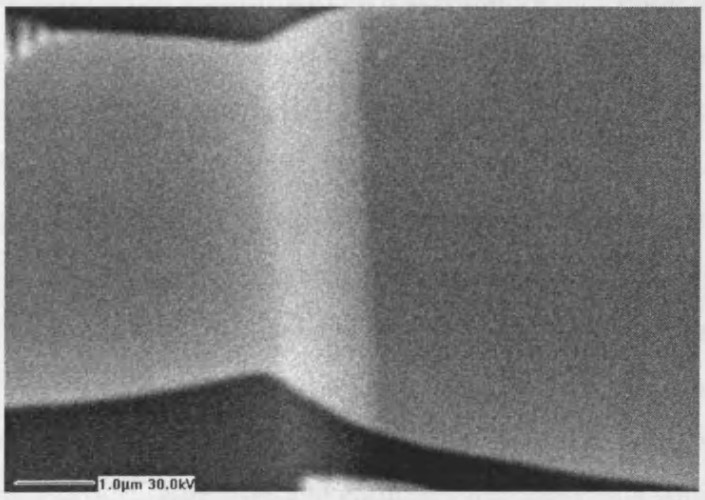

Figure 6-29 Higher magnification image of Figure 6-28

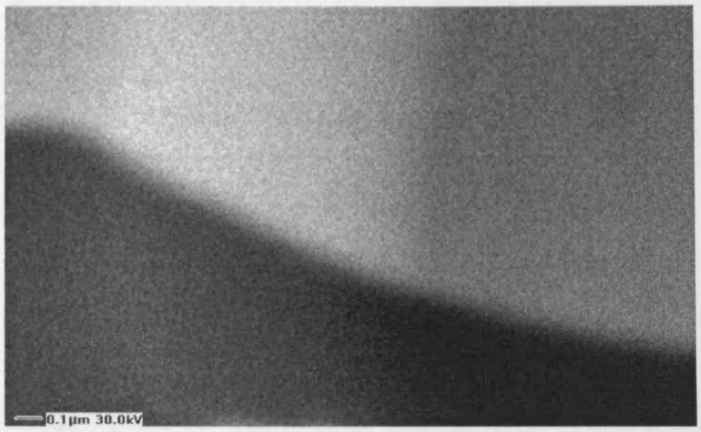

Figure 6-30 The gate metal over the mesa shown in Figure 6-28 and Figure 6-29 at the same magnification as the feature shown in Figure 6-19

6.4 Mesa etches

The HFET material used in this study was fabricated on a two-inch silicon wafer (a schematic of the layer structure is given in Figure 6-31). The AlN/(Al)GaN transition layer is used to relax the strain in the layer and reduce the number of dislocations and defects, caused by heteroepitaxial growth on a substrate with a quite large lattice mismatch with GaN, that propagate into the devices layers (the 1µm buffer layer and upwards). The micron of GaN combined with the 175Å of AlGaN causes a 2-DEG to form at the GaN/AlGaN interface providing the AlGaN is of sufficient thickness. The GaN cap layer decreases the 2-DEG sheet carrier density and hence increases the Hall mobility which can lead to an increase in the sheet resistance [285]. The GaN cap layer has also been shown to reduce gate leakage current for material similar to that shown in Figure 6-31. This was thought to be due to the piezoelectric effect shown in Figure 2-6 but could easily also be due to the increased quality of the gallium nitride layers compared to the AlGaN [285]. *Nitronex*, the company that grew this wafer, have had some success with devices made from 10 cm diameter substrates [286].

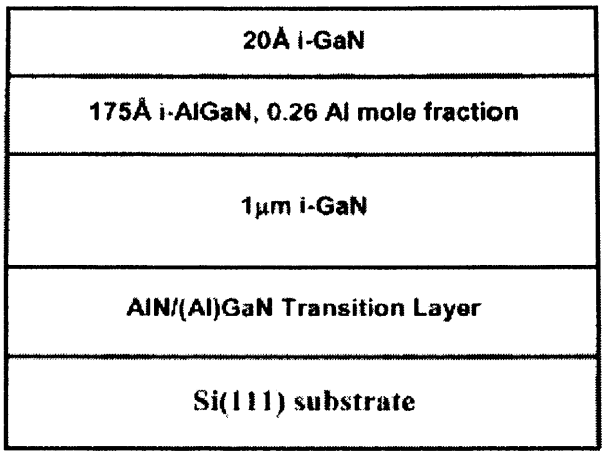

Figure 6-31 Schematic of the structure of the wafer bought from *Nitronex* for the purpose of fabricating HFETs

During the tests of the mesa etches described below it was found that 50 nm was a suitable depth for the mesas. A 10 nm etch was too shallow to be seen even with a microscope and although 30 nm could be seen with a microscope, it could not be seen through the bi-layer resist and therefore made alignment difficult. The sheet resistance of the wafer was found to be approximately 700 to 800 ohms/square this compares with 300 ohms/square for the Nitronex material presented in [286] and 500 ohms/square for that in [287].

6.4.1 Results and Discussion

As seen in Table 6-1 there seems to be a correlation between the sheet resistance of the materials once etched and the dc bias of the etches, the exception being the etch which showed no conductivity due most likely to the fact that the etch depth was too great. A factor that could have contributed to the decreased sheet resistance could be the damage of the surface through the photoresist by the plasma; *Nitronex* themselves have noticed that if the wafer is covered immediately with silicon nitride before any processing is carried out, the final device performance is improved [288]. Whether an interaction with the surface is the cause of the drop in conductivity could be checked by using a tougher mask such as SiO_2 or metal, or by using a thicker mask such as that created by several layers of S1813 SP15. A third reason for the drop in conductivity could be relaxation of strain in the heterostructure layers. As was shown in the introduction, 2-DEGs formed with III-nitride heterostructures are due to a polarity

discontinuity at the interface and a charge caused by strain in the layers. It could be that the mesa etch causes the layers to relax reducing the electron density in the 2-DEG.

Etch depth (nm)	Sheet resistance (Ω/□)	Etch rate (nm/min)	Helium Pressure (torr)	Table Temp. (°C)	Chamber Pressure (mtorr)	ICP Power (W)	DC bias (V)	RF Power (W)	Flow rate (sccm)	
									BCl_3	Cl_2
400	-	80	10	20	10	1000	190	100	25	15
77	750	15	10	20	10	300	110	50	25	15
54	850	108	10	20	10	0	420	300	25	15
32	700	11	10	20	10	2500	40	20	25	15

Table 6-1 Details of the plasma etching (generated in the ICP 380) that were used to etch device mesa isolations, also included is the sheet resistance taken from TLM patterns fabricated on the mesa etched material.

6.5 Ohmic contact studies

Ohmic contacts were fabricated using the method outlined in the Appendix D after a mesa was etched with the plasmas as described above. In order to characterise the contacts made to the HFET material the transfer length method (TLM method) was used. To characterise ohmic contacts using the TLM method an array of contacts is required with different spacings between adjacent contacts (Figure 6-32)

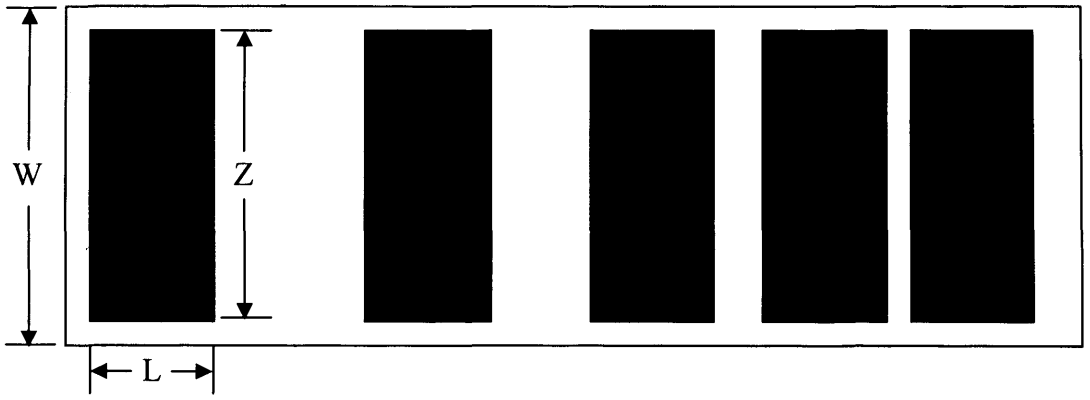

Figure 6-32 Schematic diagram of the layout of contacts used in the TLM method (contacts shown as black rectangles with identical width Z and length L. The width of the conducting channel is W).

The total resistance R_{tot} measured between two adjacent contacts is given by

$$R_{tot} = \frac{R_{sh}x}{W} + 2R_c + R_p \quad \text{Equation 6-1}$$

Where R_{sh} is the sheet resistance in Ω/□, x is the distance between the two contacts, W is the width across which conduction occurs between contacts, R_c is the contact resistance and R_p is the resistance of the probes used to take the measurement. If R_p is negligiable and the width of the conducting channel between contacts is made equal to the width of the contacts (normally this is achieved by etching a channel in the semiconductor) then the resistance will vary linearly as a function of the distance between the contacts with an intercept at x equal to zero of $2R_c$ and a gradient of R_{sh}/Z [289]. Hence, by plotting the resistance between adjacent channels as a function of the distance separating the contacts both the sheet resistance and the contact resistance may be calculated.

From [289] contact resistance is given by

$$R_c = \frac{r_c}{L_T Z}\coth\left(\frac{L}{L_T}\right) \quad \text{Equation 6-2}$$

Where

$$L_T = \sqrt{\frac{r_c}{R_{sh}}} \quad \text{Equation 6-3}$$

L_T is called the transfer length and it is length of contanct that is required for approximately 63% of the total current flow to transfer from the semiconductor to the contact. r_c is the specific contact resistance measured in Ωcm^2. From Equation 6-2 when $L \geq 1.5\ L_T$

$$R_c \approx \frac{r_c}{L_T Z} \quad \text{Equation 6-4}$$

Inserting Equation 6-4 into Equation 6-1 gives

$$R_{tot} = \frac{R_{sh}}{Z}(x + 2L_T) \quad \text{Equation 6-5}$$

From Equation 6-5 the intercept of the resistance dependence with the abscissa (extrapolated from the observed dependence of resistance on contact spacing) will yield twice the transfer length. The transfer length and sheet resistance once know may be used to calculate the specific contact resistance using Equation 6-3.

The above analysis assumes that the fabrication of the contact to the semiconductor has not changed the sheet resistance underneath the contact. This assumption can only be said to hold true for unalloyed, epitaxially grown contacts. For other contacts, especially those that are annealed, diffusion of metals into the semiconductor will cause a low resistance layer (sheet resistance r_{sc}) to form under the contacts [290]. This leads Equation 6-5 to become

$$R_T = \frac{R_{sh}x}{Z} + 2\frac{r_{sc}L_{Tc}}{Z} \quad \text{Equation 6-6}$$

Where

$$L_{Tc} = \sqrt{\frac{r_c}{r_{sc}}}$$ ..... **Equation 6-7**

In order to calculate the transfer length and the specific contact resistivity for this second case the end resistance of the contacts must be measured. For the case shown in Figure 6-34

$$R_{end} = \frac{V_{23}}{I_{12}}$$ ..... **Figure 6-33**

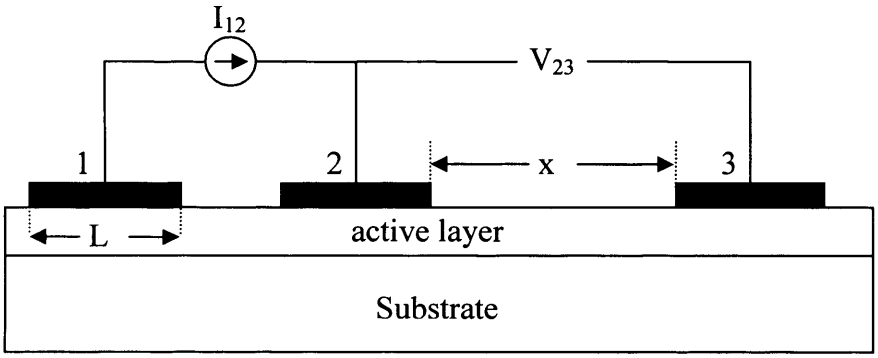

Figure 6-34 Showing possible method of measuring end resistance, the contacts and conducting channel are the same width Z.

From [290]

$$\frac{R_C}{R_{end}} = \cosh\left(\frac{L}{L_{Tc}}\right)$$ ..... **Equation 6-8**

And

$$R_{end} = \frac{r_{sc} L_{Tc}}{\sinh\left(\frac{L}{L_{Tc}}\right) Z}$$ ..... **Equation 6-9**

From Equation 6-8 and Equation 6-9 the new transfer length and the sheet resistance under the contact may be found. From Equation 6-7, once L_{Tc} and r_c are known, the specific contact resistance is found.

In Figure 6-35 an example of the TLM measurements used to characterise the contacts to the HFET material is given. The contact shown in Figure 6-35 is for 15nm/100nm/50nm/100nm Ti/Al/Ti/Au contacts. The results for the contacts that yielded sensible TLM measurements are given in Table 6-2. The 30/180/40/130 nm Ti/Al/Ti/Au contacts shown in Table 6-2 were adapted from the optimum Ti/Al/Ni/Au contact reported in [291], the others were adapted from this contact as the experiments progressed. The use of the Pt layer in 15/100/50/40/200 nm Ti/Al/Ti/Pt/Au contact was in order to stop the Au and the Al mixing which, was thought to be a problem. Other results were taken but are not shown here as these results were taken without mesa etching a defined conduction channel. It was believed that this would only result in a small difference between results taken with a mesa defined channel but this proved not to be the case with large discrepancies between the etched and un-etched results.

For comparison with the values acquired here contact resistances of 0.7-2.3 Ω mm was measured by Bardwell et al [292], whereas recently a Ti/Al/Ti/Au contact with a contact resistance of 0.5 was fabricated [293]. As may be seen from the table of contact resistances our best results were roughly an order of magnitude higher than those found in the literature, reasons why this may have been the case are given below. From the average value of the sheet resistance (~760Ω/□) the sheet carrier density in the 2-DEG may be calculated. Assuming an electron mobility in the range 600-1400 cm^2/Vs the 2-DEG sheet carrier density is calculated as being within the range $1.4x10^{13} - 5.9x10^{12}$ electrons/cm^2

Figure 6-36 shows an example of the dependence of the conductivity of a contact as the anneal temperature is varied. The minimum at a particular temperature is well known to occur.

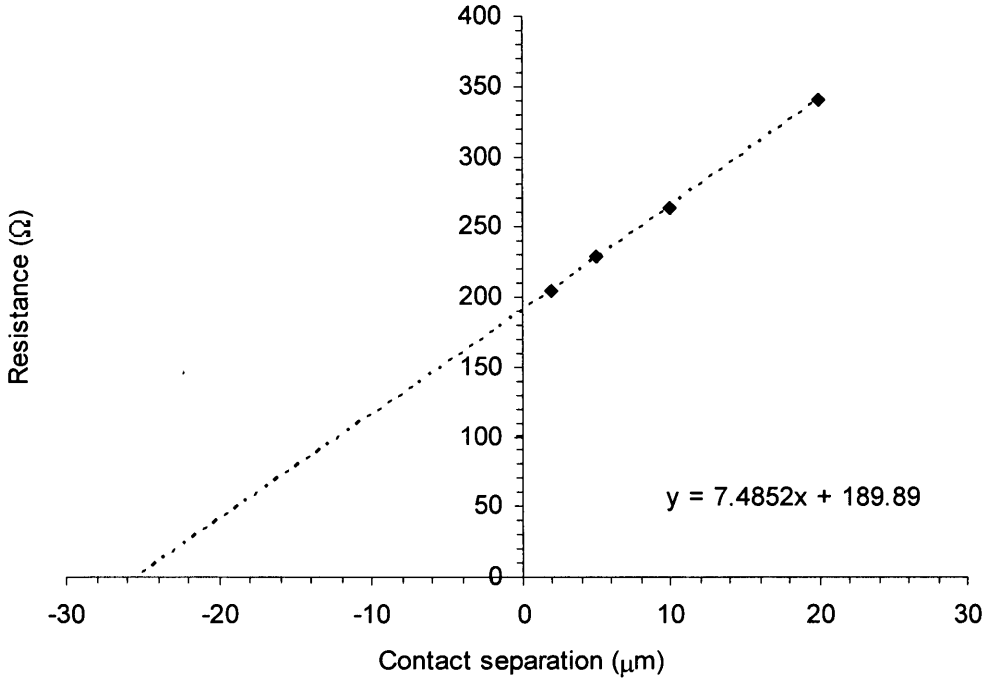

Figure 6-35 TLM measurements of 15/100/50/100 nm Ti/Al/Ti/Au ohmic contacts on GaN/AlGaN/GaN HFET annealed for 30s at 800°C. The mesa width was 100 microns.

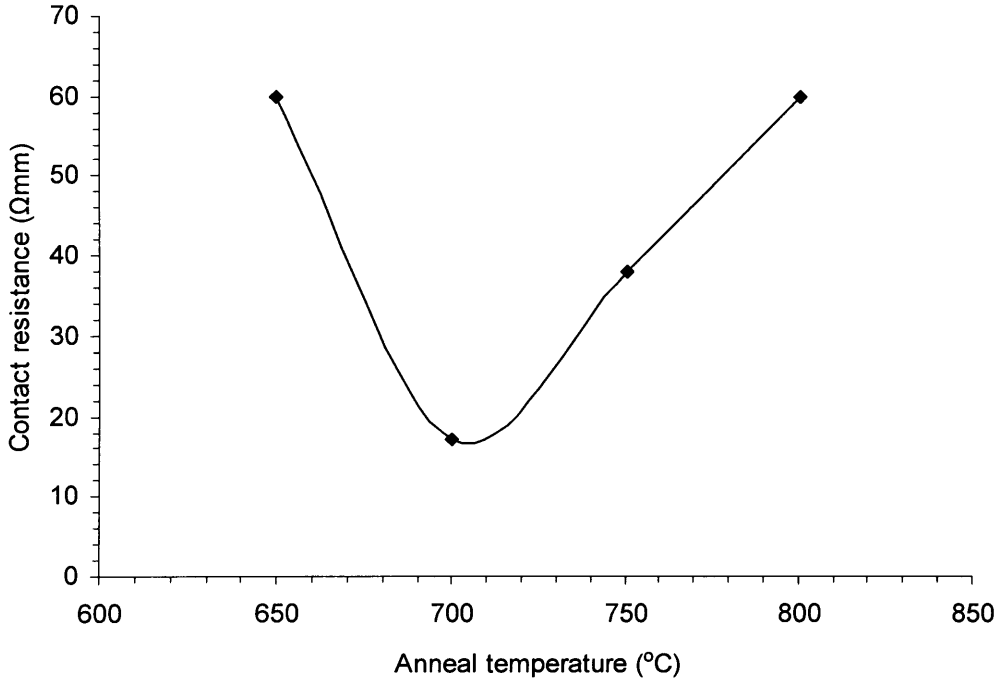

Figure 6-36 Dependence of 30nm/180nm/40nm/150 nm Ti/Al/Ti/Au ohmic contact resistance as a function of temperature of a 30s anneal.

Metals	Thickness of each metal (nm)	Anneal temperature and time (°C/s)	Contact resistance (Ω)	Contact resistance (Ω.mm)	Sheet resistance (Ω/□)	Transfer length (μm)
Ti/Al/Ti/Pt/Au	15/100/50/40/200	500/30	800	80.0	-	5
Ti/Al/Ti/Au	15/100/50/100	800/30	93	9.3	740	14
Ti/Al/Ti/Au	30/180/40/130	700/30	80	8.0	700	7
Ti/Al/Ti/Au	30/150/40/130	700/30	120	7.2	850	7

Table 6-2 Summary of the ohmic contact resistances and sheet resistivities found for various contacts to the etch HFET material bought from *Nitronex* (note, the transfer lengths were taken assuming that there was no change to the sheet resistance under the contact, an assumption that is likely false and which will lead to inaccurate values).

6.5.1 Failure mechanisms

If a representative value of the material resistivity of between 200 and 400 Ohm/square is taken and combined with a representative value of contact resistance for a good contact of 0.5 Ohms, we find that for a 20 micron gap one-hundred microns wide we would expect a current flow of between approximately 12 and 24 mA at 1V. The reason such values were not seen is due both to the high ohmic contact resistance of the source and drain contacts and the higher than expected contact resistance. In the following sections several failure mechanisms for the contacts fabricated here are suggested. Often for a particular contact, several of these mechanisms would present themselves at once, which factor was dominant for each contact fabricated is not known absolutely though it is suspected that it would have varied dependent on the particular contact with each being partially to blame for a poor contact.

6.5.1.1 Gold cap layer too thin

30/100/30/30 nm Ti/Al/Ti/Au contacts were used by the optoelectronic physics group based in Cardiff and a study of these contacts similar to these has been reported in the literature [294]. These contacts as fabricated here were found to be unreliable sometimes giving what seemed to be a good ohmic contact and sometimes giving no contact at all. An oxide layer was found to form on the surface of this contact after annealing, which was believed to be due to the gold cap layer being too thin permitting Al and Ti to diffuse into the surface and oxidise in large amounts; this process might have been helped by the fact that the chamber of the rapid thermal annealer (RTA) was not pumped during annealing. The oxide layer exhibited itself through several effects. Firstly at low voltages (several tenths of a volt) there was no conduction between probes placed on the same piece of metal whereas over 10 mA would be drawn at the same voltages on a true metal. Secondly, a breakdown effect was seen both when both probes were placed on the same metal and when conduction was between two contacts; this breakdown effect was such that at higher voltages ~3V current would suddenly begin to flow in large amounts, as expected. After breakdown, currents

would flow in their expected amounts even at low voltages or if the voltage was reduced to zero and then increased again; however, the breakdown was also localised as, if the probe was lifted from the contact and replaced, current would once again not flow in the expected amounts.

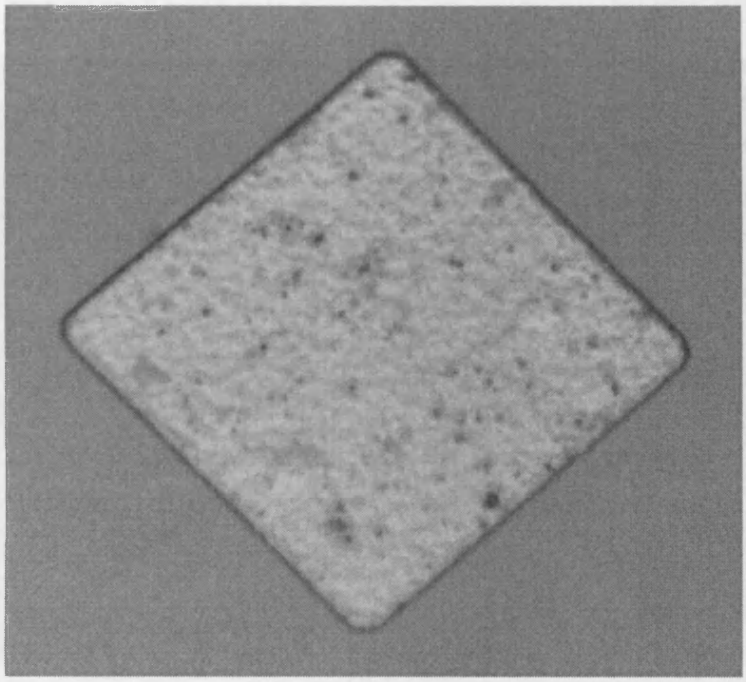

Figure 6-37 Optical microscope image of 30/100/30/30 nm Ti/Al/Ti/Au annealed at 800°C for 30s

6.5.1.2 Gold cap layer islanding

Several contacts were annealed with ≥ 150nm of Au as a top surface. These contacts were, in order of increasing gold thickness, 15/200/40/200 nm Ti/Al/Ti/Au, 15/100/50/40/200 nm Ti/Al/Ti/Pt/Au, 30/180/40/300 nm Ti/Al/Ni/Au, 30/180/40/600 nm Ti/Al/Ni/Au. The gold on all these contacts would island when annealed at different temperatures, but ≥ 600°C; however, gold islanding was not isolated to contacts with very thick cap layers, 25/100/70/90 nm Ti/Al/Ti/Au and 25/100/60/10/80 nm Ti/Al/Ti/Ni/Au contacts both exhibited this phenomena (see Figure 6-40) though in both cases there was a higher gold coverage of the uncovered areas. Figure 6-38 shows an example of what a contact looks like once gold islanding has occurred. EDX spectra of the light and dark regions in Figure 6-38 are given in Figure 6-41 and Figure 6-42, respectively.

Gold is put on the surface of a contact to stop the reactive metals underneath from oxidising, if the gold islands like this metal oxidation should occur leading to a poor contact. This means that the high temperatures needed to make the titanium and aluminium layers react and diffuse through the GaN cap layer cannot be reached.

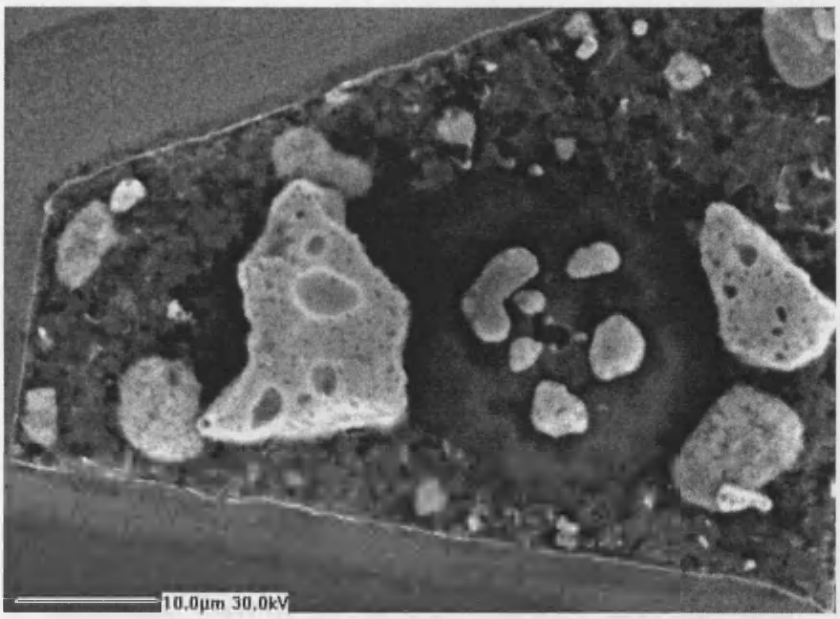

Figure 6-38 SEM image of the 15/200/40/200 nm Ti/Al/Ti/Au annealed at 800°C for 30s, the light regions are area of coalesced gold whereas the dark regions are predominantly aluminium.

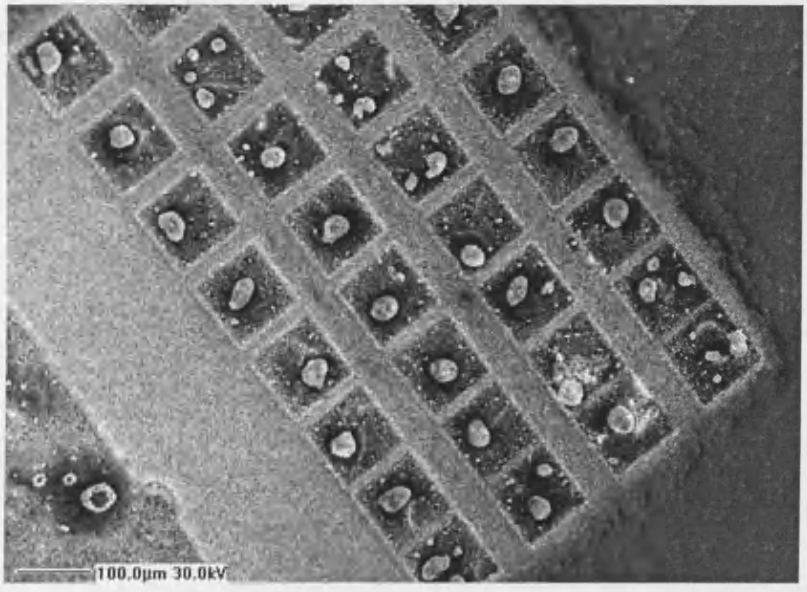

Figure 6-39 SEM image of 30/180/40/300 nm Ti/Al/Ni/Au contacts annealed at 700°C for 30s. The light regions surrounding the contacts were identified as by EDX analysis as Si.

It was initially thought that it was the thickness of the gold that decided whether the gold would island; however, it seems to be more complex than this as 30/180/40/150 nm Ti/Al/Ti/Au contacts were found to form no islands whereas, as mentioned above, thinner layers of gold with thinner aluminium and thicker titanium layers did; this would seem to imply that there is a reaction between the metals and the gold which stops the gold from islanding.

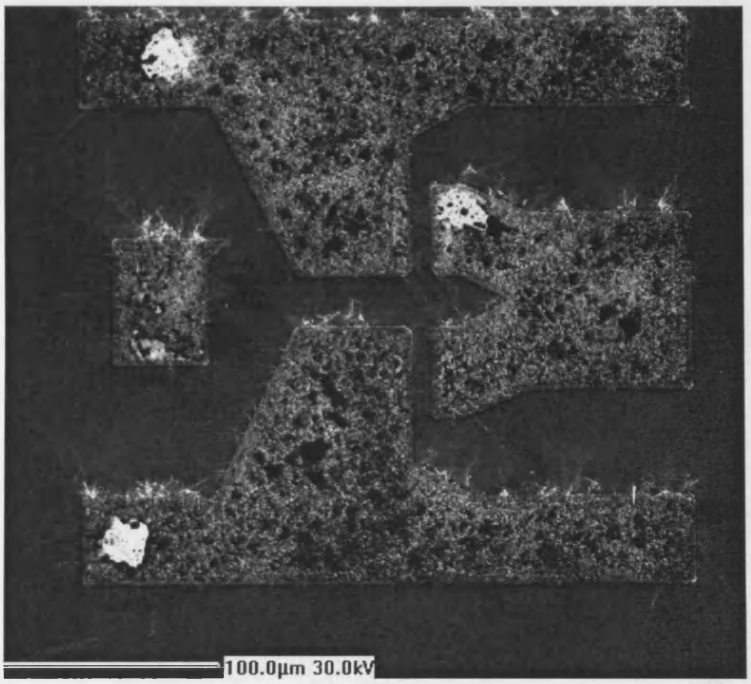

Figure 6-40 SEM image showing islanding on a 25/100/60/10/80 nm Ti/Al/Ti/Ni/Au contact. The whiskers around the contacts are thought to be titanium

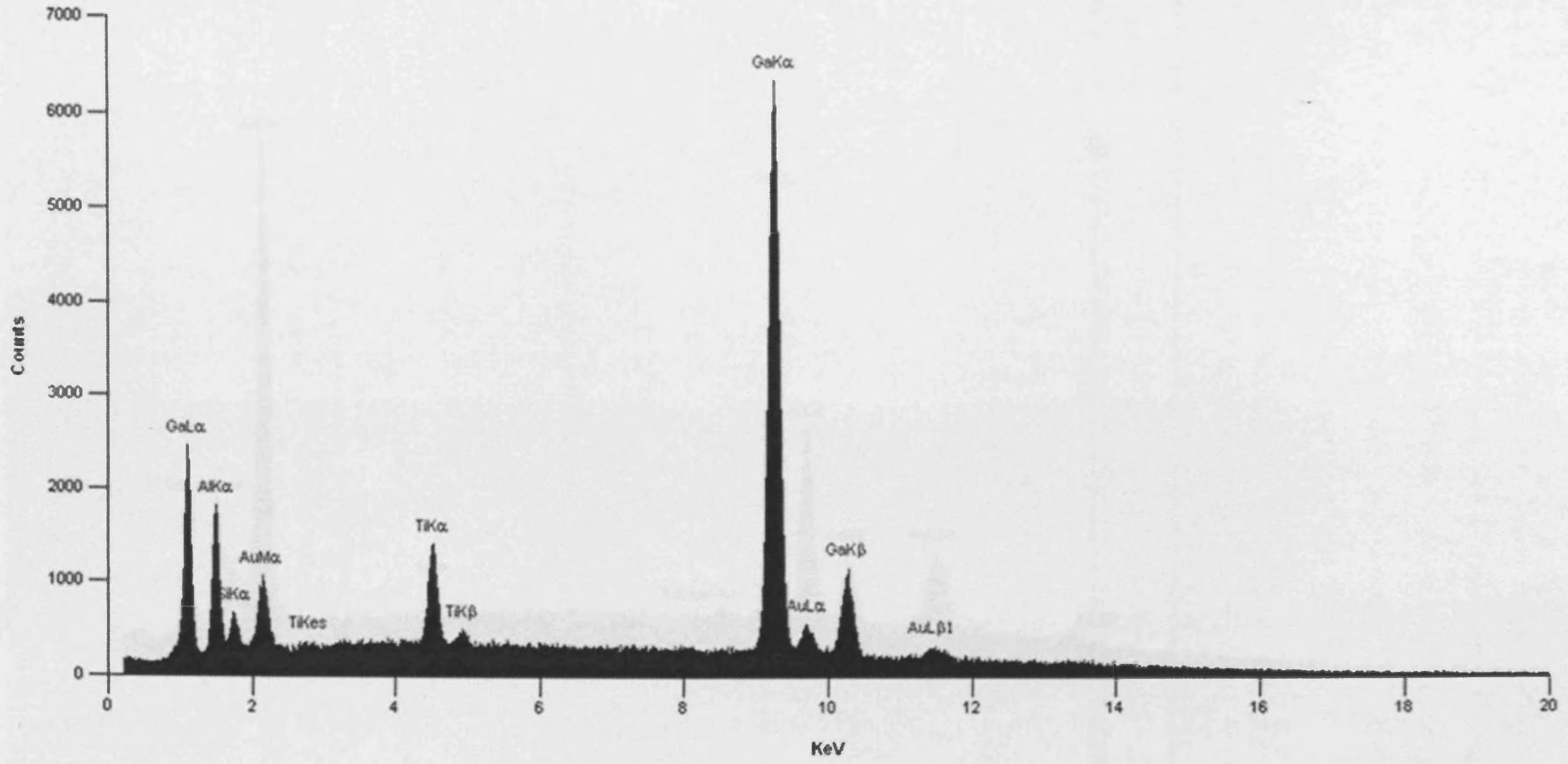

Figure 6-41 EDX spectra of the dark regions of Figure 6-38, attention is drawn to the small amounts of gold, large amounts of gallium and presence of silicon when compared to the spectra taken before the anneal. (Figure 6-45)

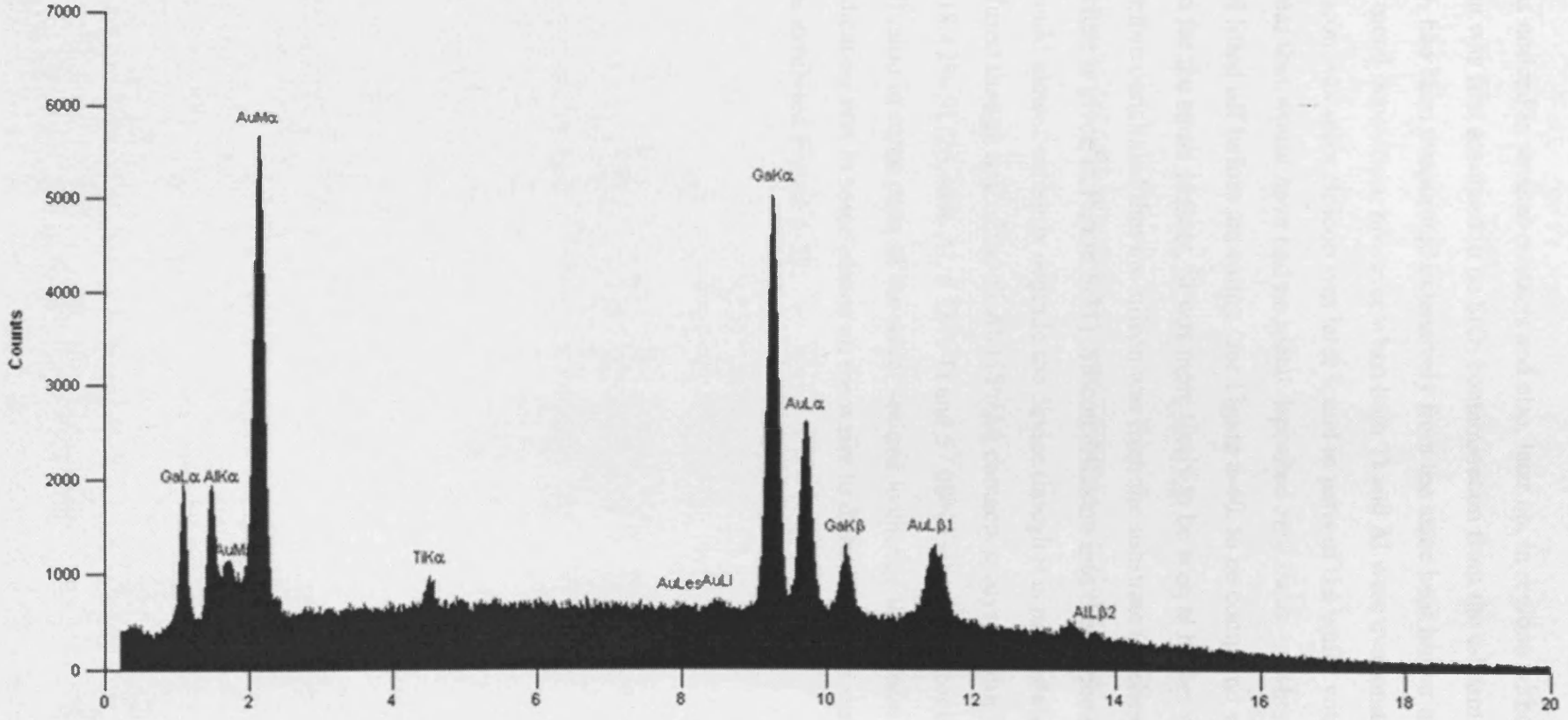

Figure 6-42 EDX spectra of the light regions of the contact shown in Figure 6-38. Note the larger amount of gold, smaller amount of Al and lack of Si, also the large amounts of gallium as seen as-well in Figure 6-41 when compared to the un-annealed sample (Figure 6-45)

6.5.1.3 Silicon Diffusion

Silicon was noticed in several contacts and also, later on, in regions without contacts. This silicon was first assumed to be SiO_2 contamination from the e-beam evaporator where SiO_2 had been evaporated extensively from the same boat holder as the Al before the metal deposition; however when both Ti and Al were evaporated on their own no silicon was seen. Silicon was later found in parts of the wafer without contacts present, areas that would have had no metal deposited onto them, or where the entire contact had lifted off before annealing (see Figure 6-40, to be compared with Figure 6-44). Also for the same contact, Si was more likely to be seen at higher temperatures. It was therefore concluded that the silicon was from the substrate (a schematic of the wafer structure is given in Figure 6-31). Silicon diffusion into the device layers and contacts would almost certainly degrade the device though it is not certain how far the silicon diffused though one of the Ti/Al/Ti/Pt/Au contacts analysed with EDX contained 18.42% Si (25.48% Al, 5.78% Ti and 57.08% Ga) a significant proportion. Also Si diffusion in some parts of the wafer seemed to change the texture of the surface, indicating that in some places on the wafer Si diffusion to the surface or near surface was exhibited Figure 6-39.

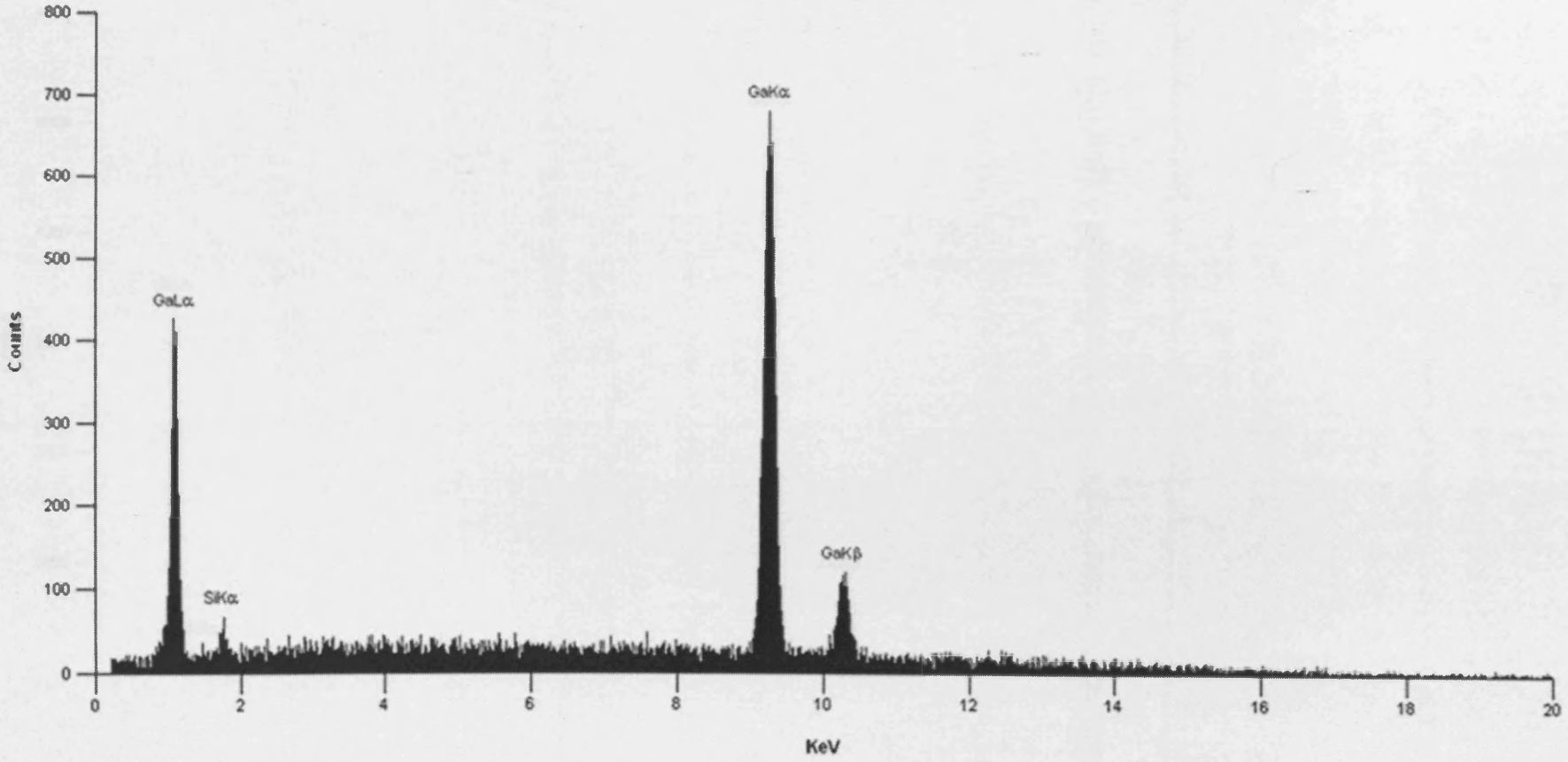

Figure 6-43 EDX spectra of a blank region of the HFET wafer after annealing

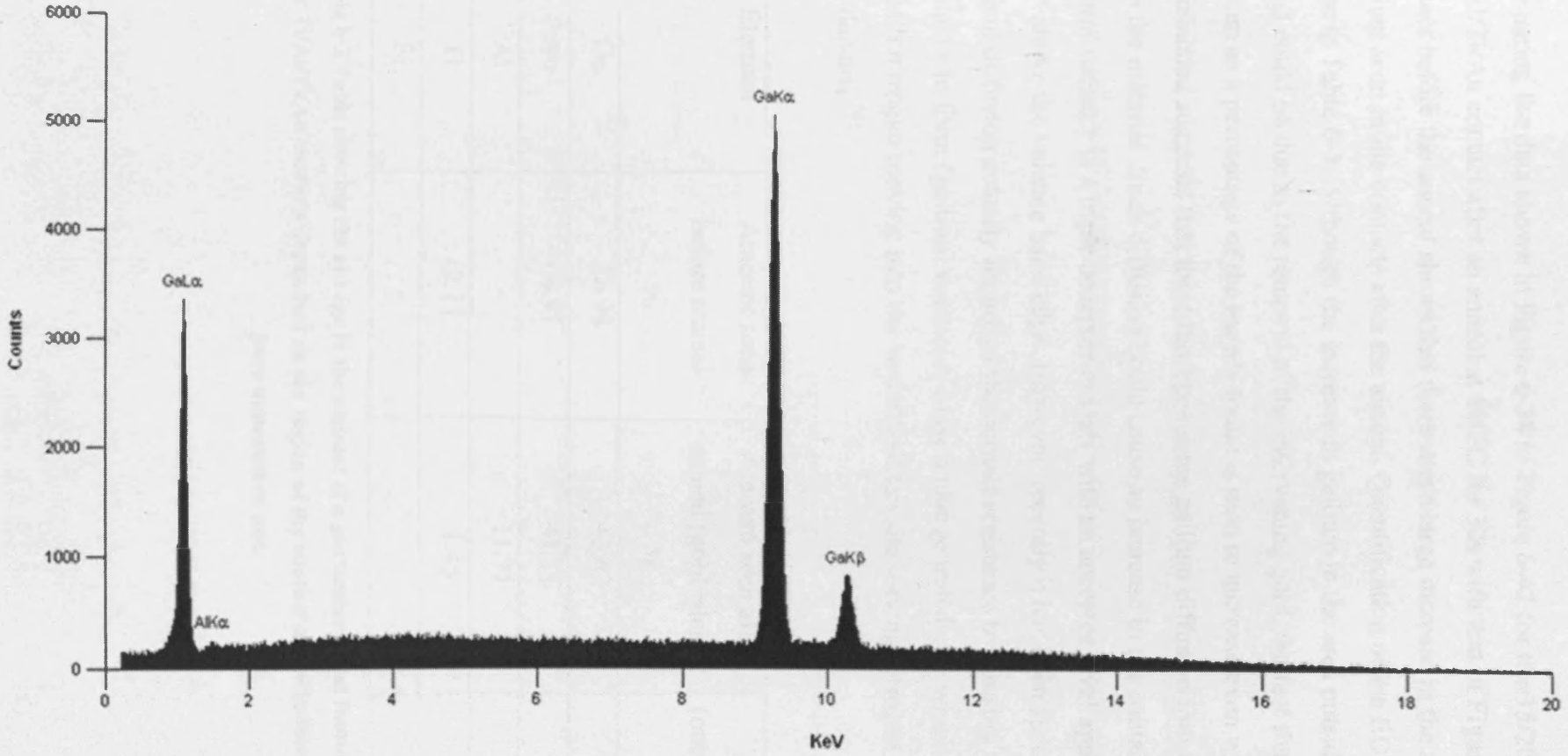

Figure 6-44 EDX spectra of a blank region of the HFET wafer before annealing

6.5.1.4 Gallium Diffusion

Comparing the data shown in Figure 6-38 to Figure 6-42 for the 15/200/40/200 nm Ti/Al/Ti/Au contact after an anneal at 800°C for 30s with that of Figure 6-45 for the contact before the anneal shows that there was a large increase in the amount of gallium seen in the contacts after the anneal. Quantification of the EDX spectra are given in Table 6-3. Although the increase in gallium in the area outside of the gold island could be due to the removal of the intervening gold, the fact that the amount of gallium as a percentage of the metals found is seen to increase even where the gold has islanded suggests that there has been some gallium diffusion into the contacts from the material. Such diffusion could cause an increase in the contact resistivity as gallium vacancy is a triple acceptor in GaN with an acceptor level approximately 140 meV above the valence band edge. However, recently it has been speculated that the gallium diffusion actually improves the contact resistance by causing nitrogen vacancies to form (gallium vacancies cause a charge imbalance which is compensated for with nitrogen moving into the vacant gallium site leaving nitrogen vacancy a n-type dopant) [293].

Element	Amount seen before anneal %	Amount seen after anneal (gold island) %	After anneal (outside gold island) %
Ga	28.98	43.63	70.61
Au	68.91	43.21	-
Al	-	11.71	21.79
Ti	2.11	1.45	2.55
Si	-	-	5.05

Table 6-3 Table showing the change in the amount of a particular metal found in 15/200/40/200 nm Ti/Al/Ti/Au contacts dependent on the region of the contact and whether the contact had been annealed or not.

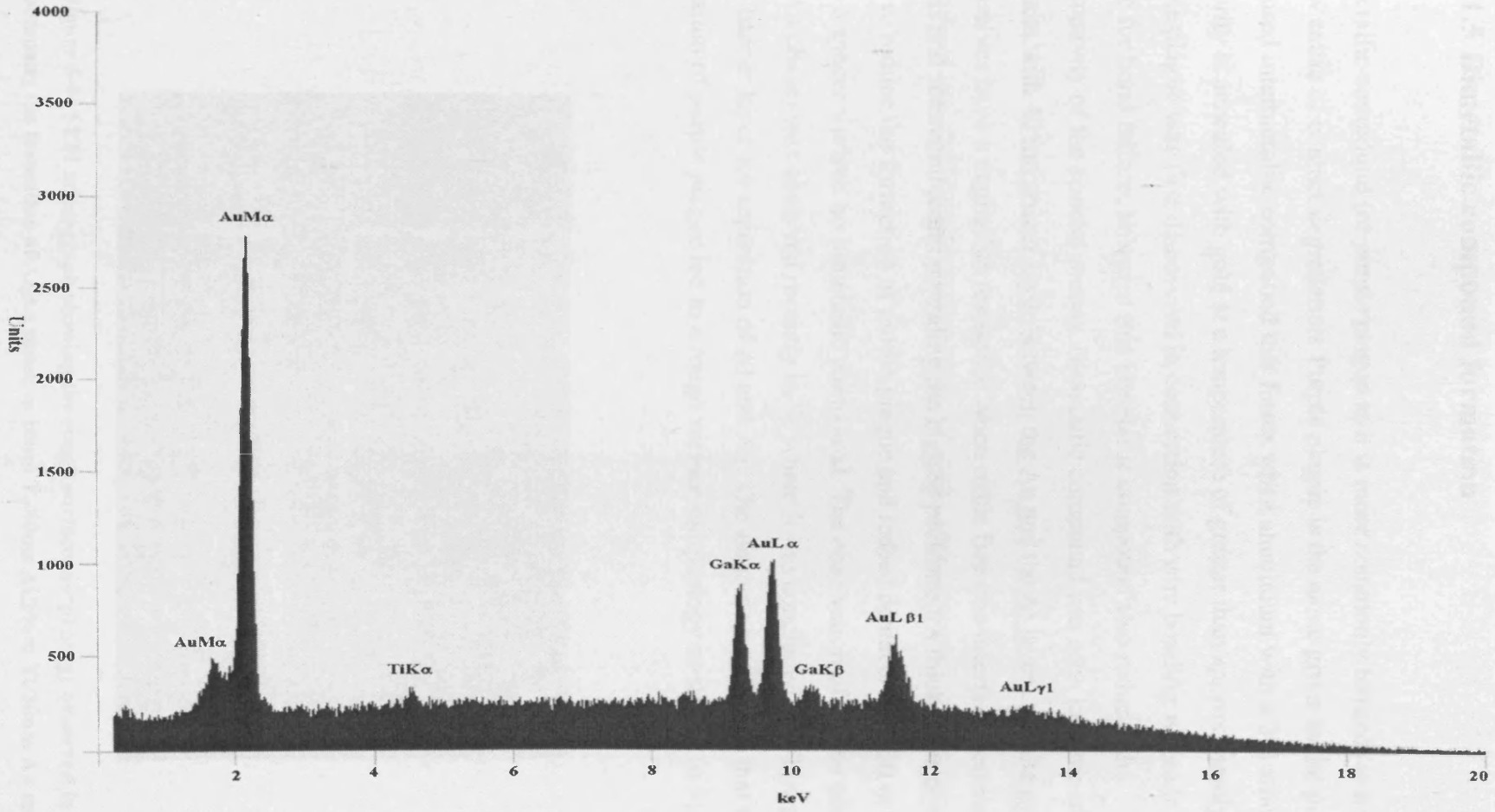

Figure 6-45 EDX spectra of the 15/200/40/200 nm Ti/Al/Ti/Au contacts shown in Figure 6-41, Figure 6-42 before the anneal

6.5.1.5 Bimetallic compound formation

Bimetallic compound (or purple plague as it is more commonly termed) is a well know cause of contact degradation. Purple plague is the name given to the purple coloured intermetallic compound that forms when aluminium with a 2% silicon impurity is annealed with gold at a temperature of greater than approximately 200°C. Purple plague was first discovered in connection with wire bonding where it was a cause for bond failure; however this bimetallic compound also reduces the conductivity of the contact metals. Bimetallic compound was seen in some of the contacts with 40 nm spacer layer between the Au and the Al layers. As the metals themselves have a negligible resistance when oxide free (the interface between the metals and semiconductors providing the biggest problems), a thick layer could be used to reduce the formation of purple plague and indeed contacts with 60 or 70 nm of Ti as a spacer showed no bimetallic compound. The observation of purple plague (Al_2Au phase) was observed recently in [293] where it was concluded that Ti was not a good barrier layer for separation of Al and Au. The authors also noticed that the formation of purple plague led to a rough surface morphology as shown in Figure 6-46.

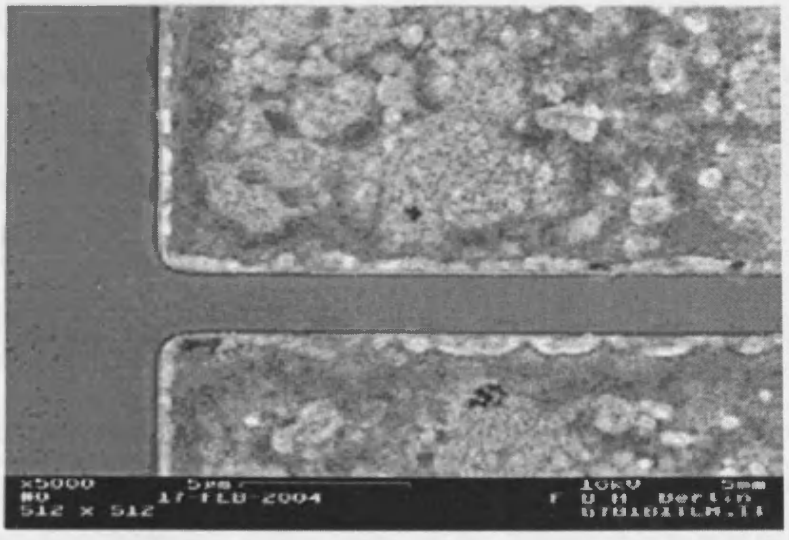

Figure 6-46 SEM micrograph showing the rough surface morphology observed in [293] to accompany the formation of Al_2Au phase in 10nm Ti/50nm Al/20nm Ti/30nm Au contacts.

6.6 Schottky contacts

The voltage current characteristic of a Schottky diode according to the thermionic emission theory is given by [295]

$$I = I_S\left[\exp\left(\frac{q(V - R_S I)}{nkT}\right) - 1\right] \approx I_S \exp\left(\frac{q(V - R_S I)}{nkT}\right) \quad \text{Equation 6-10}$$

Where R_S is the series resistance which includes the contact resistance of the metal and the sheet resistances of the metal to semiconductor junction and the GaN film; n is an ideality factor that indicates how well the observed I-V characteristics fit thermionic emission theory ($n=1$ being an ideal fit). I_s is the saturation current given by

$$I_S = S \cdot A^{**} T^2 \exp\left(-\frac{q\phi_b}{kT}\right) \quad \text{Equation 6-11}$$

Where S is the contact area, ϕ_b the Schottky barrier height. A^{**} is the effective Richardson constant given by

$$A^{**} = 120\left(\frac{m_e^*}{m_e}\right) \quad \text{Equation 6-12}$$

Where m_e^* is the effective mass of an electron in the material the Schottky contact is being made to. Using a value $0.22m_e$ for the effective electron mass in GaN, A^{**} is calculated as $26 \text{Acm}^{-2} \text{K}^{-2}$ [295].

Equation 6-10 may be simplified to

$$I = I_S \exp\left(\frac{qV}{nkT}\right) \quad \text{Equation 6-13}$$

When the current multiplied by the sheet resistance $I.R_S$ is small compared to the applied voltage V. If the natural logarithm of the current is plotted as a function of applied voltage then there will, at low voltages, be a linear region where Equation 6-13 holds true. From extrapolation of the linear region to the abscissa intersection the saturation current I_s and hence the Schottky barrier height φ_b may be found and from the gradient of the linear region the ideality factor n may be found. The sheet resistance R_s may be estimated from the linear region of conventional forward bias I-

V plot and this estimate may be used with Equation 6-10 to increase the linear region of the *ln(I)=f(V)*.

6.6.1 30/60 nm Ni/Au

A 30/60 nm Ni/Au Schottky contact was the first examined. A sample of the I-V characteristics of this contact are shown in Figure 6-47. These contacts were of a very poor quality, exhibiting performance many times worse than the state of the art (see the caption of Figure 6-47); particularly poor was the ideality factor, the saturation current and the breakdown voltage. Ni/Au contacts have been shown to form into the ((1,1,1) phase on GaN (both Ni and Au are observed in the (1,1,1) phase). In this phase Ni has a slightly higher work function than Au and should therefore form slightly better Schottky contacts.

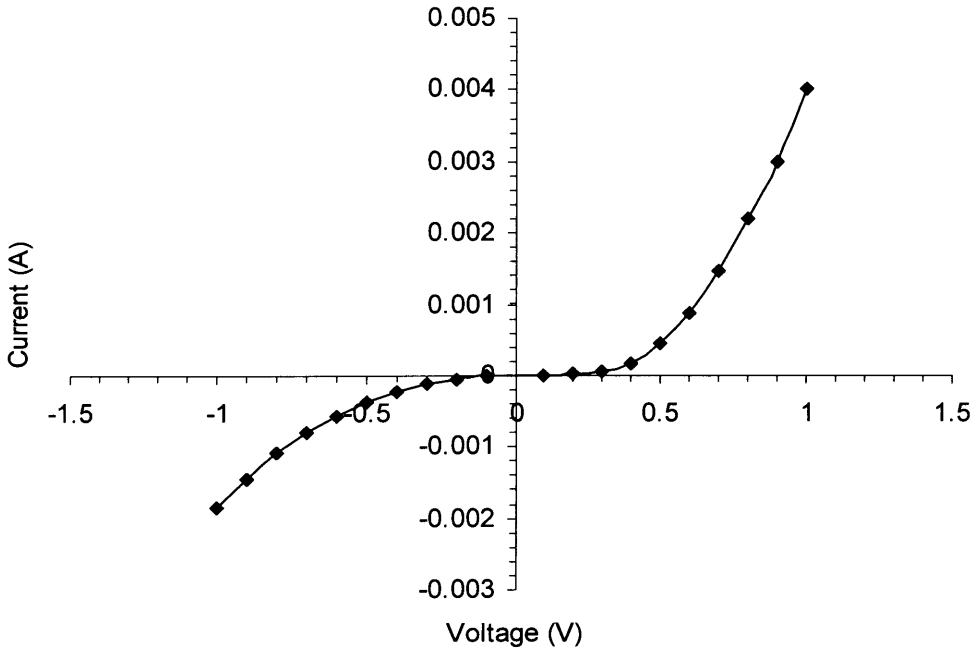

Figure 6-47 (0.15cm)^2 30/60 nm Ni/Au Schottky contact fabricated on GaN, the ohmic contacts used to probe the Schottky contact were 30/100/30/30 Ti/Al/Ti/Au contacts annealed at 800°C for 30s. These contacts exhibited an Is of 5.6x10^{-6} A, an ideality factor of 4.3 and a barrier height of 0.56V (averaged over four contacts) and a reverse leakage current of -1.853 mA at -1V.

6.6.2 150 nm Au

After the first set of contacts an all gold contact was tried. Gold contacts have exhibited varying performances highly dependent on the surface pre-treatment [295] [296]. However, all the published results have reported results significantly better that the ones found here (Figure 6-48). This being said gold would not be this author's first choice of contact as gold contacts tend to flake off during probing and also, as reported recently [297], may be more prone to degradation than Ni/Au contacts which are also more durable during probing as-well.

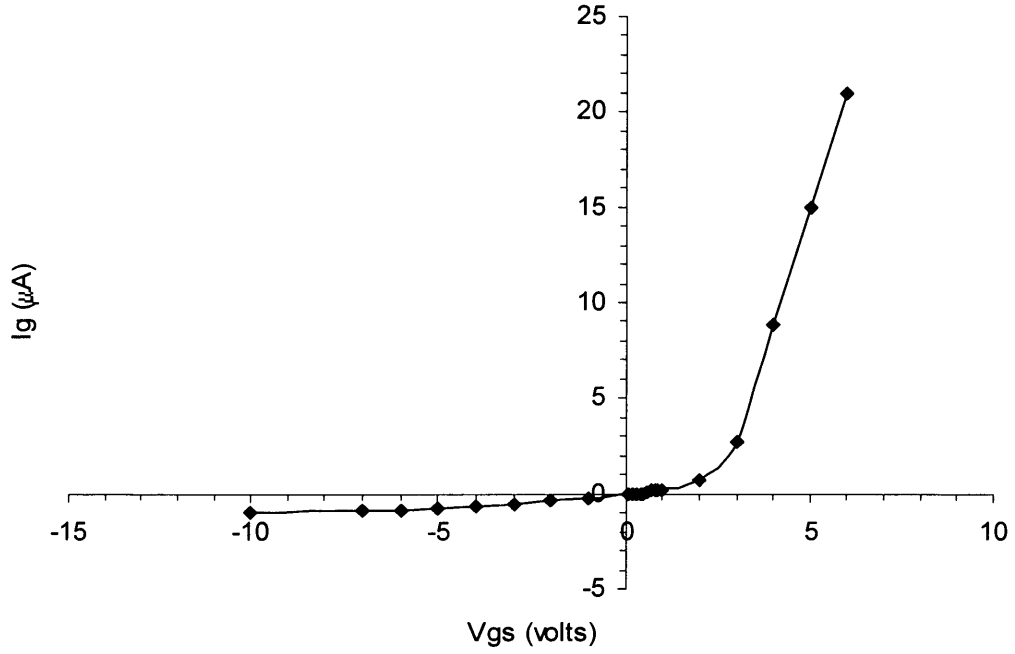

Figure 6-48 The gate current as a function of source gate voltage for a one hundred micron device with a 160 nm Au gate. The saturation current Is was 2.8×10^{-8} A, the ideality factor was 18.1 and the barrier height was 0.48 V (gate area was taken as 250 microns square), the reverse leakage current reached -1 micro-amp at -10V.

6.6.3 6/150 nm Ni/Au

The third Schottky contact that was tested used only a very thin layer of Ni to improve the durability of the mostly Au Schottky contact. Fortunately this very thin layer of

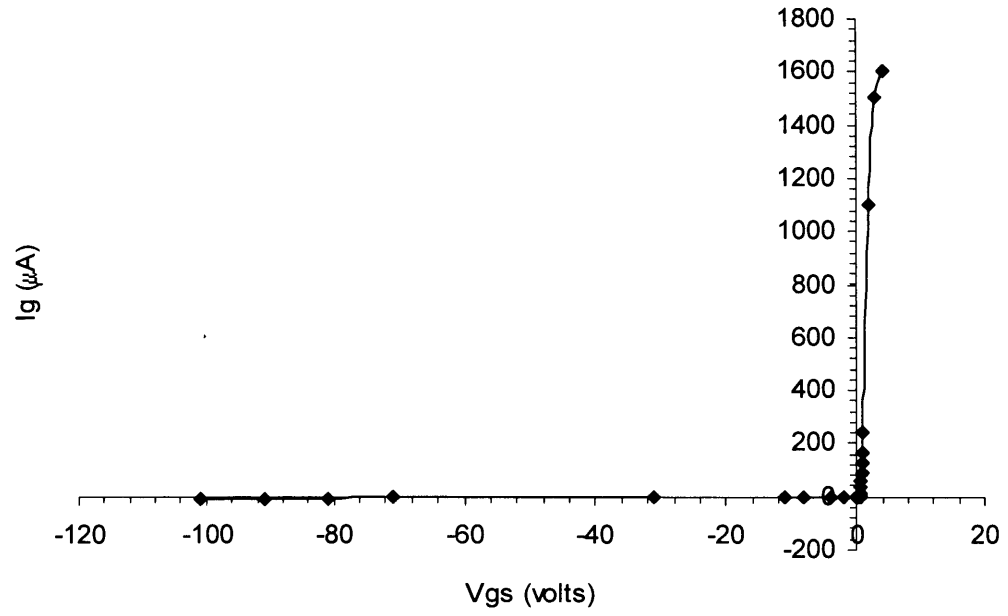

Figure 6-49 The gate current as a function of source gate voltage for a one hundred micron device with a 6/150 nm Ni/Au gate. The saturation current Is was 1.8×10^{-11} A, the ideality factor was 1.86 and the barrier height was 0.66 eV (gate area was taken as 250 microns square), the reverse leakage current reached -1 micro-amp at -10V and -10 micro-amps at -90V.

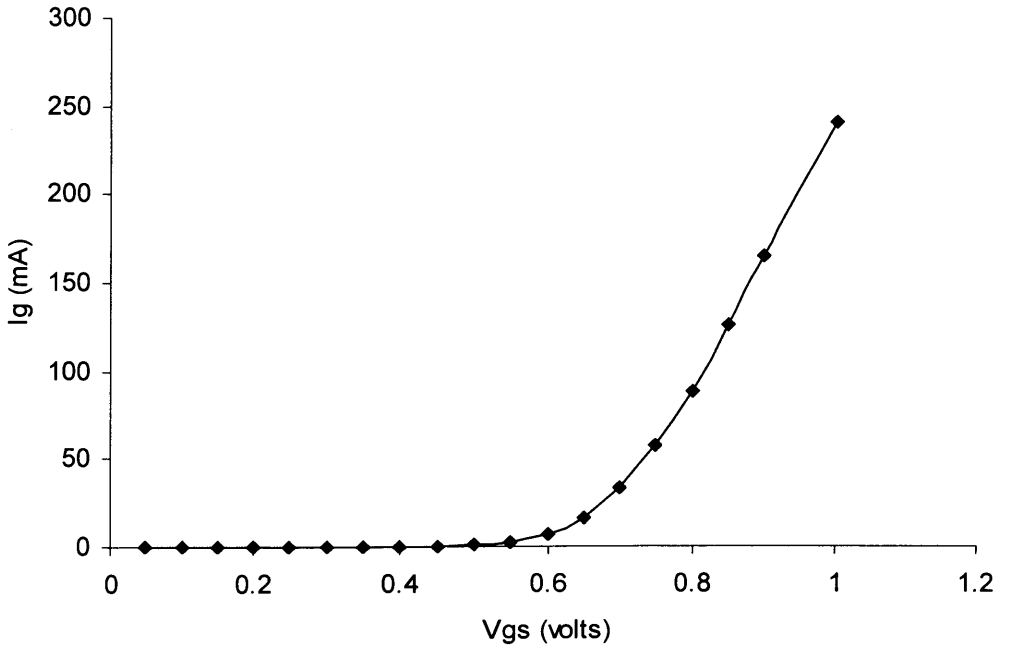

Figure 6-50 More detailed forward turn-on characteristics of the 6/150 nm Ni/Au Schottky contact detailed in Figure 6-49.

nickel also improved the characteristic of the diode which now exhibited a ideality factor of 1.86 and a barrier height of 0.66V. Although this was still far short from the best contact being reported in the literature at the time (see [296] or [298] among others) these contacts had a high breakdown voltage and a reverse leakage current that was very low. The ideality factor and the barrier height could both almost certainly be improved by treatment of the surface prior to the metal deposition.

The $ln(I)=f(V)$ and $ln(I)=f(V-IR_s)$ plots for this 6nm/150nm Schottky contact are shown in Figure 6-51. R_s was estimated from the linear part of Figure 6-50 (from 0.8-1V) as being 1162Ω, this high resistance was most likely due to the small size of the contact.

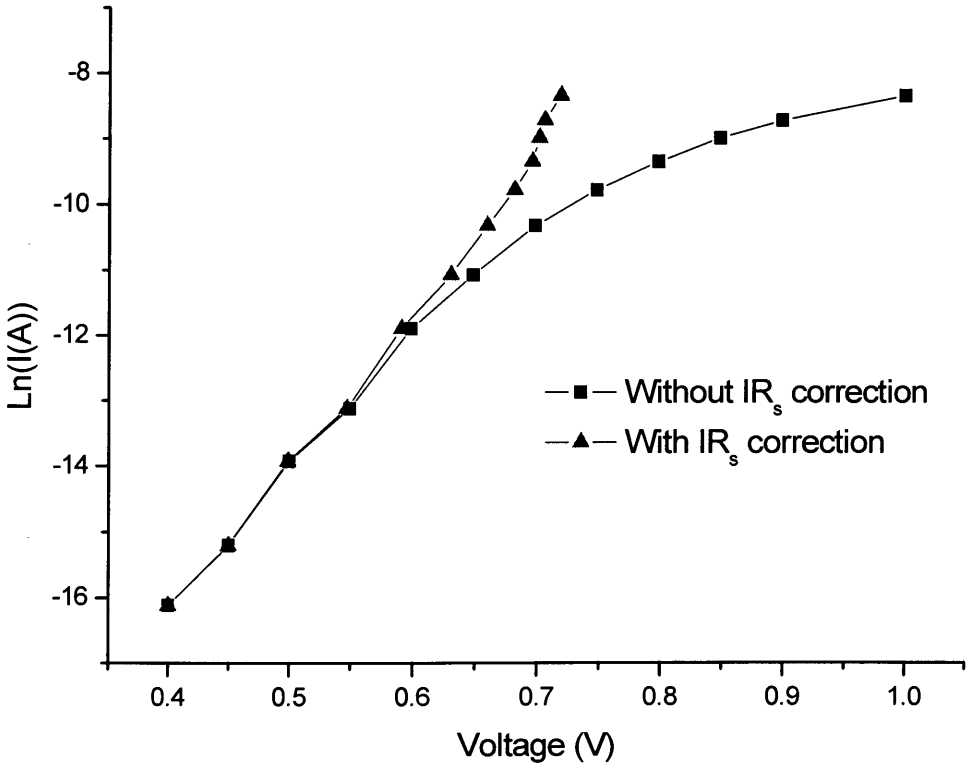

Figure 6-51 Variation of the natural logarithm of the forward current measured as a function of applied voltage without taking account of the series resistance (black squares) and with (red triangles).

The reasons for the behaviour of the Schottky contacts reported above are given in [299]. Due to the short range nature of bonds between metals, for good adhesion surfaces must be adjacent. In [299] the authors report on an oxy-nitride layer on the surface of GaN which separates Au contacts from the GaN surface. Ni layers remove this interface layer whereas Au does not; this was thought to be due to the much greater solubility of oxygen and nitrogen in Ni than in Au. This thin interfacial layer explains the poor adhesion of the Au contacts compared to the Ni/Au contacts. Also reported in [299] was the much greater crystal quality of Ni/Au contacts compared to Au gold contacts. This is due to the much greater lattice mismatch between Au and GaN compared to Ni and GaN. As is reported in [299], thin Ni layers form epitaxially on GaN i.e. the Ni and GaN lattices align; furthermore, the Au layer will align with the Ni layer, yielding a high structural quality. The above is true for thin films of Ni (~5nm), but the structural quality is found to deteriorate as the Ni thickness is increased; this explains why the 6nm/150nm Ni/Au contact was observed to have much better properties than the 30nm/60nm Ni/Au contact.

6.7 Device theory and results

In this section first a device model is presented and use to model a MESFET type device reported in the literature. After the theoretical dc IV curves generated with the model are compared with the experimental results reported the dc IV curves of one of the HFET devices fabricated by the author are presented. From this dc IV curve the drain current as a function of gate voltage is plotted and from the fit to these data the transconductance of the device as a function of the gate voltage is also plotted.

6.7.1 Device model

In this section the MESFET model presented in [14] is applied to a MESFET with the parameters of the GaN based device reported in [300]. These parameters were a gate width Z_G of 100μm, a gate length L_G of 0.3 μm, a active layer depth W of 200 nm, a doping level N of $2.7\text{x}10^{17}$ cm^{-3}, a mobility μ of 270 $cm^2V^{-1}s^{-1}$ and a source gate and gate drain $L_{sg} = L_{gd} = 1$ μm. The gate metalisation was Pt/Au and using values for the

work function of GaN and Pt of 4.1 and 5.65 the built in voltage across the depletion region associated with Schottky diode V_{BO} is 1.55V.

Figure 6-52 shows a schematic of a realistic MESFET device. In order to calculate a basic model of the behaviour of such a device several simplifying assumptions are made: both the drain and source resistances are neglected, the depletion region underneath the gate is taken to slope linearly from the source edge of the gate to the drain edge where it ends abruptly, one-dimensional conduction in the x-direction only is assumed, hot electron effects such as the substrate current shown are neglected and the electric field is assumed to vary linearly as a function of distance along the channel. This situation is shown schematically in Figure 6-53.

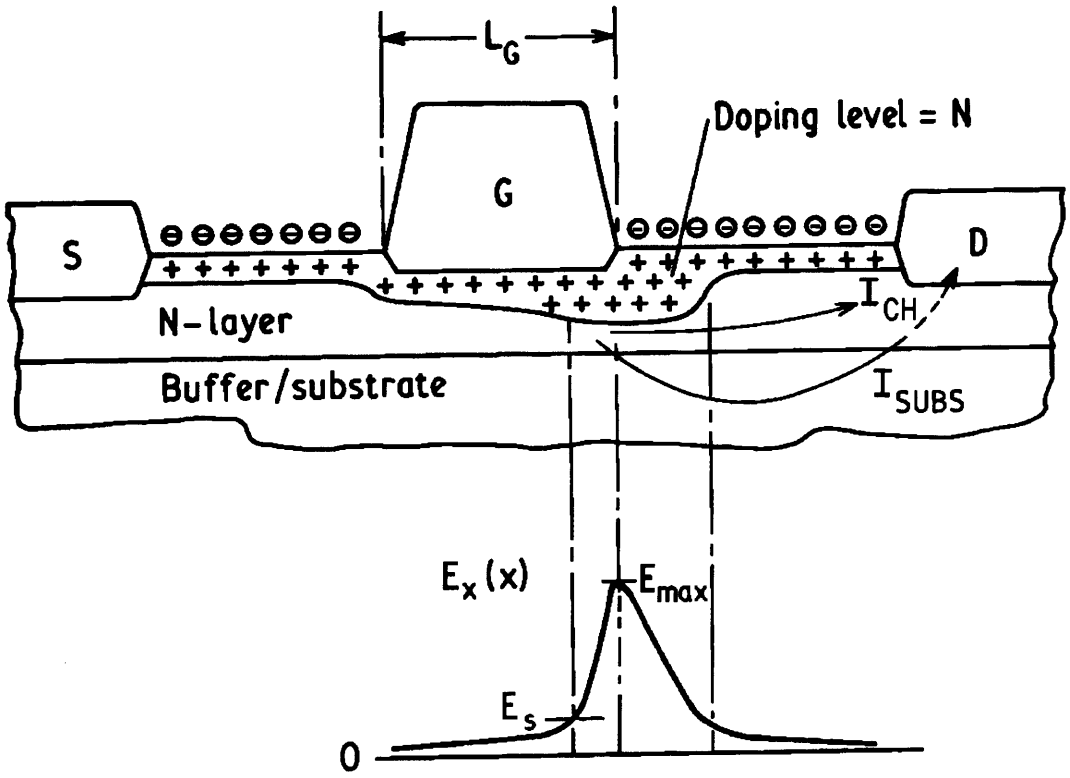

Figure 6-52 (above) schematic of an n-type MESFET showing depletion region at the surface and under the gate and channel and substrate current. (Below) Approximate variation of the electric field from left to right in the region from under the left-hand side of the gate to the edge of the drain.

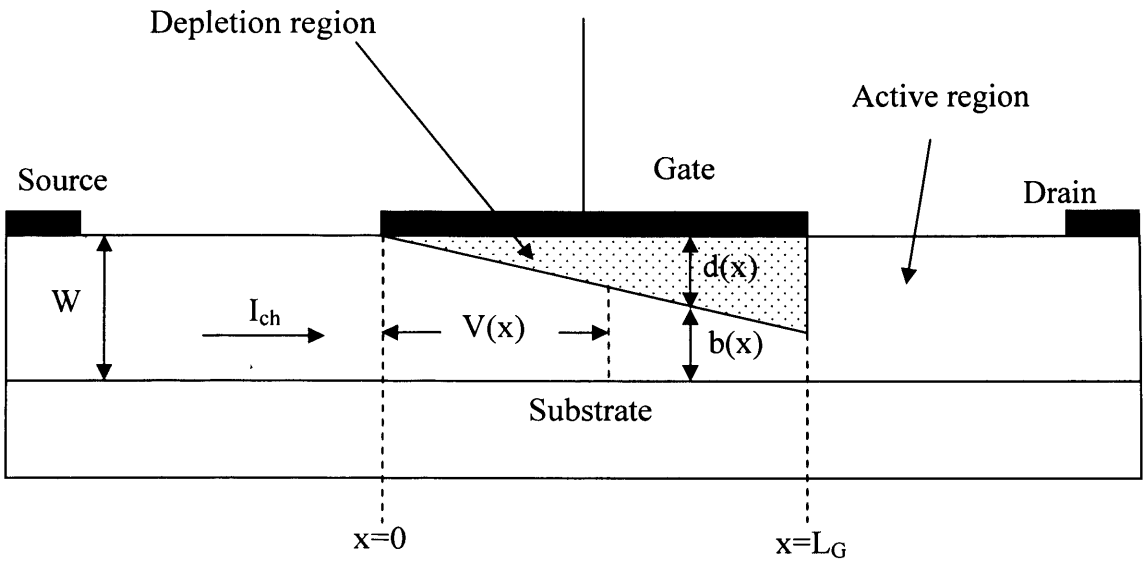

Figure 6-53 Schematic of the simplified physical model that will be used to model the dc IV output characteristic of a MESFET

When the source drain voltage is zero the voltage across the depletion region is

$$V_{across\ depletion} = V_{BO} + V_{SG} \quad \text{Equation 6-14}$$

Where V_{SG} is the voltage of the source relative to the gate. From [14]

$$V_{BO} + V_{SG} = \frac{q \cdot N \cdot d^2}{2\varepsilon} \quad \text{Equation 6-15}$$

Where ε is the dielectric constant of the semiconductor and q is the charge of an electron. Hence the device will become pinched off when a the souce-gate voltage equals the pinch-off voltage

$$V_P = \frac{q \cdot N \cdot W^2}{2\varepsilon} - V_{BO} \quad \text{Equation 6-16}$$

When a voltage is applied across the device Equation 6-15 becomes

$$V_{BO} + V_{SG} + V(x) = \frac{q \cdot N \cdot d(x)^2}{2\varepsilon} \quad \text{Equation 6-17}$$

Using dividing Equation 6-17 by Equation 6-16 and rearranging one finds that

$$b(x) = W\left[1 - \left(\frac{V_{BO} + V_{SG} + V(x)}{V_P + V_{BO}}\right)^{1/2}\right] \quad \text{Equation 6-18}$$

An element of the channel length Δx has a resistance

$$\Delta R = \frac{\Delta V(x)}{\Delta R} = \frac{\Delta V(x) \cdot b(x) \cdot qN\mu \cdot Z_G}{\Delta x} \quad \text{Equation 6-19}$$

Letting Δx tend to zero and eliminating $b(x)$ using Equation 6-18, Equation 6-19 may be written.

$$I_d \cdot dx = qN\mu WZ_G \left[1 - \left(\frac{V_{BO} + V_{SG} + V(x)}{V_P + V_{BO}} \right)^{1/2} \right] \cdot dV(x) \quad \text{Equation 6-20}$$

Where I_d is the drain current. Using the boundary conditions inherent with the linearly tapered depletion region with neglected source and drain resistances i.e. at x=0 V(x)=0 and at $x=L_G$ $V(x)=V_{ds}$, where V_{ds} is the drain-source voltage, and intergrating we have

$$I_d = \frac{qN\mu WZ_G}{L_G} \left[V_{ds} - \frac{2}{3}(V_P + V_{BO}) \left(\frac{V_{BO} + V_{SG} + V_{ds}}{V_P + V_{BO}} \right)^{3/2} + \frac{2}{3}(V_P + V_{BO}) \left(\frac{V_{BO} + V_{SG}}{V_P + V_{BO}} \right)^{3/2} \right] \cdot dV(x)$$

Equation 6-21

Where Equation 6-21 is valid when $V_{SG} \geq V_P - V_{dss}$ and $V_{ds} \leq V_{dss}$ for $V_{SG} < V_P - V_{dss}$. Equation 6-21 is plotted for the GaN MESFET reported in [300] in Figure 6-54. As may be seen by comparing Figure 6-54 with Figure 6-55 (the experimental results for the device modelled in Figure 6-54) the model predicts well the threshold voltage of the device and if the drain current density were an order of magnitude lower the model would fit the observed characteristics well.

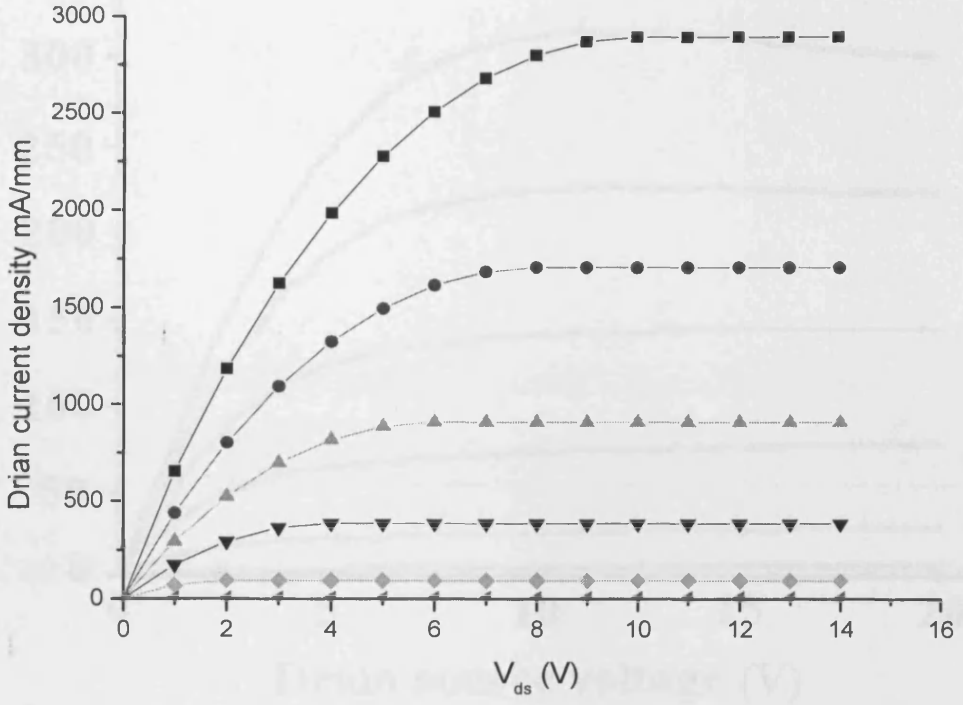

Figure 6-54 The theoretical curves generated from using the parametes given in the text. The experimentally observed I-V characteristics are shown in Figure 6-55, the order of magnitude difference between the theoretical and experimental results are due to the theorectical model neglecting the source and drain resistances. The gate voltage is shown varied from +1 to -9V in 2V steps

The reason that the drain current density is an order of magnitude higher for the theorectical devices compared to the experimentally observed characteristics is due to the fact that the source-gate and gate-drain resistances were neglected in the model. From [14] the resistance of a region of semiconductor is given by

$$R_S = \frac{L}{qN\mu WZ_G} \quad \text{..... Equation 6-22}$$

Equation 6-22 gives for the devices considered here a source-gate resistance (equal to the gate-drain resistance) of 47Ω and a resistance for the region under the gate of 14Ω. Hence the device model has a total resistance of 14 Ω whereas the actual device would have a resistance in the range of 108 Ω approximately an order of magnitude higher. This explains the higher drain current density predicted by the model.

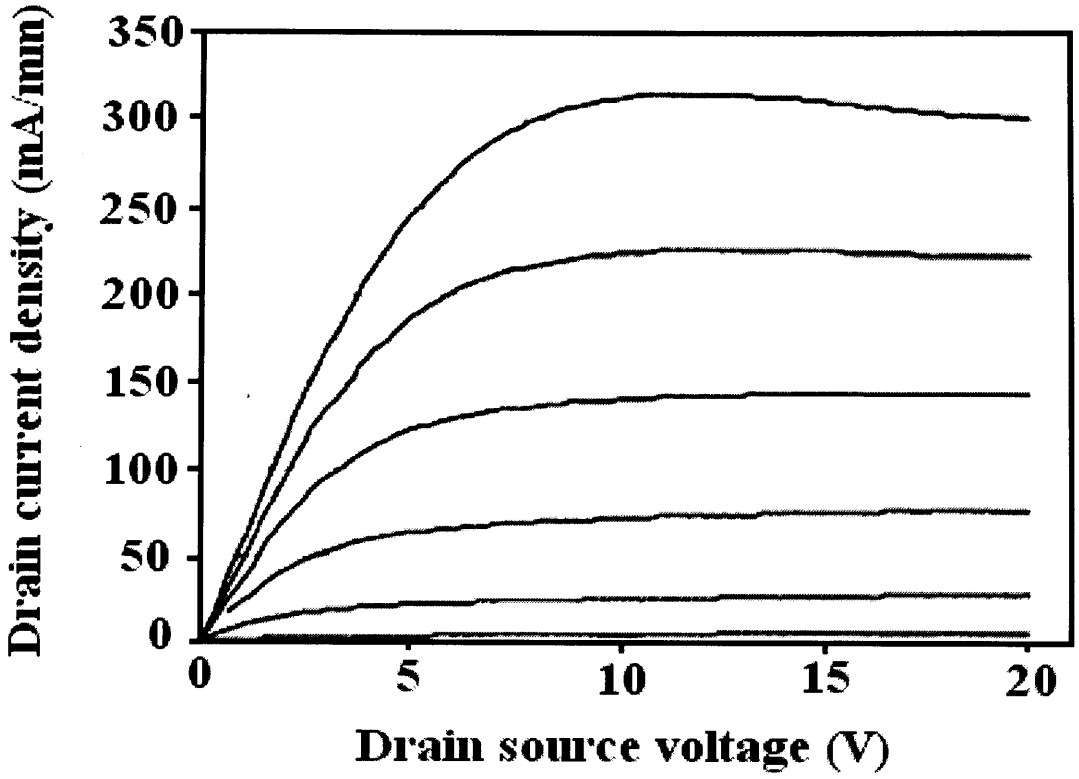

Figure 6-55 Experimental dc IV characteristics of the device reported in [300] the parameters of which were used to generate the theoretical dc IV curves shown in Figure 6-54. The gate voltage is shown varied from +1 to -9V in 2V steps

6.7.2 Experimental results

Despite the poor ohmic contacts and the high sheet resistance of the mesa isolated HFET material with the 15/100/50/100 nm Ti/Al/Ti/Au ohmic contacts annealed at 800°C for 30s a device was fabricated using this sample. The gates were fabricated with 6 nm of nickel followed by approximately 150 nm of gold. There was a large deviation in the saturation current exhibited across the wafer which ranged from approximately 0.2 mA to 2.3mA. The characteristics for the 2.3mA I_{Dmax} device are shown in Figure 6-56.

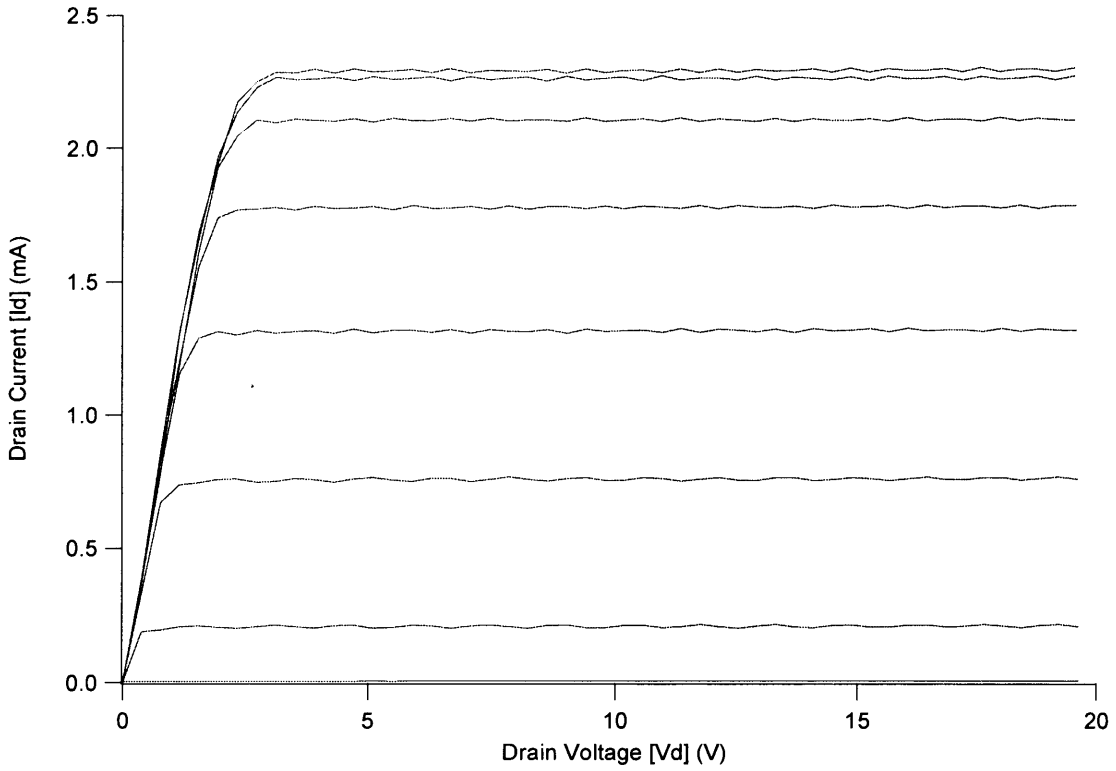

Figure 6-56 Device dc characteristics for a 100 micron gate length device, 15/100/50/100 nm Ti/Al/Ti/Au ohmic contacts annealed at 800°C for 30s and 6/150 nm Ni/Au Schottky contacts. Saturation occurs at Vg = 0V with Vg = +0.5V showing no significant current increase. Device was pinched of at Vg = -3V. Gate voltage is shown stepped in 0.5V steps.

The device is pinched off at -3V gate voltage with saturation occurring more or less at 0V, +0.5V hardly increases the drain current at all. These devices started to break down at around 90V, this is quite a high breakdown voltage for a gate with no specific design such as gate pads to mitigate the high fields at the drain side edge of the gate such as a gate pad. This high breakdown voltage is either due to the small current that was being drawn through the device or to the fact that there was a offset of the gate towards the source in these devices.

From Figure 6-56 the drain current as a function of gate voltage could be determined. A graph of this device characteristic is given in Figure 6-57. From the polynomial fit to the I_{ds} versus V_{gs} data the transconductance given by Equation 6-23 may be found.

$$g_m = \frac{dI_d}{dV_{sg}} \quad \text{Equation 6-23}$$

The transconductance a function of gate voltage is given in Figure 6-58.

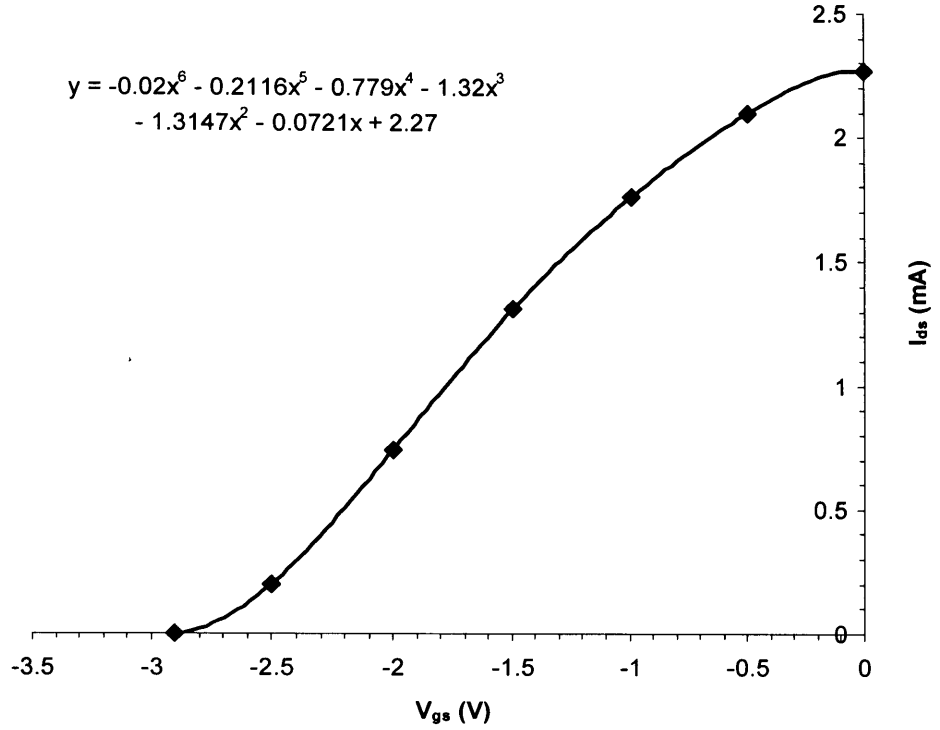

Figure 6-57 Variation of I_{dss} as a factor of the gate voltage applied (grounded source). The line shown is a fit to the data shown by the equation shown. Pinch-off is estimated from the fit to the data to be -2.9V.

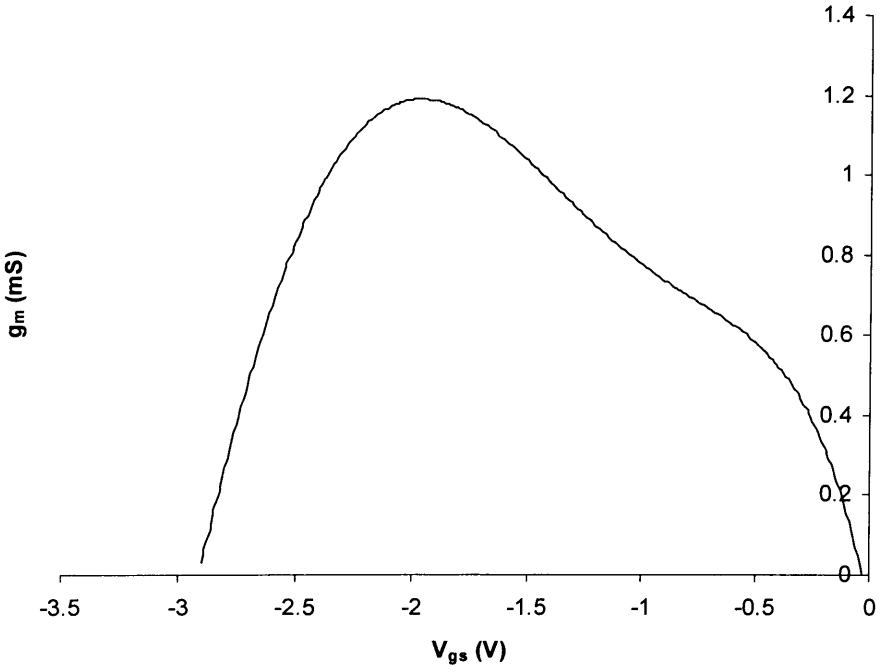

Figure 6-58 Variation of transconductance as a function of the applied gate voltage for the device whose IV characteristics are shown in Figure 6-56

6.8 Summary

Three steps must be achieved in order to fabricate a basic working field effect transistor: the device must be isolated, ohmic contacts with a low contact resistance and a rectifying gate contact must be formed. The HFET material that was used in this work had a higher sheet resistance than would have been expected (300 to 400 ohm/square would have been preferred); however, it was not possible to take advantage of what current carrying capacity the material offered as the ohmic contacts that were fabricated in this work gave contacts with resistance that were two orders of magnitude too high. Various reasons for this high contact resistance are given in the text including oxidation of the Ti and Al and diffusion of Si and Ga. The quality of ohmic contacts to HFET material is very sensitive to a number of different interrelated parameters and it is important to obtain the combination exactly right otherwise, as was seen above, only poor results will be found. This is especially true for GaN and AlGaN because of their wide band gaps and high density. A workable Schottky contact has been demonstrated though special cleaning and annealing methods could be developed to improve on the results found. Despite the high sheet and contact resistance a device showing a transconductance was fabricated; however because of the low current, and the fact that the device pitch was 100 μm smaller than the pitch of the probes available at the time it was not possible to make any RF measurements of the device.

7 Thesis summary and future work

Alloying of the III-nitrides allows heterostructure devices to be fabricated. Due to the strong ionic bonds of AlN and GaN they and their alloys are wide band gap material and hence once fabricated into devices can hold high voltages, suffer from low noise and can be run at higher temperatures than traditional III-V and silicon based devices. Due to the way in which 2-DEGs form in III-nitride heterostructure field effect transistors an electron concentration orders of magnitude higher than that found in III-V HFETs is possible, this high current carrying capability coupled with the high voltages leads to high power devices. Because the III-nitrides may be engineered into heterostructure field effect transistors with high transconductance, and because of the low relative permittivity and hence low gate capacitance, high frequency operation should be possible. Couple this with high power and with operation possible in both high temperature or otherwise hostile environments e.g. space, gallium nitride based transistors become enabling devices for a wide range of novel system formats or improvements, such as on engine sensors, improved power amplifiers for mobile phone base stations or satellite communications.

Some properties of gallium nitride and of field effect transistors made from this material are presented in this thesis. The crystal structure of the lowest energy (and therefore the most common) state of gallium nitride, wurtzite gallium nitride is presented. The thermal properties of gallium nitride including its melting point, thermal conductivity and thermal expansion coefficient are given. The thermal conductivity of gallium nitride, which theoretical predictions have given to be as high as that of silicon carbide, is one of the reasons that gallium nitride makes such good high power devices. The band structure of wurtzite gallium nitride and its variation with temperature and stress is presented as well as the effective electron mass and the ionisation energies of some of the dopants of gallium nitrides. Some of the mechanical properties of GaN are offered including the hardness, which is of course a relative scale whereby harder materials scratch less hard materials (diamond is the hardest material known to man). The electrical properties of gallium nitride are discussed including the reason for the n-type conductivity of intrinsic gallium nitride,

the DX-centre like behaviour of some of the dopants of gallium nitride (Section 3.5.1), and the mobility and velocity of electrons in gallium nitride.

A new method of measuring the conductivity of a semiconductor wafer that is non-destructive, requires no wafer processing and that works on thin, micron-thick semiconductors is presented. This method utilises the effect that conduction in a semiconductor has on the bandwidth of the resonant peak of a microwave dielectric that is placed near to it. The increase in the bandwidth that is exhibited when the microwave dielectric is placed near the semiconductor is due to ohmic power loss in the semiconductor. Because during resonance the electric and magnetic fields outside the dielectric drop exponentially as a function of distance away from the dielectric, as the dielectric is move towards and away from the semiconductor wafer there is a noticeable change in the bandwidth of the resonant peak as the electrics fields in the wafer increase and decrease and the amount of power lost through ohmic heating is increased or decreased. This increase or decrease of the bandwidth of the resonant peak as a function of distance towards or away from the semiconductor may be measured experimentally and correlated to the conductivity of the semiconductor if the thickness of the conductive region is known. The experimental results taken from a wafer of gallium nitride are presented; these results were in accordance with the expected conductivity calculated from the charge carrier concentration of the wafer given by the manufacturer and mobility values taken from the literature.

A relevant background to ICP etchers is presented; this includes how ICP plasmas are initiated and sustained, and how inductively coupled plasmas are used in the semiconductor processing industry. A literature review of the uses of chlorine based ICPs in etching the III-nitrides, principally gallium nitride, is given, this includes trends in the etch rate as a function of $\%Cl_2$ in the plasma, pressure, temperature, power to the coil antenna, and power used to create dc bias. After this a section giving some theory about effects that could limit the etch rate of any particular material in a given plasma are given though again the emphasis is on the etching of gallium nitride with chlorine based plasmas. Experimental results are presented for the etching of gallium nitride with a photoresist mask in both Oxford Instruments ICP 180 an ICP 380 systems. Measurements of the etch rate of gallium nitride and the selectivity of gallium nitride to photoresist are given. The experiments performed in the ICP 180

were supposed to yield an etch that was highly selective of GaN over photoresist; the best results were gained after an extension to the original experiment and were an etch rate of 660 nm/min coupled with a selectivity of 0.9 which, was comparable with results found in the literature. The results taken with the ICP 380 show good trends for all the system parameters that were varied, the uncertainty associated with these measurements was much less than those associated with the ICP 180 due to the method of measurement.

Plasmas generated using the ICP 380 were used to electrically isolate the heterostructure field effect transistors that were fabricated at Cardiff University using material that was supplied by *Nitronex* a company that specialises in the growth of III-nitride heterostructure material for FET fabrication on silicon. In order to facilitate the easy traverse of the mesa edge by the gate, source and drain metals a method of flow baking the resist to make the sidewalls of the etched mesas acute was developed. A workable Schottky contacts to this HFET was developed. The best ohmic contact reported here had a resistance of 7.2 Ω/mm approximately an order of magnitude worse than the best results found in the literature. Despite the poor ohmic contacts and a material sheet resistance that was higher than would have been ideally liked a batch of working devices was fabricated. These FETs exhibited a minute source drain current but dc I-V characteristics were taken and those for the best device fabricated are presented.

There are several extensions that could be made to the above work. The first and most obvious flaw in the work is the lack of a good ohmic contact to the material. It is very important that a good ohmic contact is found at the start of the project, and it should be the first thing that is attempted once the process operator has enough experience to ensure that mistakes are kept to a acceptable minimum. The problem with contact formation is that there are a great deal different, interrelated factors that will affect the final contact. In this respect it could be that the orthogonal experimental design could offer a way of finding a good contact quickly. Whatever the method a systematic search varying the metal thickness of all the metals in the contact as well as the anneal temperature and time should be conducted. In order for such a search for a good contact to be successful a large amount of time, effort and money would have to spent, this is especially irksome as even afterwards it is not guaranteed that the

contact will work on any material other than that on which it was first fabricated. It would be interesting (but costly) to see how the contact had to be varied for different materials parameters i.e. the thickness of cap or spacer layers etc. It has previously been reported in the literature that etching of the gallium nitride surface has the effect of improving the contact resistance of ohmic contacts made to the etched surface; this is thought to be due to the preferential etching of the lighter more reactive nitrogen atom leading to nitrogen vacancies which dope the surface n-type. Once a reliable contact is found it could be improved by etching of the surface in this though of course experiments to find a suitable etch would need to be performed.

For the method of measuring the conductivity it would be interesting to know how well the cylindrical co-ordinate based system used by *Superfish* works approximating the conductivity of small square samples (such an experiment was performed but it was before the method had been corrected for various errors that were leading to erroneous results). If a good approximation was given then this method would become useful even after the wafer had been cleaved; this would mean that the method would be useful for all wafer sizes not just the size for which a cavity had been fabricated for.

Further work to be carried out on the Schottky contacts includes developing better surface preparation procedures to improve the barrier height and the ideality factor of the contacts; however, until a good ohmic contact is fabricated this is not critical as, as has been mentioned, this Schottky contact seems to work well enough.

8 Appendixes

Appendix A. Wurtzite Miller-Bravais indices [301]

MILLER-BRAVAIS INDICES for planes in hexagonal lattices (start)

- Define a set of *four* basis vectors, a_1, a_2, a_3, and c as shown at right:
- Determine the ***intercepts*** of the plane of interest on the four basis vectors
- Take the ***reciprocals*** of the intercepts
- Multiply the reciprocals by the smallest common factor that will ***clear all fractions***
- Enclose in parentheses ***(h k i l)***

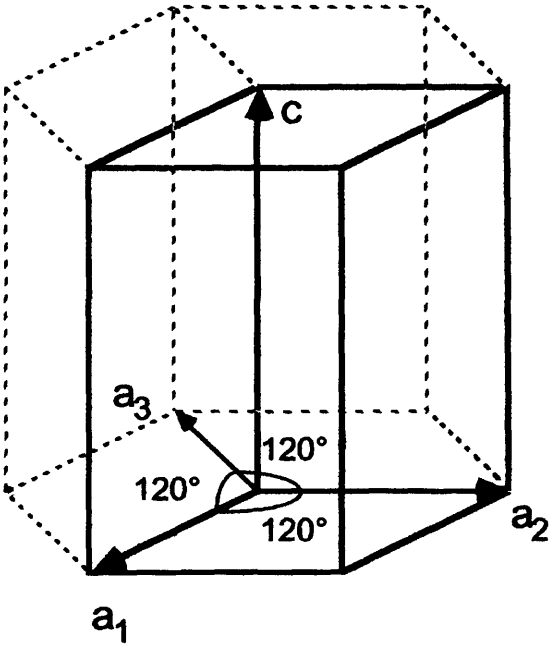

Examples:

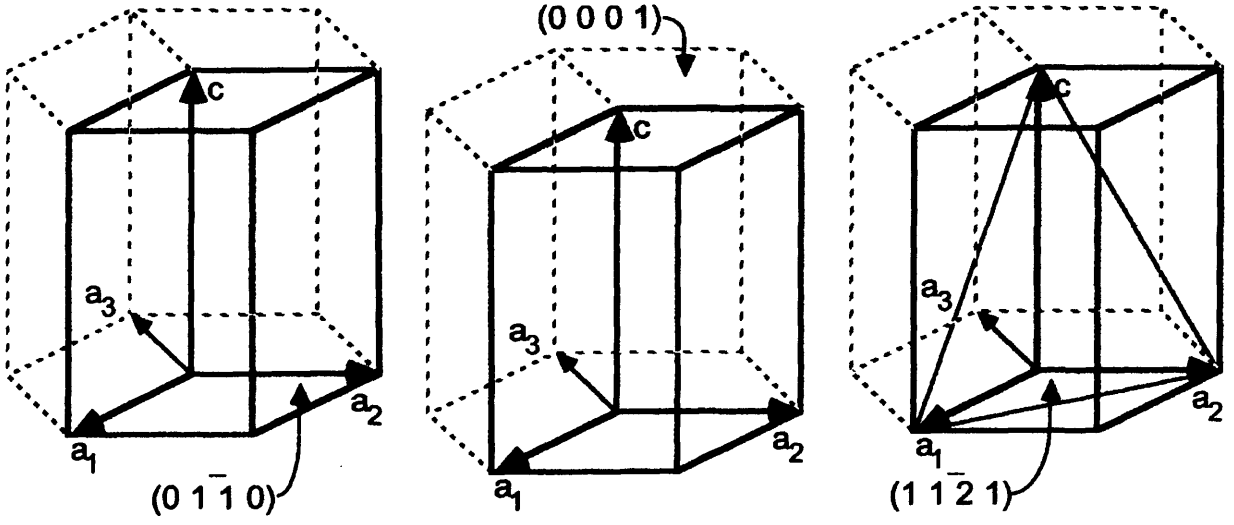

- Note: the relationship between a_1, a_2, and a_3 is such that

$$-i = h + k$$

Q: Why bother with an extra index?

A: Now planes in the same ***family*** are identified by ***permutations*** of the (first three) indices, as with Miller indices for the other systems:

e.g. $\{11\bar{2}0\}$ consists of

$(1\,1\,\bar{2}\,0)$ $(\bar{1}\,2\,\bar{1}\,0)$ $(\bar{2}\,1\,1\,0)$ $(\bar{1}\,\bar{1}\,2\,0)$ $(1\,\bar{2}\,1\,0)$ $(2\,\bar{1}\,\bar{1}\,0)$

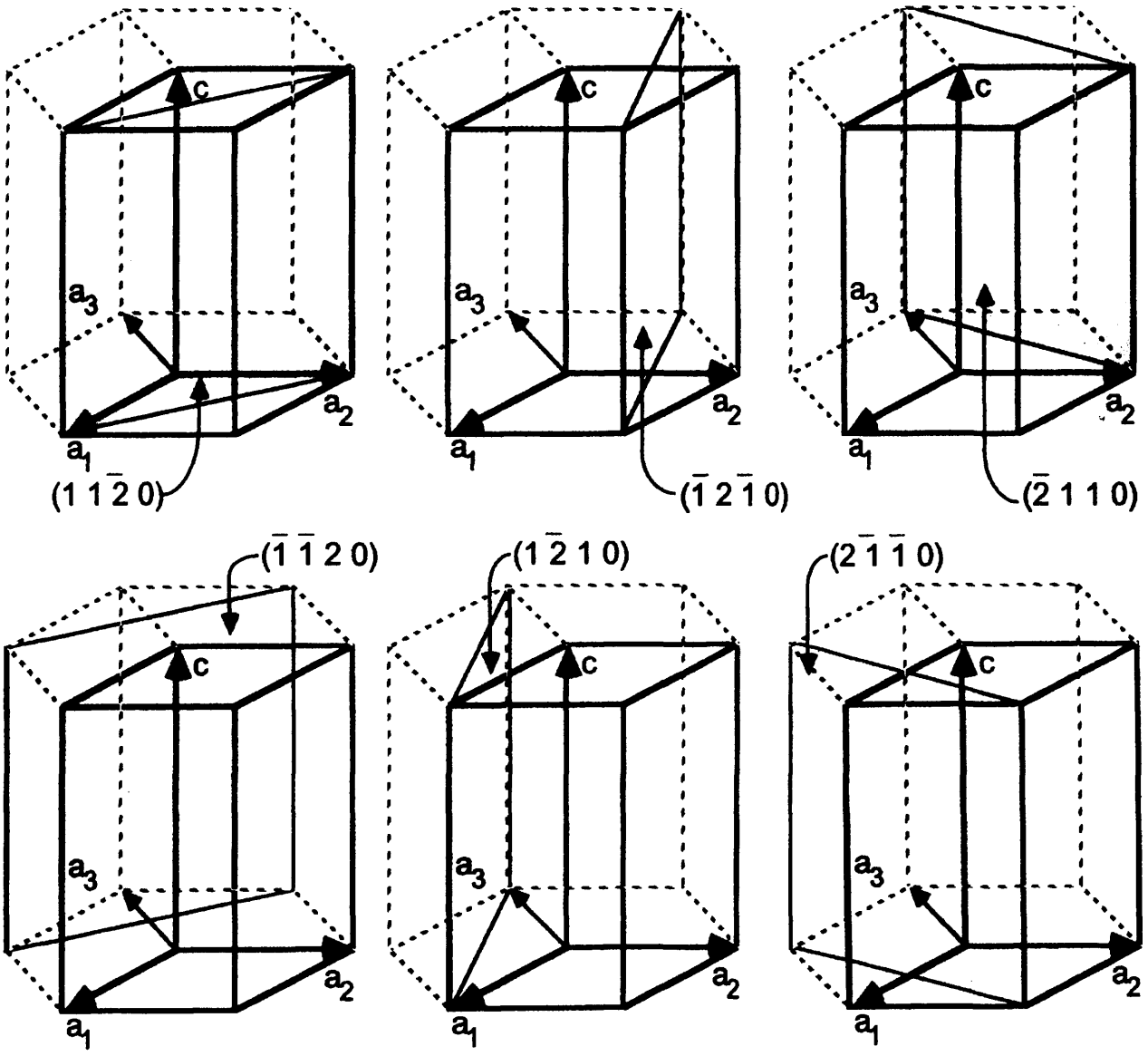

Appendix B: Superfish.

A large part of the following discussion is extracted from the help documentation that comes as part of the Superfish package; the reader is directed to this source for further information on any of the points covered below.

Fish and CFish are the radio-frequency field solvers of the collection of programs called Superfish. Fish solves problems with real fields. CFish is a version of Fish that uses complex variables for the RF fields, permittivity, and permeability. Both programs must be run after Automesh for radio-frequency field problems. The codes are run in the following order:

- Automesh
- Fish or CFish
- WSFplot (optional)
- SF7

Fish assumes cylindrical symmetry unless told not to; hence, for a problem with cylindrical symmetry only half of the radial cross-section of the problem needs to be described and the fields solved for. Figure 8-1 shows the area defined for solution for the case of a cylindrical cavity; this cylindrical cavity has a ledge with a height of approximately half the cavity's height; on the ledge is placed a semiconductor wafer; in the centre of the wafer there is placed a cylindrical quartz stand and on the quartz stand there is a dielectric resonator which is resonating. Figure 8-1 shows the field lines of the solution generated by Superfish for this case. The dielectric is actually quite hard to see due to the density of field lines within and near to it. The actual cavity which Figure 8-1 describes could be formed completely by rotating Figure 8-1 by 360° with its right hand edge of the figure as the axis of rotation.

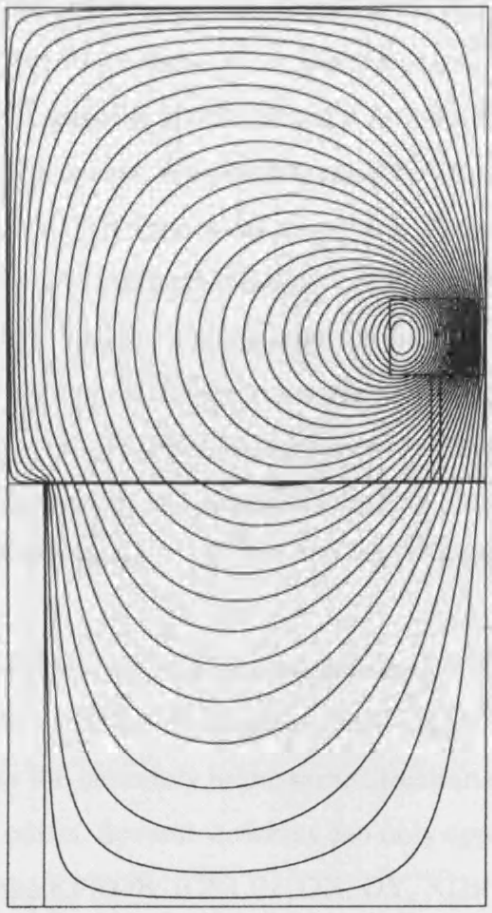

Figure 8-1 showing how the problem area defined for Superfish (here shown solved with field lines) is only half the radial cross section of the complete cylindrical volume.

Figure 8-1 is actually the graphical output of the fields generated by the code in Figure 8-2. In order to describe a problem such as that in Figure 8-1 code such as that shown in Figure 8-2 must be written for input to the Automesh program; this problem description is usually written, modified and run as a *.txt* file but the file type *.am* may be used to run Automesh. The title of the input file, in Figure 8-2 "Gallium nitride wafer. Wafer-dielectric separation 6mm" is entered before the first REG namelist. Titles of up to ten 80-character title lines are allowed. Each Superfish subprogram prints the problem title in its respective output file. Automesh will write a warning message if the input file contains no title lines or more than ten title lines.

Automesh can read four sets of namelist variables named REG (for region), PO (for point), MT (for material table) and POA (for single-point boundary values). Namelist sections start with &REG, &PO, &MT, or &POA or with $REG, $PO, $MT, or

$POA and end with &END or just & or with $END or $. The REG namelist defines properties of a region defined by a series of connected points. The connected points, defined by consecutive PO namelist entries, usually forms a closed region with straight lines connecting the points. A boundary condition may be defined by the user on an unclosed region (a series of connected points that do not form a polygon) using the IBOUND variable. The PO points that define a region must follow their associated REG namelist. A new REG namelist starts a new region. The order of occurrence of REG and PO sections is important. If different regions overlap or share a boundary, subsequent regions replace properties defined by previous regions. The lines that connect different points defined by the namelist variables PO are straight lines by default but may be made non-linear.

The PO namelist points for the first region must define a closed area that all other regions must fit into. Points in other regions may lie along the region 1 boundary but these points must traverse the boundary in the same direction used for region 1 to avoid potential meshing errors. Several variables can only appear in the first REG namelist. These include the KPROB, ICYLIN, DX, DY, XDRI,YDRI NBSUP, NBSLO, NBSLT and NBSRT. Other variables that are not used by Automesh that are passed to the solver codes through the Automesh solution file can appear in any REG namelist, but it is recommended that they appear in the first region. Automesh stores only the last entry for a variable in the solution file. FREQ and MAXCY, also shown at the top of Figure 8-2 are respectively a guess value (or starting value) of the resonant frequency of the system and the maximum number of iterations FISH will cycle through trying to fit the resonant conditions [181].

KPROB specifies the problem type: KPROB = 1 is Superfish problem (RF frequency), KPROB = 0 is a Poisson or Pandira problem (electrostatics). ICYLIN specifies the co-ordinate system 0: rectangular; 1: cylindrical. For problems with cylindrical symmetry, the correspondence between coordinates R,Z and X,Y depends upon the type of problem. For Superfish problems, X and Y refers to Z and R respectively. The default co-ordinates of a Superfish problem are cylindrical. DX and DY specify the X and Y mesh size in the first region. The default value of DX is 2% of the maximum X value and the default Y value is calculated from the X value depending on the problem [181]. XDRI and YDRI designate the x and y co-ordinates of

the point that the system is driven from. In the case of Figure 8-1 the excitation point is shown by the black dot in the centre of the dielectric.

NBSUP, NBSLO, NBSLT and NBSRT are the variables used to define the boundary conditions of region 1 and they are only used for this first region, IBOUND being used for all others. NBSUP, NBSLO, NBSLT and NBSRT define respectively the boundary conditions for the upper, lower, left-hand and right-hand edges of the first region. The Poisson Superfish codes can accommodate two types of boundary conditions. The Dirichlet boundary, in honor of P. G. L. Dirichlet (1805-1859) and the Neumann boundary, in honor of Karl Gottfried Neumann (1832-1925). The essential characteristics of the Neumann and Dirichlet boundary conditions are given in Table 8-1.

Field	Dirichlet	Neumann
Magnetic	parallel to boundary.	perpendicular to boundary.
Electric	perpendicular to boundary.	parallel to boundary.

Table 8-1 Table showing characteristics of magnetic and electric fields at Neumann and Dirichlet boundaries [181].

From these conditions and a knowledge of the problem needing to be solved the boundary conditions at the various boundaries may be set. For a Dirichlet boundary set the relevant parameter (e.g NBSUP, NBSLT, IBOUND etc.) equal to 0 and for a Neumann boundary set it equal to 1.

The default boundary conditions for the outside edge of the system and the interfaces between regions are shown in Table 8-2 and Table 8-3.

Variable	Superfish
NBSUP	1
NBSLO	0
NBSRT	1
NBSLF	1

Table 8-2 Table showing default values for NBSUP, NBSLO, NBSRT and NBSLF the boundary conditions for the outermost edge of the system being modelled.

Default values in:	Superfish
First region	IBOUND = 1
Other regions	IBOUND = 1

Table 8-3 Table showing default values for the boundaries between materials defined within region 1.

The REG namelist variable MAT is the material number for a region. Every new region uses the default value MAT = 1 if the variable does not appear in the REG namelist. MAT = 0 is assumed to be metal ($\varepsilon_r = \infty$ and $\mu_r = \infty$), and MAT = 1 is assumed to be air or vacuum ($\varepsilon_r = 1$ and $\mu_r = 1$). If numbers other than 0 or 1 are used in a Fish or CFish problem, then MT namelist sections must be used to define the permittivity and permeability of each material using the variable names EPSILON for the relative permittivity and MU for the relative permeability (for TM modes); in Fish problems values of the relative permeability and permittivity are real only. MTID = *number* is used in an MT namelist to assign material properties to the material with MAT = *number*. By default each MT namelist is given an ID number that corresponds to its sequential location in the file. Default MTID numbers start with 2 in Superfish problems.

```
Gallium nitride wafer. Wafer-dielectric separation 6mm
&reg kprob=1, dx=0.03, dy=0.03, nbsup=0, nbslo=0, nbsrt=0, nbslf=0,
XDRI=3.343, YDRI=0.265, freq = 2940, maxcy=10 &

&po x=0.0, y=0.0 &
&po x=5.1, y=0.0 &
&po x=5.1, y=2.65 &
&po x=0.0, y=2.65 &
&po x=0.0, y=0.0 &

&reg mat=3 &
&po x=2.4, y=0.0 &
&po x=2.41, y=0.0 &
&po x=2.41, y=2.5 &
&po x=2.4, y=2.5 &
&po x=2.4, y=0.0 &

&reg mat=4 &
&po x=2.41, y=0.25 &
&po x=3.01, y=0.25 &
&po x=3.01, y=0.3 &
&po x=2.41, y=0.3 &
&po x=2.41, y=0.25 &

&reg mat=5 &
&po x=3.01, y=0.0 &
&po x=3.44, y=0.0 &
&po x=3.44, y=0.53 &
&po x=3.01, y=0.53 &
&po x=3.01, y=0.0 &

&reg IBOUND= 0 &
&po x=0.0, y=2.45 &
&po x=2.4, y=2.45 &
&po x=2.4, y=2.65 &

&mt mtid=3
epsilon=1.0
mu=9.418 &

&mt mtid=4
epsilon=1.0
mu= 4.25 &

&mt mtid=5
epsilon=1.0
mu=106 &
```

Figure 8-2 Example of a Superfish program for the gallium nitride on sapphire wafer (mu=9.418) a 6mm quartz stand (mu = 4.25) and the TiO_2 resonator (mu=106)

Appendix C: Mathcad code

Transfer of data from Superfish to Mathcad.

The fields calculated by Fish are written to an output file by SF7: *Outsf7.txt*. The fields in *Outsf7.txt* are in the form of a table of field magnitudes, with each set of magnitudes corresponding to one point of the mesh used in finding the problem's solution. If this file is cleaned of all the text except the field magnitudes and converted to a *.prn* file from a *.txt* file Mathcad can read the numerical field data into an array and perform calculations with it. The code used to calculate *g(h)* and to fit g(h) and then to fit the fit to g(h) to the experimentally observed variation of bandwidth with height above the wafer is given below.

Appendix D: FET fabrication process

Sample Cleaning

The sample of semiconductor was cleaned following the standard operating procedure (SOP) for cleaning at the time. Four beakers, one containing trichloroethane, one containing acetone, one containing methanol and one containing isopropanol (IPA) were placed on a hot plate set to ~ 110°C for ten minutes. While the beakers were still on the hotplate set to ~110°C the sample was placed in each beaker for five minutes in the order trichloroethane, acetone, methanol, isopropanol. The sample was blown dry with nitrogen before transferring it from one beaker to another and was blown dry with nitrogen after the final soak in IPA. After this the sample was examined with a microscope. If there was dirt still on the sample the sample would be put in acetone and then wiped with a cotton bud until clean as viewed under the microscope apart from the steps after the source-drain metal deposition when the risk of removing the metalisation prevented this.

Photolithography

Mesa pattern

In this case only S1813 SP15 was needed and this was spun on at 6000rpm with a spin time of 50s. Once the spin had finished the sample was removed and placed on a 97°C hotplate (on a glass microscope slide) for three minutes; this soft bake removed the solvent from the resist making it less likely to stick to the mask during mask alignment.

The mesa pattern was exposed for approximately 5s and developed for approximately 15 seconds in AZ240l developer; however the exposure time was dependent on the state of the mask aligner lamp which changes with time hence these figures are only

an approximation. Once the photoresist was patterned with the mesa pattern the sample was baked at 180°C for 15 minutes in order to reduce the angle of the sidewalls.

Edge bead removal

To remove the edge beads found on samples without tapered edges the mask pattern shown in the right hand side of Figure 6-1 could be used. To remove the edge beads the sample was first brought into firm contact with the mask to stop any movement of the sample as the photoresist dried during exposure. The sample was then given a long exposure of at least 36 seconds. The sample was then developed for approximately two minutes in 6:1 deionised water: AZ2401 developer solution until the edge beads were removed.

Metal lift-off

To define metal contacts a bi-layer resist lift-off process was used. The samples were cleaned as explained before. Next, two drops of EXP04002 lift-off photoresist were dropped onto the sample and spun on at 6000rpm. This lift-off photoresist was baked for one minute at 97°C followed by two minutes at 125°C, this was achieved using two separate hotplates and it was important that the sample be placed directly onto the hotter hot plate once it was removed from the cooler one, failure to do this resulted in the develop time of the lift-off resist being too quick. Once the lift-off photoresist had been baked a layer of SP1813 SP15 was spun onto the sample. For thin contacts a 6000rpm spin speed was used, giving a total photoresist thickness of about 0.6 microns after the oxygen plasma ash (see below); these sample was baked for two minutes at 97°C. For thicker contacts 2 layers of as SP1813 SP15 photoresist were spun on at 4000rpm; after a layer was spun-on at 4000 rpm the sample was baked for 3 minutes at 97°C, two 4000 rpm spin-ons gave a thickness of approximately 1.6 microns after the oxygen plasma ash (see below).

After the resist had been spun on edge beads were removed and the pattern would be exposed and developed. The expose time in this case was approximately 5s for the thinner photoresist and approximately 7.5s for the thicker. The sample would first be developed in AZ2401 for 20 seconds and then in neat PSC developer for approximately 2-3 minutes, though in practice the sample would be developed in the PSC developer in 20-30s steps until the required length was well known; only a very small amount of undercutting was needed (the undercutting would only be barely visible on the highest magnification of the optical microscopes in the clean room at the time) over developing could lead to distortion of features particularly the thin lines of photoresist separating the contacts of the TLM pattern.

After the source-drain metallisation pattern had been developed a plasma ash (exposure to an oxygen plasma) was needed in order to remove any photoresist that remained in the exposed areas. Without one of these etches the metal once deposited would lift-off, or would come loose under probe contact. The plasma ash was accomplished in the barrel plasma asher in the Materials and Mineralogy department. The etch rate of photoresist in the barrel asher was a strong function of the sample's position in the chamber (see Figure 8-3). The reason for the change in etch rate as a function of distance into the chamber was presumed to be due to the fact that the electrodes which generated the plasma were set-back a couple of centimetres from the chamber entrance. The samples used earlier on were placed next to the chamber door for 30s; however, in later studies (due to concerns about whether any photoresist was being left on the surface) the samples were placed at approximately 3.5 cm into the chamber and etched for 30s, even though an EDX study did not show any significant difference between a control sample and samples placed at 0cm, 3.5cm or 7cm from the chamber entrance.

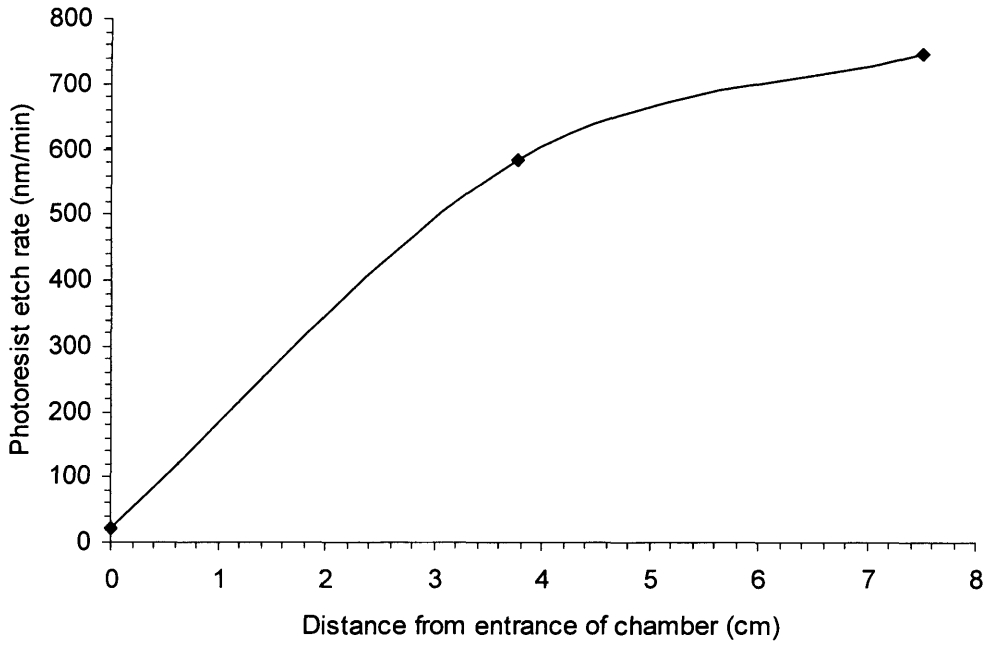

Figure 8-3 Photoresist etch rate as a function of distance into the barrel asher chamber.

Ohmic and Schottky contact metallisations

Ohmic contacts anneal program

Samples were left in the rapid thermal annealer (RTA) for five minutes with nitrogen flowing into the chamber at 100 flow units as measured by the *sho-rate* flow meters installed in the RTA. The program for the anneal was a 1min ramp from 20°C to ten degrees celsius below the desired temperature followed by a 15s ramp from ten degrees below the desired temperature to the desired temperature, followed by a 30s anneal at the desired temperature followed by a two minute ramp down to 20°C with nitrogen flowing. This was followed by an automatic cooling step.

Schottky contacts

Schottky contacts were made using the lift-off process described above; however, instead of the oxygen plasma ash, a 30s 1:9 HF acid:H_2O dip was used instead. The

samples were transferred from the dilute HF acid etch to the metal evaporator as quickly as possible (less than five minutes).

Plasma etches

Plasma etch used for development of flowbake

Gas flow rate (sccm)		RF Power (W)	DC bias (V)	ICP Power (W)	Chamber Pressure (mtorr)	Table Temp. (°C)	Helium Pressure (torr)	Etch rate (Å/min)
Cl_2	BCl_3							
15	25	100	190	1000	10	20	10	800

Samples were etched for two minutes, thermal contact between the silicon sample and the silicon carrier wafer was ensured by fomblin oil.

[1] S. Logothetidis, J. Petalas, M. Cardona, and T. D. Moustakas. Optical properties and temperature dependence of the interband transitions of cubic and hexagonal GaN. Phys. Rev. B. **50** (24) 1994 pp 18017-18029.

[2] J. Petalas et al. Optical and electronic-structure study of cubic and hexagonal GaN thin films. Phys. Rev. B. **52** (11) 1995 pp 8082 – 8091.

[3] Z. Z. Bandic et al. High voltage (450V) GaN Schottky rectifiers. Appl. Phys. Lett. **74** (9) 1999 pp 1266-1268.

[4] V. A. Dmitriev et al. Electric breakdown in GaN p-n junctions. Appl. Phys. Lett. **68** (2) 1996 pp 229-231.

[5] R. T. Kemerley, H. B. Wallace and M. N. Yoder. Impact of Wide Band gap Microwave Devices on DoD Systems. Proc. IEEE **90** (6) 2002 pp 1059-1064.

[6] D. I. Florescu et al. Thermal conductivity of fully and partially coalesced lateral epitaxial overgrown GaN/Sapphire (0001) by scanning thermal microscopy. Appl. Phys. Lett. **77** (10) 2000 pp 1464-1466.

[7] U. V. Bhapkar and M. S. Shur. Monte Carlo calculation of velocity-field characteristics of wurtzite GaN. J. Appl. Phys. **82** (4) 1997 pp1649-1655.

[8] A. Matulionis et al. Drift velocity saturation and hot-phonon disintergration in AlGaN/AlN/GaN channels. WOCSDICE 2005 pp 71-72.

[9] V. Bougrov et al. IN: Properties of advanced semiconductor materials GaN, AlN, InN, BN, SiC, SiGe. Ed M. E. Levinshtein, S. L. Rumyantsev and M. S. Shur. John Wiley and Sons, Inc. UK. 2001 p6.

[10] Delage, S. Project outline. http://www.telecom.gouv.fr/rnrt/rnrt/projets/res_02_38.htm.

[11] M. S. Shur. GaN based transistors for high power applications. Solid State Electron. **42** (12) 1998 pp 2131 – 2138.

[12] M. Hatcher. Wide-band gap device makers need to find high-volume uses. Compound Semiconductor Online Journal. www.compoundsemiconductor.net. Nov. 2004.

[13] R. T. Kemerley, H. B. Wallace and M. N. Yoder. Impact of Wide Band gap Microwave Devices on DoD Systems. Proc. IEEE. **90** (6) 2002 pp 1059-1064.

[14] Ladbrooke P. H. MMIC Design: GaAs FETs and HEMTs. Artech House Inc. 1989. U.S.A.

[15] U. K. Mishra, P. Parikh and Y. Wu. AlGaN/GaN HEMTs—An Overview of Device Operation and Applications. Proc. IEEE. **90** (6) 2002 pp 1022-1031.

[16] S. Yoshida. Growth of cubic III-nitride semiconductors for electronics and optoelectronics application. Physica E. **7** (3-4) 2000 pp 907-914.

[17] N. X. Nguyen et al. Robust low microwave noise GaN MODFETs with 0.60 dB noise figure at 10GHz. Electron. Lett. **36** (5) 2000 pp 469-471.

[18] Larry Sadwick, Jennifer Hwu and Dean Anderson. Microfabricated Next-Generation Millimeter-Wave Power Amplifiers. Power Electronics Technology, March 2004

[19] O. Ambacher et al. Two-dimensional electron gases induced by spontaneous and piezoelectric polarization charges in N- and Ga-face AlGaN/GaN heterostructures. J. Appl. Phys. **85** (6) 1999 pp 3222-3232.

[20] I. P. Smorchkova et al. Polarization-induced charge and electron mobility in AlGaN/GaN heterostructures grown by plasma-assisted molecular-beam epitaxy. J. Appl. Phys. **86** (8) 1999 pp4520-4526.

[21] J. P. Ibbetson et al. Polarization effects, surface states, and the source of electrons in AlGaN/GaN heterostructure field effect transistors. Appl. Phys. Lett. **77** (2) 2000 pp 250-252.

[22] P. M. Asbect et al. Enhancement of base conductivity via the piezoelectric effect in AlGaN/GaN HBTs. Solid State Electron. **44** (2) 2000 pp 211-219.

[23] E. T. Yu et al. Schottky barrier engineering in III-V nitrides via the piezoelectric effect. Appl. Phys. Lett. 73 (13) 1998 pp 1880-1882.

[24] B. Jogai. Free electron distribution in AlGaN/GaN heterojunction field-effect transistors. J. Appl. Phys. **91** (6) 2002 pp 3721-3729.

[25] S. C. Binari, P. B. Klein and T. E. Kazior. Trapping effects in GaN and SiC microwave FETs. Proc. IEEE. **90** (6) 2002 pp 1048-1058.

[26] S. C. Binari et al. Trapping effects and microwave power performance in AlGaN/GaN HEMTs. IEEE Trans. Elec. Dev. **48** (3) 2001 pp 465 – 471.

[27] S. Arulkumaran, T. Egawa, H. Ishikawa and T. Jimbo. Comparitive study of drain-current collapse in AlGaN/GaN high-electron-mobility transistors on sapphire and semi-insulating SiC. Appl. Phys. Lett. **81** (16) 2002 pp 3073-3075.

[28] P.B. Klein et al. Current collapse and the role of carbon in AlGaN/GaN high electron mobility transistors grown by metalorganic vapor-phase epitaxy. Appl. Phys. Lett. **79** (21) 2001 pp 3527-3529.

[29] M.A. Khan, M. S. Shur, Q. C. Chen and J. N. Kuznia. Current/voltage characteristic collapse in AlGaN/GaN heterostructure insulated gate field effect transistors at high drain bias. Electron. Lett. **30** (25) 1994 pp 2175-2176.

[30] Koudymov et al. Maximum current in nitride-based heterostructure field-effect transistors. Appl. Phys. **80** (17) 2002 pp 3216-3218.

[31] E. M. Chumbes. Microwave performance of AlGaN/GaN metal insulator semiconductor field effect transistors on sapphire substrates. IEEE Trans. Elec. Dev. **48** (3) 2001 pp 416-419.

[32] A. Tarakji et al. DC and microwave performance of a GaN/AlGaN MOSHFET under high temperature stress. Solid State Electron. **46** (8) 2002 pp 1211-1214.

[33] B. Gaffey, L. J. Guido, X. W. Wang and T. P. Ma. High-quality oxide/nitride/oxide gate insulator for GaN MIS Structures. IEEE Trans. Elec. Dev. **48** (3) 2001 pp 458-464.

[34] Y. F. Wu et al. Very-high power density AlGaN/GaN HEMTs. IEEE Trans. Elec. Dev. **48** (3) 2001 pp 586-590.

[35] S.W. King, R. J. Nemanich and R. F Davis. Band offsets at interfaces between AlN, GaN and InN. In Edgar, James, H. (ed), Properties, Processing and Applications of Gallium Nitride and Related Semiconductors. London, 1999, pp 500-505.

[36] X. Hu et al. Si_3N_4/AlGaN/GaN-metal-insulator-semiconductor heterostructure field-effect transistors. Appl. Phys. Lett. **79** (17) 2001 pp 2832-2834.

[37] I. Daumiller et al. Current instabilities in GaN-based devices. IEEE Electron Device Lett. **22** (2) 2001 pp 62-64.

[38] A. Tarakji et al. Mechanism of radio-frequency current collapse in GaN-AlGaN field-effect transistors. Appl. Phys. Lett. **78** (15) 2001 pp 2169–2171.

[39] Meneghesso G. et al. Surface-related drain current dispersion effects in AlGaN-GaN HEMTs. IEEE T. Electron Dev. **51** (10) 2004 pp 1554-1561.

[40] R. Ventury et al. The impact of surface states on the DC and RF characteristics of AlGaN/GaN HFETs. IEEE Trans. Elec. Dev. **48** (3) 2001 pp 560-566.

[41] S. Trassaert et al. Trap effects studies [sic] in GaN MESFETs by pulsed measurements. Electron. Lett. **35** (16) 1999 pp 1386-1388.

[42] J. C. Huang et al An AlGaAs/InGaAs pseudomorphic high electron mobility transistor with improved breakdown voltage and X- and Ku- band power applications. IEEE Trans. Microwave Theory Tech. **41** (5) 1993 pp 752-759.

[43] E. Kohn et al. Large signal frequency dispersion of AlGaN/GaN heterostructure field effect tranisistors. Electron. Lett. **35** (12) 1999 pp 1022-1024.

[44] G. Simin et al. Induced strain mechanism of current collapse in AlGaN/GaN heterostructures field-effect transistors. Appl. Phys. Lett. **79** (16) 2001 pp 2651-2653.

[45] R. Coffie et al. p-capped GaN-AlGaN-GaN high electron mobility transistors (HEMTs). IEEE Electron Device Lett. **23** (10) 2002 pp 588 – 590.

[46] J. K. Gillespie et al. Effects of Sc_2O_3 and MgO passivation layers on the output power of AlGaN/GaN HEMTs. IEE Electron. Device. Lett. **23** (9) 2002 pp 505-507.

[47] W. S. Tan, P. A. Houston, P. J. Parbrook, G. Hill and R. J. Airey et al. The effects and mitigation of electron traps in AlGaN/GaN HFETs and MISFETs. PREP 2002 book of abstracts (oral presentations) pp 17-19.

[48] Kohn E. et al.Transient characteristics of GaN-based heterostructure field-effect transistors. IEEE T. Microw. Theory. **51** (2) 2003 pp 634-642.

[49] P. G. Neudeck, R. S. Okojie, and C. Liang-Yu . High-temperature electronics - a role for wide band gap semiconductors? Proc. IEEE. **90** (6) 2002 pp 1065- 1076

[50] JCPDS International Centre for Diffraction Data; Powder diffraction file 1996: PDF- 2 databases sets 1-46; Pennsylvania, 1996.

[51] M. Leszczynski, T. Suski, J. Domagala and P. Prystawko; Lattice parameters of the group III nitrides. In Edgar, James, H. (Ed), Properties, Processing and Applications of Gallium Nitride and Related Semiconductors. London, 1999, pp 6-9.

[52] M. Leszczynski et al., Thermal expansion of gallium nitride. J. Appl. Phys. **76** (8), 1994, pp 4909-4911.

[53] Bougrov V., Levinshtein M.E., Rumyantsev S.L., Zubrilov A., in Properties of Advanced SemiconductorMaterials GaN, AlN, InN, BN, SiC, SiGe . Eds. Levinshtein M.E., Rumyantsev S.L., Shur M.S., John Wiley & Sons, Inc., New York, 2001, 1-30.

[54] A. Trampert, O. Brandt, and K. H. Ploog ; Crystal Structure of Group III Nitrides. In Jacques I. Pankove and Theodore D. Moustakas (Eds.), Gallium Nitride (GaN) 1. San Diego, 1997, pp167-192

[55] O. Lagerstedt and B. Monemar, Variation of lattice parameters in GaN with stoichiometry and doping. Phys. Rev. B. 19 (6) 1979 pp 3064-3070.

[56] M. Leszczynski, et al. Lattice parameters of gallium nitride; Appl. Phys. Lett. **69** (1) 1996 pp 73-75.

[57] M. Leszczynski, et al. Lattice parameters of GaN single crystals, homoepitaxial layers and heteroepitaxial layers on sapphire. Journal of Alloys and Compounds **286** (2) 1999 pp 271-275.

[58] M. Leszczynski et al., Lattice constants, thermal expansion and compressibility of gallium nitride. J. Phys. D: Appl. Phys. **28** (4A) 1995 pp A149-A153.

[59] S. C. Jain, M. Willander, and H. Maes. Stresses and strains in epilayers, stripes and quantum structures of III–V compound semiconductors. Semicond. Sci. Technol. **11** (5) 1996 pp 641-671; Erratum **11** (6) 1996 pp 975.

[60] S. F. Fang et al. Gallium arsenide and other compound semiconductors on silicon. J. Appl. Phys. **68** (7) 1990 pp R31-R58.

[61] S. Porowski. Growth and properties of single crystalline GaN substrates and homoepitaxial layers. Mat. Sci. Eng. B. **44** (1-3) 1997 pp 407-413.

[62] S. Porowski and I. Grzegory. Thermodynamical properties of III-nitrides and crystal growth of GaN at high N_2 pressure. J. Crystal Growth. **178** (1-2) 1997 pp 174-188.

[63] G. A. Slack. J. Phys. Chem. Solids. **34** (?) 1973 pp 321-335

[64] X. L. Chen et al. Structure and Debye temperature of WZ GaN. Modern Physics Letters B. **13** (9-10) 1999 pp 285-290.

[65] S. Krukowski, M. Leszczynski and S. Porowski. Thermal properties of the group III nitirides. In Edgar, James, H. (ed), Properties, Processing and Applications of Gallium Nitride and Related Semiconductors. London, 1999, pp 402-408.

[66] A. Witek. Some aspects of thermal conductivity of isotopically pure diamond - A comparison with nitrides. Diamond Relat. Mater. **7** (7) 1998 pp 962-964.

[67] J.C. Nipko, C. -K. Loong, C. M. Balkas, and R. F. Davis. Lattice Dynamics and Thermodynamic Properties of Bulk Gallium Nitride: A Neutron-Scattering Study. Appl. Phys. Lett. **73** (1) 1998 pp 34-35.

[68] D. Kotchetkov, et al. Effect of dislocations on thermal conductivity of GaN layers. Appl. Phys. Lett. **79** (26) 2001 pp 4316-4318.

[69] E. K. Sichel and J. I. Pankove. Thermal conductivity of GaN, 25-360 K. J. Phys. Chem. Solids **38** (3) 1977 pp 330.

[70] D. I. Florescu et al. High spatial resolution thermal conductivity Raman spectroscopy investigation of hydride vapor phase epitaxy grown n-GaN/sapphire (0001): Doping dependence. J. Appl. Phys. **88** (6) 2000 pp 3295-3300.

[71] D. I. Florescu et al. Thermal conductivity of fully and partially coalesced lateral epitaxial overgrown GaN/Sapphire (0001) by scanning thermal microscopy. Appl. Phys. Lett. **77** (10) 2000 pp1464-1466.

[72] R. Berman. Comment on Witek's paper on thermal conductivity of some nitrides. Diamond Relat. Mater. **8** (11) 1999 pp 2016-2017.

[73] A. Trampert, et al. Structural properties of GaN epilayers directly grown on on-axis 6H-SiC (0001) by plasma-assisted MBE. J. Crystal Growth. **201-202** 1999 pp 407-410.

[74] M. Suzuki and T. Uenoyama. Electronic band structures of GaN and AlN. In Edgar, James, H. (ed), Properties, Processing and Applications of Gallium Nitride and Related Semiconductors. London, 1999, pp 159-167.

[75] M. Suzuki and T. Uenoyama. Electronic and optical properties of GaN-based quantum wells. In Group III Nitride semiconductor Compounds Physics and Applications. Bernard Gill (Ed). Oxford Science Publications. 1998.

[76] Rubio. A et al. Quasi particle band structure of AlN and GaN. Phys. Rev. B. **48** (15-16) 1993 pp 11810-11816.

[77] Y. C. Yeo, T. C. Chong, and M. F. Li. Electronic band structures and effective-mass parameters of WZ GaN and InN. J. Appl. Phys. **83** (3) 1998 pp1429-1436.

[78] W. R. L. Lambrecht et al. UV reflectivity of GaN: Theory and experiment. Phys. Rev. B. **51** (19) 1995 pp 13516-13532.

[79] M. Goano et al. Band structure non-local pseudopotential calculation of the III-nitride WZ phase materials system. Part I. Binary compounds GaN, AlN, and InN. J. Appl. Phys. **88** (11) 2000 pp 6467-6475.

[80] J. Kolnik et al. Electronic transport studies of bulk ZB and WZ phases of GaN based on an ensemble Monte Carlo calculation including a full zone band structure. J. Appl. Phys. **78** (2) 1995 pp 1033-1038.

[81] J. Petalas et al. Optical and electronic-structure study of cubic and hexagonal GaN thin films. Phys. Rev. B. **52** (11) 1995 pp 8082 – 8091.

[82] M. Suzuki, T. Uenoyama, and A. Yanase. First principles calculations of effective mass parameters of AlN and GaN. Phys. Rev. B. **52** (11) 1995 pp 8132-8139.

[83] Su-Huai Wei and Alex Zunger. Valence band splittings and band offsets of AlN, GaN and InN. Appl. Phys. Lett. **69** (18) 1996 pp 2719-2721.

[84] S. C. Jain, M Willander, J. Narayan and R. Van Overstraeten. III-Nitrides: Growth, characterisation, and properties. J. Appl. Phys. **87** (3) 2000 pp 965-1006.

[85] B. Monemar. Fundamental energy gap of GaN from photoluminescence excitation spectra. Phys. Rev. B. **10** (2) 1974 pp 676-681.

[86] Amane Shikanai et al. Biaxial strain dependence of exciton resonance energies in WZ GaN. J. Appl. Phys. **81** (1) 1997 pp 417-424.

[87] I. Vurgaftman and J. R. Meyer. Band parameters for nitrogen-containing semiconductors. J. Appl. Phys. **94** (6) 2003 pp 3675-3696.

[88] M. Suzuki and T. Uenoyama. First principles calculation of effective mass parameters of GaN. Solid-State Electronics. **41** (2) 1997 pp 271-274.

[89] I. Vurgaftman, J. R. Meyer and L. R. Ram-Mohan. Band parameters for III-V compound semiconductors and their alloys. J. Appl. Phys. **89** (11) 2001 pp 5815-5875.

[90] M. Suzuki, T. Uenoyama, and A. Yanase. First-principles calculation of effective-mass parameters of AlN and GaN. Phys. Rev. B. **52** (11-15) 1995 pp 8132-8139.

[91] Y. P. Varshni. Temperature dependence of the energy gap in semiconductors. Physica **34** (?) 1997 pp 149-154.

[92] M. Omar Manasreh. Properties of III-nitride semiconductors. MRS Internet J. Nitride Semicond. Res. People, discussions 1996.

[93] H. Teisseyre et al. Temperature dependence of the energy gap in GaN bulk single crystals and epitaxial layer. J. Appl. Phys. **76** (4) 1994 pp 2429-2433.

[94] Annamraju Kasi Viswanath, Joo In Lee, Sungkyu Yu, Dongho Kim, Yoonho Choi and Chang-hee Hong. Photoluminescence studies of excitonic transitions in GaN epitaxial layers. J. Appl. Phys. **84** (7) 1998 pp 3848-3859.

[95] R. Pässler; Dispersion-related assessments of temperature dependences for the fundamental band gap of hexagonal GaN; J. Appl. Phys. **90** (8) 2001 pp 3956-3964.

[96] W. Shan et al. Strain effects on excitonic transitions in GaN: deformation potentials. Phys. Rev. B. **54** (19) 1996 pp 13460-13463.

[97] B. Monemar et al. Electronic structure and temperature dependence of excitons in GaN. Mat. Sci. Eng. B. **43** (1-3) 1997 pp 172-175.

[98] O. Gfrörer, T. Schlüsener, V. Härle, F. Scholz, and A. Hangleiter. Relaxation of thermal strain in GaN epitaxial layers grown on sapphire. Mat. Sci. Eng. B. **43** (1-3) 1997 pp 250-252.

[99] S. Strite and H. Morkoç. GaN, AlN and InN: a review. J. Vac. Sci. Technol. B. **10** (4) 1992 pp 1237-1266.

[100] M. E. Levinshtein, S. L. Rumyantsev and M. S. Shur (Eds). Properities of Advanced Semiconductor Materials GaN, AlN, InN, BN, SiC, SiGe. John Wiley & Sons. UK. 2001.

[101] S. J. Pearton, F. Ren, A. P. Zhang and K. P. Lee. Fabrication and performance of GaN electronic devices. Mat. Sci. Eng. R. **30** (3-6) 2000 pp 55-212.

[102] S. J. Pearton et al. Ion implantation doping and isolation of GaN. Appl. Phys. Lett. **67** (10) 1995 pp 1435-1437.

[103] J. C. Zolper et al. Electrical and structural analysis of high-dose Si implantation in GaN. Appl. Phys. Lett. **70** (20) 1997 pp 2729-2731.

[104] J. C. Zolper et al. Ca and O ion implantation doping of GaN. Appl. Phys. Lett. **68** (14) 1996 pp 1945-1947.

[105] J. A. Fellows, Y. K. Yeo, R. L. Hengehold and D. K. Johnstone. Electrical activation studies of GaN implanted with Si from low to high dose. Appl. Phys. Lett. **80** (11) 2002 pp 1930-1932.

[106] C. Kittel. Introduction to Solid State Physics, 7th Ed. John Wiley & Sons. 1996.

[107] S.O. Kucheyev et al. Nanoindentation of epitaxial GaN films. Appl. Phys. Lett. **77** (21) 2000 pp 3373-3375.

[108] M. D. Drory et al. Hardness and fracture toughness of bulk single crystal gallium nitride. Appl. Phys. Lett. **69** (26) 1996 pp 4044-4046.

[109] G. Yu et al. Mechanical properties of the GaN thin films deposited on sapphire substrate. J. Cryst. Growth. **189/190** 1998 pp 701-705.

[110] R. Nowak et al. Elastic and plastic properties of GaN determined by nano-indentation of bulk crystal. Appl. Phys. Lett. **75** (14) 1999 pp 2070-2072.

[111] M. D. Drory et al. Hardness and fracture toughness of bulk single crystal gallium nitride. Appl. Phys. Lett. **69** (26) 1996 pp 4044-4046.

[112] A. F. Wright. Elastic properties of zinc-blende and WZ AlN, GaN, and InN. J. Appl . Phys. **82** (6) 1997 pp 2833-2839.

[113] R. B. Schwarz, K. Khachaturyan and E. R. Weber. Elastic moduli of gallium nitride. Appl. Phys. Lett. **70** (9) 1997 pp 1122-1124.

[114] Y. Takagi et al. Brillouin scattering study in the GaN epitaxial layer. Physica B. **219-220** (1-4) 1996 pp 547-549.

[115] A. Polian, M. Grimsditch, and I. Grzegory. Elastic constants of gallium nitride. J. Appl. Phys. **79** (6) 1996 pp 3343-3344.

[116] C. Kisielowski et al. Strain-related phenomena in GaN thin films Phys. Rev. B. **54** (24) 1996 pp 17745-17753.

[117] D. C. Look. Electrical transport properties of III-nitrides. Mat. Sci. Eng. B. **50** (1-3) 1997 pp 50-56.

[118] H.P. Maruska and J. J. Tietjen. The preparation and properties of vapor-deposited single-crystalline GaN. Appl. Phys. Lett. 15 (10) 1969 pp 327-329.

[119] M. Ilegems and H. C. Montgomery. Electrical properties of n-type vapor-grown gallium nitride. J. Phys. Chem. Solids. **34** (1973) pp 885-895.

[120] Jörg Neugebauer and Chris G. Van de Walle. Atomic geometry and electronic structure of native defects in GaN. Phys. Rev. B. **50** (11) 1994 pp 8067- 8070.

[121] P. Boguslawski, E. L. Briggs and J. Berholc. Native defects in gallium nitride. Phys. Rev. B. **51** (23) 1995 pp 17255-17258.

[122] D. W. Jenkins, J. D. Dow, and M. H. Tsai. N-vacancies in $Al_xGa_{1-x}N$. J. Appl. Phys. **72** (9) 1992 pp 4130-4133.

[123] C. G. Van de Walle, C. Stampfl and J. Neugebauer. Theory of doping and defects in III-nitrides. J. Cryst. Growth. **189/190** (1998) pp 505-510.

[124] T. Mattila and R. M. Nieminen. Ab initio study of oxygen point defects in GaAs, GaN and AlN. Phys. Rev. B. **54** (23) 1996 pp 16676-16682.

[125] G. Y. Zhang et al. Relationship of background carrier concentration and defects in GaN grown by metalorganic vapor phase epitaxy. Appl. Phys. Lett. **71** (23) 1997 pp 3376-3378.

[126] D. C. Look et al. Deep-center hopping conduction in GaN. J. Appl. Phys. **80** (5) 1996 pp 2960-2963.

[127] W. Kim et al. On the incorporation of Mg and the role of oxygen, silicon, and hydrogen in GaN prepared by reactive molecular beam epitaxy. J. Appl. Phys. **82** (1) 1997 pp 219-226.

[128] R.C. Powell, N. -E. Lee, Y. –W. Kim and J. E. Greene. Heteroepitaxial wurtzite and zinc-blende structure GaN grown by reactive-ion molecular-beam epitaxy: Growth kinetics, microstructure, and properties. J. Appl. Phys. **73** (1) 1993 pp 189-204.

[129] B. C. Chung and M. Gershenzon. The influence of oxygen on the electrical and optical properties of GaN crystals grown by metalorganic vapor phase epitaxy. J. Appl. Phys.**72** (2) 1992 pp 651-659.

[130] J. K. Sheu and G. C. Chi. The doping process and dopant characteristics of GaN. J. Phys.: Condens. Matter. **14** (22) 2002 pp R657-R702.

[131] D. C. Look et al. Defect donor and acceptor in GaN. Phys. Rev. Lett. **79** (12) 1997 pp 2273-2276.

[132] Perlin et al. Towards the identification of the dominant donor in GaN. Phys. Rev. Lett. **75** (2) 1995 pp 296-299.

[133] C. Wetzel et al. Pressure induced deep gap state of oxygen in GaN. Phys. Rev. Lett. **78** (20) 1997 pp 3923 – 3926.

[134] C. Wetzal et al. DX-like behaviour of oxygen in GaN. Physica B. **302-303** 2001 pp 23-38.

[135] http://www.lbl.gov/msd/PIs/Haller/98/98_4_Haller_GaN.html

[136] K. H. Ploog and O. Brandt. Doping of group III nitrides. J. Vac. Sci. Technol. A **16** (3) 1998 pp 1609-1614.

[137] M. A. di Forte-Poisson et al. Relationship between physical properties and gas purification in GaN grown by metalorganic vapor phase epitaxy. J. Cryst.Growth. **195** 1998 pp 314-318.

[138] D. Meister et al. A comparison of the Hall-effect and secondaru ion mass spectroscopy on the shallow oxygen donor in unintentional doped GaN films. J. Appl. Phys. **88** (4) 2000 pp 1811-1817.

[139] http://www2.parc.com/eml/members/vandewalle/gan-theory/doping.html

[140] C. Wetzel et al. Carrier localization of as-grown n-type gallium nitride under large hydrostatic pressure. Phys. Rev. B. **53** (3) 1996 pp 1322-1326.

[141] W. Götz et al. Hall-effect characterization of III-nitride semiconductors for high efficiency light emitting diodes. Mat. Sci. Eng. B. **59** (1-3) 1999 pp 211-217.

[142] J. C. Zolper. Ca and O ion implantation doping of GaN. Appl. Phys. Lett. **68** (14) 1996 pp 1945-1947.

[143] W. J. Moore, J. A. Freitas, Jr. R. J. Molnar. Zeeman spectroscopy of shallow donors in GaN. Phys. Rev. B **56** (19) 1997 pp 12073-12076.

[144] W. J. Moore. Identification of Si and O donors in hydride-vapor-phase epitaxial GaN. Appl. Phys. Lett. **79** (16) 2001 pp 2570-2572.

[145] H. Wang and A. -B. Chen. Calculation of shallow donor levels in GaN. J. Appl. Phys. **87** (11) 2000 pp 7859-7863.

[146] F. Mireles and S. E. Ulloa. Zeeman splitting of shallow donors in GaN. Appl. Phys. Letts. **74** (2) 1999 pp 248-250.

[147] G. L. Pearson and J. Bardeen. Electrical Properties of Pure Silicon and Silicon Alloys Containing Boron and Phosphorus. Phys. Rev. **75** (1-5) 1949 pp 865-869. And Erratum by same authors Phys. Rev. **77** (2-15) 1950 pp 303.

[148] A. Ferreira da Silva and C. Persson. Critical concentration for the doping-induced metal–nonmetal transition in cubic and hexagonal GaN. J. Appl. Phys. **92** (5) 2002 pp 2550-2555.

[149] J.D. Albrecht, P.P. Ruden, E. Bellotti, and K.F. Brennan. Monte Carlo simulation of Hall effect in n-type GaN. MRS Internet J. Nitride Semicond. Res. 4S1, G6.6 (1999).

[150] W. Götz et al. Activation energies of Si donors in GaN. Appl. Phys. Lett. **68** (22) 1996 pp 3144-3146.

[151] Y. J. Wang et al. Magneto-optical studies of GaN and GaN/$Al_xGa_{1-x}N$: Donor Zeeman spectroscopy and two dimensional electron gas cyclotron resonance. J. Appl. Phys. **79** (10) 1996 pp 8007-8010.

[152] J. Jayapalan, B. J. Skromme, R. P. Vaudo. And V. M. Phanse. Opitical spectroscopy of Si-related donor and acceptor levels in Si-doped GaN grown by hydride vapor phase epitaxy. Appl. Phys. Lett. **73** (9) 1998 pp 1188-1190.

[153] D. Huang et al. Hall mobility and carrier concentration in free-standing high quality GaN templates grown by hydride vapor phase epitaxy. Solid-State Electron **45** (5) 2001 pp 711-715.

[154] F. Yun et al. Electrical, structural, and optical characterization of freestanding GaN template grown by hydride vapor phase epitaxy. Solid-State Electron. **44** (12) 2000 pp 2225-2232.

[155] Q. S. Zhu and N. Sawakia. Nitrogen vacancy scattering in n-GaN grown by metal-organic vaporphase epitaxy. Appl. Phys. Lett. **76** (12) 2000 pp 1594-1596.

[156] X. Du et al. Cubic phase in hexagonal GaN thin film and its influence on mobility. Solid State Commun. **107** (10) 1998 pp 543-546.

[157] H. M. Ng et al. The role of dislocation scattering in n-type GaN films. Appl. Phys. Lett. **73** (6) 1998 pp 821-823.

[158] H. W. Choi, J. Zhang, S. J. Chua. Dislocation scattering in n-GaN. Mat. Sci. Semicon. Proc. **4** (6) 2000 pp 567-570.

[159] D. C. Look and J. R. Sizelove. Dislocation scattering in GaN. Phys. Rev. Lett. **82** (6) 1999 pp 1237-1240.

[160] N. G. Weimann et al. Scattering of electrons at threading dislocations in GaN. J. Appl. Phys. **83** (7) 1998 pp 3656-3659.

[161] M. Fehrer et al. Impact of defects on the carrier transport in GaN. J. Cryst. Growth. **189/190** 1998 pp 763-767.

[162] R. J. Molnar, T. Lei, and T. D. Moustakas. Electron transport mechanism in gallium nitride. Appl. Phys. Lett. **62** (1) 1993 pp 72-74.

[163] D. C. Look et al. Deep-centre hopping conduction in GaN. J. Appl. Phys. **80** (5) 1996 pp 2960-2963.

[164] C. S. Hung and J. R. Gliessman. Resistivity and Hall effect on germanium at low temperatures. Phys. Rev. **96** (5) 1954 pp 1226-1236.

[165] D. C. Look and R. J. Molnar Degenerate layer at GaN/sapphire interface: Influence on Hall-effect measurements. Appl. Phys. Lett. **70** (25) 1997 pp 3377-3379.

[166] D.C. Look et al. Dislocation-independent mobility in lattice-mismatched epitaxy: application to GaN. Solid State Communications **117** (10) 2001 pp 571-575.

[167] D. C. Look. Electrical transport properties of III-nitrides. Mat. Sci. Eng. B. **50** (1-3) 1997 pp 50-56.

[168] W. Götz et al. Hall-effect analysis of GaN films grown by hydride vapor phase epitaxy. Appl. Phys. Lett. **72** (10) 1998 pp 1214-1216.

[169] X. Xu et al. Residual donors and compensation in metalorganic chemical vapor deposition as-grown n-GaN. J. Appl. Phys. **90** (12) 2001 pp 6130 – 6134.

[170] X. L. Xu. Formation mechanism of a degenerate thin layer at the interface of a GaN/sapphire system. Appl. Phys. Lett. **76** (2) 2000 pp 152-154.

[171] M. G. Cheong et al. Conductive layer near the GaN/sapphire interface and its effect on electron transport in unintentionally doped n-type GaN epilayers. Appl. Phys. Lett. **77** (16) 2000 pp 2557-2559.

[172] Z-Q. Fang et al. Deep centers in n-GaN grown by reactive molecular beam epitaxy. Appl. Phys. Lett. **72** (18) 1998 pp 2277-2279.

[173] J. M. Barker et al. High-field transport studies of GaN. Physica B **314** 2002 pp 39-41.

[174] M. Wraback et al. Time-resolved electroabsorption measurement of the electron velocity-field characteristic in GaN. Appl. Phys. Lett. **76** (9) 2000 pp 1155-1157.

[175] J. D. Albrecht et al. Electron transport characteristics of GaN for high temperature device modeling. J. Appl. Phys. **83** (9) 1998 pp 4777-4781.

[176] L. D. Bell et al. Ballistic-electron-emission microscopy and spectroscopy of metal/GaN interfaces. Appl. Phys. Lett. **72** (13) 1998 pp 1590-1592.

[177] U. V. Bhapkar and M. S. Shur. Monte Carlo calculation of velocity-field characteristics of wurtzite GaN. J. Appl. Phys. **82** (4) 1997 pp 1649-1655.

[178] J. M. Wagner and F. Bechstedt. Properties of strained wurtzite GaN and AlN: *Ab initio* studies; Phys. Rev. B; **66** (11) 2002 art.no. 115202.

[179] K. Karch, J. M. Wagner, F. Bechstedt. *Ab initio* study of structural, dielectric, and dynamical properties of GaN; Phys. Rev. B. **57** (12) 1998 pp 7043-7049.

[180] T Amhata, T Sota:, K Sumki and S Nakamura. Polarized Raman spectra in GaN; J. Phys.: Condens. Matter. **7** (10) 1995 pp LI29-Ll33.

[181] J. H. Billen and L. M. Young. Superfish Documentation, SFCODES. 1992.

[182] D. Kajfez and P. Guillon Eds. Dielectric Resonators 2nd edition. Noble Publishing Corporation. 1998. USA.

[183] http://laacg1.lanl.gov/laacg/services/psann.html#ftp

[184] J. H. Billen and L. M. Young . Superfish Documentation, SFPHYS5. 1992.

[185] R. E. Collin. Foundations for Microwave Engineering. McGraw-Hill International Book Company. 1966. Singapore.

[186] P. R. Karme., G. D. Colef and R. L. Camisa. Introduction to Electromagnetic and Microwave Engineering. John Wiley & Sons. 1997. USA.

[187] M. Sucher and J. Fox Eds. Handbook of Microwave Measurements 3rd Edition Vol. II. Polytechnic Press of the Polytechnic Institute of Brooklyn (a division of John Wiley & Sons). 1963. USA.

[188] A. Porch. Un-published work. 2006

[189] J. Krupka and J. Mazierska. Single-crystal dielectric resonators for low-temperature electronics applications. IEEE Trans Microwave Theory Tech. **48** (7) 2000 pp 1270-1274.

[190] T Amhata, T Sota:, K Sumki and S Nakamura. Polarized Raman spectra in GaN; J. Phys.: Condens. Matter. **7** (10) 1995 pp LI29-Ll33.

[191] J. M. Wagner and F. Bechstedt. Properties of strained wurtzite GaN and AlN: *Ab initio* studies; Phys. Rev. B; **66** (11) 2002 art.no. 115202.

[192] K. Karch, J. M. Wagner, F. Bechstedt. *Ab initio* study of structural, dielectric, and dynamical properties of GaN; Phys. Rev. B. **57** (12) 1998 pp 7043-7049.

[193] I. Lajoie et al. High Q microwave resonators using quartz monocrystal. Electron. Lett. **36** (2) 2000 pp 150-152.

[194] R. G. Geyer and J. Krupka. Microwave dielectric properties of anisotropic materials at cryogenic temperatures. IEEE T. Instrum. Meas. **44** (2) 1995 pp 329-331.

[195] A. Nakayama. A measurement method of complex permittivity at pseudo microwave frequencies using a cavity resonator filled with dielectric material. IEICE Trans. Electron. **E77-C** (6) 1994 pp 894-899.

[196] X. L. Zu et al. Formation mechanism of a degenerate thin layer at the interface of a GaN/sapphire system. Appl. Phys. Letts. **76** (2) 2000 pp 152-154.

[197] M. G. Cheong et al. Conductive layer near the GaN/sapphire interface and its effect on electron transport in unintentionally doped n-type GaN epilayers. Appl. Phys. Letts. **77** (16) 2000 pp 2557-2559.

[198] D. C. Look. Electrical transport properties of III-nitrides. Mat. Sci. Eng. B. **50** (1-3) 1997 pp 50-56.

[199] W. Götz et al. Hall-effect analysis of GaN films grown by hydride vapour phase epitaxy. Appl. Phys. Letts. **72** (10) 1998 pp 1214-1218.

[200] D.C. Look and R. J. Molnar. Degenerate layer at GaN/sapphire interface: Influence on Hall-effect measurements. Appl. Phys. Lett. **70** (25) 1997 pp 3377-3379

[201] Chapman B. N. Glow discharge processes: sputtering and plasma etching. New York, Chichester, Wiley, 1980.

[202] Lieberman M. A. and Lichtenberg A. J. Principles of plasma discharges and materials processing. New York, Wiley, 1980.

[203] Thiel F. and Stibila M. The Benefits of Trench Isolation in High-Voltage, High-Bandwidth Semiconductors. Analog ZONE. http://www.analogzone.com/nett0614.pdf

[204] J. J. Thomson. On the discharge of electricity through exhausted tubes without electrodes. Phil. Mag. **32** (5) 1891 pp 321-36 & 445-464.

[205] J. J. Thomson. Electrodeless discharges through gases. Phil. Mag. **4** (7) 1927 pp 1128-1160.

[206] J. S. Townsend & R. H. Donaldson. Electrodeless discharges. Phil. Mag. **5** (7) 1928 pp 178-191.

[207] K. A. MacKinnon. On the origin of electrodeless discharge. Phil. Mag. **8** (7) 1929 pp 605-616.

[208] J. Amorin, H. S. Maciel, and J. P. Sudano. High-density plasma mode of an inductively coupled radio frequency discharge. J. Vac. Sci. Technol. B. **9** (2) 1991 pp 362-365.

[209] G. D. Yarnold. Discharges maintained by electrical oscillations in solenoids. Phil. Mag. **13** (7) 1932 pp 1179-1186.

[210] S. Kubota. Breakdown of gases by purely azimuthal electric fields. Phys. Soc. Jap. **17** (8) 1962 pp 1314-1315.

[211] E.W.B. Gill and A. von Engel. Starting potentials of high-frequency gas discharges at low pressure. Proc. Roy. Soc. A. **192** (1030) 1948 pp 446-463.

[212] G. Francis and A. von Engel. The growth of the high frequency electrodelss discharge. Phil. Trans. A. **246** () 1953 pp 143-180.

[213] J. Hopwood. Review of inductively coupled plasmas for plasma processing. Plasma Sources Sci. Technol. **1** (2) 1992 pp 109-116.

[214] M. A. Lieberman & A. J. Lichtenberg. Principles of plasma discharges & materials processing. John Wiley & Sons Inc. 1994.

[215] Xue-Yu Qian & Arthur. H. Sater US Patent 6,297,468 October 2, 2001.

[216] A. Schwabedissen, E. C. Benck and J. R. Roberts. Langmuir probe measurements in an inductively coupled plasma source. Phys. Rev. E. **55** (3) 1997 pp 3450-3459.

[217] J. H. Keller, John C. Forster, and Michael S. Barnes. Novel radio-frequency induction plasma processing techniques. J. Vac. Sci. Technol. A **11** (5) 1993 pp 2487-2491.

[218] Y. J. Lee et al.. Characteristics of magnetized inductively coupled plasma source for flat panel display applications. Surf. Coat. Tech. **133-134** 2000 pp 612-616.

[219] Yaoxi Wu & M. A Lieberman. A traveling wave-driven, inductively coupled large area plasma source. App. Phys. Lett. **72** (7) 1998 pp 777-779.

[220] Se-Geun Park et al.. An array of inductively coupled plasma sources for large area plasma. Thin Solid Films. **355-356** 1999 pp 252-255.

[221] Y. H. Lee et al.. Etch characteristics of GaN using inductively coupled Cl_2/Ar and Cl_2/BCl_3 plasmas. J. Vac. Sci. Technol. A. **16** (3) 1998 pp 1478-1482.

[222] H. S. Kim et al.. Effects of plasma conditions on the etch properties of AlGaN. Vacuum **56** (1) 2000 pp 45 – 49.

[223] H. S. Kim, G. Y. Yeom, J. W. Lee and T. I. Kim. Characteristics of inductively coupled Cl_2/BCl_3 plasmas during GaN etching. J. Vac. Sci. Technol. A. **17** (4) 1999 pp 2214-2219.

[224] Y. H. Lee et al.. Magnetized inductively coupled plasma etching of GaN in Cl_2/BCl_3 plasmas. J. Vac. Sci. Technol. A. **18** (4) 2000 pp 1390-1394.

[225] S. Tripathy et al.. Characterization of inductively coupled plasma etched surface of GaN using Cl_2/BCl_3 chemistry. J. Vac. Sci. Technol. A. **19** (5) 2001 pp 2522-2532.

[226] K. Remashan, S. J. Chua, A. Ramam, S. Prakash and W. Liu. Inductively coupled plasma etching of GaN using BCl_3/Cl_2 chemistry and photoluminescence studies of the etched samples. Semicond. Sci. Technol. **15** (4) 2000 pp 386-389.

[227] B.C. Cho et al.. Inductively Coupled Plasma Etching of Doped GaN Films with Cl_2/Ar Discharges. J. Electrochem. Soc. **147** (10) 2000 pp 3914-3916.

[228] H. J. Park, R. J. Choi, Y. B. Hahn, Y. H. Im and A. Yoshikawa. Dry etching of InGaN/GaN Multiple Quantum-Well LED Structures in Inductively Coupled Cl_2/Ar Plasmas J. Korean Phys. Soc. **42** (3) 2003 pp 358-362.

[229] B. C. Cho et al.. Fast Dry Etching of Doped GaN Films in Cl_2-Based Inductively Coupled High Density Plasmas. J. Korean Phys. Soc. **37** (1) 2000 pp 23-27.

[230] Y. H. Im, C. S. Choi and Y. B. Hahn. High Density Plasma Etching of GaN Films in Cl_2/Ar Discharges with a Low-Frequency-Excited DC Bias. J. Korean Phys. Soc. **39** (4) 2001 pp 617-621.

[231] Y. B. Hahn et al.. Effect of dry etching conditions on surface morphology and optical properties of GaN films in Cl2-based inductively coupled plasmas. J. Vac. Sci. Technol. A. **19** (4) 2001 pp 1277 – 1281.

[232] H. S. Kim, G. Y. Yeom, J. W. Lee and T. I. Kim. A Study of GaN etch mechanisms using inductively coupled Cl_2/Ar plasmas. Thin Solid Films **341** 1999 pp 180-183.

[233] Y. B. Hahn et al.. Effect of additive noble gases in Cl_2-based inductively coupled plasma etching of GaN, InN and AlN. J. Vac. Sci. Technol. A. **17** (3) 1999 pp 768-773.

[234] F. A. Khan, L. Zhou, T. Ping and I. Adesida. Inductively coupled plasma reactive ion etching of AlxGa1-xN for application in laser facet formation. J. Vac. Sci. Technol. B. **17** (6) 1999 pp 2750-2754.

[235] Y. H. Im et al.. Cl_2-based dry etching of GaN films under inductively coupled plasma conditions. J. Vac. Sci. Technol. A. **18** (5) 2000 pp 2169-2174.

[236] S. A. Smith et al.. High rate and selective etching of GaN, AlGaN, and AlN using an inductively coupled plasma. Appl. Phys. Lett. **71** (25) 1997 pp 3631-3633.

[237] H. Cho et al.. Cl_2-Based dry etching of the AlGaInN system in inductively coupled plasmas. Sol. State Elect. **42** (12) 1998 pp 2277-2281.

[238] J. K. Sheu et al.. Inductively coupled plasma etching of GaN using Cl_2/Ar and Cl_2/N_2 gases. J. Appl. Phys. **85** (3) 1999 pp 1970-1974.

[239] H. Cho et al.. Comparison of inductively coupled plasma Cl_2 and CH_4/H_2 etching of III-nitrides. J. Vac. Sci. Technol. A. **16** (3) 1998 pp 1631-1635.

[240] R. J. Shul et al.. Patterning of GaN in high-density Cl_2- and BCl_3- based plasmas. Mat. Res. Soc. Symp. Proc. **468** pp 355-366.

[241] H. S. Kim et al.. Etch characteristics of GaN using inductively coupled Cl_2/HBr and Cl_2/Ar plasmas. Mat. Res. Soc. Symp. Proc. **468** pp 367-372.

[242] H. Cho et al.. Low bias dry etching of III-ntrides in Cl_2-based inductively coupled plasmas. J. Electron. Mat. **27** (4) 1996 pp 166-170.

[243] R. J. Shul et al.. Selective inductively coupled plasma etching of group-III nitrides in Cl_2- and BCl_3- based plasmas. J. Vac. Sci. Technol. A. **16** (3) 1998 pp 1621-1626.

[244] S. Kim et al.. Inductively coupled plasma etching of III-N layers by using a Cl_2/N_2 Plasma. J. Korean Phys. Soc. **41** (2) 2002 pp L184-L187.

[245] S. Tripathy, S. J. Chua and A. Raman. Electronic and vibronic properties of n-type GaN: the influence of etching and annealing. J. Phys.: Condens. Matter. **14** (17) 2002 pp 4461-4476.

[246] J. M. Lee, S. W.Kim and S. J. Park. Dry etching of GaN/InGaN multiquantum wells using inductively coupled $Cl_2/CH_4/H_2/Ar$. J. Electrochem. Soc. **148** (5) 2001 pp G254-G257.

[247] R. J. Shul et al.. Comparison of dry etch techniques for GaN. Electron. Lett. **32** (15) 1996 pp 1408-1409.

[248] R. J. Shul et al.. Group-III Nitride etch selectivity in BCl_3/Cl_2 plasmas. MRS Internet J. Nitride Semicond. Res. 4S1, G8.1 (1999).

[249] R. J. Shul et al.. Inductively coupled plasma-induced etch damage of GaN p-n junctions. J. Vac. Sci. Technol. A. **18** (4) 2000 pp 1139-1143.

[250] R. J. Shul et al.. High-density plasma etch selectivity for the III-nitrides. Sol. State Elect. **42** (12) 1998 pp 2269-2276.

[251] J. M. Lee, K. M. Chang, S. J. Park and H. K. Jang. Inductively coupled $Cl_2/Ar/O_2$ plasma etching of GaN, InGaN and AlGaN. J. Korean Phys. Soc. **37** (6) 2000 pp 842-845.

[252] S. A. Smith et al.. Selective etching of GaN over AlN using an inductively coupled plasma and an $O_2/Cl_2/Ar$ chemistry. J. Vac. Sci. Technol. A **18** (3) 2000 pp 879-881.

[253] J. M. Lee, K. M. Chang, I. H. Lee and S. J. Park. Highly selective dry etching of III nitrides using an inductively coupled $Cl_2/Ar/O_2$ plasma. J. Vac. Sci. Technol. B **18** (3) 2000 pp 1409-1411.

[254] H. S. Kim et al.. Effects of inductively coupled plasma conditions on the etch properties of GaN and ohmic contact formations. Mat. Sci. Eng. B. **50** (1-3) 1997 pp 82-87.

[255] J. M. Lee, K. M. Chang, I. H. Lee and S. J. Park. Cl_2-Based dry etching of GaN and InGaN using inductively coupled plasma the effects of gas additives. J. Electrochem. Soc. **147** (5) 2000 pp 1849-1863.

[256] R. J. Shul et al.. Inductively coupled plasma etching in GaN. Appl. Phys. Lett. **69** (8) 1996 pp 1119-1121.

[257] Franz G, Hösler W and Treichler R. Sidewall passivation of GaAs in BCl_3-containing atmospheres. J. Vac. Sci. Technol. B. **19** (2) 2001 pp 415-419.

[258] M. A. Lieberman and A. J. Lichtenberg, Principles of plasma discharges and materials processing. New York, John Wiley & Sons, Inc. 1994 chapter seven and erratum on internet http://www.eecs.berkeley.edu/~lieber/errata8/errata8.html.

[259] Oxford Instruments Plasma Lab 100 series user manual, notes for ICP 380

[260] M. E. Levinshtein, S. L. Rumyantsev and M. S. Shur, Properties of advanced semiconductor materials GaN, AlN, InN, BN, SiC, SiGe. John Wiley & Sons, U.K. 2001 pp 1.

[261] S.J. Pearton, F. Ren, A.P. Zhang, K.P. Lee. Fabrication and performance of GaN electronic devices. Mat. Sci. Eng. R. 30 (2000) pp 42-43.

[262] D. M. Manos and D. L. Flamm. Plasma Etch An Introduction. San Diego, Academic Press. 1988 p 107.

[263] G. D. Billing. Dynamics of molecule surface interactions. New York, John Wiley & Sons, Inc. 2000 p 11.

[264] B. N. Chapman and V. J. Minkiewicz. Flow rate effects in plasma etching. J. Vac. Sci. Technol. **15** (2) 1978 pp 329-332.

[265] W. H. Weinberg and R. P. Merrill. A Simple Classical Model for Trapping in Gas-Surface Interactions. J. Vac. Sci. Technol. **8** (6) pp 718-724.

[266] Jenichen A and Engler C. Etching of GaAs(100) Surfaces by Halogen Molecules: Density Functional Calculations on the Different Mechanisms. J. Phys. Chem. B. **105** (10) 2001 pp 1956-1960.

[267] V. A. Voronin, V. A. Prokhorov, M. Chub, V. A. Goliusov, L. N. Luchka. Chemical-equilibrium in the Ga-H-Cl system. Inorg. Mater. **22** (9) 1986 pp 1273-1276.

[268] H. F. Winters. The role of chemisorption in plasma etching. J. Appl. Phys. **49** (10) October 1978. pp 5165-5170.

[269] M. R. Ranade et al.. Enthalpy of Formation of Gallium Nitride. J. Phys. Chem. B. **104** (17) 2000 pp4060-4063

[270] R. J. Shul et al.. Inductively coupled plasma-induced etch damage of GaN p-n junctions. J. Vac. Sci. Technol. A. **18** (4) 2000 pp 1139-1143.

[271] F. A. Khan, L. Zhou, V. Kumar, and I. Adesida. Plasma-induced damage study for n-GaN using inductively coupled reactive ion etching. J. Vac. Sci. Technol. B. **19** (6) 2001 pp 2926-2929.

[272] Y. H. Lee et al. J. Vac. Sci. Technol. A. **18** (4) 2000 pp 1390-1394.

[273] B. Humphreys, M. Govett and A. Goodyear. **51** (4) 1998 pp 511-517.

[274] G. Z. Yin and D. W. Jillie. Solid State Technol. **30** (5) 1987 pp 127-132.

[275] National Institute of Standards Chemistry Web Book:
http://webbook.nist.gov/chemsitry/

[276] Private conversation with Gareth Edwards 2005.

[277] D.W. Kim et al. Solid State Electron. **47** (3) 2003 pp 549–552.

[278] Schroder D. K. Semiconductor material and device charaterization. John Wiley & Sons Inc. 1998. 2nd Edition. USA & Canada.

[279] Jones T. (Cardiff University) private conversations 2004

[280] P. A. Lomax. GaInP/InGaAs MODFET fabrication & characterisation. Cardiff School of Engineering, University of Wales. February 2002.

[281] Westwood D. (Cardiff University) and Dineen M. (Oxford Instruments Plasma Technology) private conversations 2004.

[282] H. W. Choi,a) C. Liu, E. Gu, G. McConnell, J. M. Girkin, I. M. Watson, and M. D. Dawson. Appl. Phys. Letts. **84** (13) 2004, pp 2253-2255.

[283] S-H Park, H Jeon, Y-J Sung, and G-Y Yeom. Appl. Optics. **40** (22) pp 3698-3702.

[284] Cornell Photolithography Manual,
http://www.nnf.cornell.edu/equipment/2002PhotolithManual.pdf

[285] P. Kordos, J. Bernat and M. Marso. Impact of layer structure on performance of unpassivated AlGaN/GaN HEMT. Mircoelectron Journal. **36** (3-6) 2005 pp 438-441.

[286] J. W. Johnson, et al. IEEE Elec. Dev. Lett. **25** (7) 2004 pp459 -461.

[287] Rajagopal P. et al. M.R.S. Symp. Proc. **743** (3) 2003

[288] Johnson J. W. et al. Proc. Electrochem. Soc. **6** 2004, p 405

[289] Schroder D. K. Semiconductor Material and Device Characterization (sic). New York, Wiley, 1990.

[290] M. Shur. GaAs Devices and Circuits. New York, Plenum Press, 1986.

[291] Jacobs B., Kramer M. C. J. C. M., Geluk E. J. and Karouta F. J. Crys. Growth. **241** (1-2) 2002 pp 15-18.

[292] J. A. Bardwell et al. Comparison of two different Ti/Al/Ti/Au ohmic metallization schemes for AlGaN/GaN. J. Vac. Sci. Technol. B. **20** (4) 2002 pp 1444-1447.

[293] N. Chaturvedi, U. Zeiner, J. Würfl and G. Tränkle. Mechanism of ohmic contact formatin in AlGaN/GaN high electron mobility transistors. Semiconductor Science and Technology. **21** (2) 2006 pp 175-179.

[294] Wang D. F. et al. J. Appl. Phys. **89** (11) 2001 pp 6214-6217.

[295] B. Akkal et al. Mater Chem Phys. **85** (1) 2004 pp 27-31.

[296] Maffeis T. G. G. et al. J. Appl. Phys. **92** (6) 2002 pp 3179-3186.

[297] Readinger E. D. & Mohney S.E. J. Electron. Mater. **34** (4) 2005 pp 5375-5381

[298] Liu Y. et al. Appl. Phys. Letts. **85** (24) 2004 pp 6030-6032

[299] A.V. Davydov et al. Combinatorial investigation of structural quality of Au/Ni contacts on GaN. Applied Surface Science **223** (1-3) 2004 pp 24–29.

[300] C. Gaquiere, S. Trassaert, B. Boudart and Y. Crosnier. High-power GaN MESFET on sapphire substrate. IEEE Microwave & Guided Wave Letters. **10** (1) 2000 pp 19-20.

[301] M. R. De Guire. Electronic, Magnetic and Optical Properties of Materials. 1999. http://vulcan2.mse.cwru.edu/classes/EMSE201/overheads/MillBrav.pdf